

# PHYSIK–DEPARTMENT



Observation of VHE  $\gamma$ -Rays from the Vicinity  
of magnetized Neutron Stars  
and  
Development of new Photon-Detectors for  
Future Ground based  $\gamma$ -Ray Detectors

Dissertation

von

Adam Nepomuk Otte



TECHNISCHE UNIVERSITÄT

MÜNCHEN



# Technische Universität München

Max-Planck-Institut für Physik  
(Werner-Heisenberg-Institut)

## Observation of VHE $\gamma$ -Rays from the Vicinity of magnetized Neutron Stars and Development of new Photon-Detectors for Future Ground based $\gamma$ -Ray Detectors

Adam Nepomuk Otte

Vollständiger Abdruck der von der Fakultät für Physik der Technischen Universität München zur Erlangung des akademischen Grades eines  
Doktors der Naturwissenschaften  
genehmigten Dissertation.

Vorsitzender: Univ.-Prof. Dr. H. Friedrich  
Prüfer der Dissertation:  
1. Hon.-Prof. Dr. S. Bethke  
2. Univ.-Prof. Dr. F. v. Feilitzsch

Die Dissertation wurde am 8. 6. 2007 bei der Technischen Universität München eingereicht und am 14. 9. 2007 durch die Fakultät für Physik angenommen.



*For Pia*

*The reasonable man adapts himself to the world; the unreasonable one persists in trying to adapt the world to himself. Therefore, all progress depends on the unreasonable man.*

George Bernard Shaw  
Irish dramatist & socialist (1856 — 1950)



# Summary

This thesis reports on the measurement of Very High Energy (VHE)- $\gamma$ -rays produced in the vicinity of magnetized, spinning neutron stars with the Major Atmospheric Gamma-ray Imaging Cherenkov telescope (MAGIC). In the second part the results of the development of a novel semiconductor photon detector for future improved IACTs (as well as for other detectors requiring low level light detection) are presented.

In the observational part of this thesis three pulsars are studied in the energy range between 60 GeV and several TeV: The Crab, PSR B1951+32 and PSR B1957+20.

It was a goal of this thesis to detect for the first time a  $\gamma$ -ray pulsar with a ground based experiment. For this purpose special tools were developed and a dedicated analysis chain was arranged. An event cleaning method was developed that efficiently suppresses noise of the night sky and allows one to lower the analysis threshold of MAGIC to below 100 GeV.

**The Crab** nebula is the strongest known source of VHE  $\gamma$ -rays in our Galaxy. Here I present results from 16 hours of observation performed between October and December 2005. Gamma-ray emission from the nebula was detected with a significance of  $75\sigma$ . The energy flux of the nebula was reconstructed between 60 GeV and 9 TeV. At present this is the measurement with the lowest energy threshold of any air Cherenkov telescope and closes nearly the gap between EGRET satellite observations (up to 10 GeV). The energy spectrum is well described with a variable power-law,

$$\frac{dF}{dE} = (6.0 \pm 0.2_{\text{stat}}) \times 10^{-10} \left( \frac{E}{300 \text{ GeV}} \right)^{-(2.31 \pm 0.06_{\text{stat}} \pm 0.2_{\text{syst}}) - (0.26 \pm 0.07_{\text{stat}}) \log\left(\frac{E}{300 \text{ GeV}}\right)} \text{ cm}^{-2} \text{ s}^{-1} \text{ TeV}^{-1}$$

with a systematic error on the energy scale of 27%. The spectrum shows a clear softening towards higher energies. The measurement excludes certain scenarios in which Bremsstrahlung contributes significantly to the VHE  $\gamma$ -ray flux at GeV energies. The measured spectrum is in agreement with predictions by the Synchrotron Self Compton (SSC) model.

The inverse Compton scattering peak (IC-peak) was determined at  $77 \pm 47_{\text{stat}}^{+107} {}_{-46}^{\text{syst}}$  GeV. This is the first determination of the IC-peak. The measured position is in agreement with predictions.

For the first time the  $\gamma$ -ray flux from the nebula above 200 GeV was tested for variability on timescales between several minutes and months. At all tested timescales the flux is consistent with a steady source scenario. If variability exists then the flux should change in the observed time scales by less than 10%. The integral flux  $> 200$  GeV is:

$$F_{>200 \text{ GeV}} = (1.96 \pm 0.05_{\text{stat}}) \times 10^{-10} \text{ cm}^{-2} \text{ sec}^{-1} \quad .$$

For the first time the morphology of the  $\gamma$ -ray emission was studied in the energy range between 100 GeV and 1 TeV. Within systematic uncertainties of  $1'$ , the center of gravity of the emission coincides with the position of the Crab pulsar. The emission appears pointlike within the angular resolution of the MAGIC telescope. At 100 GeV the 39% containment radius of the emission region could be restricted to be less than  $5.2'$ . At  $\sim 250$  GeV and  $> 500$  GeV the size of the emission

region is  $< 2.4'$  and  $< 1.6'$  respectively. The derived upper limits are in agreement with predictions by the SSC model.

Optical pulsation of the Crab pulsar was observed by the MAGIC camera central pixel, which was specially modified for such a study. The effective observation time of the measurement was only  $\sim 1$  second. In the reconstructed light curve the position of the main pulse is offset in phase by  $\phi = -0.0075 \pm 0.0015$  from its corresponding position in the radio range. This indicates that the optical emission comes from a region of about 75 km above the emission region in radio or that the radio and optical beams are offset by  $2.7^\circ$  to each other.

Pulsed VHE- $\gamma$ -rays emission from the Crab pulsar was not detected. However, with an analysis optimized for the lowest energies, the data indicate that pulsed emission is present at the same position in the pulse phase profile where EGRET detected pulsed emission in the highest energy data bin (mean energy  $\sim 5$  GeV). The significance of the signal is  $3\sigma$  under the assumption that pulsed emission is expected in the phase regions  $-0.06 - 0.04$  and  $0.32 - 0.43$ , coinciding with the EGRET observations.

Under the assumption that the energy spectrum of the pulsar is attenuated by an exponential cutoff the cutoff energy could be constrained to be less than 30 GeV. If the spectral shape follows a super-exponential behavior a cutoff energy as high as 65 GeV cannot be excluded.

**PSR B1951+32** has a characteristic age of  $10^5$  years and is, therefore,  $\approx 100$  times older than the Crab pulsar. The pulsar was detected with the EGRET instrument on board CGRO up to 20 GeV without an indication of a cutoff in the energy spectrum. This observations and predictions for  $\gamma$ -ray fluxes from the pulsar wind nebula were strong arguments for a deep (31 hours) observation with MAGIC. However, VHE  $\gamma$ -ray emission was not detected from the pulsar or the pulsar wind nebula. The observation excludes the current predictions for  $\gamma$ -ray emission and shows that more complex scenarios as e.g. the movement of the pulsar through the interstellar medium have to be taken into account for a correct modelling of the system.

The third pulsar analyzed, **PSR B1957+20**, is part of a binary system. The millisecond pulsar is orbited by a low mass companion with  $0.022 M_\odot$  within 9.2 hours. In earlier observations a detection of  $\gamma$ -ray emission from the Lagrange point L4 was claimed. The orbit was about evenly covered with a 13 hour long observation. VHE  $\gamma$ -ray emission was not detected. A search for pulsed  $\gamma$ -ray emission could not be performed due to the unavailability of valid ephemeris of the pulsar and binary system. The flux limit obtained in an analysis in search for steady  $\gamma$ -ray emission does not constrain the predicted  $\gamma$ -ray flux level predicted from the pulsar.

VHE  $\gamma$ -ray astronomy experienced an incredible boost when the second generation of Cherenkov telescopes came online three years ago. These instruments have about an order of magnitude higher sensitivity compared to their precursor experiments. Much of the improvement can be attributed to a higher photon collection efficiency, due to larger reflector surfaces and better cameras. However, even the most recent experiments detect only a small fraction of about 0.1% of all Cherenkov photons. An improvement in sensitivity and in lowering the threshold energy of future ground based experiments can be expected with new solid state photon detectors, which are three to four times more sensitive than classical PMTs. This was the main motivation to investigate new photon detector concepts.

Following a short review about the requirements of photon detectors in air Cherenkov telescopes I present results from the development of a new semiconductor photon detector, the back side illuminated silicon photomultiplier (BaSiPM). In this concept a photon converts in the fully depleted detector volume and the generated photoelectron drifts into one out of many small avalanche regions on the opposite side of the photon entrance window. The avalanche regions operate in limited Geiger mode.

With finite element simulations a BaSiPM was developed, which meets the requirements in air Cherenkov telescopes. The device features  $> 95\%$  photoelectron collection efficiencies, time resolutions  $\sim 2$  nsec and a homogenous electric field in the avalanche region. The simulated structure

was translated into a technology and avalanche structures were produced with several combinations of integrated resistors and capacitors.

In the evaluation of selected test structures a linear dependence of the output amplitude on the applied bias voltage above breakdown voltage was found. The analyzed structures feature gains of up to  $10^7$ . The output signal was compared to a small signal model of the avalanche structure and found to be in good agreement with the model. Based on these comparison it can be deduced that a Geiger breakdown is quenched in the analyzed structure (area of avalanche region  $\sim 80 \mu\text{m}^2$ ) if the current flowing through the junction is limited to  $2 \dots 10 \mu\text{A}$ .

For one test structure with  $80 \mu\text{m}^2$  sensitive area the dark rates were measured at room temperature as a function of the bias voltage. The dark rate increases from 300 counts per second at an overvoltage of 7.5% above breakdown voltage to 5000 counts per second at 23% overvoltage. Starting from about 20% overvoltage the dark rate is dominated by afterpulsing. The afterpulsing effect can be reduced with smaller capacitances in future structures and will not be a limiting factor for the performance of the final device.

A Monte Carlo simulation of SiPM called SiSi was developed. SiSi simulates the so-called optical crosstalk effect. The output of the simulations was compared with the measured crosstalk characteristics of a prototype SiPM. It was found that only photons with energies between 1.2 eV and 1.4 eV contribute to optical crosstalk. This can be explained with the very strong energy dependence of the photon absorption length in silicon. It was found that photons with energies between 1.2 eV and 1.4 eV are emitted with an intensity of  $2.5 \cdot 10^{-5}$  photons per avalanche carrier crossing the junction during breakdown. This is about a factor of five higher intensity than obtained by another group. The measurement is dominated by systematic uncertainties in the geometry of the studied SiPM. The measured photon production efficiency is, therefore, uncertain by a factor of two. Simulating the crosstalk behavior of a BaSiPM it was found that for a sufficient suppression of optical crosstalk the simulated BaSiPM has to operate at a gain of  $\sim 10^4$ .

In parallel to the BaSiPM development also some studies of normal front-illuminated SiPM have been carried out, which are presented in the Appendix. As one example for the application of SiPM the first ever feasibility study of SiPM as readout element in positron emission tomography is presented (this study has been published in NIM, Otte et al., 2005). An energy resolution of 22%<sup>1</sup> FWHM for a 511 keV annihilation line and a time resolution of  $(1.51 \pm 0.07)$  nsec was found when reading out the scintillation signal of LYSO crystals. The results are comparable with the performance of classical APDs as readout elements but the handling was found to be much easier due to the much lower bias voltage and the much higher noise immunity.

A new method to measure the photon detection efficiency is presented (the method has been published in NIM, Otte et al., 2006). The procedure can be used to characterize photon detectors with single photoelectron resolution. The photon detection efficiency of a hybrid photo-detector was found to be 15% less than the quantum efficiency of its photo cathode. This can possibly be attributed to the backscattering effect and a small inefficiency to focus all photoelectrons onto the anode area. The photon detection efficiency of a SiPM with 10% geometrical efficiency was measured. At an overvoltage of 3.5% above breakdown voltage, the device showed a peak photon detection efficiency of  $\sim 3.5\%$  at 609 nm. Increasing the overvoltage to 7%, the photon detection efficiency increased to 6.5% with an indication of a saturating photon detection efficiency.

---

<sup>1</sup>improved to 12.5% in later studies



# Publications

Parts of this thesis are published in the following reviewed articles:

1. ***VHE  $\gamma$ -Ray Observation of the Crab Nebula and Pulsar with MAGIC***  
J. Albert, et al. (MAGIC collaboration); corresponding author: A. N. Otte  
*submitted to ApJ*, arXiv:0705.3244 [astro-ph], 2007
2. ***Constraints on the steady and pulsed VHE  $\gamma$ -Ray Emission from Observation of PSR B1951+32 / CTB 80 with the MAGIC Telescope***  
J. Albert, et al. (MAGIC collaboration); corresponding author: A. N. Otte  
*submitted to ApJ*, astro-ph/0702077, 2007
3. ***Prospects of using Silicon Photomultipliers for the Astroparticle Physics Experiments EUSO and MAGIC***  
A. N. Otte et al.  
*IEEE Trans. Nucl. Sci.*, **53** 636–640, 2006.
4. ***A Measurement of the Photon Detection Efficiency of Silicon Photomultipliers***  
A. N. Otte et al.  
*Nuclear Instruments and Methods in Physics Research A*, **567** 360–363, November 2006.
5. ***A Test of Silicon Photomultipliers as Readout for PET***  
A. N. Otte et al.  
*Nuclear Instruments and Methods in Physics Research A*, **545** 705–715, June 2005.



# Contents

<b>1</b>	<b>Goals of this Thesis</b>	<b>1</b>
1.1	Detection of $\gamma$ -Ray Emission from Pulsars and their Nebulae . . . . .	1
1.2	Development of a novel Semiconductor Photon Detector for Future Experiments in Astroparticle Physics . . . . .	2
1.3	Structure of this Thesis . . . . .	2
<b>2</b>	<b>Short Introduction to Very High Energy <math>\gamma</math>-Ray Astrophysics</b>	<b>3</b>
2.1	VHE $\gamma$ -Ray Astrophysics . . . . .	3
2.2	Cosmic Rays . . . . .	4
2.2.1	Sources of Cosmic Rays . . . . .	5
2.3	Production Mechanisms of VHE $\gamma$ -Rays . . . . .	6
2.3.1	Interaction of charged Particles with Electromagnetic Fields . . . . .	7
<b>3</b>	<b>Pulsars and their Nebulae</b>	<b>9</b>
3.1	Introduction to Pulsars and their Nebulae from a historical Point of View . . . . .	10
3.2	Neutron Stars . . . . .	11
3.2.1	Formation of a Neutron Star . . . . .	11
3.2.2	Evolution of Neutron Stars in Binary Systems to Millisecond Pulsars . . . . .	11
3.2.3	Structure of a Neutron Star . . . . .	12
3.2.4	Magnetosphere of a Neutron Star . . . . .	13
3.2.5	Energy Loss of a rotating and magnetized Neutron Star . . . . .	13
3.3	Overview of the Pulsar Wind Nebula Complex . . . . .	15
3.4	$\gamma$ -Ray Emission in the Magnetospheres of Pulsars . . . . .	16
3.4.1	The experimental View . . . . .	16
3.4.2	The theoretical View . . . . .	17
3.5	VHE- $\gamma$ -Ray Emission in the Pulsar Wind Nebula . . . . .	21
3.5.1	VHE- $\gamma$ -ray Emission of the Crab Nebula . . . . .	21

<b>4</b>	<b>The Imaging Air Shower Cherenkov Telescope Technique and the MAGIC Telescope</b>	<b>25</b>
4.1	Air Showers . . . . .	26
4.1.1	Air Shower Detection Techniques . . . . .	26
4.1.2	Properties of Air Showers . . . . .	27
4.1.3	Cherenkov Light Emission in Air Showers . . . . .	28
4.1.4	The Night Sky Background Light . . . . .	31
4.2	The MAGIC Telescope . . . . .	31
4.2.1	The Reflector and Telescope Frame . . . . .	31
4.2.2	The Camera . . . . .	33
4.2.3	Signal Processing, Recording and Trigger . . . . .	34
<b>5</b>	<b>Data Analysis Methods and Telescope Performance</b>	<b>37</b>
5.1	Signal Extraction and Reconstruction . . . . .	37
5.1.1	Signal Extraction . . . . .	38
5.1.2	Conversion of Signal Amplitude into Photoelectrons . . . . .	38
5.2	Event Cleaning . . . . .	39
5.2.1	Standard Image Cleaning . . . . .	40
5.2.2	Image Cleaning using additional Time Information . . . . .	40
5.3	Image Parametrization . . . . .	42
5.4	Gamma Hadron Separation and Energy Estimation . . . . .	45
5.4.1	The Random Forest Method . . . . .	45
5.5	Extraction of the $\gamma$ -ray signal . . . . .	49
5.5.1	Optimal Cut in ALPHA . . . . .	49
5.6	Sky Maps . . . . .	50
5.7	Calculation of an Energy Spectrum . . . . .	52
5.8	Pulsar Analysis . . . . .	52
5.8.1	Time Correction of Signal Propagation Delays . . . . .	53
5.8.2	Correlating the Event Time with the Period of the Pulsar . . . . .	54
5.8.3	Tests for the Search of pulsed Emission . . . . .	54
5.8.4	A Method to derive an Upper Limit on the Cutoff Energy of the Pulsar Energy Spectrum . . . . .	57
5.8.5	Optimization of the upper SIZE-Cut in the Search for pulsed Emission from a Pulsar . . . . .	57
5.9	Upper Limit Calculation . . . . .	58
5.10	Systematic Errors . . . . .	58
5.10.1	Effects that influence the Energy Reconstruction . . . . .	59

5.10.2	Effects that Influence the Flux Reconstruction . . . . .	60
5.11	Performance of the MAGIC Telescope . . . . .	60
5.11.1	Sensitivity of the MAGIC Telescope derived from Observations of the Crab Nebula . . . . .	61
5.11.2	Comparison of Monte Carlo Data with real Data . . . . .	64
<b>6</b>	<b>The Crab Nebula and Pulsar</b>	<b>71</b>
6.1	Introduction . . . . .	71
6.1.1	The Crab Nebula . . . . .	72
6.1.2	The Crab Pulsar PSR B0531+21 . . . . .	72
6.1.3	Objectives of the Analysis . . . . .	72
6.2	The Data Sample and related Information . . . . .	73
6.2.1	Selection Criteria applied to the Data Sample . . . . .	73
6.2.2	Radio Ephemeris of the Crab Pulsar . . . . .	74
6.3	Analysis of the $\gamma$ -Ray Emission from the Crab Nebula between 60 GeV and 9 TeV	75
6.3.1	The Energy Spectrum . . . . .	75
6.3.2	Search for Flux Variabilities . . . . .	81
6.3.3	Morphology of the $\gamma$ -Ray Emission Region . . . . .	81
6.4	Optical Observations of the Crab Pulsar with MAGIC . . . . .	87
6.4.1	Setup of the Central Pixel of the MAGIC Camera . . . . .	88
6.4.2	Data taken with the Central Pixel and reconstructed Light Curve of the Crab Pulsar . . . . .	89
6.4.3	Absolute Position of the Main Pulse in the optical Light Curve of the Crab Pulsar . . . . .	89
6.5	Search for pulsed $\gamma$ -Ray Emission from the Crab Pulsar . . . . .	91
6.5.1	Search for pulsed VHE $\gamma$ -Ray Emission in differential Bins of estimated $\gamma$ - Ray Energy . . . . .	91
6.5.2	Upper Limit on the Cutoff Energy of the pulsed $\gamma$ -Ray Emission of the Crab Pulsar . . . . .	91
6.6	Discussion . . . . .	95
<b>7</b>	<b>Study of the Pulsar PSR B1951+32 and associated Pulsar Wind Nebula</b>	<b>97</b>
7.1	Introduction . . . . .	98
7.1.1	The Pulsar PSR B1951+32 . . . . .	98
7.1.2	The Interaction of the Pulsar with its surrounding Medium . . . . .	98
7.2	Selection and Processing of the Data Sample . . . . .	98
7.2.1	Summary of the Data Sample . . . . .	98
7.2.2	Processing of the Data . . . . .	99

7.3	Search for steady $\gamma$ -Ray Emission from the Pulsar Wind Nebula . . . . .	100
7.3.1	Steady $\gamma$ -Ray Emission from the Location of the Pulsar . . . . .	100
7.3.2	Search for $\gamma$ -Ray Emission in the Vicinity of PSR B1951+32 . . . . .	101
7.4	Search for $\gamma$ -Ray Emission from the Pulsar . . . . .	101
7.5	Discussion . . . . .	103
<b>8</b>	<b>The Black Widow Pulsar PSR B1957+20</b>	<b>109</b>
8.1	Introduction . . . . .	109
8.2	Selection and Processing of the Data Sample . . . . .	111
8.3	Search for steady $\gamma$ -Ray Emission . . . . .	111
8.4	Search for $\gamma$ -Ray Emission from the Pulsar . . . . .	113
8.5	Discussion . . . . .	113
<b>9</b>	<b>A novel Photon Detector Concept for Experiments in High Energy Physics</b>	<b>117</b>
9.1	Need for new Photon Detectors for VHE $\gamma$ -Ray Astronomy . . . . .	117
9.2	Photon Detector Requirements for Imaging Air Cherenkov Telescopes e.g. as for a MAGIC Type Telescope . . . . .	118
9.3	The Concept of the Silicon Photomultiplier . . . . .	119
9.4	Characteristics of the Silicon Photomultiplier . . . . .	121
9.4.1	The Principle of the Geiger Avalanche Diode . . . . .	121
9.4.2	A Small Signal Model of the Silicon Photomultiplier . . . . .	123
9.4.3	The Photon Detection Efficiency of SiPMs . . . . .	125
9.4.4	Optical Crosstalk . . . . .	127
9.4.5	Dynamic Range Limitation . . . . .	129
<b>10</b>	<b>Development and Evaluation of an Avalanche Structure for a BaSiPM</b>	<b>131</b>
10.1	The Back Side illuminated Silicon Photomultiplier . . . . .	131
10.1.1	Principle . . . . .	132
10.1.2	Characteristics . . . . .	132
10.2	Design and Simulation of one Cell . . . . .	133
10.2.1	Requirements of an Avalanche Structure for a BaSiPM . . . . .	133
10.2.2	Simulated and Evaluated Avalanche Structures . . . . .	133
10.2.3	Study of the Electron Collection Properties . . . . .	134
10.2.4	The predicted Electric Field in the Avalanche Region . . . . .	138
10.2.5	Simulated Characteristics during Breakdown . . . . .	139
10.3	Test Structures . . . . .	139
10.3.1	Technology for the Production of the simulated Avalanche Structure . . . . .	140

10.3.2	Designed Test Structure . . . . .	142
10.4	Evaluation of the Test Structures . . . . .	143
10.4.1	Dependence of the Signal Charge and Amplitude on Bias . . . . .	143
10.4.2	Recovery of the Electric Field in the Avalanche Region after Breakdown . . . . .	144
10.4.3	Shape of the Output Signal . . . . .	146
10.4.4	Comparison of the Output Signal with the small Signal Model . . . . .	147
10.4.5	The Dark Count Rate . . . . .	149
10.4.6	Afterpulsing . . . . .	150
10.5	Influence of Optical Crosstalk in Back Side illuminated SiPM . . . . .	151
10.5.1	Simulation of Optical Crosstalk in Silicon Photomultipliers with the Simulation Code “SiSi” . . . . .	152
10.5.2	Study of the Production Efficiency and the effective spectral Temperature of the Photons produced in Avalanches . . . . .	155
10.5.3	Prediction of Optical Crosstalk Behavior of a Back Side illuminated Silicon Photomultiplier . . . . .	161
10.6	Discussion . . . . .	162
10.6.1	About the Development of an Avalanche Structure for a BaSiPM . . . . .	162
10.6.2	About Optical Crosstalk . . . . .	163
<b>11</b>	<b>Concluding Remarks</b>	<b>167</b>
<b>A</b>	<b>A Test of Silicon Photomultipliers as Readout for PET</b>	<b>169</b>
A.1	Introduction . . . . .	169
A.2	The SiPM used in the Test Setup . . . . .	170
A.3	Experimental Setup . . . . .	171
A.3.1	Mechanics . . . . .	171
A.3.2	Signal Readout . . . . .	171
A.4	Energy Resolution and Calibration . . . . .	172
A.5	Influence of the Recovery Time on the measured Spectrum . . . . .	175
A.6	Time Resolution . . . . .	176
A.7	Position Resolution of a Point Source . . . . .	176
A.8	Conclusions and Discussion of the Results . . . . .	177
<b>B</b>	<b>A new Method to measure the PDE of Photon Detectors with Single Photon Resolution</b>	<b>181</b>
B.1	Introduction . . . . .	181
B.2	Measurement Principle . . . . .	181
B.3	Measurement Procedure . . . . .	183

## CONTENTS

---

B.3.1	Mechanical Setup . . . . .	183
B.3.2	Calibration of the Setup . . . . .	184
B.3.3	Measurement Procedure of the PDE . . . . .	185
B.4	Results . . . . .	185
B.4.1	PDE of a HPD . . . . .	185
B.4.2	PDE of a SiPM . . . . .	186
B.5	Summary . . . . .	187
<b>C</b>	<b>Central Pixel</b>	<b>189</b>
C.1	Modification of the Central Pixel Readout . . . . .	189
C.1.1	Test of the Drift of the MAGIC System Clock . . . . .	189
C.1.2	Sensitivity of the Central Pixel . . . . .	190
C.1.3	Future Improvements of the Central Pixel . . . . .	191
	<b>Acknowledgement</b>	<b>209</b>

# List of Figures

2.1	Main scientific targets of VHE $\gamma$ -ray astrophysics that are addressed by current ground based $\gamma$ -ray experiments. . . . .	3
2.2	Energy spectrum of the cosmic rays. Note that for better visibility of structures, the spectrum is multiplied with energy to the power of three. from Blasi (2005) . . .	4
2.3	The Hillas plot shows up to which energies cosmic objects can in principle confine cosmic rays. First compiled by Hillas (1984) . . . . .	5
2.4	Schematic illustration of the main processes of $\gamma$ -ray production. from Tonello (2006)	6
3.1	Cover of "Unknown Pleasures" the first album by Joy Division, released in 1979. It shows 100 hundred radio pulses of the first discovered pulsar PSR B1919+21. . . . .	9
3.2	Possible evolutions of a pulsar in a binary system (Lorimer, 2005). . . . .	12
3.3	Competing structure and novel phases of subatomic matter of neutrons stars predicted by theory (from Weber, 2005) . . . . .	13
3.4	Calculations by Spitkovsky (2006) of the magnetosphere of an oblique rotator ( $60^\circ$ inclination) in the corotating frame. Color represents the toroidal field. A sample three-dimensional flux tube is traced in white. . . . .	14
3.5	Schematic view of the pulsar-wind-nebula complex and the emitted radiation (adapted from Aharonian and Bogovalov, 2003). Note that the graph is not to scale. Indicated dimensions are valid for the Crab nebula. . . . .	15
3.6	Pulse phase profiles of the six pulsars detected by EGRET in $\gamma$ -rays above 5 GeV (black) and above 100 MeV (yellow). Each panel shows one full rotation of the neutron star. From Thompson (2004). . . . .	17
3.7	Broad-band spectral energy distribution of the seven $\gamma$ -ray pulsars detected by EGRET, from Thompson et al. (1999) . . . . .	18
3.8	Cross-section of the poloidal plane of the pulsar magnetosphere. Indicated are possible sites where an electric potential can build up and particles are accelerated. Popular sketch by A. Harding. . . . .	19
3.9	Characteristic phase-averaged spectrum for a young $\gamma$ -ray pulsar. Solid lines show the curvature spectrum (CR), the synchrotron emission (Sy) and the thermal surface flux (kT). For comparison, the dotted curve gives the mono-energetic primary curvature spectrum with the same cutoff energy as for curvature radiation. The dashed curve gives the TeV pulsed spectrum from Compton upscattering of the synchrotron spectrum on the primary $e^\pm$ (from Romani, 1996). . . . .	20

3.10	Expected radial distribution of the magnetic field and surface brightness of the Crab nebula in VHE- $\gamma$ -rays (from De Jager and Harding, 1992). . . . .	22
3.11	Non-thermal radiation of the Crab Nebula. The solid and the dashed curve correspond to the synchrotron and inverse Compton components of the radiation, respectively, calculated in the framework of the spherically symmetric MHD wind model of Kennel and Coroniti (1984a,b). Indicated with arrows are the electron energies related to the peak energy of the synchrotron photons. (from Aharonian and Atoyan, 1998) . . . . .	23
4.1	Popular illustration of the situation encountered in $\gamma$ -ray astrophysics from ground. A $\gamma$ -ray converts into a $e^\pm$ -pair in the atmosphere and a particle shower develops with the shower maximum in 10 km altitude. The ultrarelativistic secondary particles generate Cherenkov light that propagates in a narrow cone along the primary direction. The light is illuminating an approximately circular area with a radius of $\sim 120$ m. An imaging air Cherenkov telescope records some of the Cherenkov light with its $\sim 100$ m <sup>2</sup> large light collector, provided the telescope is located within the “pool” of Cherenkov light. Typically 0.1% of the Cherenkov light is recorded . . . . .	25
4.2	Schematic view of the development of a $\gamma$ -ray induced air shower (left) and an air shower that was started with a hadronic interaction (right). . . . .	27
4.3	Space Shuttle breaking the sound barrier (see faint shock wave). In the same way a superluminal charged particle generates a photonic shockwave (Cherenkov emission) as it travels through matter. . . . .	28
4.4	Simulated Cherenkov photon distribution at 2200 m above sea level from one air shower induced by a 50 GeV $\gamma$ -ray of vertical incidence. The impact point of the $\gamma$ -ray is at (0, 0). The majority of photons arrive within a radius of 100 m from the impact point. Due to the increasing Cherenkov angle with increasing shower depth a maximum in the photon distribution is seen at the rim at $\sim 100$ m. The maximum is often referred to as the “hump”. The region closer to the shower axis collects the light principally from the shower tail, while the region up to the hump is dominated by light coming from the shower core. Beyond the hump the light comes from halo particles of the shower. . . . .	29
4.5	Cherenkov photon densities emitted by $\gamma$ -ray showers of different energies before absorption (solid lines) and after taking into account absorption losses in the atmosphere (dashed lines). The zenith angle is $0^\circ$ . (calculations done by P. Majumdar)	30
4.6	Simulation of the Cherenkov light signal from a $\gamma$ -ray shower vs. $\gamma$ -ray energy. The Cherenkov signal is given in units of detected photoelectrons by the MAGIC telescope. The distances between the impact points of the $\gamma$ -rays and the telescope are $< 150$ m. The zenith angle range of the simulated $\gamma$ -rays is $0^\circ \dots 30^\circ$ . . . . .	30
4.7	Photograph of the MAGIC telescope. One can make out the tessellated reflector surface, the camera in the focal plane of the reflector, the azimuthal rail and the camera access tower in the front. . . . .	32
4.8	Photograph of the camera of the MAGIC telescope with opened lids while the Winston cones are being installed. The inner part of the camera consists of 397 PMTs of $1''$ that are surrounded by 180 PMTs of $1.5''$ diameter. . . . .	33
4.9	Camera readout and processing of the data recorded by MAGIC (from Wagner, 2006)	34
4.10	Sketch of the trigger topology in the MAGIC camera. The inner camera is segmented into 19 macrocells of 37 pixels each. The logic of a macrocell is based on 36 pixels. The pixel not connected to the macrocell logic is highlighted in the figure. . . . .	35

5.1	Illustration of the cleaning of an event . . . . .	39
5.2	Example of an event that has been cleaned with 6 photoelectrons (core-pixel) and 4 photoelectrons (boundary-pixel) using the standard-cleaning (left) and the time-cleaning (right). In the standard-cleaning a fluctuation in the NSB is picked up, which is suppressed in the time-cleaning. . . . .	41
5.3	Flowchart of the time-cleaning procedure. See text for explanation. . . . .	42
5.5	Examples of real shower events. From left to right: $\gamma$ -ray candidate, two hadron events, a muon. The top row shows the pixel contents in units of photoelectrons, the middle row the signal-times in units of FADC slices (1 slice = 3.3 nsec) and the bottom row the cleaned events. . . . .	43
5.4	Parameterization of a shower image with Hillas-parameters. . . . .	44
5.6	The upper plot shows the distribution of the parameter HADRONNESS vs. SIZE. The background events are marked blue and the MC $\gamma$ -ray events red. Note that below a SIZE of 300 photoelectrons most of the background events are hidden behind the simulated $\gamma$ -ray events. For bins in SIZE the HADRONNESS cut (black stars) is found that yields the highest quality factor (yellow dots). The dashed line is a fit to the HADRONNESS values. The quality factor (without an ALPHA-cut) is given in the lower plot. . . . .	47
5.7	Left panel: true energy of a $\gamma$ -ray vs. its estimated energy (migration matrix); Right panel: profile histogram of the relative deviation between the estimated energy and the true energy of a $\gamma$ -ray. The error bars denote the energy resolution. . . . .	48
5.8	$ \text{ALPHA} $ -distribution of a Crab data sample (ON) and a data sample of a region in the sky where no $\gamma$ -ray source is expected (OFF). . . . .	49
5.9	The upper plot shows the cut in $ \text{ALPHA} $ for different bins of SIZE optimized for maximum quality factor. The corresponding quality factors are shown in the lower graph. . . . .	50
5.10	Size dependence of the Q-factor for optimal $ \text{ALPHA} $ -cut, HADRONNESS-cut and the Q-factor for the combination of $ \text{ALPHA} $ -cut and HADRONNESS-cut. . . . .	51
5.11	Differential collection area after hardware trigger (triangles) and after cuts and $\gamma$ /hadron-separation (circles). The collection area after cuts shrinks again at higher energies due to the requirement in the analysis that the shower image has to be fully contained within the inner camera. . . . .	53
5.12	Illustration of propagation delays within the solar system (from Schmidt, 2005). . . . .	54
5.13	Results of the H-test obtained from a Crab data sample for randomly chosen test frequencies. . . . .	56
5.14	$Q$ vs. upper SIZE-cut $S_{\text{up}}$ . For a SIZE-cut of $\text{SIZE} < 300$ phe or higher maximum sensitivity is obtained. . . . .	58
5.15	Collection area after optimized $ \text{ALPHA} $ - and HADRONNESS-cuts and an upper SIZE-cut of $\text{SIZE} < 300$ phe is applied. . . . .	58
5.16	Only about 10 VHE $\gamma$ -ray sources were known in 2000 (left figure). With the new generation of more sensitive IACTs, the number of detected sources increased to more than 40 in 2006 (right panel). . . . .	61
5.17	Alpha Plot of the total Crab data sample below $20^\circ$ zenith angle. . . . .	63
5.18	MC-Data Comparisons of the WIDTH parameter in bins of SIZE ( 6/4 cleaning) . . . . .	66
5.19	MC-Data Comparisons of the LENGTH parameter in bins of SIZE ( 6/4 cleaning) . . . . .	67

LIST OF FIGURES

---

5.20	MC-Data Comparisons of the DIST parameter in bins of SIZE ( 6/4 cleaning) . . .	68
5.21	MC-Data Comparisons of the CONC2 parameter in bins of SIZE ( 6/4 cleaning) . .	69
6.1	Dynamic rings, wisps and jets of electrons and positrons around the pulsar in the Crab Nebula. Observations in X-ray light by Chandra (1999). The inner ring is about one light year across. . . . .	71
6.2	Differential energy spectrum of the Crab nebula between 60 GeV and 9 TeV. The spectrum was unfolded with the method by Bertero (1989). The upper part in the figure shows in addition to the unfolded data points also results of a power-law fit and a variable power-law fit. The lower panel shows the relative residuals between the fit results and the data points. A parameterization of the spectrum with a curved power-law is favored. . . . .	77
6.3	ALPHA -distribution for events with estimated energy between 80 GeV and 100 GeV. ON Events: $292721 \pm 503$ , normalized OFF Events; $248380 \pm 602$ , Excess Events; $4341 \pm 784$ , Significance: 5.53, effective ontime: 58000 sec. Applied  ALPHA -cut to extract the $\gamma$ -ray signal $< 20^\circ$ . The excess rate is $4.5\gamma$ -rays per minute. . . . .	78
6.4	Compilation of different $\gamma$ -ray measurements and one model of the Crab nebula. See text for discussion. . . . .	79
6.5	Measured spectral index derived from differential flux points (dots) and derived from the variable power-law fit (black solid line, the dashed line gives the $1\sigma$ confidence interval); also shown are predictions by Aharonian et al. (2004) (blue curve), Atoyan and Aharonian (1996b) (green curve) and Aharonian and Atoyan (1998) (red curve). . . . .	80
6.6	Light curves of the integral flux above 200 GeV from the Crab nebula for each of the 14 nights in a binning of 10 minutes. The black horizontal line in each light curve is the result of a fit of the light curve, assuming a constant $\gamma$ -ray emission. . . . .	82
6.7	Average flux above 200 GeV of each observed night. The dashed blue line gives the average flux of all nights and the blue shaded region the statistical uncertainty of the average flux. . . . .	83
6.8	Sky-maps of excess events from the Crab nebula for different $\gamma$ -ray energies ( $\sim 160$ GeV, $\sim 250$ GeV and $> 500$ GeV). The position of the pulsar is marked by the black cross and the angular resolution is indicated by the circle. . . . .	84
6.9	Emission of the Crab nebula in different energy bands. The position of the Crab pulsar is marked with a black star. The Chandra X-ray image is shown in light blue, the Hubble Space Telescope optical images are in green and dark blue, and the Spitzer Space Telescope's infrared image is in red (picture from Chandra, 2006). Overlaid on top are the center of gravity of the $\gamma$ -ray emission at different energies (simple cross $> 500$ GeV; dot $\sim 250$ GeV; square $\sim 160$ GeV). The error bars indicate the statistical uncertainty in the position of the cog. The upper limits (95% confidence level) on the 39% containment radius of the $\gamma$ -ray emission region that were derived from the $\theta^2$ -distributions are indicated with circles (dashed $> 500$ GeV; solid $\sim 250$ GeV). . . . .	87
6.10	Background subtracted $\theta^2$ -distributions produced with the DISP- method for different energies. See text for discussion. . . . .	88
6.11	Optical light curve of PSR B0531+21 measured with MAGIC. The figure includes data obtained on seven nights between December 2005 and February 2006. The total observation time is 12.5 hours. However, the effective observation time is only $\sim 1$ sec. For better visibility the light curve is shown twice. . . . .	89

6.12	Expanded view of the main pulse of the Crab pulsar in optical. The different rise and fall times of the main-pulse are nicely resolved. The slopes of the main-pulse were fitted with two straight lines. The peak position of the main-pulse is given by the intersection of the two curves. . . . .	90
6.13	Upper limits on the pulsed $\gamma$ -ray flux from the Crab pulsar; upper limits in differential bins of energy are given by the blue points. The upper limit on the cutoff energy of the pulsed emission is indicated by the dashed line. The red arrow indicates the analysis threshold when the upper limit on the cutoff energy was derived. It should be noted that the Celeste limit is based on a two times lower Crab flux than found by MAGIC. . . . .	92
6.14	Pulse phase profiles obtained after applying SIZE dependent HADRONNESS-cuts (Section 5.4.1) and  ALPHA -cuts (Section 5.5.1) for two different SIZE-cuts. The optical light curve of the Crab pulsar is shown in the bottom of the pulse phase profiles. Indicated by the vertical bars are the regions where EGRET detected pulsed emission above 100 MeV (cf. Figure 3.6) . . . . .	93
6.15	Pulse phase profiles obtained after applying SIZE dependent HADRONNESS-cuts (Section 5.4.1) and  ALPHA -cuts (Section 5.5.1) for four different upper SIZE-cuts. The EGRET data above 5 GeV are given in blue and the corresponding scale is shown on the right side (cf. Figure 3.6). In all profiles an excess is visible in the VHE- $\gamma$ -ray data at the position of the interpulse (phase range between 0.32 and 0.43) in coincidence with the EGRET data. The excess in this phase range is monotonically increasing with increasing upper SIZE-cut. . . . .	94
7.1	H $\alpha$ emission around PSR B1951+32 (grey) and X-ray emission (contours) that can be associated to the pulsar wind nebula that is powered by PSR B1951+32. The arrow shows the direction of the proper motion of the pulsar. A striking difference to Crab is that PSR B1951+32 has a much higher proper motion (240 km/s), which results in the formation of a bow shock. Picture from Moon et al. (2004). . . . .	97
7.2	The left panel shows the $\theta^2$ -distribution after background subtraction. The right panel shows the  ALPHA -distribution of ON-events (black) and OFF-events (red). In both cases no hint of a signal is visible. The cuts are chosen in both cases such that the energy threshold of the analysis is 280 GeV . . . . .	100
7.3	Integral upper limits (95 % Confidence Level) on the steady emission from the direction of PSR B1951+32. For comparison, the $\gamma$ -ray flux of the Crab nebula (Wagner et al., 2005) is also indicated. . . . .	101
7.4	Sky maps of excess events in the region around PSR B1951+32 smoothed with a Gaussian kernel of $0.1^\circ$ . . . . .	102
7.5	Significance of VHE $\gamma$ -ray emission from the region around PSR B1951+32. Left side: calculated significance of VHE $\gamma$ -ray emission $\gtrsim 300$ GeV in bins of $(0.1 \times 0.1)$ degrees <sup>2</sup> . Overlaid in black are contours of radio observations (Castelleti et al., 2003) and in white contours of IR observations (Fesen et al., 1988). Right side: distribution of significances. The distribution has a mean of 0.03 and a RMS of 0.84, compatible with randomly distributed data. Figures provided by E. Aliu. . . . .	103
7.6	Upper limits (95 % Confidence Level) on the integral $\gamma$ -ray emission $> 200$ GeV, calculated in bins of $(0.05 \times 0.05)$ degrees <sup>2</sup> . Figure provided by E. Aliu. . . . .	104
7.7	Results of the analysis in search for pulsed emission from PSR B1951+32. Upper limits are given for a 95 % confidence level. The red curve shows the spectrum measured by Fierro (1996) but extended by an exponential cutoff of 32 GeV. . . . .	105

LIST OF FIGURES

---

7.8 Pulse phase profile obtained after selecting events with a SIZE < 300 photoelectrons. The shaded areas indicate phase regions where PSR B1951+32 is emitting at low GeV energies (Ramanamurthy et al., 1995). See also Figure 3.6. . . . . 106

7.9 Scan around the frequency of the radio ephemeris. An upper size cut of 300 photoelectrons was adopted for this analysis. The left figure shows the result of the H-Test, the right figure shows the result of the  $\chi^2$ -Test. . . . . 106

7.10 Results of the test by Gregory and Loredo (1992) from a scan around the frequency of the radio ephemeris. For this analysis an upper size cut of 300 photoelectrons was used. . . . . 107

8.1 X-Ray data from Chandra smoothed to a resolution of 5" (contours) and overlaid on an H $\alpha$  image obtained from Taurus Tunable Filter service mode observations on the Anglo Australian Telescope on 3rd of August 2000. The x-ray tail is located well inside the boundaries of the H $\alpha$  emission and also close to its symmetry axis. The x-ray contour levels are shown at 0.9, 1.2, 5.3, 35.0, and 78.8% of the peak x-ray surface brightness. The optical residuals correspond to incompletely subtracted stars. Picture and Caption from Stappers et al. (2003). . . . . 109

8.2 Schematic view of the binary system with the pulsar PSR B1957+20. The dimensions of the companion star and the distance between the star and the pulsar are shown in the correct proportions. The magnetic field configuration is magnified for better visibility. . . . . 110

8.3 Integral upper limits (95 % Confidence Level) for the steady emission from the direction of PSR B1957+20 . . . . . 113

8.4 Sky maps of the region around PSR B1957+20. The skymaps are smoothed with a Gaussian kernel of 0.1°. The position of the pulsar is marked with a cross. . . . . 114

8.5 Flux measurements of PSR B1957+20 in phase bins of the binary orbit. Upper row: for energies > 200 GeV; lower row: for energies > 400 GeV. On the left side the measured flux is given whereas in the right panels the 95 % confidence level upper limits on the flux are shown. The position of the eclipse of the radio emission as well as the positions of the Lagrange points L4 and L5 are also indicated. . . . . 115

9.1 The silicon photomultiplier; The left picture shows four cells of a SiPM and the right photograph a prototype SiPM comprising 576 cells. The device was developed and produced by MEPHI and Pulsar enterprize. . . . . 120

9.2 Left figure: Sketch of the multiplication process in an avalanche diode that is reverse-biased slightly below breakdown voltage—multiplication only by electrons (proportional mode). Right Figure: Multiplication process in an avalanche diode that is reverse-biased above breakdown voltage—multiplication by electrons and holes (Geiger mode). In Geiger mode the avalanche diverges, whereas in proportional mode the avalanche stops automatically as the avalanche “propagates” only in one direction. . . . . 121

9.3 Simulated pulse height distribution of output signals of an APD operating in proportional mode for different input signals. The average gain is 1000 per initial photoelectron. . . . . 122

9.4 Small signal replacement circuit of a SiPM. To the left the replacement circuit of two SiPM-cells is shown. The characteristics of the output network is described with a RC-low-pass filter. Connected to ground is the load resistor, which is followed by an amplifier. . . . . 124

9.5	Simulated output pulse of a SiPM. See text for details. . . . .	125
9.6	Different scenarios that can occur when a photon hits a SiPM: 1. Absorption of the photon in the non depleted substrate; 2. Absorption in the depleted region and subsequent drift of the photoelectron into the high field region; 3. Absorption between two cells; 4. Absorption in the SiO <sub>2</sub> or non depleted implantation below the surface; 5. Reflection on the surface . . . . .	126
9.7	Two photographs are overlaid on top of each other. The lower one shows the surface structure of a SiPM. Shown on top is the light intensity that is emitted from the avalanche cells. The SiPM (from MEPhI and Pulsar enterprize) was operated at 50V. The light emission was integrated for 300sec. The colors give the intensity of the emitted light. Photo from C. Merck. . . . .	128
9.8	The left picture shows an oscilloscope screen shot of many overlaid SiPM noise pulses (2nsec division in time and 2 mV in amplitude). Most of the time, only one cell of the SiPM shows a signal. With lower probability, 2, 3, or even more cells can fire simultaneously due to optical crosstalk. The right panel shows the pulse height distribution of the output of a SiPM integrated for 4 nsec after one cell has fired on a dark count. The signal shows nicely the quasi digital output as a function of the simultaneously fired cells. . . . .	129
9.9	Response of three different SiPM with 576, 1024 and 4096 cells as a function of photoelectrons in the active area (from Dolgoshein, 2006b) . . . . .	130
10.1	Side profile of three cells of a back side illuminated SiPM. Note that the drawing is not to scale. . . . .	131
10.2	Cross section of the designed cylindrical avalanche structure that can be embedded into a drift structure. Free electrons drift into the center of the structure as indicated by the dashed arrow. The potential is shaped by appropriate voltages applied to the back side implantation and two drift rings on the front side of the device. The first drift ring is indicated in the lower corners of the figure. The different implantations are marked with numbers. The doses and type each implantation is given in the table. . . . .	134
10.3	Simulation of a drifting electron cloud in a back side illuminated SiPM cell. The charge was generated at $r=40 \dots 45 \mu\text{m}$ , $z=448 \mu\text{m}$ (the smallest blob in the top of the figure). The picture shows the location of the drifting electrons in time steps of 2 nsec. Note the difference in notation $r=x$ and $z=y$ . . . . .	135
10.4	Expanded view of the avalanche region of the simulated cell shown in Figure 10.3. The charge is completely collected in the avalanche region ( $r=0 \dots 5 \mu\text{m}$ and $z=0 \dots 2 \mu\text{m}$ ) 20 nsec after its generation. Note the difference in notation $r=x$ and $z=y$ . . . . .	136
10.5	Temporal evolution of the electron density in the avalanche region. For this simulation electrons have been generated at three different locations in the cell at time $t=0$ . . . . .	137
10.6	Electric field in the avalanche region before breakdown. Bias voltage $-60 \text{ V}$ . . . . .	138
10.7	Current and electric potential at the cathode during breakdown. In this simulation the avalanche structure is biased to $-40 \text{ V}$ . The cathode is connected via a $500 \text{ k}\Omega$ resistor to ground. A $100 \text{ fF}$ capacitance is connected in parallel to the resistor. . . . .	139
10.8	Snapshots of the technology at eight steps in the production. The dimensions of the $r$ - and $z$ -axis are micrometers. The implantation doses are given in units of dopants per $\text{cm}^3$ . The pictures have been compiled by Rainer Richter with the technology simulation Dios. . . . .	141

LIST OF FIGURES

---

10.9 Four different examples of avalanche test structures designed for the technology outlined in Section 10.3.1. The diameters of the avalanche regions are  $10\ \mu\text{m}$ ,  $18\ \mu\text{m}$ ,  $70\ \mu\text{m}$  and  $100\ \mu\text{m}$ , respectively. . . . . 142

10.10 Avalanche structure with a  $500\ \text{k}\Omega$  resistor and  $50\ \text{fF}$  capacitance combination connected in series with the anode contact. The avalanche region has a diameter of  $10\ \mu\text{m}$ . . . . . 143

10.11 Evaluation board that was especially designed for the readout of the test structures. The signal of a test structure is amplified by a broadband (Monolithic Microwave Integrated Circuit) MMIC-amplifier type MAR-8ASM from Mini-Circuits. . . . . 144

10.12 Signal charge and amplitude dependence as a function of the bias voltage for four different RC-combinations. The values of the capacitors obtained from the slope of the signal-charge vs. bias voltage are given in brackets. . . . . 145

10.13 Multiple triggers of dark counts for the structure with  $1\ \text{M}\Omega$  and  $100\ \text{fF}$  and a bias voltage of  $49.5\ \text{V}$ . . . . . 146

10.14 Signal shape in case of the structure with the RC-combination  $1\ \text{M}\Omega$  and  $100\ \text{fF}$  biased at  $49.5\ \text{V}$ . . . . . 146

10.15 Output signal shapes for different RC-combinations connected in series to the avalanche diode structure. The bias voltage is in all cases  $49.5\ \text{V}$ . The signal amplitude is positive in the lower two figures because the signal was tapped from the cathode and not from the anode. Note that an inverting amplifier was used and that the time scales as well as amplitude scales are different in each figure. . . . . 147

10.16 Output signal shapes of the avalanche diode structure with  $500\ \text{k}\Omega/50\ \text{fF}$  connected in series, at different supply voltages. Note that both the time and amplitude scales are different in both screenshots. . . . . 148

10.17 Measured pulse shape of the structure with  $1\ \text{M}\Omega$  and  $100\ \text{fF}$  and four different model pulse shapes. (s. text for details) . . . . . 149

10.18 Dark count rate as a function of the bias voltage. . . . . 149

10.19 Afterpulsing measurement of the  $500\ \text{k}\Omega/50\ \text{fF}$ -structure at a bias voltage of  $46\ \text{V}$ . . . . . 151

10.20 Cross section of the geometry of the SiPM that is simulated in SiSi. Also indicated are five different possible fates of photons, which are simulated: 1. Absorbtion of the photon in the depleted volume of a cell but the photoelectron will not drift into the avalanche region. 2. Reflection of the photon from any surface of the detector and subsequent absorbtion in the depleted and sensitive volume of a different cell (can start another avalanche). 3. Absorbtion of the photon in the non-depleted volume of the detector and subsequent diffusion of the electron in the depleted and sensitive volume of a cell. (can start another avalanche) 4. Absorbtion of the photon in the non depleted volume of the detector and absorbtion of the generated photoelectron. 5. Transmission of the photon through any surface of the detector. . . . . 153

10.21 Flowchart of the SiSi Monte Carlo program that is simulating optical crosstalk in SiPM. . . . . 154

10.22 Absorption lengths of photons in silicon. Data from EMIS Datareviews Series, No. 4 (1988). . . . . 156

10.23	Distribution of the number of cells, fired by optical crosstalk if one cell of the SiPM fires at random. The upper row shows the simulated distributions (black) for two sets of temperature and efficiency parameters, which result in a good agreement with the measured distribution (blue). In the lower plot the parameters from Lacaita et al. (1993) were used in the simulation. The efficiency is given in units of emitted photons with energies $> 1.015$ eV per charge carrier in the avalanche. The errors on the measured distribution can be neglected and thus are not shown. . . . .	157
10.24	Result of a $\chi^2$ -test between the simulated and the measured crosstalk-distribution from a scan in the parameters temperature of the photon spectrum (X-axis) and efficiency of photon production in the avalanche (Y-axis). . . . .	158
10.25	Two simulated events where additional cells are fired due to crosstalk. . . . .	158
10.26	Result of a $\chi^2$ -test between the simulated and the measured crosstalk distribution. Each bin gives the $\chi^2$ value obtained for one simulated pair of photon production efficiency (X-axis) and electron lifetime in the non-depleted detector volume (Y-axis). A spectral temperature of the emitted photons of 4500K is assumed in the left panel and a temperature of 2000K in the right panel. . . . .	159
10.27	Simulated and measured distribution of crosstalk events. The residuals can be explained as dark counts, which are not simulated. Parameters in the model have been a photon temperature of 4500 K, a photon production efficiency of $1.45 \cdot 10^{-4}$ and an electron lifetime in the bulk of 60 nsec. . . . .	160
10.28	The left panel shows two simulated energy distributions of photons that where produced in a breakdown and caused a breakdown of another cell. The right panel shows the photon emission spectra that were assumed in the simulation. Despite the very different emission spectra of 2000K and 4500K one finds an almost identical crosstalk behavior. . . . .	160
10.29	Geometry of the simulated BaSiPM . . . . .	162
10.30	Probability for optical crosstalk as a function of gain for a front side illuminated SiPM (stars and dots) and a BaSiPM (crosses and triangles) . . . . .	163
10.31	Probability distribution that X additional cells fire due to crosstalk in a BaSiPM for three different gains. The blue distribution was measured with a front side illuminated SiPM and is shown for comparison. . . . .	164
A.1	Photograph of the detector setup used in this study. For details see text. . . . .	171
A.2	Reflectivity of the dielectric foil by 3M measured at four different positions on a sample. . . . .	172
A.3	Block diagram of the electronics used in this test. . . . .	172
A.4	$\gamma$ -pulse height distributions of a $^{22}\text{Na}$ positronium source. The distribution on the left side was measured by triggering on a coincidence of the two channels. The dashed vertical lines indicate the cuts applied in order to restrict the analysis of the time resolution to the photopeak signal. For the distribution on the right a minimum amplitude in the detector channel was required. The 511 keV peak as well the 1.275 MeV shoulder are clearly visible. Note that for the right hand picture no amplifier was used and that the signal was attenuated (18dB). . . . .	173
A.5	Pulse height distributions of $^{133}\text{Ba}$ and $^{137}\text{Cs}$ . The peaks at lower energy are caused by dark counts where, due to optical crosstalk, many standardized signals are produced within $\ll 1$ nsec and the summed up signal is high enough to pass the discriminator threshold. . . . .	173

LIST OF FIGURES

---

A.6	Correlation between $\gamma$ -ray energy and signal height (in units of charge, respectively number of fired cell). . . . .	174
A.7	Spectrum of dark count pulses in the used SiPM. Each peak corresponds to a different number of cells fired per event. The distribution was measured without any preamplifier but the passive splitter (1:2) still included. The insert box lists the fit result for the first peak. . . . .	174
A.8	Distribution of time differences of the two detector channels. For this measurement the time was measured by triggering on the first photoelectron of each signal with a leading edge discriminator. . . . .	176
A.9	Coincidence rate as function of the $^{22}\text{Na}$ $\gamma$ -source position. . . . .	177
B.1	Pulse height distribution of a SiPM during a measurement of the PDE. Pedestal events can be very well separated due to the large and standardized output signals of the SiPM. Note the logarithmic scale of the y-axis and that the output signal of the SiPM is negative. . . . .	182
B.2	Left side: Horizontal cut through the mechanical setup used for the measurement of the PDE. Right side: Photograph of the mechanical setup with the opened cap. A pulsed LED emits light into the sphere through the hole in the cap. The setup guarantees a fixed light splitting ratio between the reference detector (PiN diode) and the photon detector under investigation. . . . .	183
B.3	Pulse height distribution of the PiN diode irradiated with a 59 keV $\gamma$ -source ( $\text{Am}^{241}$ ). The photo-peak is very well visible. . . . .	184
B.4	Block diagram of the setup used in the measurement of the PDE. . . . .	186
B.5	Photon detection efficiency of a SiPM vs. wavelength. The SiPM tested here has 1024 cells on one square millimeter sensor area with a geometrical efficiency of about 10%. . . . .	186
B.6	Photon detection efficiency of a SiPM vs. bias voltage. The measurement shows the strong dependence of the PDE on the bias voltage and indicates a saturation of the PDE at an over-voltage of 7% above breakdown. . . . .	187
C.1	Blockdiagram of the modified signal chain of the Central Pixel of the MAGIC camera. . . . .	189
C.2	Schematics of the optical receiver for CP-readout with the DAQ of MAGIC. . . . .	190
C.3	Scan around the frequency of the radio ephemeris. See text for details. . . . .	191
C.4	$\chi^2$ vs. the number of events used to calculate the light curve of the Crab pulsar. The number of degrees of freedom is 17. . . . .	191
C.5	Dependence of the Sensitivity of the Central Pixel on the optical PSF and the radius of an aperture placed in front of the CP. . . . .	192
C.6	Dependence of the Sensitivity of the Central Pixel on electronic noise. . . . .	193

# List of Tables

5.1	Integral sensitivities ( $> 250$ GeV ) derived from the measurement of the Crab nebula; In the last row of the table the average values of each column are given. The numbers in brackets give the RMS of the values in each column. . . . .	64
5.2	Integral sensitivities of the MAGIC telescope on the $\gamma$ -ray emission of the Crab nebula for several analysis thresholds. . . . .	64
6.1	Parameters of PSR B0531+21 (Manchester et al., 2005). . . . .	72
6.2	Some parameters of the selected data. The extinction coefficients for an effective photon wavelength of 625 nm are from public data available from the Carlsberg Meridian Telescope. . . . .	74
6.3	Ephemerides of the Crab pulsar provided by the Jodrell Bank Radio Telescope (2006) relevant for the analysis. MJD is the reference day of the ephemeris and $t$ is the time of appearance of the first main pulse after midnight on the reference day. . . . .	74
6.4	Mean energy and differential flux of the spectral points shown in Figure 6.2. . . . .	76
6.5	Center of gravity of the $\gamma$ -ray emission of the Crab nebula obtained for different energies. In the first column the applied SIZE-cut is stated. The second column shows the corresponding $\gamma$ -ray energies (peak value and full width at half maximum of the distribution of Monte Carlo $\gamma$ -ray events). The last two columns give the position of the cog and the statistical uncertainty. . . . .	85
6.6	Measured and simulated widths of the $\gamma$ -ray excess in the 2D-skymaps. In the last column upper limits on the 39% containment radius of the $\gamma$ -ray emission region are given. . . . .	86
6.7	Results of the fit of the $\theta^2$ -distributions with an exponential and thereof derived upper limits on the extension of the emission region (39% containment radius). . . . .	86
6.8	Analysis results for a cut selecting events with SIZE $> 100$ photoelectrons . . . . .	92
6.9	Analysis results for a cut selecting events with SIZE $< 300$ photoelectrons . . . . .	95
7.1	Summary of the observation of PSR B1951+32 with MAGIC. The extinction coefficients are taken from public available data of the Carlsberg Meridian Telescope that is located on the same site as MAGIC. The extinction coefficient is for an effective wavelength of 625nm. . . . .	99
7.2	Results from an analysis of steady emission from PSR B1951+32. . . . .	100
7.3	Ephemeris of PSR B1951+32 from Lyne (2006). Uncertainties are given in brackets. . . . .	103
7.4	Results of the analysis for periodicity within the PSR B1951+32 data sample. . . . .	104

LIST OF TABLES

---

8.1	Summary of the observation of PSR B1957+20 with MAGIC. The extinction coefficient was taken from public data available from the Carlsberg Meridian Telescope. The coefficient provides the extinction for an effective wavelength of 625 nm. A night is considered to have a good photometric quality in optical astronomy if the extinction coefficient (Ext. Coef.) is 0.09 mag and if the scatter of the extinction coefficient (Sc. Ext. Coef.) over the whole night is below 0.06 mag. . . . .	111
8.2	Results from an analysis of steady emission from PSR B1957+20 averaged over all observed orbital phases. . . . .	112
10.1	Parameters of the modelled pulse shapes that are shown in Figure 10.17 . . . . .	148
10.2	Results of the afterpulsing measurements at three different bias voltages at room temperature. Note that the sum of the $P_i$ 's in each row is more than 100%. This is because no condition was imposed during the fit, which enforces an overall probability of 100%. . . . .	150
A.1	Specifications of the SiPM used in this study. . . . .	170
B.1	Measurement of a HPD Typ R9792U-40 by Hamamatsu. <b>PDE</b> <sub>(this meas.)</sub> is the result of my measurement, <b>QE</b> <sub>(in house)</sub> is the result of a “conventional” QE-measurement performed at the institute and <b>QE</b> <sub>(Hamamatsu)</sub> the values from the HPD ticket . . . . .	185

# List of Acronyms and Abbreviations

AGASA	Akeno giant air shower array
AGN	Active galactic nucleus
AMC	Active mirror control
a.s.l.	Above sea level
Az	Azimuth
BaSiPM	Back side illuminated SiPM
CANGAROO	Collaboration of Australia and Nippon (Japan) for a gamma-ray observatory in the outback
CAT	Cherenkov array at Themis
CELESTE	Cherenkov low energy sampling and timing experiment
CF	Constant fraction
CGRO	Compton gamma-ray observatory
CMB	Cosmic microwave background
CORSIKA	Cosmic ray simulations for KASCADE
CR	Cosmic ray(s)
CR	Curvature radiation
CT	Cherenkov telescope
DAC	Digital to analog converter
DAQ	Data acquisition
EAS	Extended air shower
EC	Extinction coefficient
EGRET	Energetic gamma-ray experiment telescope
EM	Electromagnetic
EMI	Electromagnetic interference
FADC	Flash analog to digital converter
FOV	Field of view
FWHM	Full width at half maximum
GBIP	General Purpose Interface Bus
GLAST	Gamma-ray large area space telescope
GMRT	Giant meterwave radio telescope
GP	Giant pulse

GRB	Gamma-ray burst
GZK	Greisen–Zatsepin–Kuz'min
H.E.S.S.	High energy stereoscopic system
HE	High energy
HEGRA	High energy gamma-ray astronomy
IACT	Imaging atmospheric Cherenkov telescope
IC	Inverse Compton
IC	Integrated Circuit
IR	Infrared
ISM	Interstellar medium
KASCADE	Karlsruhe shower core and array detector
LED	Light emitting diode
LIDAR	Light Detection and Ranging
LSO	Lutetium orthosilicate (scintillator crystal)
LYSO	Lutetium Yttrium Orthosilicate (scintillator crystal)
MAGIC	Major atmospheric gamma-ray imaging Cherenkov
MARS	MAGIC analysis and reconstruction software
MEPhI	Moscow Engineering Physics Institute (State University)
MC	Monte Carlo [simulations]
MHD	Magnetohydrodynamic
MJD	Modified Julian day
MMIC	Monolithic Microwave Integrated Circuit
NS	Neutron star
NSB	Night–sky background
PCE	Photoelectron collection efficiency
PDE	Photon detection efficiency
PET	Positron emission tomography
phe	photoelectrons
PiN	Positive intrinsic negative [diode]
PMT	Photomultiplier tube
PSF	Point spread function
PWN	Pulsar wind nebula
QE	Quantum efficiency
RA	Right ascension
R&D	Research and Development
RF	Random forest <sup>TM</sup>
RMS	Root mean square
ROOT	An object–oriented data analysis framework
SED	Spectral energy distribution
SiPM	Silicon photomultiplier
SNR	Supernova remnant
SNR	Signal to noise ratio

SSC	Synchrotron-self Compton
UV	Ultraviolet
VCSEL	Vertical cavity surface emitting laser
VERITAS	Very energetic radiation imaging telescope array system
VHE	Very high energy ( $> 30$ GeV)
Zd	Zenith distance



# Chapter 1

## Goals of this Thesis

This thesis deals with two topics:

1. The detection and analysis of  $\gamma$ -ray emission from pulsars and their nebulae.
2. The development of a novel semiconductor photon detector for future experiments in astroparticle physics.

In the following I summarize the main goals in each of the two topics, at first for the pulsar studies and secondly for the detector development. The structure of this thesis is outlined at the end of this chapter.

### 1.1 Detection of $\gamma$ -Ray Emission from Pulsars and their Nebulae

Pulsars are highly magnetized, fast spinning neutron stars. Some are known to emit  $\gamma$ -rays up to energies of at least  $\sim 10$  GeV. This experimental result is based on observations with the spaceborne detector EGRET. Observations at  $\gamma$ -ray energies  $\gtrsim 100$  GeV so far failed to detect  $\gamma$ -ray emission from pulsars. From these studies it is clear that the energy dependent flux of pulsars undergoes a dramatic change, basically a cutoff, in an experimentally unexplored energy region between 10 GeV and 100 GeV. A cutoff in the energy spectrum is also predicted in various models for  $\gamma$ -ray emission from pulsars. Spectroscopy of the  $\gamma$ -ray spectrum between 10 GeV and 100 GeV will contribute in disentangling between models.

**It was a goal of this thesis to detect, for the first time,  $\gamma$ -rays from a pulsar with a ground based experiment with a many orders of magnitude ( $\sim 10^5$ ) larger collection area than satellite detectors. Special analysis techniques were developed to search for pulsed emission and to lower the analysis threshold of MAGIC. MAGIC is the first air Cherenkov telescope with a trigger threshold below 100 GeV. Therefore, it is a predestined instrument to perform such studies.**

Pulsars are powerful emitters of low frequency electromagnetic radiation and charged particles (pulsar wind). In the vicinity of the NS a nebula forms, which is a source of non-thermal emission. The Crab nebula is such a source of non-thermal emission and well studied in many wavelengths. One of the few unexplored energy regions is between 10 GeV and  $\sim 400$  GeV.

**Another goal of this thesis was to measure and characterize the  $\gamma$ -ray emission from the Crab nebula in the unexplored energy range between 60 GeV and 400 GeV.**

## 1.2 Development of a novel Semiconductor Photon Detector for Future Experiments in Astroparticle Physics

A detection of  $\gamma$ -ray emission from pulsars with ground based experiments is only possible with low enough energy thresholds. In these experiments (air Cherenkov telescopes),  $\gamma$ -rays are typically detected by recording the Cherenkov light that is emitted in air showers. The energy threshold of an air Cherenkov telescope is determined by the fraction of the Cherenkov light that it records. Photon detectors play a key role in defining the energy threshold.

All current second generation air Cherenkov telescopes use conventional photomultiplier tubes with average quantum efficiencies (QE) of  $\sim 15 - 20\%$  for photon wavelengths between 300 nm and 600 nm. A promising photon detector replacement candidate in the future might be the silicon photomultiplier (SiPM). The SiPM is a novel semiconductor photon detector, which has, besides other favorable characteristics, the potential to detect photons with efficiencies of 80% or higher.

**It was the main goal of this thesis to investigate the SiPM for future experiments in astroparticle physics as well as for other applications (e.g. in positron emission tomography (PET)).**

An option of this new type of detector is a configuration that is illuminated from the back side (back side illuminated SiPM or BaSiPM). When I started this thesis first basic ideas for BaSiPMs existed but no working device.

**It was a goal of this thesis to find a realization of a BaSiPM and predict its characteristics. For this purpose intensive finite element simulations were performed and test structures designed, produced and evaluated. A Monte Carlo simulation of a SiPM was developed to study the optical crosstalk effect.**

## 1.3 Structure of this Thesis

The  $\gamma$ -ray observations of pulsars and their nebulae with MAGIC are presented in Chapters 2 to 8. I give a short introduction to VHE  $\gamma$ -ray astrophysics in Chapter 2. In Chapter 3 I overview the physics of pulsars and the relation to  $\gamma$ -ray emission. In Chapter 4, I describe the general concept of the imaging air Cherenkov technique and the MAGIC telescope. Chapter 5, I outline the general data analysis before I present the analysis of the Crab in Chapter 6. The analysis of PSR B1951+32, a middle aged pulsar, is discussed in Chapter 7 and the analysis of the millisecond pulsar PSR B1957+21 is summarized in Chapter 8.

In the second part of the thesis (Chapter 9 to 10 and Appendices A to B) I present my work on SiPMs. I introduce the concept of the device and describe its characteristics in Chapter 9. The development of the BaSiPM and optical crosstalk studies are discussed in Chapter 10. The thesis concludes with a short outlook.

Appendix A discusses the first application study of SiPM in positron emission tomography. Difficulties that arise when measuring the photon detection efficiency (PDE) of SiPMs are discussed in Appendix B. In the same Chapter a new method to measure the PDE is presented.

## Chapter 2

# Short Introduction to Very High Energy $\gamma$ -Ray Astrophysics

### 2.1 VHE $\gamma$ -Ray Astrophysics

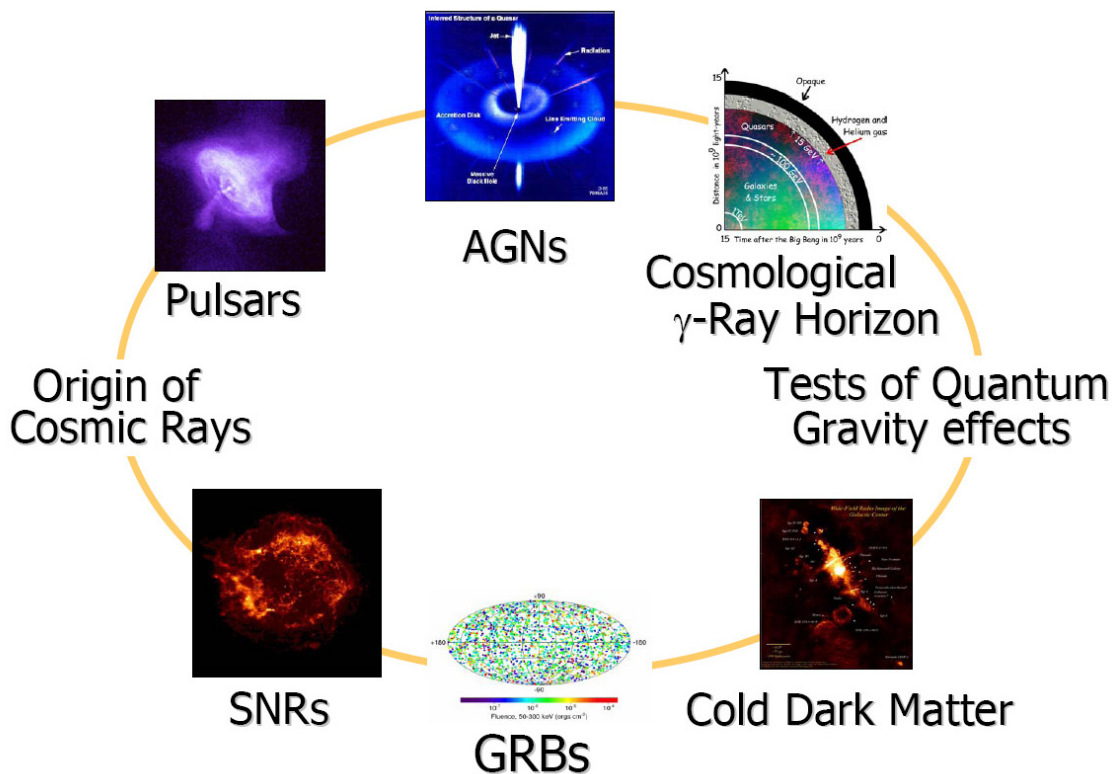


Figure 2.1: Main scientific targets of VHE  $\gamma$ -ray astrophysics that are addressed by current ground based  $\gamma$ -ray experiments.

Currently known sources of high energy  $\gamma$ -rays are limited to the most extreme places in the universe: the remnants of supernovae, the ultrarelativistic jets emerging from supermassive black holes at the center of active galaxies, their smaller galactic counterpart the Microquasars, the still

mysterious gamma-ray bursters (GRBs) and

**pulsars and their surrounding nonthermal nebulae,**

which are discussed in this thesis. All these sources have in common that they are closely linked to the longstanding question: Where do Cosmic Rays accelerate to the most extreme energies of up to  $> 10^{20}$  eV? The reason why this question is so difficult to answer is that Cosmic Rays are deflected by the interstellar magnetic fields and, therefore, cannot be traced back to their origin. On the other hand  $\gamma$ -rays do not suffer from this deficiency and are, apart from  $\nu$ 's, the only direct information carriers (also called messengers) we have from distant acceleration sites. While understanding these objects is of basic interest, the emitted  $\gamma$ -rays can also be used as probes of the radiation fields in the universe and possibly of spacetime itself.

A fixed definition of what the energy range of very high energy (VHE)  $\gamma$ -rays is, does not exist. I will use the term VHE- $\gamma$ -rays whenever I talk about  $\gamma$ 's with energies larger than 30 GeV.

## 2.2 Cosmic Rays

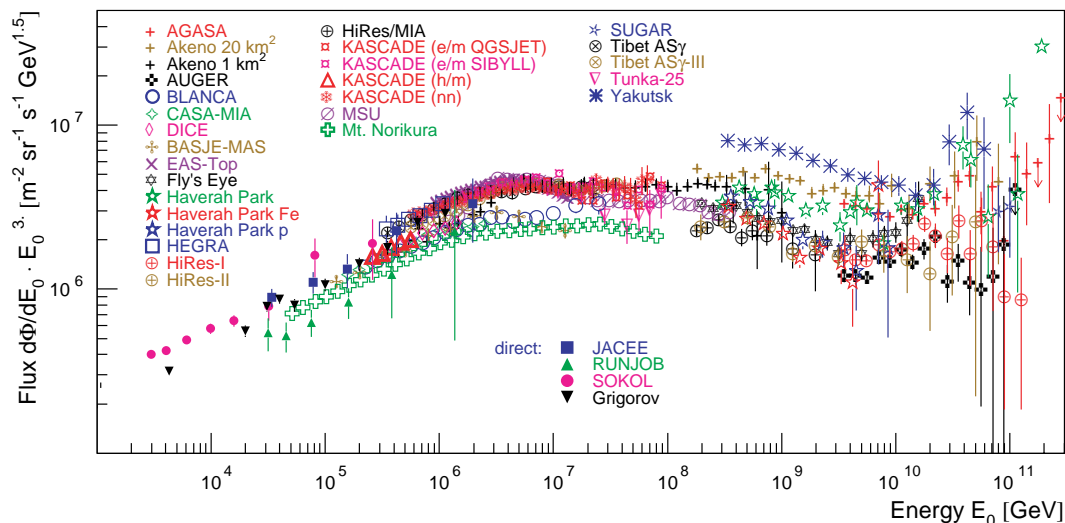


Figure 2.2: Energy spectrum of the cosmic rays. Note that for better visibility of structures, the spectrum is multiplied with energy to the power of three. from Blasi (2005)

In 1912, Victor Hess discovered cosmic rays (CR) (Hess, 1912) or, to be more precise, the showers of charged particles induced by CRs in the atmosphere (Auger et al., 1939, and references therein). In the first decades after the discovery of extensive air showers many previously unknown particles could be identified ( $e^+$ ,  $\Lambda$ ,  $\mu$ , ...) as being part of the showers. The discovery of new particles gave rise to a completely new field in physics — particle physics.

A compilation of the energy spectrum (multiplied by  $E^3$ ) of CRs from 32 different experiments is shown in Figure 2.2 and is a good illustration of the ongoing research efforts. The spectrum is well described with a pure power-law that changes its slope at about  $10^{15}$  eV. There, the index of the power-law steepens from 2.7 to 3.1 This structure change is called the *knee*, which is believed to be caused by a change in the composition of the primary particles. Another peculiarity in the spectrum at  $10^{19}$  eV is called the *ankle*, where the spectrum flattens again. The ankle is most probably caused by an interplay between CRs of galactic and extragalactic origin. CRs with energies above  $\sim 10^{20}$  eV can interact with the cosmic microwave background (CMB) to produce

pions. This leads to a cutoff in the CR-spectrum, also known as the GZK-cutoff (Greisen, 1966; Zatsepin and Kuz'min, 1966).

### 2.2.1 Sources of Cosmic Rays

Cosmic rays have given rise to several fascinating discoveries, but the most intriguing question about their origin is still an unsolved mystery since almost 100 years after they have been discovered.

A number of cosmic objects could be pinpointed as potential sites where particle acceleration can take place (see Figure 2.3). In supernova remnants (SNR) e.g. the acceleration mechanism is believed to be diffusive shock acceleration (1st order Fermi acceleration). In this process particles are accelerated by crossing multiple times the shock front of a remnant<sup>1</sup>.

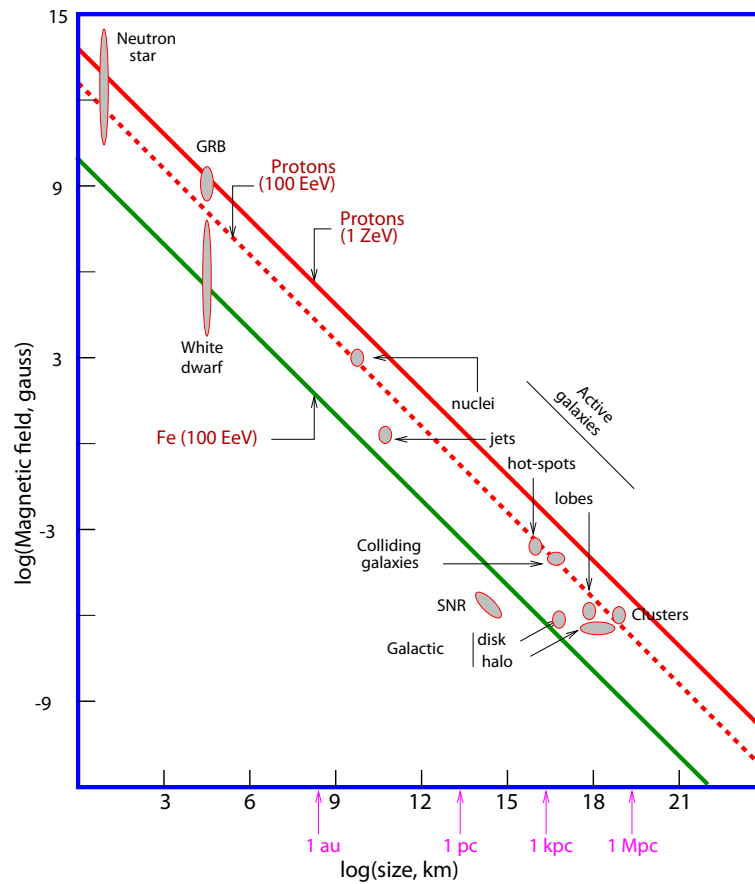


Figure 2.3: The Hillas plot shows up to which energies cosmic objects can in principle confine cosmic rays. First compiled by Hillas (1984)

The maximum energies attainable by diffusive shock acceleration in SNRs are limited to  $< 10^{15}$  eV due to finite acceleration times, finite volumes as well as synchrotron losses of the accelerated particles. But where are CRs accelerated to energies  $> 10^{15}$  eV? A general condition that has to be fulfilled is that the cosmic accelerator has to confine the accelerated particle up to the highest energies. Following this argument leads to the expression:

$$E_{max} \leq \Gamma e Z B R \quad (2.1)$$

<sup>1</sup>A detailed description of the Fermi acceleration mechanism is out of the scope of this work. For further details the interested reader is pointed to Protheroe (1998); Torres and Anchordoqui (2004)

where  $\Gamma$  is the Lorentz factor of the shock matter,  $Z$  is the charge of the accelerated particle,  $B$  is the magnetic field,  $e$  is the elementary charge and  $R$  is the linear dimension of the object. This is sometimes also called the ‘‘Hillas criterion’’ and is not only valid for shock acceleration but in similar form also for acceleration in electric fields (‘‘one shot acceleration’’). One shot acceleration takes place e.g. in the magnetosphere of a pulsar. With the Hillas criterion one can restrict possible acceleration sites to a few objects as is seen in the ‘‘Hillas plot’’ (Figure 2.3) (Hillas, 1984).

From the Hillas criterion it follows that neutron stars (pulsars) can in principle accelerate particles up to ultra high energies. However, this dimensional limit is not fully reached when realistic models of pulsar magnetospheres are constructed. The large potential drop along the magnetic field lines is significantly short-circuited by electron and positrons moving in opposite directions along the field lines (Venkatesan et al., 1997).

For a recent review on cosmic rays that is covering the subject of cosmic ray acceleration with great detail the reader is pointed to e.g. Blasi (2005).

### 2.3 Production Mechanisms of VHE $\gamma$ -Rays

The most efficient way to study sources of cosmic rays are through the detection of  $\gamma$ -rays, which are produced either within the cosmic accelerator or while CRs propagate through the interstellar medium (ISM). Several production mechanisms exist which produce  $\gamma$ -rays with energies of several GeV up to tens of TeV. The most relevant ones are shown in Figure 2.4 and addressed in the following. A more comprehensive review can be found e.g. in Longair (1992).

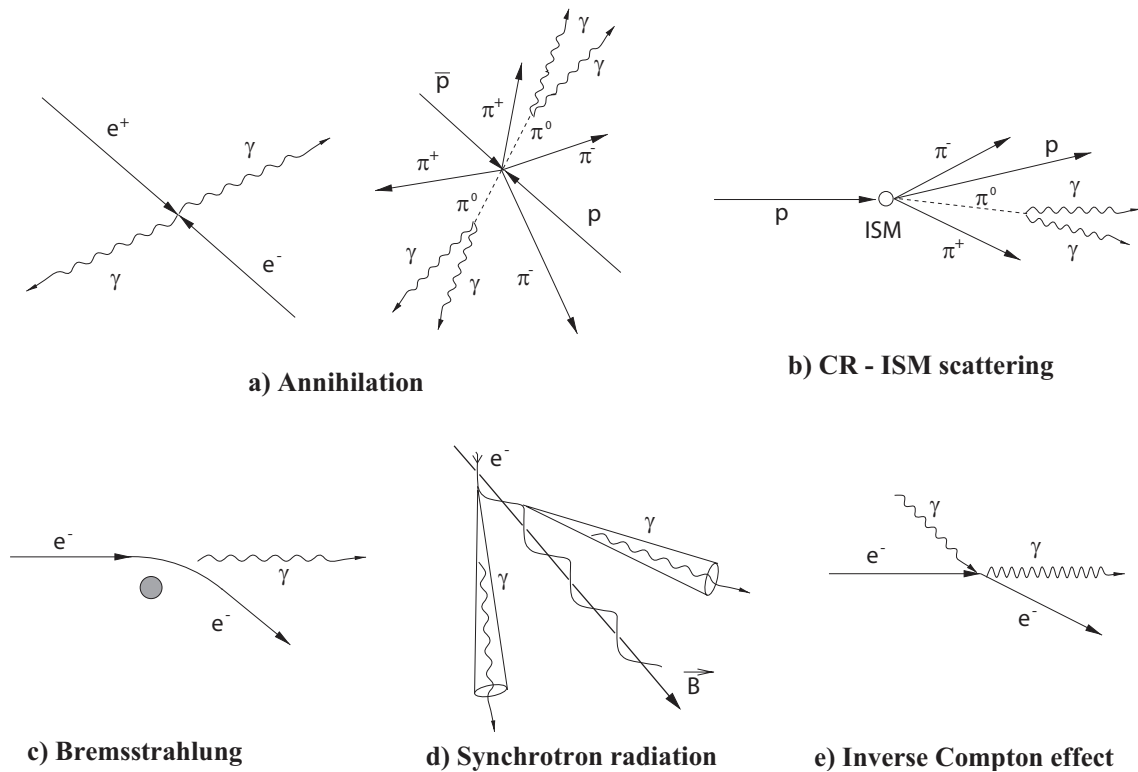


Figure 2.4: Schematic illustration of the main processes of  $\gamma$ -ray production. from Tonello (2006)

The first process shown in Figure 2.4 a is the production of  $\gamma$ -rays in the annihilation process of a positron and an electron. Two photons are emitted under an angle of 180 degrees, each with an energy of 511 keV in the center of mass system. In the annihilation of hadronic matter and

antimatter (e.g.  $p\bar{p}$ )  $\pi^0$ 's are produced, which decay with a branching ratio of 98.8% into two  $\gamma$ -rays.  $\pi^0$ 's are also produced in any interaction, which involves hadronic particles with high enough kinetic energies (Figure 2.4 b). The threshold energy for the production of  $\pi^0$ 's by protons is  $\sim 280$  MeV.

### 2.3.1 Interaction of charged Particles with Electromagnetic Fields

Charged low mass particles, mostly electrons, can interact in various ways with electromagnetic fields and can thus produce  $\gamma$ -rays. The lower row in Figure 2.4 shows three processes. The first one shows the Bremsstrahlung-mechanism, which is caused by the deflection of particles in the vicinity of nuclei. This process is important in the development of particle showers induced by CRs in the atmosphere (cf. Section 4.1.2).

#### Synchrotron Radiation

If particles are forced by magnetic field to follow a curved trajectory they emit synchrotron radiation (Figure 2.4 d). The classical theory of synchrotron radiation was developed by V.V. Vladimírsky and J. Schwinger in 1948/49. A contemporary derivation can be found in Jackson (2003). Note that the radiated synchrotron power  $P$ :

$$P = \frac{1}{6\pi\epsilon_0} \frac{e^2 a^2}{c^3} \gamma^4 \quad \text{where } a \text{ is the centripetal acceleration} \quad (2.2)$$

is a strong function of the mass  $m$  of the particle  $\propto 1/m^4$ , which is the reason why synchrotron radiation in most applications is only relevant for electrons/positrons.

The spectrum of synchrotron radiation of mono-energetic electrons is a continuum that peaks at

$$E_\gamma \simeq 1.5 \cdot 10^{-5} \left( \frac{E_e}{[\text{TeV}]} \right)^2 \cdot \left( \frac{B}{[\text{G}]} \right) \text{ GeV}, \quad (2.3)$$

where  $E_e$  is the energy of the electron and  $B$  is the magnetic field component perpendicular to the plane of the particle's trajectory. An important parameter is the time an electron needs to radiate half of its energy as synchrotron radiation. This so-called cooling time  $\tau_{1/2}$  is

$$\tau_{1/2} \sim 2.8 \cdot 10^8 \left( \frac{B}{3 \cdot 10^{-4} \text{G}} \right)^{-2} \gamma^{-1} \text{ yr}, \quad (2.4)$$

where  $\gamma$  is the Lorentz factor of the electron.

#### Curvature Radiation

In the strong field of a pulsar magnetosphere, a charged particle quickly radiates away its components of momentum perpendicular to the field lines (synchrotron radiation). The electron will eventually be confined to its lowest Landau level and follows the curved field lines of the magnetosphere while propagating outwards. Following a curved trajectory the particle produces emission that is called "curvature radiation". Curvature radiation is among the strongest sources of VHE- $\gamma$ -rays in contemporary models of high energy emission in pulsar magnetospheres.

### Inverse Compton Scattering

In Inverse Compton (IC) a low energy photon will be “upscattered” by a relativistic electron (Figure 2.4 e). In this process a considerable fraction of the electron energy (several TeV) can be transferred to the photon. One distinguishes two different regimes, the Thomson limit ( $\gamma\epsilon \ll m_e c^2$ ) and the Klein-Nishina Limit ( $\gamma\epsilon \gg m_e c^2$ ), where  $\epsilon$  is the photon energy before the scattering process and  $\gamma$  the Lorentz factor of the relativistic electron. The average energy of the photon after the scattering process is

$$\langle E_\gamma \rangle \approx \begin{cases} \frac{4}{3} \langle \epsilon \rangle \gamma^2 & \text{(Thomson limit)} \\ \frac{1}{2} \langle E_e \rangle & \text{(Klein-Nishina limit)} \end{cases} \quad (2.5)$$

$E_e$  is the energy of the electron. Typical target photon fields in IC-scattering are the 2.7 K cosmic microwave background radiation, synchrotron radiation and thermally generated photons from stars or clouds. The cross sections  $\sigma_{\text{IC}}$  for IC are

$$\sigma_{\text{IC}} = \begin{cases} \sigma_{\text{T}} \left(1 - \frac{2\gamma\epsilon}{m_e c^2}\right) & \text{(Thomson limit)} \\ \frac{3}{8} \sigma_{\text{T}} \left(\frac{m_e c^2}{\gamma\epsilon}\right) \left[\ln\left(\frac{2\gamma\epsilon}{m_e c^2}\right) + \frac{1}{2}\right] & \text{(Klein-Nishina limit)} \end{cases} \quad (2.6)$$

In the Klein-Nishina limit the cross section for IC-scattering is highest if the product of the energy of the scattered photon and the produced  $\gamma$ -ray is similar to the energy squared of the electron rest mass.

### Absorption of $\gamma$ -Rays in the Magnetosphere of a pulsar

In the magnetosphere of a pulsar basically two processes result in efficient absorption of  $\gamma$ -rays. Either pair production takes place by absorption of a virtual photon from the magnetosphere or by absorption of a low energy photon from thermal or synchrotron origin. The cross sections are the same as for the IC process. An extensive discussion of various absorption mechanisms in pulsar magnetospheres is out of the scope of this work and can be found in Harding and Lai (2006).

## Chapter 3

# Pulsars and their Nebulae

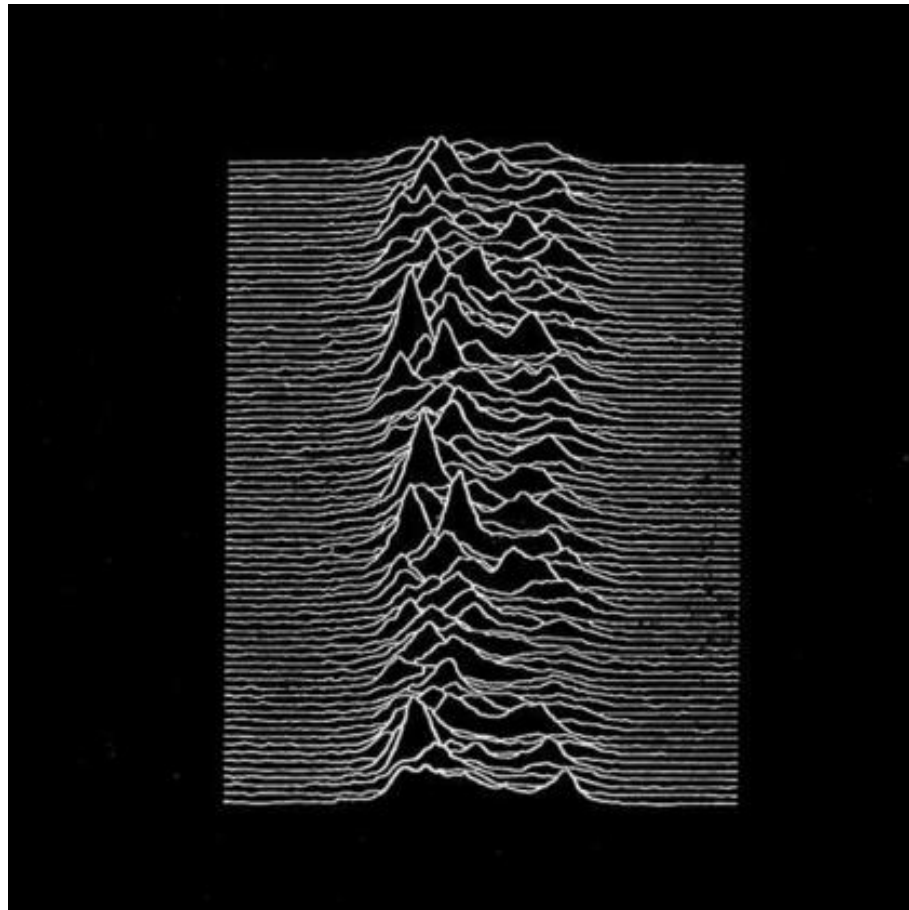


Figure 3.1: Cover of "Unknown Pleasures" the first album by Joy Division, released in 1979. It shows 100 hundred radio pulses of the first discovered pulsar PSR B1509-58.

Little doubt exists that pulsars are rapidly rotating, magnetized neutron stars (NS). This gives rise to two effects (Goldreich and Julian, 1969).

1. High electric fields  $\propto (\vec{v} \times \vec{B})$  are induced within the magnetosphere of the pulsar. In these huge potentials of up to  $\sim 10^{12}$  V charged particles can accelerate to ultrarelativistic energies.
2. The axis of rotation and the magnetic dipole moment are normally not aligned in a NS. This leads to powerful electromagnetic (em) dipole radiation at the rotational frequency of the NS.

The picture that NSs are powerful sources of energy is widely accepted and was partially predicted to explain the emission of the Crab nebula. The situation is in fact more complicated and despite several theoretical and experimental efforts a self consistent picture that explains the magnetosphere of the NS with all its implications for particle acceleration, does not exist yet. The unknown structure of a NS introduces further uncertainties. It is not clear e.g. if ions are bound to the surface of the neutron star and, if this is the case, if they can overcome their binding energy and are accelerated in the electric field, which is generated in the magnetosphere.

Relativistic particles (electrons) are influenced by ambient magnetic fields and emit em-radiation (cf. Section 2.3). Inside the inner magnetosphere, charged particles follow the curvature of magnetic field lines and radiate photons up to several tens of GeV (synchro-curvature radiation). Further out, at a standing reverse shock the magnetic field of the pulsar is rising to several tens up to more than hundred micro Gauss. In such strong magnetic fields the relativistic light particles rapidly lose their kinetic energy by synchrotron radiation and as well produce VHE  $\gamma$ -rays by inverse Compton up-scattering of synchrotron photons, photons of thermal origin or photons of the cosmic microwave background (CMB).

Below I overview the current understanding of neutron stars, their magnetospheres and implications for particle acceleration both inside and outside of the magnetosphere. In the same context the observability of  $\gamma$ -rays is discussed from a theoretical and experimental point of view.

### 3.1 Introduction to Pulsars and their Nebulae from a historical Point of View

It was only in 1968 that pulsars were discovered and identified as neutrons stars. Before the discovery of pulsars and in particular before the discovery of the pulsar in the Crab nebula the origin of the continuum emission of the nebula extending from radio to optical wavelengths remained a mystery. With the detection of X-Rays from the Crab Nebula by Bowyer et al. (1964b,a) the continuum emission could be explained as synchrotron radiation by relativistic electrons (see Woltjer, 1964). The detection of X-Rays and their association with synchrotron radiation implied that the synchrotron emitting electrons lose their energy in less than 100 years and thus a mechanism must exist that constantly replenishes the nebula with new relativistic electrons, i.e. a cosmic accelerator must exist in the direct vicinity of the nebula.

Hoyle et al. (1964) discussed the idea that a neutron star can oscillate about its stable configuration and thus could be a powerful emitter of em-radiation due to simultaneous oscillations of the strong magnetic field of the NS. The same authors argued that the radiation will be reflected from any cloud of gas whose plasma frequency exceeds the radiation frequency. Thus pressure is exerted onto the cloud. This pressure is balanced by the internal pressure of the cloud. The internal pressure is provided by relativistic electrons accelerated in the zone of reflection.

A few years later e.g. Chau (1967) showed that any vibrational mode of a neutron star is rapidly damped by the emission of gravitational waves. Therefore, the proposed oscillations could not provide the em-radiation necessary to power the Crab nebula. In the same year Pacini (1967)

pointed out that instead of vibrational modes the rotation of a NS could be a powerful source of magnetic dipole radiation, which would explain the observed luminosity of the nebula. Remarkably Pacini published his predictions around the same time when Jocelyn Bell-Burnell, at that time a graduate student with Hewish, discovered by chance an extraterrestrial source of periodic radio emission with a period of 1.337 sec (see Figure 3.1) (Hewish et al., 1968). This source is today known as the pulsar PSR B1919+21. The name pulsar derives from “pulsating star”.

It soon turned out that a plausible source of such stable radio pulses could be a fast spinning neutron star. Gold (1968) predicted that if this association is correct one should observe a steady but slow increase of the observed period and detect pulsars with much shorter periods. These predictions could be confirmed with the detection of a pulsar with a period of 33 ms in the Crab nebula (Staelin and Reifenstein, 1968) and the observation that its period increases by 36.5 ns per day (Richards and Comella, 1969). The period increase implies an energy loss that is sufficient to explain the luminosity of the Crab nebula Gold (1969). Moreover, the discovery of a pulsar in the Crab nebula confirms that a NS is formed in a supernova explosion, as predicted by Baade and Zwicky (1934).

After this rather short outline of the historic development, which leads to the conclusion that pulsars can be identified with neutron stars, and that they provide the energy that powers the Crab nebula, I will in the following elaborate more on some features of neutron stars and their magnetospheres. Afterwards, I will summarize our current understanding of the pulsar wind nebula complex, which consists of a pulsar and a surrounding nebula. The following material is a summary extracted from literature.

## 3.2 Neutron Stars

### 3.2.1 Formation of a Neutron Star

Baade and Zwicky (1934) predicted that a compact object might be formed in a supernova and it is nowadays generally accepted that a NS is formed in a supernova explosion at the end of the life of a massive ( $\gtrsim 5 - 10M_{\odot}$ ) star. After the ejection of the shell of the star and the termination of the nuclear fusion process the gravitational pressure of the core is not more balanced by radiation pressure and the core collapses. If the mass of the core is  $> 1.44M_{\odot}$  the gravitational pressure overcomes the pressure of the degenerated electron gas (Chandrasekhar, 1931). Protons and electrons combine to neutrons and the core collapses further until the gravitational collapse is stopped by the neutron degeneracy pressure. In its final configuration a NS has a radius of 10 km–20 km. A few days after its formation a NS has cooled to ( $\simeq 10^7$  K); it further cools to a few  $10^6$  K within a few thousand years.

Only a small fraction of the angular momentum of the progenitor star is carried away by  $\nu$ 's and ejected matter. Therefore, most of the angular momentum is transferred to the NS, which explains the fast rotation periods of young pulsars of less than 100 ms.

### 3.2.2 Evolution of Neutron Stars in Binary Systems to Millisecond Pulsars

As a matter of fact most stars are part of a binary system. Therefore, it is interesting to note what happens, if a NS is formed in a binary. Figure 3.2 from Lorimer (2005) shows possible scenarios. In most cases the binary will disrupt because of large mass losses and any impulsive “kick” velocity the neutron star received at birth from a slightly asymmetric explosion (Hills, 1983). If the binary survives, the companion star continues its evolution and loses mass to the NS when it has evolved into e.g. a red giant. In this way the NS gains angular momentum and spins up. During the accretion of matter onto the NS-surface X-Rays are emitted (X-ray binary).

If the companion is massive enough it also explodes in a supernova and the binary either disrupts or a double neutron star binary is formed (Hulse and Taylor, 1975). If the companion does not explode, the evaporation eventually continues until the companion is completely ablated. This seems to be the case for the ms-pulsar PSR B1957+20, which is orbited by a  $0.02 M_{\odot}$  companion (Fruchter et al., 1990).

A more detailed review on possible evolution scenarios can be found in Lorimer (2005) and references therein.

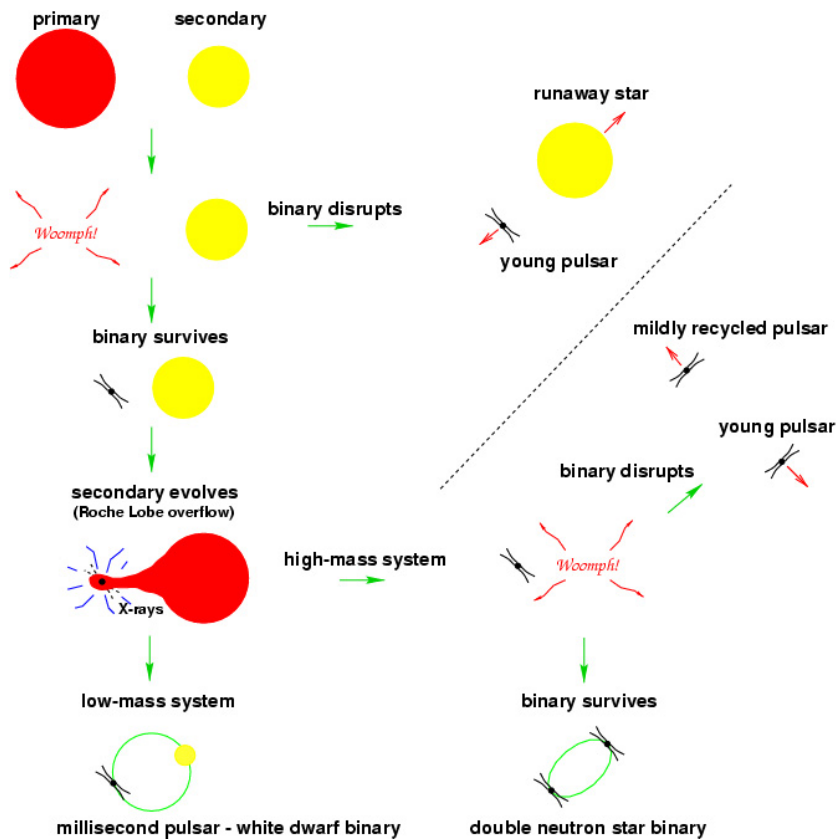


Figure 3.2: Possible evolutions of a pulsar in a binary system (Lorimer, 2005).

### 3.2.3 Structure of a Neutron Star

An upper limit on the mass of a NS is placed by the equation of state of nuclear matter. Despite the uncertainties that exist the upper mass is most likely  $\simeq 1.8 M_{\odot}$ . The uncertainties of the structure of a NS are mainly due to the unknown behavior of nuclear matter at densities  $\gg 10^{14} \text{ g/cm}^3$  and temperatures much below what is accessible by heavy ion colliders. A contemporary review of the competing models of the inner structure of a NS can be found in Weber (2005). Figure 3.3, taken from this review article, shows the structure of a NS in different models. In the standard NS model the surface consists of a stiff crust of iron-nuclei. Below the surface density increases and it is energetically more favorable for matter to form nuclei with high number of neutrons. Further inside the NS where the density is above the neutron drip point ( $\sim 10^{11} \text{ g/cm}^3$ ), nuclei start to become unstable and are embedded in a superfluid of neutrons. At even higher densities a large variety of scenarios is possible, ranging from normal nuclear matter to strange-quark matter.

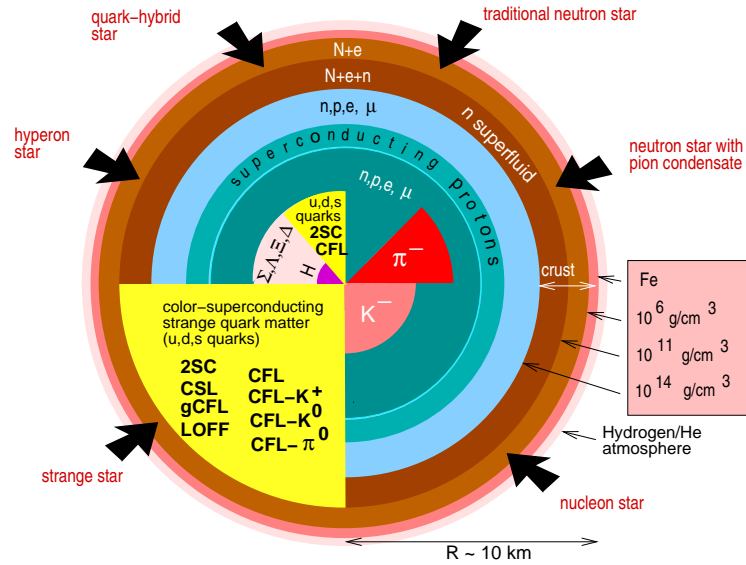


Figure 3.3: Competing structure and novel phases of subatomic matter of neutrons stars predicted by theory (from Weber, 2005)

### 3.2.4 Magnetosphere of a Neutron Star

During the formation of a neutron star the magnetic field of the progenitor star cannot be dissipated as fast as the NS is formed because of the high conductivity of the plasma. The magnetic flux is conserved, i.e. the field strength increases as  $1/R^2$  during the contraction of the stellar core. Therefore, field strengths as high as  $10^{10} - 10^{14}$  G can be expected at the surface of the NS by extrapolating from the magnetic field of the progenitor star (Woltjer, 1964; Pacini, 1967).

The magnetosphere of a NS is divided into the inner magnetosphere, which extends to the light cylinder and the outer magnetosphere beyond the light cylinder (see Figures 3.5 and 3.8). The light cylinder  $R_{LC}$  is defined as the distance from the center of the NS where the velocity of a corotating magnetosphere reaches the speed of light (see also Figure 3.5), i.e.:

$$R_{LC} \equiv \frac{c}{\Omega}, \quad (3.1)$$

where  $c$  is the speed of light and  $\Omega$  is the rotational frequency of the NS.

If the magnetic dipole is aligned with the axis of rotation (aligned rotator), Goldreich and Julian (1969) showed that the magnetosphere of a NS is likely populated with a nearly force-free plasma. The more general and realistic case of an inclined (oblique) rotator remained a mystery due to the difficulty of finding an analytic solution. Only with the availability of numerical solutions, insight could be gained first by Contopoulos et al. (1999) in the time-independent case. Recently, the time-dependent evolution of the magnetosphere was studied among others also by Spitkovsky (2006). He obtained the magnetosphere shown in Figure 3.4, which shows the situation when the magnetic axis is inclined by  $60^\circ$  with respect to the rotational axis of the NS. The vertical cut shows the magnetic field lines in the poloidal plane, i.e. the plane defined by the vector of the magnetic dipole and the rotational axis. The horizontal plane shows the corresponding cut in the equatorial plane perpendicular to the rotational axis.

### 3.2.5 Energy Loss of a rotating and magnetized Neutron Star

The magnetosphere co-rotates with the NS and em-radiation is emitted because the magnetic moment of the magnetosphere is not aligned with the spin axis. Assuming a perfect dipole in

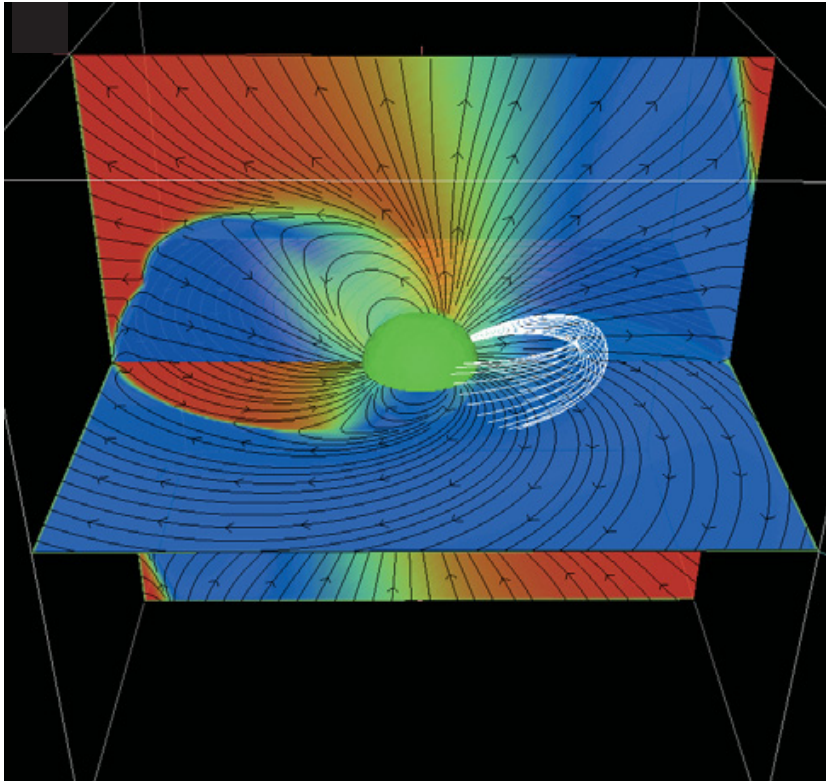


Figure 3.4: Calculations by Spitkovsky (2006) of the magnetosphere of an oblique rotator ( $60^\circ$  inclination) in the corotating frame. Color represents the toroidal field. A sample three-dimensional flux tube is traced in white.

vacuum with a magnetic dipole moment  $\vec{\mu}$  inclined with the angle  $\alpha$  against the spin axis  $\vec{\Omega}$  of the NS, the luminosity  $L_{\text{Dip-vac}}$  of the emitted dipole radiation is given by (e.g. Jackson, 2003)

$$L_{\text{Dip-vac}} = \frac{2}{3} \sin^2 \alpha \cdot \frac{\mu^2 \Omega^4}{c^3} \quad . \quad (3.2)$$

In the more realistic magnetosphere simulation (Spitkovsky, 2006), that also includes currents flowing inside of the magnetosphere, one obtains a twice higher luminosity  $L_{\text{Dip-sim}}$ .

$$L_{\text{Dip-sim}} \simeq (1 + \sin^2 \alpha) \frac{\mu^2 \Omega^4}{c^3} \quad . \quad (3.3)$$

The emitted energy is supplied by the kinetic energy of the NS. Thus the energy loss rate or spin-down luminosity of a NS ( $\dot{E}$ ) can directly be inferred from the observed period ( $P \sim 0.1$  sec) and first derivative of the period ( $\dot{P} = 10^{-13} \text{ sec}^{-1}$ ), if one assumes a typical mass ( $\sim 1.4 M_\odot$ ) and radius ( $\sim 10$  km) of the NS

$$\dot{E} = I \Omega \dot{\Omega} = - (2\pi)^2 I \frac{\dot{P}}{P^3} \sim 10^{36} \text{ erg sec}^{-1} \quad , \quad (3.4)$$

where  $I$  is the moment of inertia of the NS. Using the relation between the spin-down luminosity and the dipole radiation it is straightforward to calculate the magnetic field on the surface of the NS. In the simulations of Spitkovsky (2006) the surface magnetic field is given by

$$B_* = 2.6 \times 10^{19} \sqrt{\frac{P \dot{P}}{1 + \sin^2 \alpha}} \text{ G} \quad , \quad (3.5)$$

which is be up to 1.7 times smaller than the estimate from the vacuum formula. Magnetic fields of  $\sim 10^{12}$  Gaus are obtained for values of  $P = 10^{-1}$  sec and  $\dot{P} = 10^{-13}$  sec $^{-1}$ , typical for young pulsars.

### 3.3 Overview of the Pulsar Wind Nebula Complex

Radiation from a Pulsar-wind-nebula complex

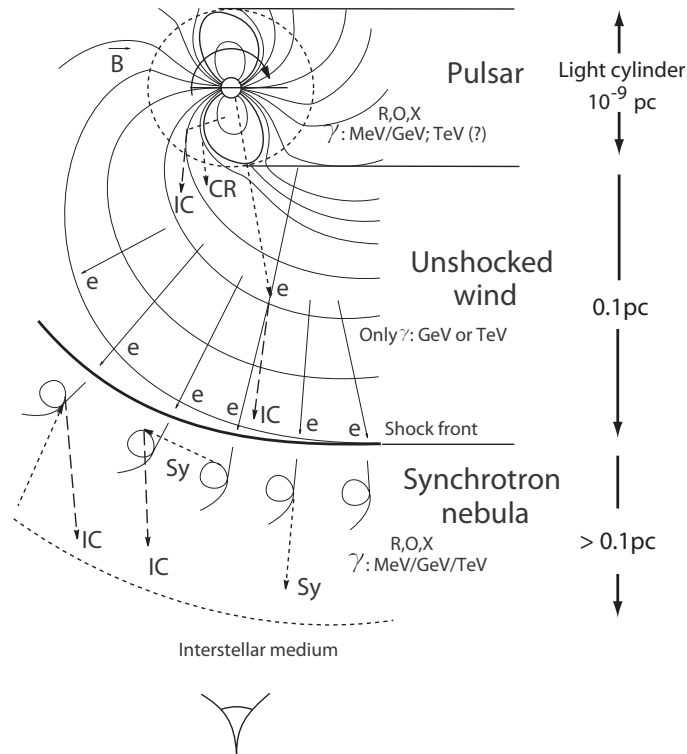


Figure 3.5: Schematic view of the pulsar-wind-nebula complex and the emitted radiation (adapted from Aharonian and Bogovalov, 2003). Note that the graph is not to scale. Indicated dimensions are valid for the Crab nebula.

After this short introduction into the characteristics of NSs one should remember that the concept of a rotating magnetized NS was introduced by Pacini (1967) in order to explain the continuum emission of the Crab nebula. The observed emission from the pulsar and the nebula is tightly coupled to the magnetosphere of the neutron star. Therefore, it is natural to consider the pulsar and the nebula as an entity, the so called pulsar-wind-nebula complex (s. Figure 3.5). Below I give an overview of the PWN complex. The  $\gamma$ -ray emission from the inner magnetosphere is discussed in section 3.4 and the  $\gamma$ -ray emission from the nebula in section 3.5.

The dynamics at the center of the pulsar wind nebula complex (PWN-complex) are dominated by processes in the inner magnetosphere, i.e. within the radius of the light cylinder (Equation 3.1), which is typically located at a distance of  $\sim 1000$  km or  $\sim 100$  NS-radii from the spin axis. Radiation from within the light cylinder is expected to be (a) pulsed because of the dipole structure of the rotating magnetosphere and (b) the duty cycle of the emission over one rotational period is expected to be about  $\sim 10\%$  because of propagation arguments of the radiation in the inner magnetosphere. Moreover, electrons and positrons are produced in pair-cascades in the inner magnetosphere and stream out along open field lines (pulsar wind).

Models indicate that only a small fraction ( $10^{-4} - 10^{-5}$ ) of the pulsar's spin-down luminosity is converted into particle kinetic luminosity (e.g. Ruderman and Sutherland, 1975; Arons, 1979; Michel, 1982; Cheng et al., 1986a). In other words, the energy flux at the light cylinder is most likely Poynting flux dominated. This is quantified by the ratio of the Poynting flux to particle kinetic energy flux, the so-called magnetization parameter  $\sigma$ . While  $\sigma$  is  $\sim 10^4$  at the light cylinder the presence of a strong shock in the Crab nebula at a distance of 0.1 pc from the pulsar predicates a kinetic energy dominated flux, i.e.  $\sigma < 1$ . In the Crab nebula  $\sigma$  is  $\sim 10^{-3}$ . A plausible explanation for this exceptionally small value is the small translational velocity observed for the Crab pulsar, which allows the shock distance to grow to larger distances in the Crab nebula than in other PWNe. The transfer from a Poynting dominated flux to a kinetic dominated flux with Lorentz factors  $\sim 10^6$  is not completely understood. Contopoulos and Kazanas (2002) derived from their solution of the axisymmetric pulsar magnetosphere (Contopoulos et al., 1999) and the conservation laws of the associated (magnetohydrodynamic) MHD flow that a linear increase of the Lorentz factor of the outflowing plasma with distance is possible. This region of the unshocked pulsar wind (see Figure 3.5) where the transformation from a Poynting dominated to a kinetic dominated flux occurs is underluminous in X-rays and lower energies. Bogovalov and Aharonian (2000) discuss inverse Compton scattering of the relativistic particles on soft photons from either the pulsar or the CMB as a possible source of  $\gamma$ -radiation from this otherwise invisible region.

Further out a standing reverse shock forms where the ram pressure provided by the luminosity of the pulsar is balanced by the pressure of the nebula (in the Crab nebula at  $\sim 0.1$  pc or  $3 \cdot 10^{12}$  km from the NS) (Rees and Gunn, 1974; Kennel and Coroniti, 1984a,b). At the shock, the wind particles are accelerated to ultra relativistic energies ( $\sim 10^{16}$  eV in the Crab nebula) and their pitch angles are randomized. Downstream of the shock the toroidal magnetic field is wound up and thus further amplified. In the down stream region about 20% of the spin-down luminosity of the Crab pulsar is dissipated by synchrotron radiation of the relativistic particles. The remaining 80% is plausibly ascribed to adiabatic losses from the expansion of the Nebula against a confining external pressure. The Crab nebula is visible in VHE- $\gamma$ -rays because of inverse Compton upscattered low energy photons (Gould, 1965; De Jager and Harding, 1992; Aharonian et al., 1997; Bednarek and Bartosik, 2003) as will be explained later in more detail.

### 3.4 $\gamma$ -Ray Emission in the Magnetospheres of Pulsars

The inner magnetosphere of a NS is probably filled with a corotating plasma (Goldreich and Julian, 1969), which shorts-out the induced electric fields in all except a few locations within the light cylinder. Two presumable sites where a substantial potential can build up and charged particles are accelerated to ultrarelativistic energies are above the poles of the NS and in gaps of the inner magnetosphere.

In the presence of the strong magnetic field, particles accelerated in these regions rapidly lose their kinetic energy transverse to the direction of the field lines by synchrotron radiation. This forces the particles to move along the curved magnetic field lines. The movement along the curved field lines results in radiation of  $\gamma$ -rays up to several tens of GeV (see section 2.3).

#### 3.4.1 The experimental View

The EGRET experiment on board the CGRO detected six  $\gamma$ -ray emitting pulsars above 1 GeV with high confidence and three possible  $\gamma$ -ray emitting pulsars (see e.g. Thompson, 2004). As a matter of fact EGRET is currently the only experiment that detected  $\gamma$ -ray emission from pulsars up to energies of  $\sim 10$  GeV.

Figure 3.6 shows the pulse phase profile of the six detected pulsars, for energies  $> 100$  MeV in yellow and  $> 5$  GeV in black. Above 100 MeV all six light curves show a double peak structure.

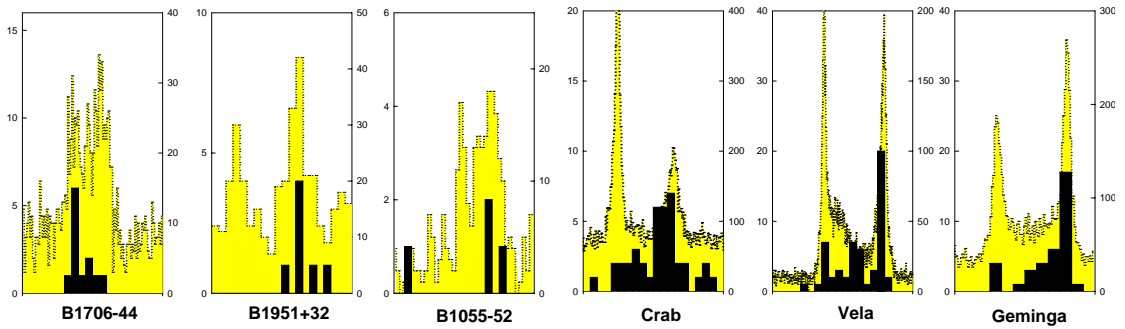


Figure 3.6: Pulse phase profiles of the six pulsars detected by EGRET in  $\gamma$ -rays above 5 GeV (black) and above 100 MeV (yellow). Each panel shows one full rotation of the neutron star. From Thompson (2004).

At energies  $> 5$  GeV one of the two peaks seems to fade. However, statistics is not large enough to allow for a solid statement (Thompson, 2004).

While pulsations identify sources as rotating neutron stars, the observed energy spectra reflect the physical mechanisms that accelerate charged particles and help to identify interaction processes that produce the pulsed radiation. The broad band spectra of the six beforehand mentioned pulsars  $> 5$  GeV and PSR B1509-58, which was detected up to 10 MeV, are shown in Figure 3.7. In the Figure the fluxes are shown multiplied with the energy squared (spectral energy distribution or SED) and thus the observed emitted power per energy interval.

It is evident from the spectra that most of the power is emitted at the highest detected energies. The peak of the observed intensity is followed by a sharp cutoff as suggested by non-detections of pulsed emission at energies  $\gtrsim 100$  GeV. Even though the cutoff is indicated at energies  $< 10$  GeV in most of the presented pulsars, the limited sensitivity and restricted energy range of EGRET did not allow for a precise spectroscopic measurement of any cutoff. Such measurements would provide valuable information for our understanding of particle acceleration in pulsar magnetospheres. Another feature worth mentioning in the spectra of Vela, Geminga, and B1055-52 is the evidence of a thermal component in X-rays ( $\sim 10^6$  K), which is believed to be a signature of the hot neutron star surface.

### 3.4.2 The theoretical View

The basic features that the broad-band spectra in Figure 3.6 exhibit can be fairly well explained by theory except for the radio emission. Whilst the radio emission is believed to originate from an unknown coherent process e.g. like in a MASER, the high energy emission of a pulsar is generated by relativistic particles that travel through the magnetosphere (see Michel, 1982, for a review).

Differences between models of  $\gamma$ -ray emission are mainly due to different assumed acceleration sites. It was already mentioned that the electric field induced by the rotating magnetosphere is shorted-out at all but a few locations due to a conductive, corotating plasma. The acceleration sites of the three most popular models (s. Figure 3.8) are above the polar cap and in a vacuum gap above the surface that is inscribed by the last closed field lines and can extend out to the light cylinder (outer gap, slot gap). Some of the differences between these models are addressed in the following.

#### The Polar Cap Model

In polar cap (PC) models (e.g. Sturrock, 1971; Ruderman and Sutherland, 1975; Daugherty and Harding, 1982, 1996; Usov and Melrose, 1995) it is believed that particle acceleration takes place

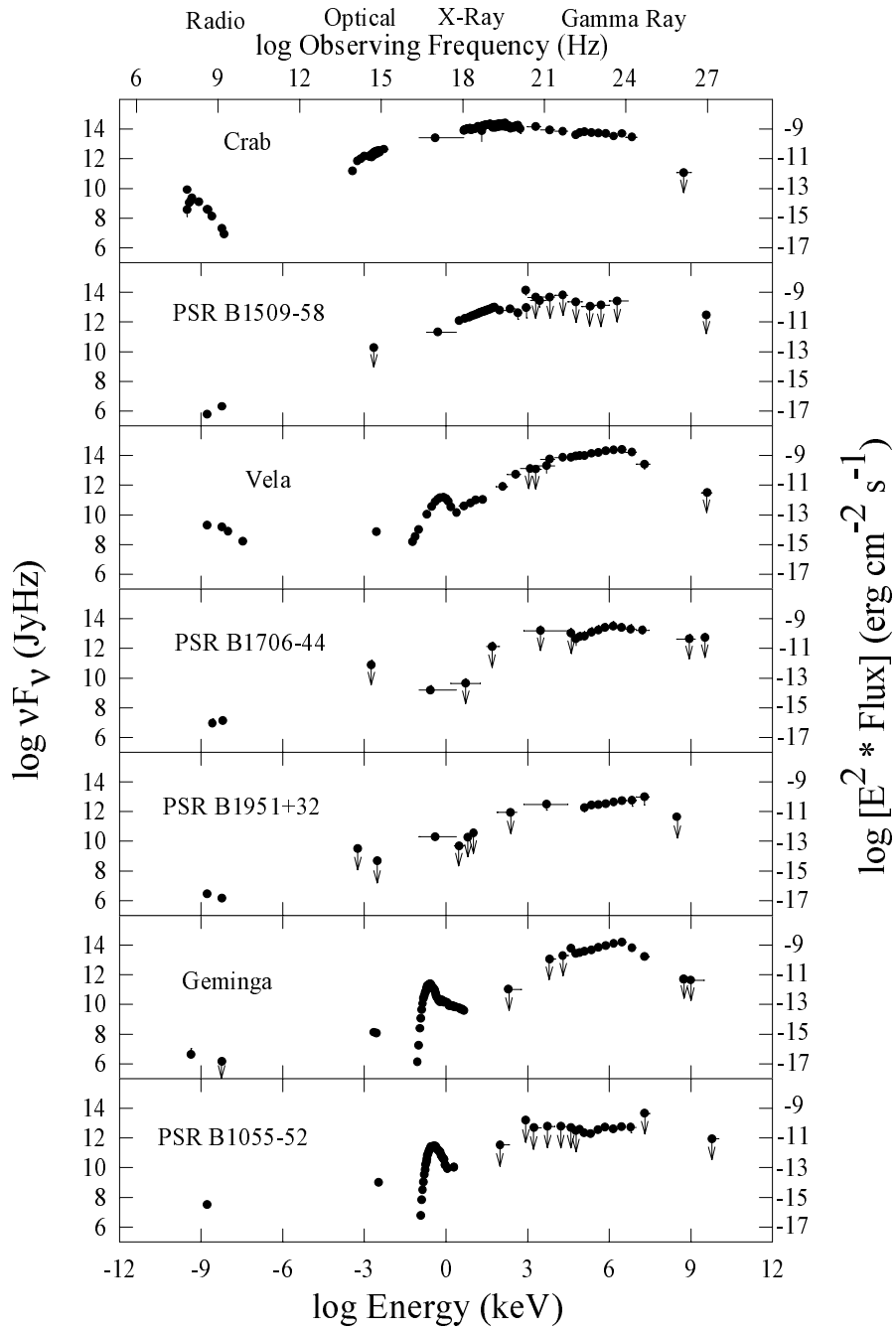


Figure 3.7: Broad-band spectral energy distribution of the seven  $\gamma$ -ray pulsars detected by EGRET, from Thompson et al. (1999)

near the NS-surface. There exist some variants of polar cap models, with the primary division being whether or not there is free emission of particles from the NS-surface (Harding, 2002). In all PC-models  $\gamma$ -rays are emitted by curvature radiation, synchrotron radiation and inverse Compton upscattering of low energy photons from the NS-surface. The highest energy photons ( $> 1$  GeV) have a high probability to interact with the magnetic field and induce pair cascades. The pair-production rate is believed to be sufficient high to short-out a large fraction of the induced electric potentials within the inner magnetosphere. However, it was found (Harding and Muslimov, 2002) that the electric field above the PC is not completely shielded, thus allowing acceleration to Lorentz factors  $\sim 10^7$ . In young pulsars the acceleration voltage is nearly independent of the rotational period of the NS and its surface magnetic field of the NS (Harding and Muslimov, 2002). In older pulsars pair production is suppressed. The acceleration voltage is then only limited by the geometry of the polar cap, which itself depends on the period and the surface magnetic field of the NS.

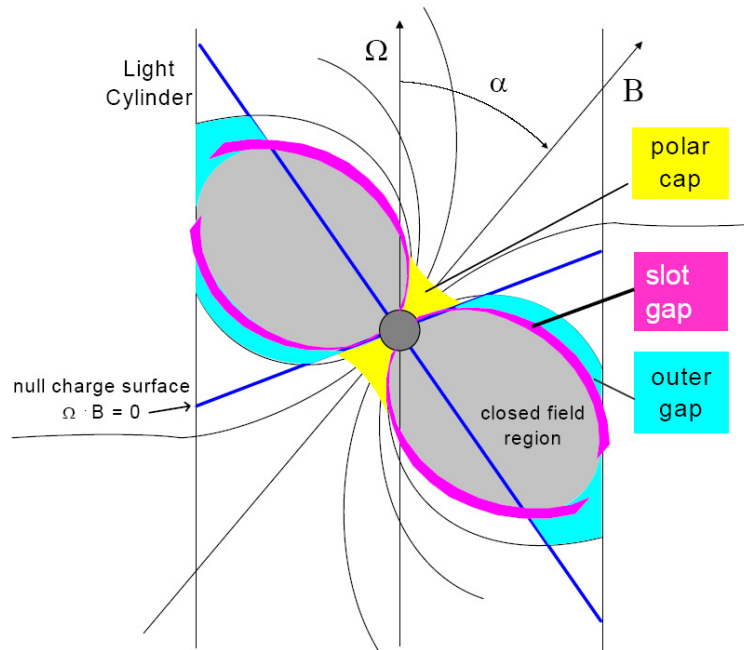


Figure 3.8: Cross-section of the poloidal plane of the pulsar magnetosphere. Indicated are possible sites where an electric potential can build up and particles are accelerated. Popular sketch by A. Harding.

A distinct feature of polar cap models is a sharp “super-exponential” cutoff in the energy spectrum, which is caused by efficient one-photon pair production attenuation at the pair escape energy (Harding et al., 1997)<sup>1</sup>. Polar cap models predict a dependence of the cutoff energy that is inversely proportional to the surface magnetic field strength. For ms-pulsars Bulik et al. (2000) predict that the spectral cutoff is not determined by magnetic pair production. In this case the acceleration zone extends from the NS-surface to the outer magnetosphere and the cutoff of the curvature radiation spectrum can extend up to  $\gamma$ -ray energies of 50 – 100 GeV.

### The Slot Gap Model

(Scharlemann et al., 1978) found that in the polar cap scenario the potential gap above the polar cap increases when approaching the last closed field line. Based on these findings, Arons (1983) pointed out the possibility of a high-altitude acceleration region or “slot gap”. Within the slot gap

<sup>1</sup>The pair escape energy is the highest energy for which the photon can escape the magnetosphere without being subject of pair production

scenario it is possible to solve the problem of too narrow predicted beam sizes of traditional polar cap models. (Muslimov and Harding, 2003; Harding, 2005) have revisited the slot gap model by including general relativistic frame dragging and succeeded in producing wider pulse profiles.

### The Outer Gap Model

Cheng et al. (1986a,b) assumed a global current flow pattern in the magnetosphere. Doing so they could show that a charge depleted slablike volume can form in the magnetosphere because particles that stream out of the gap along open field lines cannot be replenished from below. The gap boundaries are given on one side by the last closed field lines and on the other by a charged layer on a surface of “open” magnetic field lines, which is limited by pair creation. The starward end of the gap is near the null surface, which is defined by  $\vec{\Omega} \cdot \vec{B} = 0$ . On the opposite side, the gap extends to the light cylinder (cf. Figure 3.8).

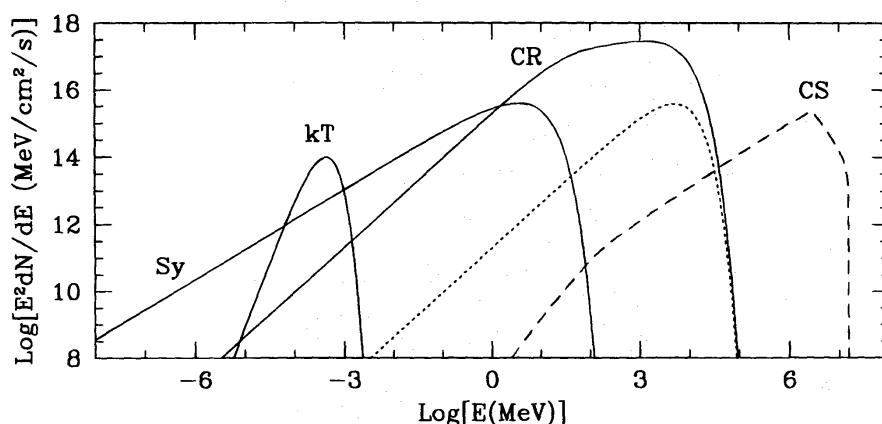


Figure 3.9: Characteristic phase-averaged spectrum for a young  $\gamma$ -ray pulsar. Solid lines show the curvature spectrum (CR), the synchrotron emission (Sy) and the thermal surface flux (kT). For comparison, the dotted curve gives the mono-energetic primary curvature spectrum with the same cutoff energy as for curvature radiation. The dashed curve gives the TeV pulsed spectrum from Compton upscattering of the synchrotron spectrum on the primary  $e^\pm$  (from Romani, 1996).

Pair production is an essential ingredient in all outer gap models, which allows the gap to sustain. Beyond a death line (Chen and Ruderman, 1993), which falls about periods larger  $\sim 0.3$  sec and surface magnetic fields of less than  $\sim 10^{12}$  G, pair production is not supported anymore and the gap cannot form. In young pulsars the hard  $\gamma$ -rays for pair production are provided by curvature radiation and IC scattering of softer (synchrotron) photons.

Unlike in the polar cap model, high-energy photons emitted in the outer magnetosphere are not affected by one-photon pair production, because of orders of magnitude lower magnetic fields. The maximum  $\gamma$ -ray energy is determined by the maximum energy of the accelerated electron spectrum, which is limited by radiation reaction losses. Therefore, the shape of the cutoff is expected to gradually fall more than in polar cap model spectra.

In first outer gap models by Cheng et al. (1986a,b) the predicted  $\gamma$ -ray-flux extended up to TeV energies, which could be experimentally ruled out. Therefore, the magnetosphere has to be optically thick for TeV emission. One possibility is that the outer gap is immersed by X-Ray photons from thermal radiation of the NS and/or from heated polar caps and the  $\gamma$ -rays are subject to pair creation (Hirotani, 2000). However, also a pulsed TeV component due to inverse Compton scattering is predicted in outer gap models (e.g. Hirotani, 2001, 2006c). Unfortunately, the TeV-flux level depends on the emission spectrum in the infra-red (IR) band, which is notoriously difficult

to measure in most pulsars.

Figure 3.9 from Romani (1996) shows a model calculation of the high energy  $\gamma$ -ray emission. Apart from the thermal radiation of the NS-surface the emission up to several MeV is dominated by synchrotron radiation. Curvature radiation (denoted CR in the figure) is the dominant process of high energy emission up to several tens of GeV.

### 3.5 VHE- $\gamma$ -Ray Emission in the Pulsar Wind Nebula

Above I outlined possible scenarios of  $\gamma$ -ray emission in the magnetospheres of pulsars. From measurements (e.g. Musquere, 1999; Lessard et al., 2000; de Naurois et al., 2002; Aharonian et al., 2004) one knows that the pulsed emission must be strongly attenuated at a few tens of GeV. At higher energies  $\gtrsim 100$  GeV the dominant source of VHE- $\gamma$ -rays is the pulsar wind nebula. The commonly accepted dominating mechanism for  $\gamma$ -ray production in pulsar wind nebulae is inverse Compton (IC) scattering of relativistic electrons in the nebula on soft photon fields (De Jager and Harding, 1992; Aharonian et al., 1997; Bednarek and Bartosik, 2003). The target photon fields for IC can be the cosmic 2.7K radiation, photons from thermal radiation of dust or stars, or as in the case of the Crab nebula the synchrotron radiation of the relativistic particles itself (self synchrotron Compton, SSC-model). Under the assumption that the target photons for IC are solely provided by the CMB the total luminosity in VHE  $\gamma$ -rays is determined by the spin down luminosity of the pulsar, the temporal evolution of the system and the efficiency at which the spin-down luminosity is converted into the kinetic energy of particles (e.g. Bednarek and Bartosik, 2005b). It has to be mentioned that IC of  $e^\pm$  is not the only process that gives rise to VHE- $\gamma$ -rays. It is as well possible that ions are also present in the pulsar wind. Through hadronic interactions and VHE- $\gamma$ -rays could be produced by secondary  $\pi^0$ -decay (Atoyan and Aharonian, 1996b; Bednarek and Protheroe, 1997; Bednarek and Bartosik, 2003, 2005b). As a matter of fact, ions are probably a necessary ingredient for the acceleration mechanism of particles in the standing reverse shock (Hoshino et al., 1992).

#### 3.5.1 VHE- $\gamma$ -ray Emission of the Crab Nebula

Among the pulsar wind nebulae the Crab nebula is exceptional. Because of the strong persistent emission of the nebula over 21 decades of frequencies, the Crab nebula is one of the best studied celestial objects (see Figure 3.11). It was the first object that was detected at TeV energies by the Whipple collaboration (Weekes et al., 1989) and is the strongest steady source of VHE- $\gamma$ -rays known in our Galaxy. The magnetic field within the nebula is  $\sim 10^{-4}$  G, which results in rapid cooling of relativistic electrons. Almost all energy is radiated away in synchrotron emission, leaving only a relative weak IC component (Atoyan and Aharonian, 1996a). The only reason why the Crab nebula is such a strong VHE- $\gamma$ -ray emitter is because of the unusually high apparent spin-down luminosity of the pulsar of  $5 \times 10^{38}$  erg s $^{-1}$ .

The first satisfactory model calculation of the IC-Component of the Crab nebula was carried out by De Jager and Harding (1992). They used the spatial distribution of the magnetic field from MHD calculations (Figure 3.10(a)) and the measured, spatial resolved synchrotron emission to derive energy spectra of electrons as a function of radial distance from the pulsar. The inverse Compton flux at a given energy is then obtained with the IC production rate (Jones, 1968) and integrating over the spatial distribution of synchrotron photons and electrons and their corresponding energies.

The calculations also make predictions of the expected size of the emission region (see Figure 3.10(b)), which sensitively depend on the assumed distribution of the magnetic field. In general the source size shrinks with increasing energy.

Figure 3.11 shows a contemporary model calculation of the synchrotron- and IC-emission of the Crab nebula. The overall agreement with data is good. An observational gap exists in the energy

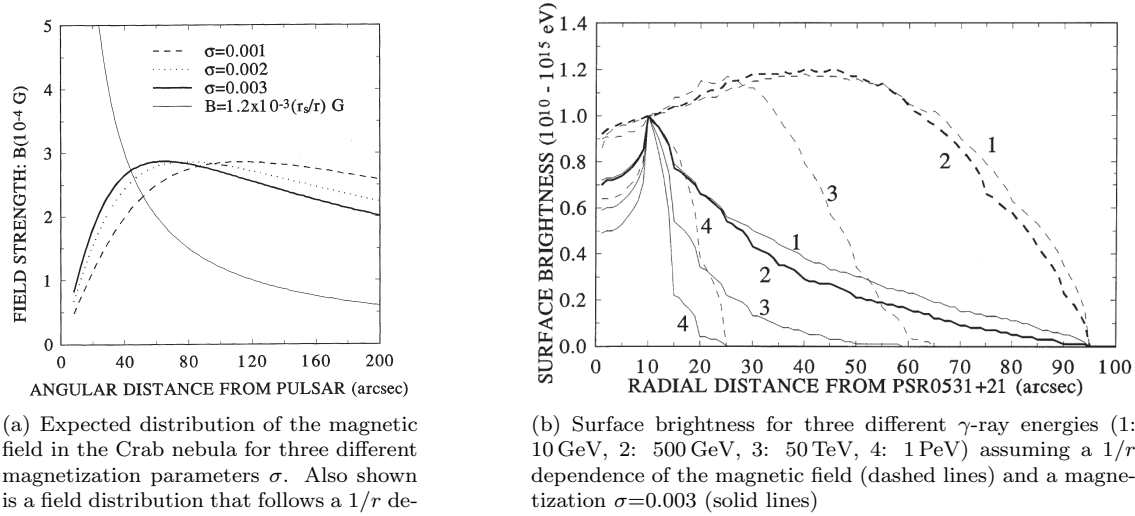


Figure 3.10: Expected radial distribution of the magnetic field and surface brightness of the Crab nebula in VHE- $\gamma$ -rays (from De Jager and Harding, 1992).

region around 100 GeV, where the peak intensity of the IC-emission is expected. Note also that the EGRET measurement at GeV energies is considerably higher than the predicted IC-flux. Above energies of  $\sim 10$  TeV  $\pi^0$ -decaying secondaries could significantly contribute to the  $\gamma$ -ray emission of the Crab nebula, a still open question, which is not yet settled by observations (Tanimori et al., 1998; Aharonian et al., 2004, 2006a).

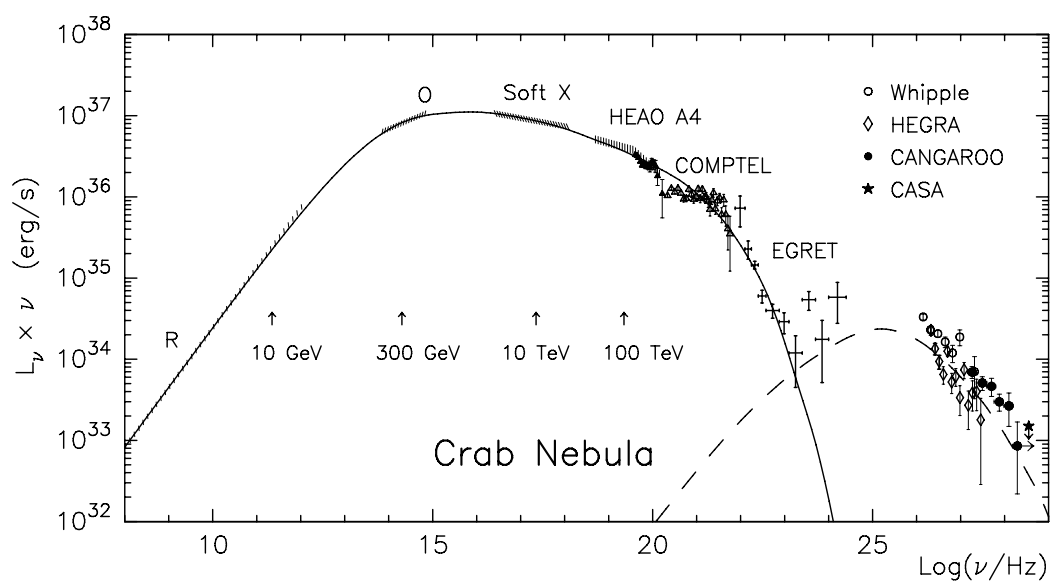


Figure 3.11: Non-thermal radiation of the Crab Nebula. The solid and the dashed curve correspond to the synchrotron and inverse Compton components of the radiation, respectively, calculated in the framework of the spherically symmetric MHD wind model of Kennel and Coroniti (1984a,b). Indicated with arrows are the electron energies related to the peak energy of the synchrotron photons. (from Aharonian and Atoyan, 1998)



## Chapter 4

# The Imaging Air Shower Cherenkov Telescope Technique and the MAGIC Telescope

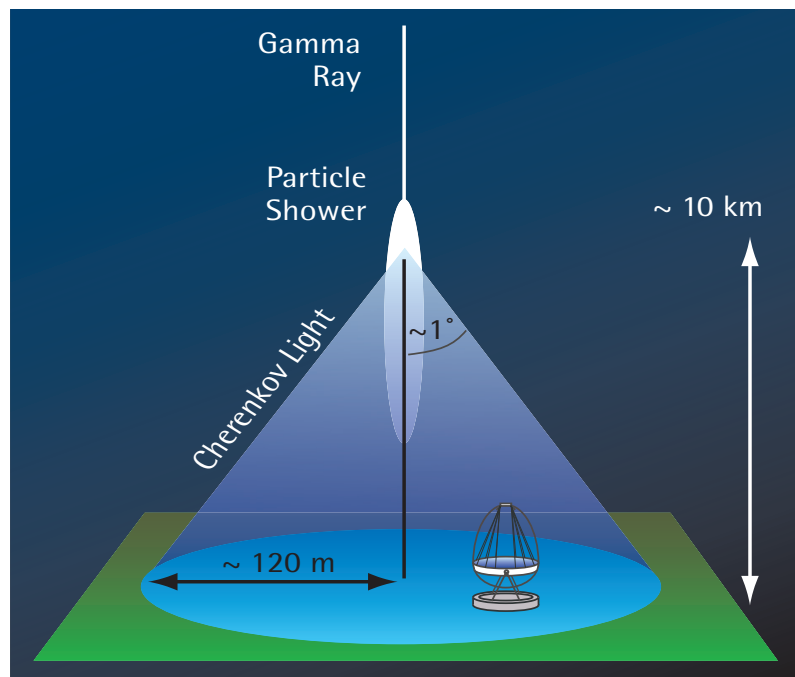


Figure 4.1: Popular illustration of the situation encountered in  $\gamma$ -ray astrophysics from ground. A  $\gamma$ -ray converts into a  $e^\pm$ -pair in the atmosphere and a particle shower develops with the shower maximum in 10 km altitude. The ultrarelativistic secondary particles generate Cherenkov light that propagates in a narrow cone along the primary direction. The light is illuminating an approximately circular area with a radius of  $\sim 120$  m. An imaging air Cherenkov telescope records some of the Cherenkov light with its  $\sim 100\text{ m}^2$  large light collector, provided the telescope is located within the “pool” of Cherenkov light. Typically 0.1% of the Cherenkov light is recorded

In this chapter I overview the experimental technique, namely the imaging technique in air shower Cherenkov telescopes, today's most sensitive method to detect VHE- $\gamma$ -ray sources. In the second half of the chapter (Section 4.2) I introduce the MAGIC telescope, which utilizes this technique.

## 4.1 Air Showers

### 4.1.1 Air Shower Detection Techniques

Cosmic rays (CR), if energetic enough, lose all their energy in a particle shower, once they enter the Earth's atmosphere. Depending on the energy, air-showers provide several information, which allows one to reconstruct the energy, the arrival direction and the arrival time of the cosmic ray.

1. **Shower particles:** From energies  $\sim 10^{12}$  eV onwards the shower penetrates down to ground, where the shower tail particles can be detected with particle counters. Arrays like e.g. AGASA, AUGER, HEGRA, Kascade, Ooty, . . . detect cosmic rays in this way and focus on the study of charged cosmic rays with energies  $> 10^{14}$  eV (just below the so-called knee of the CR-spectrum and beyond). The high altitude experiments MILAGRO, Tibet AS- $\gamma$  and Argo also detect shower particles and are sensitive to  $\gamma$ -rays with energies above a few TeV. All three experiments have the advantage of a large active area fraction and a large field of view. However, they also feature high energy thresholds of several TeV as well as very modest  $\gamma$ /hadron-separation capabilities.
2. **Fluorescence light:** A small fraction ( $\mathcal{O} \sim 10^{-5}$ ) of the energy of the shower particles goes into the excitation of atmospheric Nitrogen molecules. Upon de-excitation a distinct line spectrum is isotropically emitted in the near UV (between  $\sim 300 \dots 400$  nm). In order to use the fluorescence emission to detect cosmic rays the shower is "watched" under a large angle to record the entire shower development. This technique is used e.g. by the fluorescence telescopes in the AUGER and HIRES experiments. Another possibility to detect the faint light emission is from space. This approach was proposed by the OWL and EUSO collaborations but so far has not been realized due to the lack of robust and high efficient single photon detectors; a necessary constraint to obtain a reasonable low detection threshold of  $\sim 10^{18}$  eV.
3. **Radio emission:** Air showers are also a source of radio emission, which can be used to measure shower properties. The exact mechanism of the radio emission is not fully understood. Radio emission was investigated already in the 50's but results were useless and contradictory, partially because of limitations of the available technologies. With new technologies at hand quite promising progress has been made in the last two years. The detection of radio emission of air showers is still in its infancy and has yet to prove its feasibility. The detection threshold of a CR in the radio band is currently assumed to be about  $10^{17}$  eV.
4. **Cherenkov light:** Ultrarelativistic charged shower particles emit Cherenkov light in the atmosphere ( $\mathcal{O} \sim 10^{-3}$  of the CR-energy is converted to Cherenkov light). The Cherenkov photons are highly beamed along the tracks of the particles and typically illuminate a circle with a radius of  $\sim 120$  m on the ground (cf. Section 4.1.3 and Figure 4.1). Cherenkov light emission is the dominant source of light in air showers. It can even be an unwanted background in experiments that are only interested in fluorescence emission. CRs with energies as low as a few tens of GeV can be detected from ground by means of the Cherenkov light, whereas the shower particles will not penetrate down to ground anymore. Therefore, VHE particles can only be studied from ground by observation of Cherenkov light. Observations are restricted to clear nights.

Commonly used detection methods of the Cherenkov emission are the wavefront sampling technique (e.g. the former AIROBICC, the Tunka detectors, STACEE or CELESTE) or the

imaging air Cherenkov telescope (IACT) technique, which was pioneered by the Whipple collaboration. (Weekes et al., 1989).

One big disadvantage of the detection of CRs with air shower experiments is that only restricted information is available to learn about the initial CR. The total energy of the CR, e.g. can be determined from the light intensity emitted by the air shower or the number of shower particles detected on ground. But one of the most interesting information, the composition of the CR-spectrum is difficult to determine. In some of the detection techniques it is possible to separate between strongly interacting CRs (hadrons) and those that are subject only to electromagnetic interaction. At present, the IACT technique has the best separation power between hadrons and electromagnetically interacting CRs. The reason is explained in the next subchapter.

## 4.1.2 Properties of Air Showers

### Some Properties of the Atmosphere

The vertical mass of the atmosphere at sea level, called air mass 1, corresponds to 27 radiation lengths and 11 hadronic absorption lengths, e.g. cosmic particles  $< 10^{13}$  eV are fully absorbed like in calorimeters in high energy particle physics. At large zenith angles the air mass increases with (in first order)  $\cos(\theta)^{-1}$ ,  $\theta$  being the zenith angle. The atmosphere is transparent to light between  $\sim 300$  nm (Ozone cutoff) to  $\sim 1100$  nm. The density of the atmosphere as function of altitude ( $h$ ) is reasonably well approximated by the so-called US-standard atmosphere

$$\rho(h) = \rho(0) \cdot e^{-\frac{h}{h_0}} \quad (4.1)$$

with the scale height  $h_0 = 7$  km.

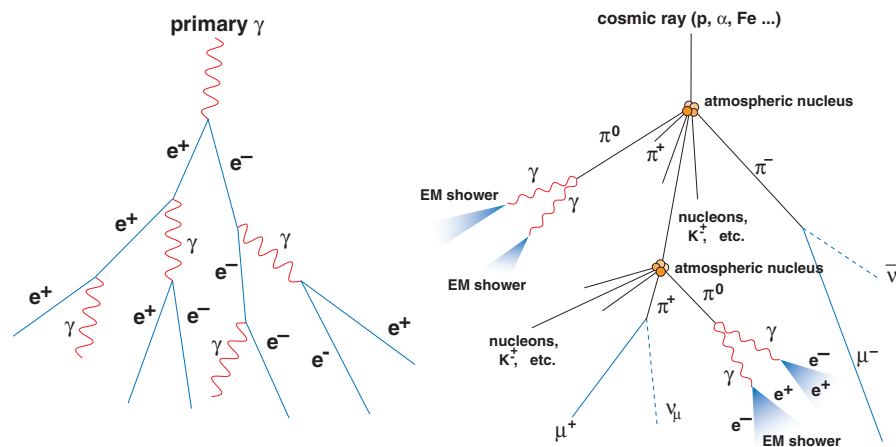


Figure 4.2: Schematic view of the development of a  $\gamma$ -ray induced air shower (left) and an air shower that was started with a hadronic interaction (right).

### Electromagnetic Showers

Electromagnetic showers are showers generated by an electromagnetically interacting cosmic particle. This can be e.g. an electron, a positron or a  $\gamma$ -ray. In the following I outline the development of an electromagnetic shower that is generated by a  $\gamma$ -ray.

If the energy of the  $\gamma$ -ray is  $> 100$  MeV, the interaction process of the  $\gamma$ -ray in the atmosphere is most likely pair creation. Assuming further that the energy of the  $\gamma$ -ray is indeed  $\gg 100$  MeV a cascade sets in, where the very first process is the decay of the  $\gamma$ -ray into an  $e^\pm$ -pair via pair creation. In the following two processes alternate. First, after traversing a characteristic distance, called radiation length  $X_0$ , the pair created electron ( $e^-$ ) and positron ( $e^+$ ) lose about  $2/3$  of their energy by Bremsstrahlung-emission of one photon. Second, the Bremsstrahlung-photons undergo pair creation on their flight paths after traversing an average distance of  $\frac{7}{9}X_0$ .

The structure of an electromagnetic shower is quite simple (cf. left panel in Figure 4.2), as the distances over which pair creation and Bremsstrahlung take place are very similar. In about each unit length of  $1 X_0$  the number of particles doubles and the energy per particle roughly halves until the average energy per charged particle reaches the so-called critical energy. At the critical energy, 83 MeV in air, the energy losses per unit length by Bremsstrahlung and Ionization are equal. At this stage of the shower development (about 8 km above sea level, for a 1 TeV vertical incident  $\gamma$ -ray and about 11 km for a 100 GeV  $\gamma$ -ray) the number of shower particles has reached its maximum. Below this height ionization losses dominate and the shower rapidly dies out.

### Hadronic Showers

A hadronic shower is generated by a strongly interacting particle. In strong interactions mainly pions are produced with about equal partition into  $\pi^+$ ,  $\pi^-$  and  $\pi^0$ . While the charged pions either interact again hadronically or decay, fuelling a muonic component, the  $\pi^0$ 's decay instantaneously ( $\tau = 10^{-16}$  sec) into 2  $\gamma$ s. On average  $1/3$  of the energy in each hadronic interaction is transferred into the electromagnetic component, such that at the shower tail most particles are electrons and  $\gamma$ s (6-7 times more) and a few muons (plus invisible  $\nu$ 's) and rarely some hadrons (cf. right panel in Figure 4.2).

Due to the fundamentally different nature of the strong interaction, secondaries receive on average a higher transverse momentum than electrons or  $\gamma$ -rays in electromagnetic interactions. Because of this, hadronic showers are broader and less homogenous than their electromagnetic counterparts, a feature that allows one to separate between both shower types.

#### 4.1.3 Cherenkov Light Emission in Air Showers



Figure 4.3: Space Shuttle breaking the sound barrier (see faint shock wave). In the same way a superluminal charged particle generates a photonic shockwave (Cherenkov emission) as it travels through matter.

In air showers, initiated by VHE cosmic particles, most secondaries are still ultrarelativistic and emit Cherenkov light provided their speed  $v$  fulfills the condition

$$v > \frac{c}{n} \quad \text{or} \quad \frac{v}{c} = \beta > \frac{1}{n}, \quad (4.2)$$

$n = n(h)$  is the refractive index of the atmosphere at the height  $h$ . Moving at superluminal velocities the surrounding matter is asymmetrically polarized and a photonic shockwave is created similar to the shockwave created when objects fly faster than the speed of sound (see Figure 4.3).

A detailed discussion of the Cherenkov process can be found in Jackson (2003) and its implication for air shower experiments in Longair (1997). It was already proposed by (Hill and Porter, 1961; Jelley and Porter, 1963) to study CRs by observing Cherenkov light. The same authors also demonstrated first observations. Here I address only some aspects that are important for the basic understanding of the imaging air Cherenkov technique or are related to the requirements of photon detectors in air Cherenkov telescopes. Most of the material presented is also covered in Yao et al. (2006).

The angle  $\theta_c$  at which a particle travelling with velocity  $\beta$  emits Cherenkov light is

$$\begin{aligned} \theta_c &= \arccos(1/n\beta) \\ &\approx \sqrt{2(1 - 1/n\beta)} \\ &\approx 1.3^\circ \text{ in air at sea level for } \beta = 1 \end{aligned} \quad (4.3)$$

With this relation one can estimate that the circle has a radius of  $\sim 100$  m on ground, which is illuminated by the Cherenkov light emitted by on-axis particles in an air shower. Some part of the light is distributed more irregularly, as secondaries deviate often from the shower axis. Figure 4.4 shows as an example the distribution of the Cherenkov photons arriving on ground of a simulated 50 GeV  $\gamma$ -ray induced air shower. The light distribution peaks around the 100 m circle due to the increasing emission angle of the Cherenkov photons as the light emitting particles penetrate deeper into the atmosphere.

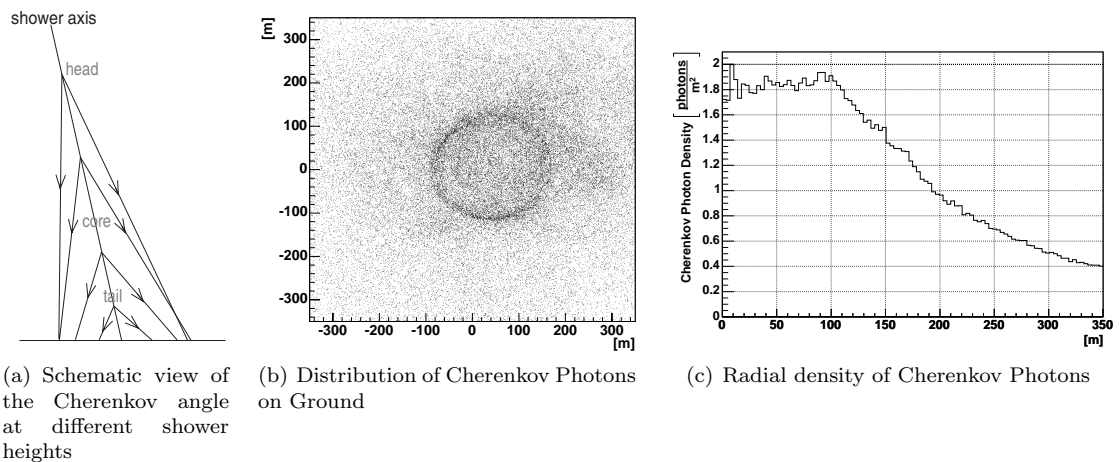


**Figure 4.4:** Simulated Cherenkov photon distribution at 2200 m above sea level from one air shower induced by a 50 GeV  $\gamma$ -ray of vertical incidence. The impact point of the  $\gamma$ -ray is at (0,0). The majority of photons arrive within a radius of 100 m from the impact point. Due to the increasing Cherenkov angle with increasing shower depth a maximum in the photon distribution is seen at the rim at  $\sim 100$  m. The maximum is often referred to as the “hump”. The region closer to the shower axis collects the light principally from the shower tail, while the region up to the hump is dominated by light coming from the shower core. Beyond the hump the light comes from halo particles of the shower.

A particle with elementary charge  $Z$  emits per path length  $x$  and per unit wavelength interval the following number of photons (Yao et al., 2006):

$$\begin{aligned} \frac{d^2N}{dx d\lambda} &= \frac{Z^2 2\pi\alpha}{\lambda^2} \left( 1 - \frac{1}{\beta^2 n^2(\lambda)} \right); \quad \alpha \text{ being the finestructure constant} \quad (4.4) \\ &\propto \frac{1}{\lambda^2} \\ \frac{d^2N}{dx dE} &\approx 370 \cdot Z^2 \cdot \sin^2 \theta_c(E) \text{ eV}^{-1} \text{ cm}^{-1} \end{aligned}$$

To transform the emitted Cherenkov spectrum into the spectral distribution that an observer receives on ground, one has to convolute the emission spectrum with the spectral transmission of the atmosphere and the velocity distribution of the shower particles. Transmission losses within the atmosphere are mainly due to Rayleigh scattering that dominantly affects photons with short wavelength ( $1/\lambda^4$  dependence of the cross section). Below 300 nm the atmosphere is opaque because of absorption by the ozone. Figure 4.5 shows the differential Cherenkov photon densities before and after taking into account atmospheric transmission losses. The calculations were done for  $\gamma$ -rays with different energies. The absorbed spectra show a sharp cutoff below 300 nm and a tail towards larger wavelengths. Taking into account the losses, on average  $\sim 150$  Cherenkov photons arrive per square meter at observatory level from an air shower initiated by a 1 TeV  $\gamma$ -ray. This intensity reduces to only 2 Cherenkov photons per square meter for a 50 GeV  $\gamma$ -ray at vertical incidence (s. Figure 4.4(c)). The Cherenkov photon intensity is to first order proportional to the energy of the  $\gamma$ -ray (Figure 4.6).

The peak position of the observed Cherenkov spectrum depends on the zenith angle of the observation and shifts to larger wavelengths as the zenith angle increases. The reason being that the amount of mass traversed by the Cherenkov photons also increases with the zenith angle. Blue/UV photons are stronger attenuated and the threshold increases.

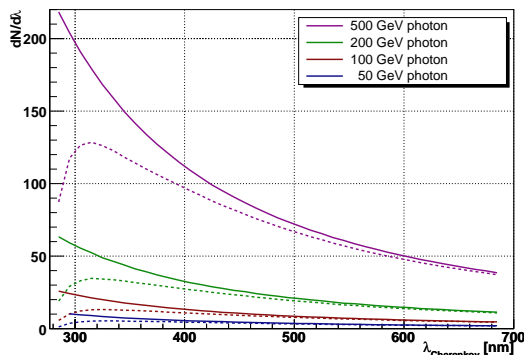


Figure 4.5: Cherenkov photon densities emitted by  $\gamma$ -ray showers of different energies before absorption (solid lines) and after taking into account absorption losses in the atmosphere (dashed lines). The zenith angle is  $0^\circ$ . (calculations done by P. Majumdar)

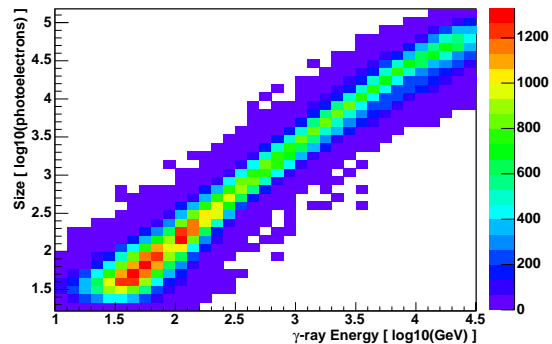


Figure 4.6: Simulation of the Cherenkov light signal from a  $\gamma$ -ray shower vs.  $\gamma$ -ray energy. The Cherenkov signal is given in units of detected photoelectrons by the MAGIC telescope. The distances between the impact points of the  $\gamma$ -rays and the telescope are  $< 150$  m. The zenith angle range of the simulated  $\gamma$ -rays is  $0^\circ \dots 30^\circ$ .

The Cherenkov light flashes are very fast. Typical time spreads for an impact parameter of  $< 140$  m are:

- single muons:  $\ll 1$  nsec
- $\gamma$ -ray showers: 1 – 3 nsec
- hadron showers: 3 – 7 nsec

Other information that can be inferred from the Cherenkov light and is used to distinguish between  $\gamma$ -ray and hadron showers is the shape of the shower. The shape is determined by reconstructing the arrival direction of the detected Cherenkov photons. This is most easily done with an imaging device as is realized with an imaging air shower Cherenkov telescope (IACT) like MAGIC (Section 4.2). In an IACT the shower is imaged with a matrix of fast photon detectors, photomultipliers (PMTs) in state of the art telescopes. Each PMT has a typical field of view of about  $0.1^\circ$  in diameter, over which the Cherenkov light is integrated.

#### 4.1.4 The Night Sky Background Light

When searching for cosmic  $\gamma$ -rays by means of the Cherenkov telescope technique one is not only confronted by the large background from hadronic showers but also by background light from the night sky (NSB). Contributions to the NSB is light coming from stars, ionospheric airglow, zodiacal light, aurora borealis, distant lightning, moonlight and from man-made origin (e.g. Benn and Ellison, 1998). The intensity of the NSB depends on the region of the sky (galactic or extragalactic) and on the location on Earth. A typical intensity of the NSB from a dark region of the sky is  $\sim 2 \cdot 10^{12}$  photons per square meter sterad and second for NSB-photons with wavelengths between 300 nm and 600 nm. The average single photoelectron rate due to NSB in one pixel<sup>1</sup> of the MAGIC camera is  $\sim 10^8$  MHz.

One aspect of the NSB is that it contaminates the Cherenkov signal of the shower. In part this can be taken care of with appropriate cleaning methods as will be explained later in 5.2. Another aspect is that the NSB determines the lowest reachable  $\gamma$ -detection energies. Accidental NSB triggers can only be reduced in MAGIC to an acceptable level by requiring a multi-fold next neighbor coincidence of several pixels with a very short coincidence time of 5 nsec and the additional condition that each pixel must exceed at least a 8 photoelectron signal. The energy threshold of an experiment depends normally on the area of the light collector and its reflectivity, the sensitivity of the used photon detectors as well as on the zenith angle; in addition the height affects both the threshold and collection area.

## 4.2 The MAGIC Telescope

The Major Atmospheric Gamma Imaging (MAGIC) telescope (s. Figure 4.7) is a detector for VHE- $\gamma$ -rays and is located on the Roque de los Muchachos in the Canary Island of La Palma (N  $28^\circ 45^m 43^s.47$  / W  $17^\circ 53^m 24^s.04$ ; 2231 m asl). MAGIC consists of a 17 m diameter tessellated parabolic shaped mirror, from which the Cherenkov photons are reflected and focused onto a 577-pixel photomultiplier camera. In the design of MAGIC emphasis was put on the condition to lower the threshold as much as possible.

In the following I describe the main features of the telescope: the reflector, the camera and the signal chain including the trigger.

### 4.2.1 The Reflector and Telescope Frame

The Cherenkov light emitted in an air shower is distributed over a circular area at ground with a radius between 100 m and 120 m (cf. Figure 4.4). This light pool is sampled by the reflector surface of MAGIC. Crucial to succeed in pushing the imaging air Cherenkov technique to energies below 100 GeV is to employ a large enough reflector surface that collects as much Cherenkov light as possible.

<sup>1</sup>The diameter of one pixel is  $0.1^\circ$  and the area of the collector surface of the telescope is  $234 \text{ m}^2$ .

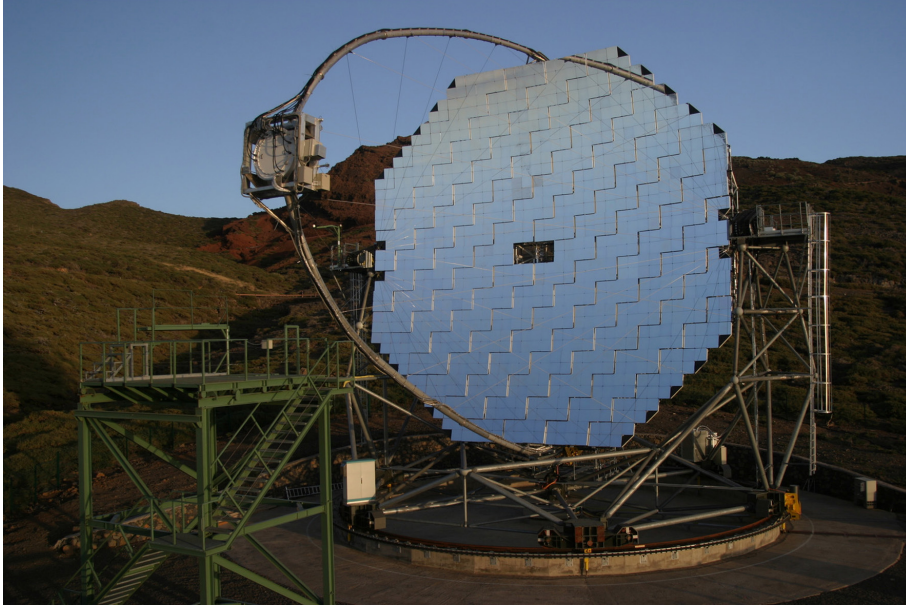


Figure 4.7: Photograph of the MAGIC telescope. One can make out the tessellated reflector surface, the camera in the focal plane of the reflector, the azimuthal rail and the camera access tower in the front.

### The Reflecting Surface

The 234 m<sup>2</sup> tessellated reflector surface has a parabolic shape (i.e.  $\langle f \rangle/d = 1.05$ ) and is composed of 964 square shaped 49.5 × 49.5 cm<sup>2</sup> diamond milled all-aluminum mirrors of a lightweight sandwich construction. The surface of the mirrors is coated with a protective quartz layer and has a high reflectivity over a broad range of wavelengths (> 80% between 250...750 nm). A detailed description and study of the performance of the reflecting elements is given by Tonello (2006).

The parabolic shape of the reflector avoids a dispersion in the arrival times of the Cherenkov photons in the plane of the camera (isochronous) and allows to reduce the time window, from which the Signal is extracted. It is thus possible to limit the contamination of the Cherenkov signal with Night Sky Background photons to an absolute minimum. Another advantage of preserving the intrinsic time structure of the Cherenkov pulse is to get a possible improvement in the separation power between hadronic and electromagnetic showers as well as isolated muons with large impact parameter that look like  $\gamma$ -ray showers. See page 30 for the mean time spreads.

During observation the mirror elements are focused to a distance of 10 km, the height of the shower maximum of a 50 GeV  $\gamma$ -ray shower at vertical incidence. In this configuration 80% of the light of a point like source is focussed into a circle with a radius of 17 mm (the size of a camera pixel). Degradations of the optical performance due to deformations of the telescope structure depending on the pointing position of the telescope are compensated by the Active Mirror Control (AMC). The AMC is continuously monitoring the declination angle of the telescope and accordingly adjusting the individual mirror elements. Details on the AMC and its performance can be found in Garczarczyk (2007).

### The Telescope Frame

One of the design criteria of the telescope was to build it as light as possible. A lightweight structure allows for a fast repositioning within a few tens of seconds. This is a necessary requirement for follow-up observations of Gamma Ray Bursts. The reflecting surface is mounted on a lightweight carbon fibre structure weighing only  $\sim 5$  tons. The support structure of the mirrors itself rests on an

undercarriage made of steel that allows one to move the reflector in elevation. The undercarriage itself moves in azimuth (alt-azimuth-mount). The total weight of MAGIC is  $\sim 64$  tons. The position of the telescope in declination and azimuth is measured with 14 bit resolution absolute shaft encoders. The position precision, as well as telescope bending corrections are improved by a starguider camera. Details on the drive system including the implemented pointing model of the telescope are given in Wagner (2006).

#### 4.2.2 The Camera



Figure 4.8: Photograph of the camera of the MAGIC telescope with opened lids while the Winston cones are being installed. The inner part of the camera consists of 397 PMTs of 1" that are surrounded by 180 PMTs of 1.5" diameter.

The camera in the focal plane of the MAGIC telescope (Figure 4.8) serves the purpose of capturing and recording the Cherenkov images of air showers. It consists of  $577^2$  hemispherical photomultipliers (PMTs) that convert the Cherenkov photons into a measurable electrical signal.

The inner part of the camera (radius  $\sim 1.1^\circ$ ) is equipped with 397 PMTs (type 9116A; 1"  $\varnothing$  from the company ET) each with a pixel diameter of  $0.1^\circ$ . The outer part of the camera is equipped with 180 PMTs (type 9117A; 1.5"  $\varnothing$  from the company ET) each with a pixel diameter of  $0.2^\circ$ . Hollow hexagonal shaped non imaging light concentrators (often called Winston cones or light catchers) are placed on top of all photomultipliers to compensate for the dead space between them. The entrance window of the PMTs is coated with a diffuse lacquer doped with a wavelength shifter (WLS) (Paneque et al., 2003). The combination of the hemispherically shaped PMT, the hollow light cone, the diffuse coating and the WLS results in a 15%-20% higher quantum efficiency (QE) compared to flat window PMTs. For protection purposes (humidity, dust) a thin entrance window made of plexiglas (type 218, with a UV cutoff around 290 nm) is placed on top of the Winston cones.

A detailed description of the Camera and its performance can be found in Gaug (2006) and Paneque (2005).

<sup>2</sup>This includes the Central Pixel that is not used to record shower images but is reserved to perform optical measurements.

### 4.2.3 Signal Processing, Recording and Trigger

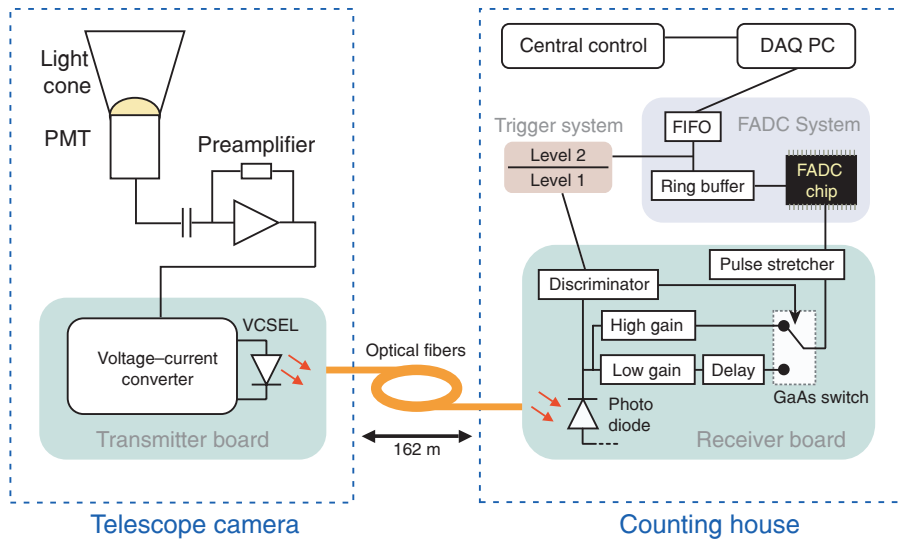


Figure 4.9: Camera readout and processing of the data recorded by MAGIC (from Wagner, 2006)

The fast analog signals from the PMTs provide the necessary information needed to detect and reconstruct the shower. In MAGIC, the analog PMT signals are directed via optical fibers from the camera to the counting house. There the trigger is formed and the signals are digitized. A sketch of the signal chain is shown in Figure 4.9.

#### Signal Processing in the Camera

The PMTs have 6 dynodes and operate at a gain of roughly 20,000 to prevent fast aging and damage from high currents by light during moonshine observations. The PMTs typically have a signal risetime of  $\sim 800$  psec, a (full width at half maximum) FWHM of 1.5 nsec and a tail extending to  $\sim 4$  nsec. At the base of the PMT the signal is AC coupled to a fast transimpedance preamplifier. The signal is limited in bandwidth by the amplifier to about 230 MHz before modulating the current of a vertical-cavity surface-emitting laser (VCSEL), which has a bandwidth of 4 GHz. The signal is then transported via an optical fiber into the counting house. The characteristics of the optical system have been studied in detail by Paneque (2005).

The conversion of the electrical signal into an optical one has the advantage of minimizing the dispersion imposed on the signal during the transmission over a distance of 160 m. Additional benefits are the reduced weight and diameter of the signal carrying cables as well as high immunity against electromagnetic interference (EMI). The dynamic range of the optical analog signal transmission chain is  $\sim 56$  dB.

#### Signal Processing in the Counting House

In the counting house the optical signal is received and converted back to an electrical one with a fast GaAs PiN photodiode. After further amplification the signal is split, and part of the signal is routed to the trigger, which is described below.

To increase the limited dynamic range of the 8-bit Analog-to-Digital-Converter the remaining signal is split into two. One half of the signal is amplified by another factor of ten, called high-gain, the other half of the signal is called low-gain. If the high-gain signal exceeds a certain amplitude,

also the 50 nsec delayed low-gain signal is digitized. In this way the usable dynamic range of the Flash-Analog-to-Digital-Converter (FADC) is extended to about 1000.

The digitization is carried out by a custom-made 8-bit FADC, which samples the input signal at a rate of 300 Ms/sec. According to the Nyquist theorem basically all information contained in a pulse is recorded if the pulse is sampled at 3-4 different positions. Therefore, the signal is shaped with a time constant of about 6 nsec before digitization. The FADC continuously writes the digitized amplitude information into a ring buffer. In case of a trigger the digitization stops and the corresponding part of the ring buffer is written onto a disk. The dead time introduced by the readout is 25  $\mu$ sec. The dead time, 1.6 %, is negligible compared to an average trigger rate of 200 Hz .

## The Trigger

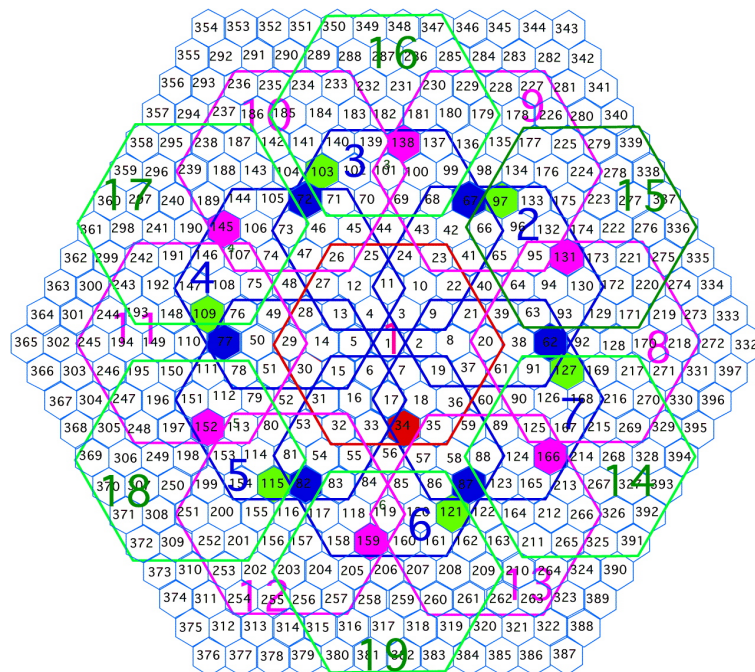


Figure 4.10: Sketch of the trigger topology in the MAGIC camera. The inner camera is segmented into 19 macrocells of 37 pixels each. The logic of a macrocell is based on 36 pixels. The pixel not connected to the macrocell logic is highlighted in the figure.

The trigger makes the decision if an event takes place so that the camera should be read out. The trigger consists of three consecutive levels, of which only the first two are in use at the moment.

**Level-0 (Discriminator):** The analog signal of a camera pixel is discriminated by a comparator that gives an approximately 6 nsec long logic output signal as soon as the amplitude of the input signal exceeds a preset threshold. The effective trigger window is 5 nsec (Turini, 2006). As the images of the air showers are extended it is not necessary to include all 577 pixels into the trigger. Only 325 pixels of the inner camera are used for the trigger generation (see Figure 4.10). The discriminator thresholds are not fixed but adapted dynamically for each pixel by means of (digital to analog converters) DACs in such a way that the individual trigger rates are about equal for all pixels. This dynamical behavior is not simulated in the Monte Carlo but is taken care of in the analysis with a substantially higher software discrimination threshold.

**Level-1:** All discriminator outputs are grouped into 19 overlapping regions (s. Figure 4.10). Level-1 will give a trigger, if in one of the regions  $N$  discriminators of next neighbor pixels are “fired” in coincidence. The usual trigger condition at level-1 is a four-fold coincidence ( $N=4$ ).

**Level-2:** Allows in principle a further discrimination based on the topology of an event that already passed level-1. Up to now level-2 has not been implemented in the usual data taking of MAGIC.

The average trigger rate of MAGIC is about 200 Hz for observations of a galactic region around zenith.

## Chapter 5

# Data Analysis Methods and Telescope Performance

In the previous chapter I explained how events are recorded with the MAGIC telescope. After the data are written onto disk, the general analysis of the extraction of a  $\gamma$ -ray signal is performed in five steps which are discussed in this chapter:

1. Event calibration and cleaning.
2. Event characterization.
3. Determination of the energy of an event and of the parameter HADRONNESS, which is a measure of the probability that the event is of electromagnetic or of hadronic origin.
4. Statistical analysis of the data sample and searching for a  $\gamma$ -ray signal.
5. In case of a positive detection of a  $\gamma$ -ray signal the underlying  $\gamma$ -ray source can be further characterized e. g. by an energy spectrum, a sky-map of the emission region or a light curve. If no  $\gamma$ -ray signal is found, upper flux limits are calculated.

For the calculation of an energy spectrum I used the tools available within the framework of the MAGIC Analysis and Reconstruction Software package (MARS) (Bretz, 2006). Within the framework of MARS I implemented a more efficient procedure to clean events from noisy pixels that result in a lower analysis threshold (cf. Section 5.2.2).

In Section 5.8, I describe the basic steps that are performed in an analysis that searches for periodic emission from a pulsar. Analysis tools for pulsar studies were not available in MARS and had to be developed.

The chapter ends with a study of the performance of the MAGIC telescope. This comprises the determination of the sensitivity of MAGIC as well as a comparison of so-called image parameters of recorded  $\gamma$ -ray images with Monte Carlo generated shower images.

### 5.1 Signal Extraction and Reconstruction

In the first step of the reconstruction process of an event, the digitized signals of the camera pixels are converted back into the number of photoelectrons that had been generated in the photocathodes of the PMTs.

This is done in two steps. In the first step the signal of each pixel is extracted from the data and then a conversion factor is applied to the extracted signal to obtain the number of photoelectrons.

### 5.1.1 Signal Extraction

After applying a base line correction to the digitized waveform, the signal amplitude is extracted from the recorded FADC-samples with the digital filtering method by Cleland and Stern (1994). The digital filter fits a fixed pulse shape to the sampled signal. The method is optimal as long as the following assumptions hold:

- a unique and known signal shape, whose only variable parameter is its amplitude.
- no correlation between signal and noise
- stable noise conditions

The first assumption partially holds as the signals are shaped before digitization with a time constant (6 nsec). However, for large size hadronic showers this is not always fulfilled. Long tails in the time spread can occur. These events are mostly rejected by the  $\gamma$ /hadron-separation. The second assumption is fulfilled as the combination of signal and noise is a linear superposition. The last assumption is only partially valid as the noise contribution of the NSB depends on the zenith angle of the observation the location in the sky (galactic / extragalactic), ambient light conditions and atmospheric conditions. Extensive tests have shown that the digital filter can be used to extract the amplitude of the recorded signal (Gaug, 2006).

The signal extractor returns two parameters:

- The fitted signal amplitude that is converted into photoelectrons in the subsequent step.
- The position in time of the peak amplitude. This time information can be used to identify pixels that very likely do not contain a signal belonging to the shower.

Implemented in MARS are also other signal extractors of which a comparative study can be found in Gaug (2006). I skip the description of the other available extractors, as for this work only the digital filtering method has been used.

### 5.1.2 Conversion of Signal Amplitude into Photoelectrons

The number of photoelectrons  $N$  in a pixel is obtained from the extracted signal amplitude  $\mu$  by assuming a linear relation between both quantities. The factor of proportionality is called the conversion factor ( $c = N/\mu$ ) and is found by dedicated “calibration” runs, in which the MAGIC camera is illuminated by a series of fast UV-light flashes<sup>1</sup> (calibration event). Also interleaved calibration events are taken at a rate of 50 Hz in parallel to the recording of shower images in order to allow one to update the conversion factors between calibration runs. The calibration system is discussed in detail by Gaug (2006).

Several methods were developed to determine the conversion factor of each pixel from the calibration events. For the calibration of the data presented here the so-called F-factor method (Mirzoyan and Lorenz, 1997) was used. In the F-factor method it is assumed that the photomultiplier as well as the signal chain and the calibration pulser are well understood and stable. This means that

---

<sup>1</sup>The emission spectrum of the 10 UV-LEDs (light emitting diodes) that produce the flashes has a peak at 375 nm and a FWHM of 12 nm. The duration of one flash is 2-3 ns FWHM

small fluctuations of the signal introduced by the amplifiers, optical transfer, FADC and instabilities of the calibration light pulser can be neglected. The major contribution to the pulse to pulse fluctuations are then the statistical fluctuations in the number of generated photoelectrons per calibration event. The number of photoelectrons are assumed to be Poisson distributed, i.e. the distribution of the photoelectrons has a mean of  $N$  photoelectrons and a root mean square of  $\sqrt{N}$ . Additional fluctuations arise from the photoelectron collection onto the first dynode and from the multiplication fluctuation at the first dynode. These fluctuations widen the initial distribution beyond  $\sqrt{N}$ . With these assumptions the relation between the relative width of the distribution of the photoelectrons ( $1/\sqrt{N}$ ) and the relative width of the distribution of the extracted signals ( $\sigma/\mu$ ) can be written as:

$$F \frac{1}{\sqrt{N}} = \frac{\sigma}{\mu} \quad (5.1)$$

$$\propto N = \left( F \cdot \frac{\mu}{\sigma} \right)^2 \quad (5.2)$$

where  $\mu$  and  $\sigma$  are the mean and the sigma of the distribution of the extracted signals after pedestal subtraction. The  $F$ -factor in equation 5.1 accounts for the additional broadening of the measured distribution beyond what is expected by Poisson statistics. The additional broadening, which is dominated by the multiplication process in the PMT, has to be individually quantified for each PMT in the laboratory. For the PMTs used in the MAGIC camera  $F$ -factors of typically 1.3 were found Gaug (2006). If the  $F$ -factor is known, equation 5.2 can be used to calculate the average number of photoelectrons  $N$  in a calibration event and in turn the conversion factor  $c$ .

I want to point the interested reader to Gaug (2006), for further in-depth discussion of the implementation and performance of the signal reconstruction and the calibration procedure of data obtained with MAGIC.

## 5.2 Event Cleaning

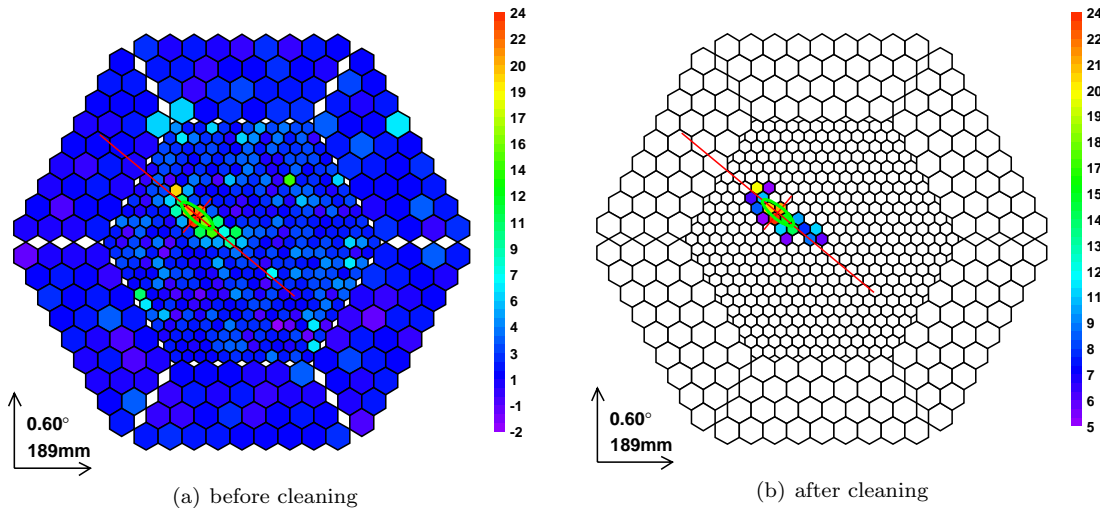


Figure 5.1: Illustration of the cleaning of an event

Besides the Cherenkov light the captured event also contains coinciding NSB (cf. Section 4.1.4). Pixels that very likely do not contain a shower signal are rejected in a procedure called image cleaning. This is necessary because the afterwards applied moment parametrization method is not robust with respect to noise. Figure 5.1 shows an event before and after the image cleaning procedure. In the following I explain the default cleaning procedure implemented in MARS

(the standard-cleaning) as well as a modified procedure that utilizes the time information (time-cleaning), which I developed and used for the analysis presented in this thesis.

### 5.2.1 Standard Image Cleaning

In “standard-cleaning” the number of photoelectrons in a pixel is the only information that is used as a criterion to decide if a pixel contains a useful signal or not. If a pixel is selected for further analysis it is also referred to as “cleaned”.

The algorithm of the standard-cleaning proceeds in three steps:

1. All pixels with a number of photoelectrons above a predefined level ( $CleanLvl1$ ) are selected.
2. A selected pixel is marked as core-pixel, if it has at least one direct neighbor also selected in the previous step.
3. The algorithm searches for so-called boundary-pixels in the direct vicinity of the core-pixels. A pixel is selected as boundary-pixel if it meets two requirements:
  - (a) It has a signal above a predefined threshold ( $CleanLvl2$ , which is less than  $CleanLvl1$ ).
  - (b) The pixel has an already cleaned direct next neighbor.

In most analyses the last step of the cleaning procedure is repeated once. Normally  $CleanLvl1$  and  $CleanLvl2$  correspond to around 10 photoelectrons and 5 photoelectrons, respectively.

### 5.2.2 Image Cleaning using additional Time Information

It is sufficient to use the standard-cleaning if the signal of the recorded shower image is well above the fluctuations of the NSB. This condition is not fulfilled for low-energy events close to the trigger threshold. Most of these events become truncated or are lost, if the (high) standard cleaning-levels for core-pixels (10 photoelectrons) and boundary-pixels (5 photoelectrons) are used.

The low-energy events are retained for the analysis, if the cleaning-levels are lowered. But while doing so with the standard cleaning, many pixels are cleaned that only contain a NSB-signal. (cf. Figure 5.2(a)). The number of cleaned pixels only containing a NSB-signal can be reduced by requesting an additional coincidence in time of the extracted signals between adjacent pixels. This is effective because the signal extractor searches for the maximum signal amplitude within the 50 nsec long recorded output of each pixel, while the expected pixel to pixel time spread is only a few nanoseconds (see Page 30).

I have implemented a new cleaning method (dubbed time-cleaning) within the framework of MARS that uses the time information of a signal in addition to the amplitude information. The time information is called signal-time hereafter. In the time-cleaning the signal-time is used as an extra coincidence requirement, which allows lowering the cleaning-levels and at the same time effectively rejects pixel that contain only a NSB-signal (cf. Figure 5.2(b)). The algorithm of the time-cleaning is presented in the next section.

#### Algorithm of the Time-Cleaning

Figure 5.3 shows the flowchart of the time-cleaning algorithm. The procedure can be broken down into seven steps. The names of the variables that have to be set by the user are given in brackets.

1. All pixels with a signal above a predefined level ( $CleanLevel1$ ) are selected.

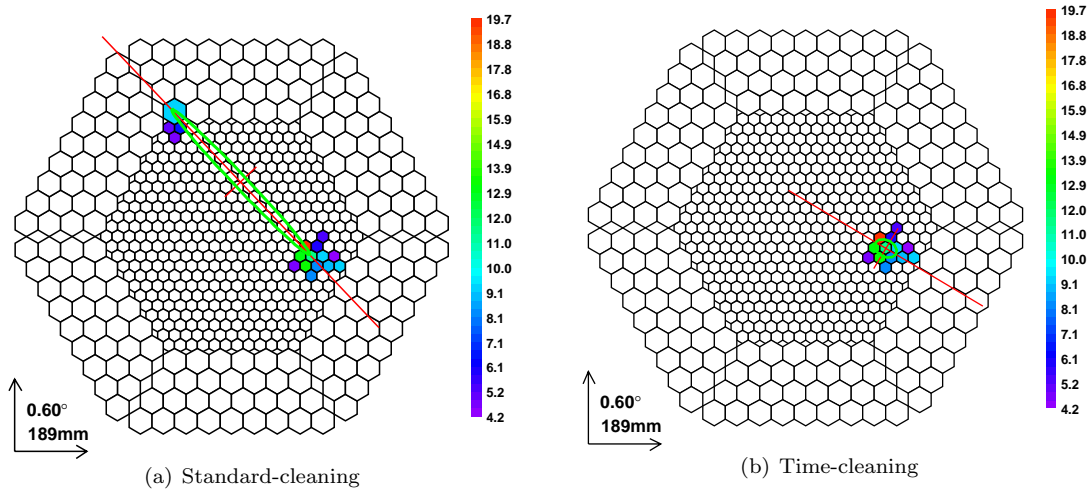


Figure 5.2: Example of an event that has been cleaned with 6 photoelectrons (core-pixel) and 4 photoelectrons (boundary-pixel) using the standard-cleaning (left) and the time-cleaning (right). In the standard-cleaning a fluctuation in the NSB is picked up, which is suppressed in the time-cleaning.

2. A selected pixel is marked as core-pixel, if it has at least one neighboring pixel:
  - that has been selected in the previous step
  - the difference of the signal-times between these two pixels is within a small time window of a few nanoseconds ( $MDeltat$ ).
3. The core-pixels that touch each other are grouped into clusters. Each cluster gets its own “cluster-time”, which is the weighted mean time of all pixels in a cluster. The number of photoelectrons of a pixel is used as its weight. In the same step the contents of the pixels in a cluster are summed up thus defining the size of a cluster. The cluster with the largest size is the “main” cluster.
4. A cluster is rejected, if the difference between its cluster-time and the cluster-time of the main-cluster is too large ( $MDeltaTIs1$ ).
5. Boundary-pixels are selected in the direct vicinity of the remaining clusters. A pixel is selected as a boundary pixel and added to a cluster if it meets two requirements:
  - (a) It has a signal above a predefined threshold ( $CleanLevel2$ , with  $CleanLevel2 < CleanLevel1$ ).
  - (b) The pixel has at least one already cleaned direct next neighbor and the signal-time between the two pixels is less than ( $MDeltaTBound$ ).

This step can be reiterated more than once ( $CleanRings$ ).
6. In the second last step all touching clusters are merged.
7. In the last step all clusters are rejected that do not fulfill the requirement of a minimum number of pixels ( $MinPixel$ ).

Figure 5.5 shows some examples of real showers before (upper row) and after (lowest row) the time-cleaning was applied. The middle row shows the signal-times of each pixel. The parameters used in the time-cleaning algorithm are:

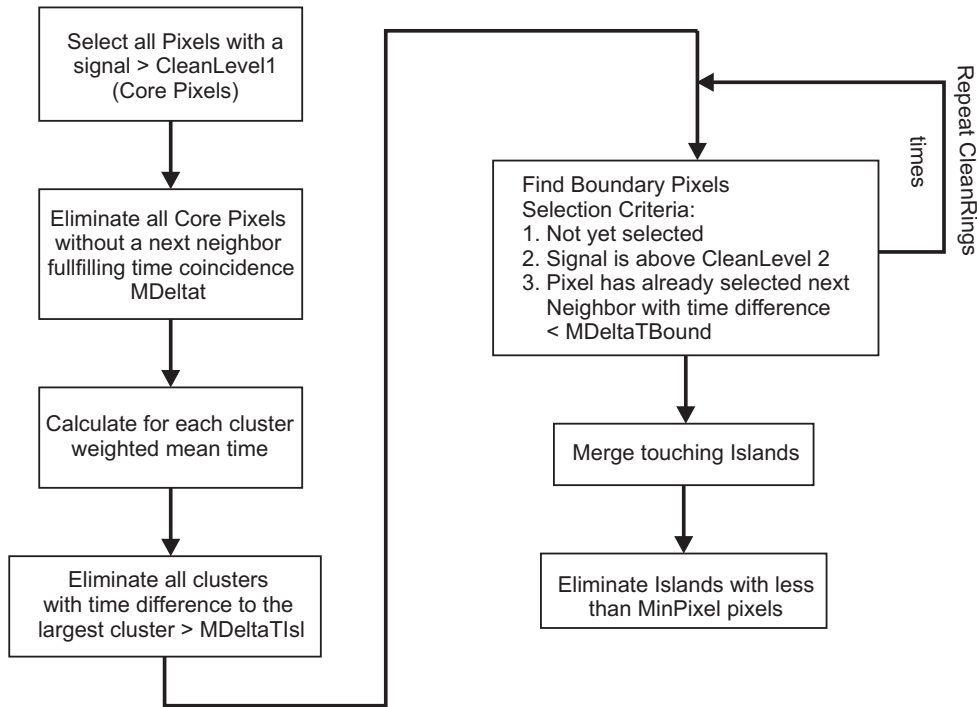


Figure 5.3: Flowchart of the time-cleaning procedure. See text for explanation.

**CleanLevel1:** 6 photoelectrons

**CleanLevel2:** 4 photoelectrons

**MDeltat, MDeltaTIsI, MDeltaTBound:** 1 FADC slice (3.3 nsec)

**CleanRings:** 2

**MinPixel:** 2 Pixels

These parameters were used in the analysis of the celestial objects presented later. Using these values in the time-cleaning 98% of all events survive the cleaning procedure.

### 5.3 Image Parametrization

Hillas (1985) suggested to parameterize a cleaned shower image with a few geometrical parameters derived from its zero, first and second moments (principal component analysis). Some of these so-called Hillas-parameters WIDTH, LENGTH, DIST and also ALPHA are shown in Figure 5.4.

In the following it is shown how these parameters are calculated. If  $x_i$  and  $y_i$  are the camera coordinates of a cleaned pixel then the 1st and 2nd moments of the image can be written as:

$$\langle x \rangle = \frac{\sum_{i=0}^N x_i w_i}{\sum_{i=0}^N w_i}, \quad \langle y \rangle = \frac{\sum_{i=0}^N y_i w_i}{\sum_{i=0}^N w_i} \quad (5.3)$$

$$\langle x^2 \rangle = \frac{\sum_{i=0}^N x_i^2 w_i}{\sum_{i=0}^N w_i}, \quad \langle y^2 \rangle = \frac{\sum_{i=0}^N y_i^2 w_i}{\sum_{i=0}^N w_i} \quad (5.4)$$

$$\langle xy \rangle = \frac{\sum_{i=0}^N x_i y_i w_i}{\sum_{i=0}^N w_i} \quad (5.5)$$

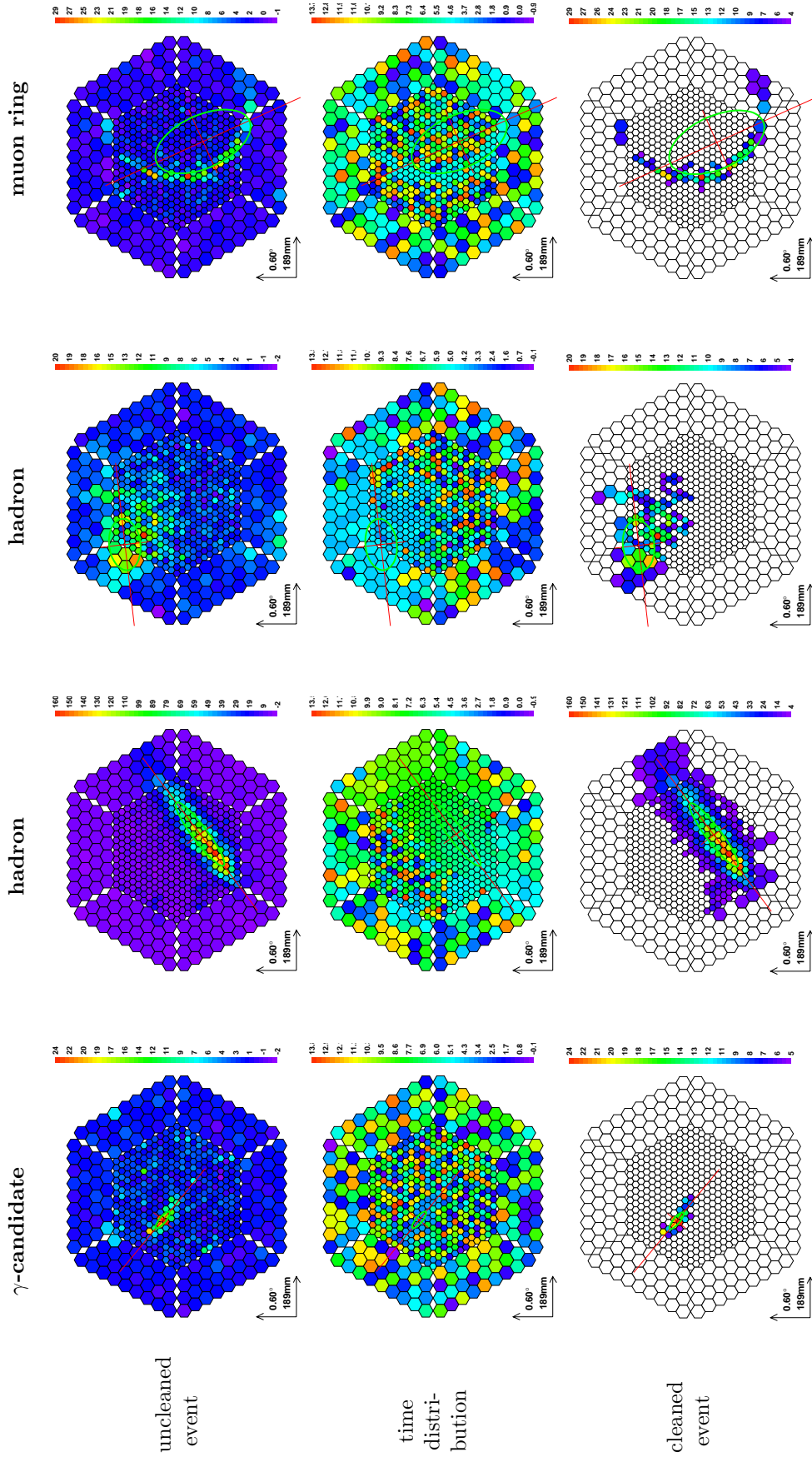


Figure 5.5: Examples of real shower events. From left to right:  $\gamma$ -ray candidate, two hadron events, a muon. The top row shows the pixel contents in units of photoelectrons, the middle row the signal-times in units of FADC slices (1 slice = 3.3 nsec) and the bottom row the cleaned events.

where  $w_i$  is the signal (photoelectrons) of a pixel raised to a power  $\geq 1$ . For the analysis presented here the exponent was chosen to be 1.5.

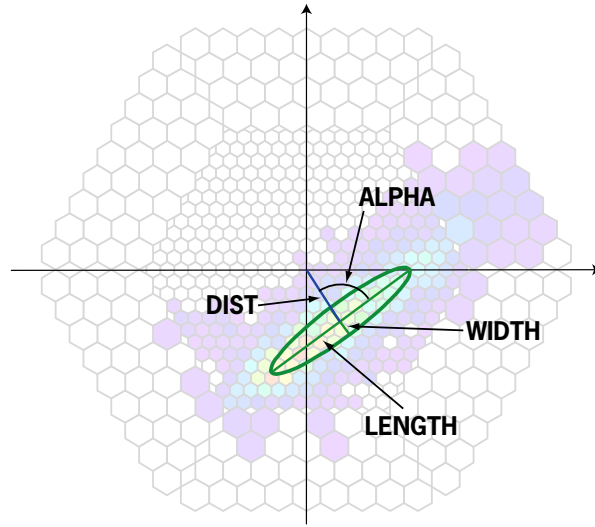


Figure 5.4: Parameterization of a shower image with Hillas-parameters.

From the moments the elements of the covariance matrix of the cleaned shower image are calculated in camera coordinates:

$$\sigma_x^2 = \langle x^2 \rangle - \langle x \rangle^2 \quad , \quad \sigma_y^2 = \langle y^2 \rangle - \langle y \rangle^2 \quad (5.6)$$

$$\sigma_{xy} = \sigma_{yx} = \langle xy \rangle - \langle x \rangle \langle y \rangle \quad (5.7)$$

WIDTH and LENGTH can be identified with the eigenvalues of the covariance matrix. The angle ALPHA between the major shower axis and the vector from the center of gravity of the shower to the center of the camera is then given by

$$\text{ALPHA} = \arccos \left( \frac{\langle x \rangle + \tan \delta \langle y \rangle}{\text{DIST} \sqrt{1 + \tan^2 \delta}} \right) \quad , \quad (5.8)$$

where the distance (DIST) of the center of gravity of the shower image to the camera center is

$$\text{DIST} = \sqrt{\langle x \rangle^2 + \langle y \rangle^2} \quad , \quad (5.9)$$

and  $\delta$  is the angle of rotation of the covariance matrix, defined by Equation 5.6 and 5.7, into diagonal form.

ALPHA is related to the arrival direction of the recorded shower and is used to extract the  $\gamma$ -ray signal (cf. Section 5.5).

Other image parameters are:

**Size:** Sum of the signals of all cleaned pixels (zeroth moment).

**ConcentrationX:** Ratio between the sum of the signals of the X pixels with the highest signal contents and SIZE.

**Leakage:** Fraction of the shower image content in the outermost ring of the camera.

## 5.4 Gamma Hadron Separation and Energy Estimation

In the same article where Hillas (1985) proposed the image parameters, it was also shown by Monte Carlo (MC) simulations that the distributions of several parameters (e.g. LENGTH and WIDTH as well as DIST) are different for  $\gamma$ -ray showers and hadron showers and thus can be used to distinguish between both populations.

**Width:**  $\gamma$ -showers have a low width because only multiple scattering and, by a lesser effect, the earth magnetic field blow up transverse development. Hadron showers are much more blown up transversely by the transverse momentum kick in hadronic interactions.

**Length:**  $\gamma$ -showers have in general for the same initial energy a shorter length. Hadron-showers are generally more extended in length because of diffractive scattering effects (a “leading” particle carries a significant part of the initial energy away in most hadronic interactions).

**Concentration:**  $\gamma$ -showers are quite concentrated. Hadron-showers have often a large longitudinal spread in energy deposit.

**Light yield:** For the same energy a  $\gamma$ -shower produces in general more light than a hadron shower, because in the latter case many secondary particles do not produce Cherenkov light. Below 200 GeV only a small fraction of hadronic showers produce Cherenkov light at all.

While at higher energies the differences in the image parameters are becoming very large, the differences shrink when approaching the threshold. On one hand, the finite pixel size does not allow anymore to detect differences when the image is spread over only a few pixels. On the other hand, most parts of a hadron shower become invisible in Cherenkov light because many particles are below the Cherenkov threshold. Eventually, only one energetic  $\pi^0 \rightarrow \gamma\gamma$  is able to generate sufficient Cherenkov light but then showers are practically indistinguishable from  $\gamma$ -induced showers. Below 100 GeV many secondaries in a hadron shower have a large angle with respect to the shower axis such that the Cherenkov light is not more falling into the FoV of the camera.

In addition a new background pops up in MAGIC close above the threshold. Due to the large mirror a single high altitude, a longflying  $\beta = 1$ , track can generate enough Cherenkov light and has a very concentrated image to be easily confused with a  $\gamma$ -shower of below 100 GeV.

On average about 1000 times more hadron (background) events than  $\gamma$ -ray events are recorded. Efficient methods are needed, which filter the data and select the  $\gamma$ -ray events. For the separation of “ $\gamma$ -ray-like” events from “hadron-like” events, Bock et al. (2004) have tested and compared different multivariate methods that exploit correlations between several image parameters. It was found that the tested multivariate methods perform similarly among each other and in general outperform other past separation methods. In the following I describe the random forest (RF) method (see e.g. Breiman, 2001), which is the standard method used in MAGIC, for the  $\gamma$ /hadron separation as well as for the energy estimation.

### 5.4.1 The Random Forest Method

#### a) for the $\gamma$ /Hadron Separation

The random forest method is based on decision trees. For the purpose of  $\gamma$ /hadron separation the forest of decision trees is grown from two data samples; one sample of MC  $\gamma$ -ray events, representing the  $\gamma$ -ray showers, and one sample of MC or real hadron events, representing the background.

A tree of the forest is grown (training) from a random subsample of  $\gamma$ -ray (signal) and background (bkg) events on the basis of image parameters (cf. Section 5.3). In each step of the growth process

one image parameter is chosen at random and a cut in this parameter that minimizes the so-called Gini index

$$Q_{\text{Gini}} = 2 \left( \frac{N_{\text{signal}}^{\text{left}} \cdot N_{\text{bkg}}^{\text{left}}}{N_{\text{tot}}^{\text{left}}} + \frac{N_{\text{signal}}^{\text{right}} \cdot N_{\text{bkg}}^{\text{right}}}{N_{\text{tot}}^{\text{right}}} \right) .$$

$N^{\text{left}}$  ( $N^{\text{right}}$ ) are the events of the subsamples that are below (above) the cut and which constitute new subspaces. Subsequently in each subspace (branch) an image parameter is chosen at random and the Gini index minimized. This procedure is repeated until in each subspace at the end of the tree the Gini index is 0, contains only few ( $<10$ ) events or events of only one category (leafs). Many trees (50 to 100) are generated in this way, each from different random samples of training events. The sample of trees forms the random forest.

For the classification of an event it passes through all generated trees ( $N_{\text{trees}}$ ). It is counted in how many trees the event ends up at a node that consists of a hadron ( $l = 1$ , otherwise  $l = 0$ ) and the HADRONNESS value is calculated

$$\text{HADRONNESS} = \frac{\sum_{i=0}^{N_{\text{trees}}} l_i}{N_{\text{trees}}} .$$

An event is more likely a  $\gamma$ -ray if it has been assigned a HADRONNESS closer to 0 and is more hadron-like if HADRONNESS is closer to 1.

A demonstration of the  $\gamma$ /hadron separation power with the random forest method is given by the upper plot of Figure 5.6. The plot shows a scatter plot of HADRONNESS vs. the parameter SIZE for real data background events (blue) and MC  $\gamma$ -rays (red)<sup>2</sup>. Image parameters used in the training of the random forest are DIST, WIDTH, LENGTH and SIZE. This representation shows the good  $\gamma$ /hadron separation power above a SIZE of 300 photoelectrons<sup>3</sup> ( $\gtrsim 200$  GeV) and how dramatically it deteriorates below 300 photoelectrons. The parameter ALPHA is not considered in the  $\gamma$ /hadron separation as it will be used to extract the  $\gamma$ -ray signal (cf. Section 5.5).

A more quantitative statement about the  $\gamma$ /hadron separation power can be made with the quality factor  $Q$

$$Q = \frac{\epsilon_{\gamma}}{\sqrt{\epsilon_{\text{bkg}}}} , \quad (5.10)$$

where  $\epsilon_{\gamma}$  is the fraction of  $\gamma$ -rays that are retained after a cut.  $\epsilon_{\text{bkg}}$  is the corresponding fraction of retained background events. The higher  $Q$  the better is the  $\gamma$ /hadron separation power. The black stars in the upper plot in Figure 5.6 denote the HADRONNESS cut in differential bins of  $\log(\text{SIZE})$  for which the  $Q$ -factor is maximum. The value of  $Q$  is given in the lower plot of Figure 5.6.

The HADRONNESS cut-values are fitted with a Fermi-Dirac function, to which a constant and a linear term have been added. One obtains the following parametrization of a SIZE dependent HADRONNESS-cut to select  $\gamma$ -ray events (dashed line in Figure 5.6):

$$\text{HADRONNESS} < \frac{0.71}{\left( e^{\frac{\log(\text{SIZE}) - 2.25}{0.045}} + 1 \right)} + 0.20 - 0.040 \cdot \log(\text{SIZE}) . \quad (5.11)$$

The above parametrization was validated and optimized on a 1.5 hour data sample of the Crab nebula. It turned out that changing the constant term in the above equation from 0.17 to 0.20, the significance of the extracted  $\gamma$ -ray signal increases by  $\sim 10\%$  (solid black line in the Figure). Increasing the constant term further, the significance reduces again.

In telescopes like HEGRA, which have smaller mirror surfaces and subsequently higher energy thresholds than MAGIC, event SIZES of 100 phe or more are normally sufficient to perform excellent  $\gamma$ /hadron-separation. Insufficient signal reconstruction is, therefore, unlikely the reason why  $\gamma$ /hadron-separation fails below 100 GeV in MAGIC.

<sup>2</sup>No pre-selection was done on the events.

<sup>3</sup> $> 2.5$  in the logarithmic scale of the plot

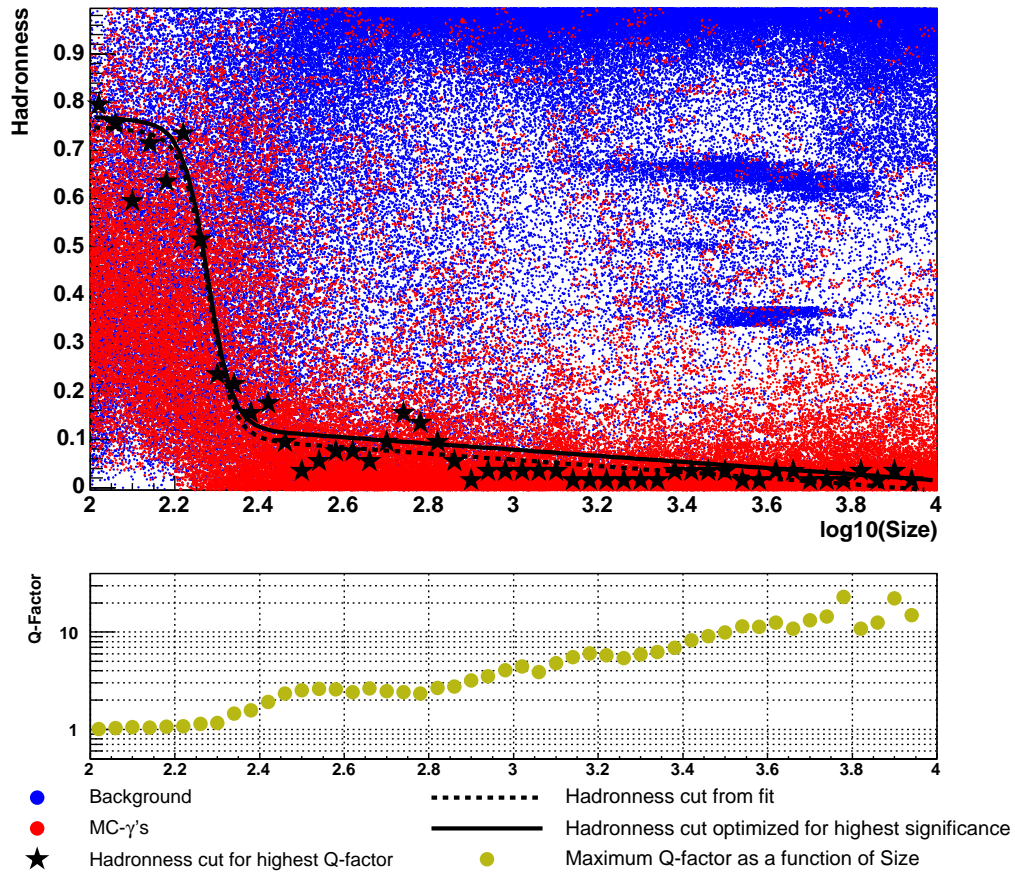


Figure 5.6: The upper plot shows the distribution of the parameter HADRONNESS vs. SIZE. The background events are marked blue and the MC  $\gamma$ -ray events red. Note that below a SIZE of 300 photoelectrons most of the background events are hidden behind the simulated  $\gamma$ -ray events. For bins in SIZE the HADRONNESS cut (black stars) is found that yields the highest quality factor (yellow dots). The dashed line is a fit to the HADRONNESS values. The quality factor (without an ALPHA-cut) is given in the lower plot.

One reason might be that the larger mirror surface of MAGIC collects enough light from a single high altitude ( $> 5$  km above the telescope) track, e.g. a muon or their hadronic parent particles, which fulfills the trigger condition and imitates a very narrow  $\gamma$ -ray shower. This event class can in principle be distinguished with fast timing and digitization, as currently prepared with new 2 GHz FADCs. Another reason for the background could be an increase in the number of events at lower energies in which a single  $\pi^0$  carries a large fraction of the initial energy, while all the other tracks inside the field of view (FOV) are below the Cherenkov threshold or are not well reconstructed.

### b) for the Energy Estimation

The number of photoelectrons summed over the cleaned image of a recorded event (SIZE) is correlated to the energy of the primary  $\gamma$ -ray (cf. Figure 4.6). For an estimate of the event energy one has to take into account that the measured SIZE depends on several parameters. A strong influence has e.g. the zenith angle of the observation, the distance of the impact point of the shower from the telescope and the applied cleaning levels in the image cleaning. These and other effects are automatically taken into account if the energy of an event is estimated by means of the random forest method.

The energy of an event is estimated with the random forest method by subdividing the energy range of interest into bins. For each bin a forest is trained that separates  $\gamma$ -rays with energies that fall within the bin from those with energies outside of the bin. In the actual energy estimation an event is assigned to the energy bin to which it fits with the highest probability.

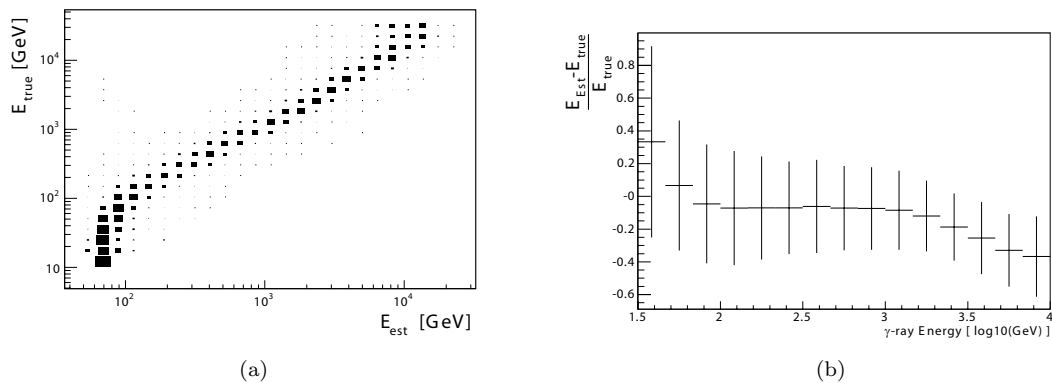


Figure 5.7: Left panel: true energy of a  $\gamma$ -ray vs. its estimated energy (migration matrix); Right panel: profile histogram of the relative deviation between the estimated energy and the true energy of a  $\gamma$ -ray. The error bars denote the energy resolution.

Figure 5.7(a) shows the distribution of the true  $\gamma$ -ray energies of simulated  $\gamma$ -rays vs. the energies estimated by the RF-method. The energy estimation works well between  $\sim 100$  GeV and  $\sim 10$  TeV with nearly constant energy resolution of  $\sim 25\%$  RMS (Figure 5.7(b)). Below 100 GeV fluctuations in the shower reduce the accuracy of the energy estimation.

Parameters used in the training of the energy estimator for the analysis presented in the following chapters are: SIZE, DIST, WIDTH, LENGTH, CONCENTRATION, CONCENTRATION5, LEAKAGE<sup>4</sup> and the zenith angle.

Details of the implementation of the random forest method in MARS and the performance of the method can be found in Hengstebeck (2006).

<sup>4</sup>Ratio between the number of photoelectrons in the most outer ring of the camera and SIZE.

## 5.5 Extraction of the $\gamma$ -ray signal

At this stage of the analysis one is able to identify a possible  $\gamma$ -ray signal in the data sample with the directional information of the parameter  $|\text{ALPHA}|$ . Shower images that are produced by  $\gamma$ -rays from the source under observation are pointing with their major axis to the source, i.e.  $|\text{ALPHA}|$  is small (typically  $\lesssim 8^\circ$  and SIZE-dependent), if  $|\text{ALPHA}|$  is calculated with respect to the source position in the camera<sup>5</sup>. On the other hand, the  $|\text{ALPHA}|$ -values of background events are in first order uniformly distributed, because the galactic magnetic field randomizes the incoming direction of hadrons. Thus the necessary (but not sufficient) signature of a  $\gamma$ -ray signal is an excess at small  $|\text{ALPHA}|$ -values. The number of excess events is extracted and the significance of the signal is calculated. It should be mentioned that the  $|\text{ALPHA}|$ -distribution widens with the extension of the  $\gamma$ -ray source.

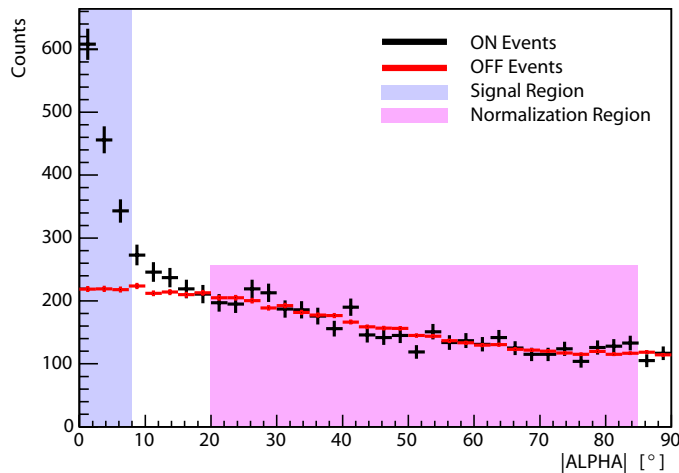


Figure 5.8:  $|\text{ALPHA}|$ -distribution of a Crab data sample (ON) and a data sample of a region in the sky where no  $\gamma$ -ray source is expected (OFF).

Figure 5.8 shows the  $|\text{ALPHA}|$ -distributions of a Crab data sample (called ON sample, which is a mixture of  $\gamma$ -ray and cosmic background events) and of a data sample obtained by pointing MAGIC to a location in the sky where no  $\gamma$ -ray source is expected (called OFF sample). The OFF distribution is scaled to the ON distribution by normalizing it in the normalization region.

The significance of the  $\gamma$ -ray signal is calculated by counting the number of OFF events ( $N_{\text{OFF}}$ ) and ON events ( $N_{\text{ON}}$ ) in the expected signal region and using Equation 17 in Li and Ma (1983):

$$S = \sqrt{2} \left\{ N_{\text{ON}} \ln \left[ \frac{1 + \alpha}{\alpha} \left( \frac{N_{\text{ON}}}{N_{\text{ON}} + N_{\text{OFF}}} \right) \right] + N_{\text{OFF}} \ln \left[ (1 + \alpha) \left( \frac{N_{\text{OFF}}}{N_{\text{ON}} + N_{\text{OFF}}} \right) \right] \right\}^{1/2} \quad (5.12)$$

where  $\alpha$  is the scaling factor that normalizes the OFF data sample to the ON data sample.

### 5.5.1 Optimal Cut in Alpha

The calculated significance depends on the choice of the signal region. In addition the width of the  $|\text{ALPHA}|$ -distribution of a  $\gamma$ -ray signal depends on the energy, resp. SIZE. In first order the expected  $|\text{ALPHA}|$ -distribution from showers from a point source follows a folded Gaussian with a SIZE dependent  $\sigma$ . According to Li and Ma the highest significance is expected for a cut at  $1.8\sigma$ , if the Gaussian sits on a flat background. Therefore, it is necessary to derive a SIZE dependent cut in  $|\text{ALPHA}|$  prior to the selection of events in a search for pulsed emission.

<sup>5</sup>In case of ON-OFF observation with respect to the camera center.

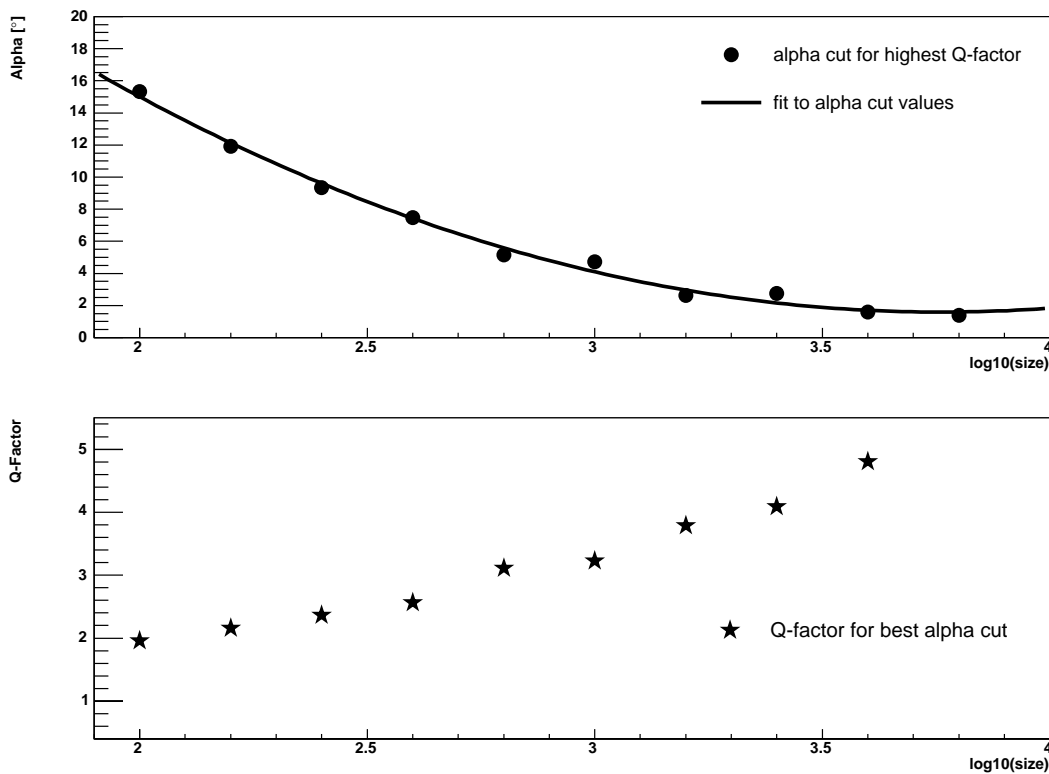


Figure 5.9: The upper plot shows the cut in  $|\text{ALPHA}|$  for different bins of  $\text{SIZE}$  optimized for maximum quality factor. The corresponding quality factors are shown in the lower graph.

Figure 5.9 shows  $\text{SIZE}$  dependent  $|\text{ALPHA}|$ -cuts that one has to apply as upper end of the signal region in order to obtain the highest possible value for the quality factor  $Q$  (Equation 5.10). The  $|\text{ALPHA}|$ -values were found by dividing a MC- $\gamma$ -ray sample and an OFF data sample into bins of  $\log(\text{SIZE})$ . In each bin the  $|\text{ALPHA}|$ -cut was changed until the quality factor was maximal. The quality factors are shown for the  $|\text{ALPHA}|$ -cut alone in the lower section of the figure. Finally, an empirical parametrization of the  $\text{SIZE}$  dependent  $|\text{ALPHA}|$ -cut is found by a fit of a second order polynomial (solid line in Figure 5.9):

$$|\text{ALPHA}|-\text{cut}(\text{SIZE}) = 1.59 + 3.76 \cdot [4.31 - \log(\text{SIZE})]^2 \quad . \quad (5.13)$$

It should be noted that the overall quality factor is the product of the quality factor obtained from the HADRONNESS-cut and the  $|\text{ALPHA}|$ -cut. Figure 5.10 shows the quality factors for the optimal  $|\text{ALPHA}|$ -cut and HADRONNESS-cut as well as the quality factor for the combination of both cuts. Above a  $\text{SIZE}$  of about 500 phe the  $\gamma$ /hadron-separation power of HADRONNESS is better than the separation power of  $|\text{ALPHA}|$ . At 100 phe the combined Q-factor is 2, only  $|\text{ALPHA}|$  is effective in separating  $\gamma$ -rays from background events. At the largest  $\text{SIZE}$  the combined Q-factor rises to 50, which is a factor 25 increase in sensitivity.

## 5.6 Sky Maps

So far it was always assumed that the location of the  $\gamma$ -ray source is known and that the emission region is point-like. If the source has an extended morphology or its position is badly known one has to estimate the incoming direction of each detected  $\gamma$ -ray. In telescope arrays multiple images

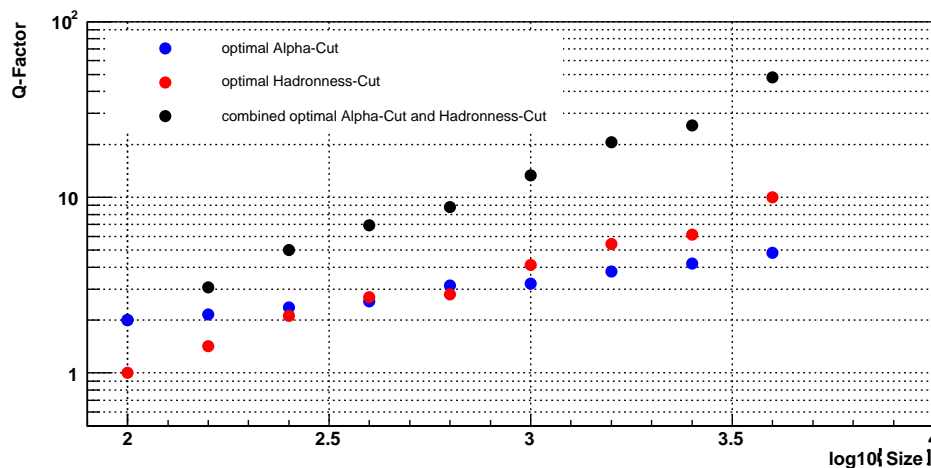


Figure 5.10: Size dependence of the Q-factor for optimal  $|\text{ALPHA}|$ -cut, HADRONNESS-cut and the Q-factor for the combination of  $|\text{ALPHA}|$ -cut and HADRONNESS-cut.

of the same shower are recorded from different positions and the direction of the  $\gamma$ -ray is given by the point of intersection of the major axes of the images.

In order to reconstruct the impact point of  $\gamma$ -ray shower if the shower is imaged by only one telescope, Fomin et al. (1994) proposed to use the feature that the images of showers with a given direction become more roundish the closer the impact point of the shower is to the telescope. A measure for the roundness of a shower is the ratio  $\text{WIDTH}/\text{LENGTH}$ . This ratio is used in the parameter  $\text{DISP}$ , which is an estimate for the angular distance between the imaged shower core and the origin of a  $\gamma$ -ray in the camera.  $\text{DISP}$  itself does not provide an information on which side of the shower the arrival direction lies. For this purpose the asymmetry of the shower image (3rd Moment) is used. The angular resolution achieved with the  $\text{DISP}$ -method is  $\sim 0.1^\circ$  (see Section 6.3.3).

The empirical parametrization of  $\text{DISP}$  is found e.g. by parameterizing the distribution  $\text{DIST}/(1-\text{WIDTH}/\text{LENGTH})$  vs.  $\log(\text{SIZE})$ . This distribution is obtained from a sample of  $\gamma$ -rays from a simulated point source that is located in the center of the camera. In this case the parameter  $\text{DIST}$ , the angular distance between the shower core and the camera center, can be used to parameterize  $\text{DISP}$  ( $\text{DIST}=\text{DISP}$ ):

$$\text{DISP} = \left(1 - \frac{\text{WIDTH}}{\text{LENGTH}}\right) [a - b \cdot \log(\text{SIZE}) + c \cdot \log(\text{SIZE})^2] \quad (5.14)$$

with the following values in units of degrees:

$$\begin{aligned} a &= 2.70 & b &= 1.59 \\ c &= 0.790 \end{aligned}$$

This parameterization provides angular resolutions  $\sim 0.1^\circ$  over a wide range of energies. It was used throughout the thesis except for the morphology studies of the Crab nebula, where I used the parameterization by Domingo-Santamaria et al. (2005). It was found that the parameterization by Domingo-Santamaria et al. (2005) results in a two times better angular resolution for energies above a few hundred GeV, which significantly improved the analysis results I present in Section 6.3.3.

## 5.7 Calculation of an Energy Spectrum

If a  $\gamma$ -ray signal is found the energy spectrum gives information about the nature of the  $\gamma$ -ray source. The energy spectrum  $F(E)$  is derived according to:

$$F(E) = \frac{dN_\gamma}{dE \cdot A(E) \cdot t} \quad (5.15)$$

with:

1. The number of excess events  $dN$  in bins of estimated energy  $dE$
2. The energy dependent collection area  $A(E)$
3. The effective on-time  $t$

The number of excess events is extracted from |ALPHA|-distributions (cf. Section 5.5) in different bins of estimated energy. The on-time is evaluated directly from the event rate, which is obtained from the distribution of the time intervals between successive events. It should be remembered that the dead time is negligible (cf. Section 4.2.3).

All the characteristics and performance of the detector are included in the calculation of the collection area. Due to the absence of a calibrated  $\gamma$ -ray source the collection area can only be determined from MC-simulations. This is one of the reasons for fairly high systematic uncertainties in the imaging air shower Cherenkov technique. The collection area  $A_{\text{Coll}}$  is calculated by simulating a virtual  $\gamma$ -ray source with a given spectral shape. The simulated  $\gamma$ -ray events  $N_{\text{sim}}$  have impact points uniformly distributed within an area  $A$  around the detector, with  $A$  being larger than any area hit by accepted events. If  $N_{\text{det}}$  are the simulated events, which were detected and passed all selection criteria, the collection area is

$$A_{\text{Coll}} = A \times \frac{N_{\text{det}}}{N_{\text{sim}}} \quad (A \gg A_{\text{Coll}}) \quad (5.16)$$

Figure 5.11 shows the energy dependence of the collection area.

The estimated energy of an event is subject to a finite resolution and a bias. This affects the reconstructed spectrum particularly at the lowest and highest energies and is taken care of by an “unfolding” procedure. Available in MARS and used in this thesis are unfolding methods by Tikhonov and Arsenin (1979), Bertero (1989) and a forward unfolding method.

## 5.8 Pulsar Analysis

In the following I describe specific changes to the analysis chain and methods that I have implemented to search for periodic emission from pulsars.

The spectra of pulsars that are known to emit  $\gamma$ -rays, feature an exponential cutoff at a few tens of GeV (cf. Section 3.4). The sharp cutoff is the reason why the detection of periodic  $\gamma$ -ray emission from pulsars is only expected close to the trigger threshold of MAGIC. The reduced sensitivity of the telescope below 100 GeV requires to search for periodicity in data sets that have been accumulated over months or even years. This has several implications for the analysis:

- The loss of kinetic energy of a pulsar manifests in its rotational slowdown. The time dependent change of the spin-period is parameterized by a Taylor expansion that is obtained by observations of the pulsar at different energies (mostly radio observations).

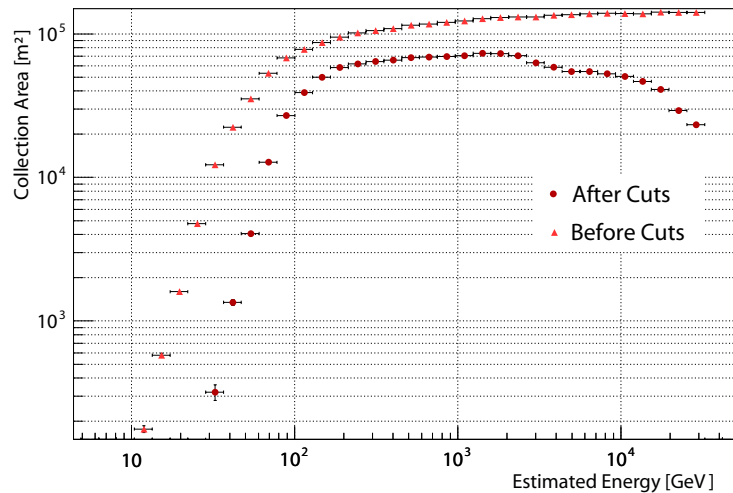


Figure 5.11: Differential collection area after hardware trigger (triangles) and after cuts and  $\gamma$ /hadron-separation (circles). The collection area after cuts shrinks again at higher energies due to the requirement in the analysis that the shower image has to be fully contained within the inner camera.

- The changing position of the Earth within the solar system introduces variations in the signal propagation times that have to be corrected. This is taken care of by the transformation of the recorded event times to the center of mass of the solar system (barycenter).
- If a pulsar is part of a binary system the propagation delays of the  $\gamma$ -rays within the binary system have also to be accounted for.
- Young pulsars like the one within the Crab nebula show irregularities in their periodic emission, which are referred to as glitches. This behavior is known for many pulsars. It is best studied for the Crab pulsar. There are currently two competing models to explain the nature of a glitch. In the starquake glitch model (Anderson and Itoh, 1975; Alpar et al., 1996) sudden deformations of the shape of the neutron star crust change the moment of inertia and thus the rotational frequency of the pulsar. Alternatively, in the vortex unpinning model of glitches (Anderson and Itoh, 1975; Alpar et al., 1984, 1993) vortices of superfluid migrate outward from the core and become pinned to nuclei in the transition region between the core and the crust of the neutron star. A differential rotation develops between the core and crust until a catastrophic unpinning of the vortices occurs, which can be observed as a glitch. A proper treatment of glitches is only possible by regular monitoring of the pulsar.

### 5.8.1 Time Correction of Signal Propagation Delays

Figure 5.12 illustrates how a varying propagation delay of the signal between the pulsar and an observer on Earth is introduced by the revolution of the Earth around the sun. This effect is taken care of by transforming the time of detection of an event (hereafter arrival time) to the barycenter, i.e. to the center of mass of the solar system. Other second order effects, mostly relativistic ones that influence the propagation of a  $\gamma$ -ray in the solar system can be neglected.

In the same way as variations in the propagation are introduced by the movement of the Earth within the solar system, the movement of a pulsar within a binary system introduces extra variations that also have to be corrected. For the barycentric correction the TEMPO timing package is used (Taylor et al., 2000). The program also includes routines to analyze propagation delays within binary systems. However, these routines are used internal in TEMPO and the output event times are not corrected for the signal propagation in the binary system. I modified the code of TEMPO that the binary corrections are included in the output of the programm.

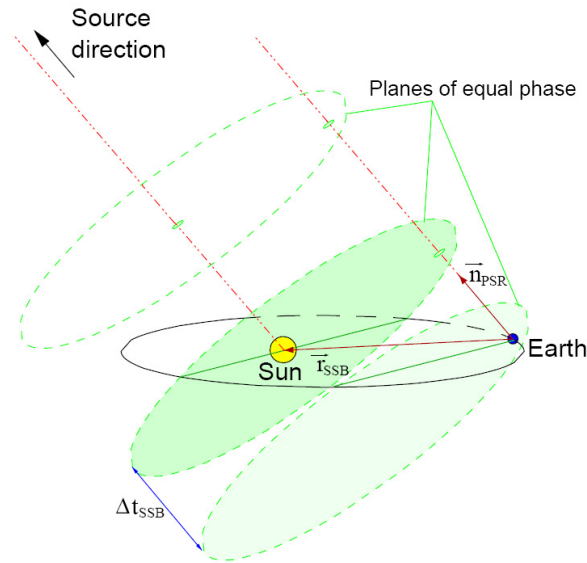


Figure 5.12: Illustration of propagation delays within the solar system (from Schmidt, 2005).

### 5.8.2 Correlating the Event Time with the Period of the Pulsar

After the event arrival times have been corrected for the propagation delays, which are described above, they are correlated to the period of the pulsar. As the rotational frequency  $\nu$  of the pulsar changes with time, the search for periodic  $\gamma$ -ray emission has to rely on a proper description of the spin-down behavior. This is done by taking higher order time-derivatives of  $\nu$  into account. The corrected arrival time  $t_j$  of the  $j$ -th event is then transformed to the period of the pulsar:

$$\phi_j = \nu(t_j - t_0) + \frac{1}{2}\dot{\nu}(t_j - t_0)^2 + \frac{1}{6}\ddot{\nu}(t_j - t_0)^3 + \dots$$

where  $\nu$ ,  $\dot{\nu}$ ,  $\ddot{\nu}$  and  $t_0$  are the ephemerides of the pulsar and are obtained from contemporary measurements, e.g. from radio observations. For the analysis presented here higher order derivatives than  $\ddot{\nu}$  can be neglected.  $\phi_j$  is the number of rotations the pulsar has spun since  $t_0$ .  $t_0$  corresponds to the appearance of the most prominent peak (main peak) of the light curve, i.e. integer numbers of  $\phi_j$  mark the position of the main peak and  $\theta = \text{modulo}(\phi_j)$  is the phase of an event with reference to the position of the main peak. If periodic emission is present it will show up in the distribution of phases (pulse phase profile), which is otherwise consistent with a uniform distribution.

### 5.8.3 Tests for the Search of pulsed Emission

As pointed out earlier, pulsed  $\gamma$ -ray emission is expected only in the lowest energy data samples measured by MAGIC. These samples are dominated by hadronic background and it will be very difficult to detect a pulsed signal. In this work a data sample is tested for periodic emission with three statistical tests:

- The  $\chi^2$ -Test
- The H-Test
- A test that uses Bayesian statistics applied to phase distributions of different binning

### $\chi^2$ -Test

The Pearson's  $\chi^2$ -test is probably the best known and most popular one. It is applied to the pulse phase profile and tests the hypothesis that the phases are uniformly distributed in the  $k$  bins of the pulse phase profile. The test value is

$$\chi^2 = \sum_{i=1}^k \frac{(n_i - \hat{n})^2}{\sigma_n^2} \quad ,$$

where  $n_i$  is the number of events in the  $i$ -th bin and  $\hat{n}$  is the average number of events per bin.  $\sigma_n^2 = n_i$  is the expected variance of the number of events per bin. If the events are randomly distributed and the average number of entries per bin is  $> 10$ , the test value follows a  $\chi^2$ -distribution with  $k - 1$  degrees of freedom.

The result of the  $\chi^2$ -test is very much dependent on the number of bins used. It can be shown (Zech, 1995) that the test becomes more sensitive if the number of bins is reduced. If on the other hand the binning is too coarse the test is insensitive to possible narrow structures in the pulse phase profile.

### H-Test

In the H-test (De Jager et al., 1989) the phases are not binned in a pulse phase profile as in the  $\chi^2$ -test. The H-test is based on Fourier decompositions. This is one of the reasons why the test is sensitive to a wide range of pulse shapes and is very powerful in the case no a priori information about the light curve is available.

The test is carried out in three steps:

1. From the phases  $\theta$  ( $0 \dots 1$ ) trigonometric moments  $\alpha(j)$  and  $\beta(j)$  are calculated for harmonic numbers  $j = 1, 2, \dots, j_{max}$ , with  $j_{max}$  typically set around 20

$$\alpha(j) = \frac{1}{N} \sum_{i=1}^N \cos j\theta, \quad \beta(j) = \frac{1}{N} \sum_{i=1}^N \sin j\theta \quad (5.17)$$

2. From these moments the value  $Z_m^2$  is calculated for  $1 < m \leq 20$ .

$$Z_m^2 = 2N \sum_{j=1}^m [\alpha^2(j) + \beta^2(j)] \quad (5.18)$$

3. Finally the result of the H-test  $H$  is

$$H = \max_{1 \leq m \leq 20} (Z_m^2 - 4m + 4) \quad (5.19)$$

If the test is randomly distributed, it is empirically following an exponential (cf. Figure 5.13):

$$\text{Prob}(H > h) \approx \exp(-0.4h) \quad . \quad (5.20)$$

De Jager (1994) gives analytic expressions for  $2\sigma$  and  $3\sigma$  upper limits of the fraction of pulsed emission from the H-test result.

$$x_{2\sigma} = (1.3 + 8.7\delta)(0.174H)^{(0.24+0.13\delta)} \exp[(0.03 + 0.13\delta) \log(0.174H)^2] \quad (5.21)$$

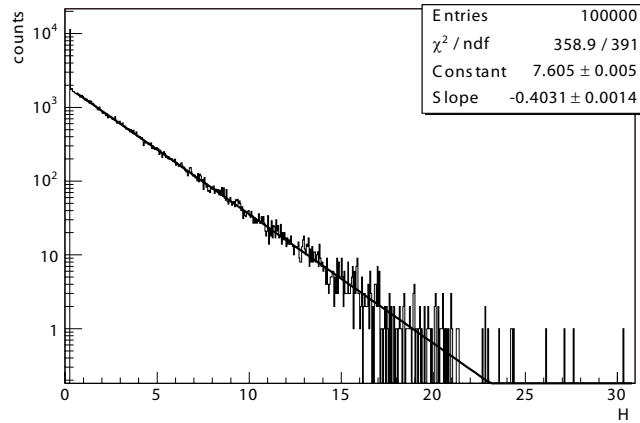


Figure 5.13: Results of the H-test obtained from a Crab data sample for randomly chosen test frequencies.

$$x_{3\sigma} = (1.5 + 10.7\delta)(0.174H)^{(0.17+0.14\delta)} \exp[(0.08 + 0.15\delta) \log(0.174H)^2] \quad (5.22)$$

Apart from the outcome of the H-test the upper limit depends only on the assumed duty cycle  $\delta$  of the pulsed emission, which is defined as the Full Width at Half Maximum (FWHM) of a Gaussian distribution. The aforementioned equations can be applied if the outcome of the H-test is larger than 0.3. An upper limit on the number of excess events is obtained by multiplying  $x_{2\sigma}$  or  $x_{3\sigma}$  with  $\sqrt{N}$ .

### A Test for Periodicity that uses Bayesian Statistics

Gregory and Loredo (1992) developed a test that is based on Bayesian statistics. For the test the phases  $\theta$  of the  $N$  events are binned in pulse phase profiles with different numbers of bins. From the pulse phase profiles the test evaluates the probability that a periodic signal is present in the data. The test result gives the ratio of the probability that periodicity is present and the probability that the phases are randomly distributed. This ratio  $O_{m1}$  is called the odds ratio in favor of an  $m$ -bin model, where  $m$  is the number of bins of the tested pulse phase profile. In case the position of the main pulse in the light curve and the period of the pulsar are unknown the odds ratio is given by

$$O_{m1} = \frac{1}{2\pi(m_{\max} - 1) \ln(\omega_{hi}/\omega_{lo})} \binom{N + m - 1}{N}^{-1} \int_{\omega_{lo}}^{\omega_{hi}} \frac{d\omega}{\omega} \int_0^{2\pi} d\phi \frac{m^N}{W_m(\omega, \phi)}, \quad (5.23)$$

$\omega$  is the rotational frequency of the pulsar that is tested.  $\omega_{hi}$  and  $\omega_{lo}$  are the upper and lower bounds of the range of rotational frequencies within one searches for periodicity.  $m_{\max}$  is the maximum number of bins of a pulse phase profile that is tested and  $m$  is the number of bins of the pulse phase profile for which  $O_{m1}$  is evaluated.  $W_m(\omega, \phi)$  is the multiplicity of the binned phases:

$$W_m(\omega, \phi) = \frac{N!}{n_1(\omega, \phi)! n_2(\omega, \phi)! \dots n_m(\omega, \phi)!}, \quad (5.24)$$

where  $n_i(\omega, \phi)$  is the number of events in the  $i$ -th bin of the pulse phase profile for the tested rotational frequency  $\omega$  and phase  $\phi$  of the light curve.

From all odds ratios ( $2 \leq m \leq m_{\max}$ ) the probability  $P$  for periodicity is calculated from

$$P = \frac{\sum_{m=2}^{m_{\max}} O_{m1}}{1 + \sum_{m=2}^{m_{\max}} O_{m1}}. \quad (5.25)$$

### 5.8.4 A Method to derive an Upper Limit on the Cutoff Energy of the Pulsar Energy Spectrum

In case of either a detection or a non-detection of pulsed emission the question about the cutoff energy of the  $\gamma$ -ray spectrum arises. Below a method is presented that allows to derive an upper limit or, in the case of a positive detection, to determine the cutoff energy of the energy spectrum of the pulsar.

1. The collection area  $A(E)$  in bins of energy is calculated:
  - with the same cuts that were applied in the analysis of the data.
  - by assuming an arbitrary source spectrum.
2. The parameterized  $\gamma$ -ray spectrum of the pulsar at lower  $\gamma$ -ray energies (from EGRET measurements  $< 30$  GeV) is extended by an exponential cutoff where  $E_{\text{Cutoff}}$  is the cutoff energy, e.g. for the Crab pulsar (Nolan et al., 1993):

$$F(E, E_{\text{Cutoff}}) = 4.11 \cdot 10^{-6} \left( \frac{E}{0.274} \right)^{-2.15} \exp\left(-\frac{E}{E_{\text{Cutoff}}}\right) \text{ photons cm}^{-2} \text{ s}^{-1} \text{ GeV}^{-1} \quad (5.26)$$

The number of expected excess events  $S$  is calculated by convoluting  $F(E, E_{\text{Cutoff}})$  with the collection area  $A(E)$  after cuts and by multiplying with the observation time  $t_{\text{obs}}$

$$S = t_{\text{obs}} \cdot \int_0^{\infty} F(E, E_{\text{Cutoff}}) \cdot A(E) dE \quad . \quad (5.27)$$

In a loop  $E_{\text{Cutoff}}$  is changed until the number of expected excess events  $S$  matches either the measured number of excess events or — in the case of a non-detection — the upper limit on the number of excess events.

3. The collection area is reevaluated, assuming a  $\gamma$ -ray source spectrum that has the same shape as the EGRET measured spectrum but extended by the exponential cutoff as derived above. With the new collection area the previous step is repeated.

It was found that  $E_{\text{Cutoff}}$  at most changes by  $\pm 3\%$  after the reevaluation of the collection area.

### 5.8.5 Optimization of the upper Size-Cut in the Search for pulsed Emission from a Pulsar

The sensitivity of MAGIC is fully exploited, if the SIZE dependent HADRONNESS-cut (cf. Section 5.4.1) and the SIZE dependent ALPHA-cut (cf. Section 5.5.1) are applied in the search for pulsed emission. However, due to the exponential cutoffs expected in the spectra of pulsars one might ask if there is an optimal upper SIZE-cut  $S_{\text{up}}$ , which further enhances the sensitivity of the analysis. For this purpose I define the quantity  $Q$ , which is, analogue to the quality factor, a measure of the sensitivity:

$$Q = \frac{\int_0^{\infty} F(E, E_{\text{Cutoff}}) \cdot A(E, S_{\text{up}}) dE}{\sqrt{B(S_{\text{up}})}} \quad (5.28)$$

where  $B$  is the number of background events that remain after all cuts,  $F$  is the pulsar spectrum with cutoff and  $A$  is the collection area after cuts. For several upper SIZE-cuts  $Q$  is shown in Figure 5.14, assuming that the energy spectrum of the Crab pulsar has a cutoff at 30 GeV. The sensitivity of the analysis monotonically increases with  $S_{\text{up}}$ . Above 300 phe  $Q$  basically does not change more. The collection area after cuts for  $S_{\text{up}} = 300$  phe is shown in Figure 5.15.

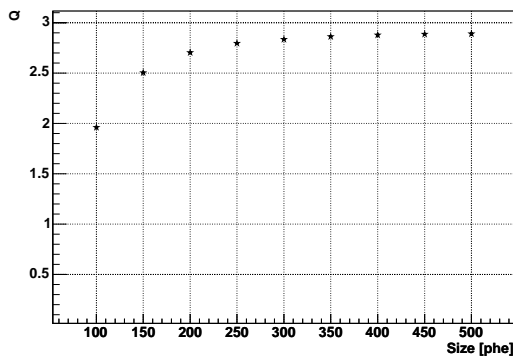


Figure 5.14:  $Q$  vs. upper SIZE-cut  $S_{\text{up}}$ . For a SIZE-cut of  $\text{SIZE} < 300$  phe or higher maximum sensitivity is obtained.

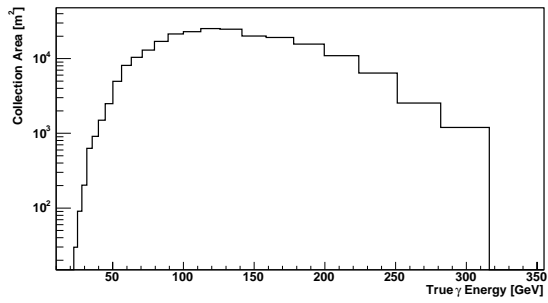


Figure 5.15: Collection area after optimized  $|\text{ALPHA}|$ - and  $\text{HADRONNESS}$ -cuts and an upper SIZE-cut of  $\text{SIZE} < 300$  phe is applied.

## 5.9 Upper Limit Calculation

If no signal is detected one has to calculate an upper limit on the number of excess events ( $N_{\text{U.L.}}$ ). For a physical interpretation it is necessary to convert the upper limit of excess events into an upper flux limit. If not otherwise stated, the upper flux limits (pulsed and unpulsed) shown in this work are calculated in the following way.

The number of expected events  $N$  is given by:

$$N = t_{\text{obs}} \cdot \int_0^{\infty} F(E) \cdot A(E) dE \quad (5.29)$$

where  $A(E)$  is the collection area after cuts. The assumed source spectrum  $F(E)$  can be written as the product of a constant term  $c$  and an energy dependent term  $G(E)$ :

$$F(E) = c \cdot G(E) \quad (5.30)$$

Using this relation, Equation 5.29 can be rewritten as

$$c = \frac{N}{t_{\text{obs}} \cdot \int_0^{\infty} G(E) \cdot A(E) dE} \quad (5.31)$$

After replacing  $N$  by  $N_{\text{U.L.}}$ ,  $c$  can be used to compute upper limits:

$$\text{Differential Upper Limits: } F_{\text{Diff}}(E) = c \cdot G(E) \quad (5.32)$$

$$\text{Integral Upper Limits: } F_{\text{Int}}(E) = c \cdot \int_E^{\infty} G(E') dE' \quad (5.33)$$

The energy  $E$  in the last equation is defined as the peak of the energy distribution of MC- $\gamma$ -ray events after cuts. The MC events follow the spectral shape  $G(E)$ .

It is noteworthy that the systematic uncertainties on  $A(E)$  introduced by choosing a certain spectral shape is  $\sim 5\%$  and can be neglected.

## 5.10 Systematic Errors

A calibration of the instrument is not possible due to the lack of a  $\gamma$ -ray source of known intensity and energy. Therefore,  $\gamma$ -ray astronomy with ground based experiments has to rely on Monte Carlo simulations and is particular susceptible to systematic uncertainties when determining the flux, spectral slopes etc. . Two different kinds of systematic errors have be addressed:

1. Effects that influence the energy determination
2. Effects that influence the flux calculation

### 5.10.1 Effects that influence the Energy Reconstruction

The energy reconstruction is affected in two ways. At first, wrongly estimated efficiencies in the light collection of the Cherenkov light result in a shift of the energy scale. Second, non-linearities in the signal chain result in a distortion of the energy scale.

#### Effects and their Impact on the Energy Scale

In brackets is indicated how the energy scale is shifted (+: overestimation of energy; -: underestimation of energy)

- Variations in the production of Cherenkov light in the atmosphere because of density fluctuations on hourly/daily/seasonal basis; estimated from MC-simulations (e.g. Bernlohr, 2000) ( $\pm 5\%$ )
- Variation of atmospheric transmission (Mie-scattering); estimated from data of the Carlsberg Meridian Telescope on La Palma ( $\pm 10\%$ )
- Reflectivity losses and reflectivity uncertainty of the MAGIC reflector surface (degradation of mirror reflectivity / loss of mirror tiles) ( $-10\%$ )
- Variations of the optical point spread function because of mechanical instabilities ( $\pm 5\%$ )
- Dust/dirt/cracks on the plexiglas entrance window of the MAGIC camera ( $-3\%$ )
- Uncertainty in the reflectivity of the foil used for the light catchers ( $\pm 3\%$ )
- Improper simulation of the light catcher / PMT-cathode geometry ( $\pm 5\%$ )
- Aging/peeling off of the coating enhancing the UV-sensitivity of the PMTs ( $-3\%$ )
- Uncertainty in the quantum efficiency of the PMT ( $\pm 5\%-10\%$ )
- Uncertainty in the photoelectron collection efficiency (PCE) of the PMT ( $- 5\%-10\%$ )
- Gain fluctuations and gain drifts of PMTs ( $\pm 10\%$ )
- Uncertainty of the F-factors used to calibrate the recorded signal ( $\pm 10\%$ )
- Different night sky background levels / pedestal subtraction ( $\pm 3\%$ )
- Uncertainties in discriminator threshold settings ( $\pm 5\%-10\%$ )

The overall systematic uncertainty in the energy scale is estimated to be 27%, by assuming Gaussian error propagation. The energy is likely underestimated as most of the effects result in a loss of Cherenkov photons.

The largest uncertainty is caused by unknown atmospheric conditions. A continuous monitoring of the atmosphere with complementary instruments and methods like LIDARs, Bolometers and absolute measurements of the extinction coefficient, would reduce these uncertainties to a few percent. Uncertainties in the reflectivity, optical PSF, transmission of the camera entrance window, etc. can also be reduced with a dedicated monitoring, if possible once per night. A proper simulation/ray tracing of the light catcher and PMT cathode would reduce the corresponding uncertainties to the level of one percent on the expense of a larger computational effort.

With the measurement method that I propose in Appendix B, the uncertainty in the PCE can be reduced to the level of about 2%. The uncertainty of the F-factor method can be avoided using a different calibration method, e.g. the blind pixel method or calibrating with a PiN-diode<sup>6</sup> (Gaug, 2006).

### Effects that result in a distortion of the energy scale

- Gain non-linearities in the PMT
- Non-linearities in the amplifiers
- Non-linearities in the optical transmission (transmitter/reciever)
- Non-linearities in the FADC
- Signal extractor (digital filter) / the assumption of a fixed pulse shape leads to non-linearities especially at the lowest energies (Gaug, 2006).

The last point is dominating the systematic uncertainties especially at lower energies. The overall non-linearity is about 10% estimated from the characteristics of the VCSELs that are used in the optical transmission and contribute most to the nonlinearities. Based on experience with previous Cherenkov telescopes, the impact on the slope of the measured  $\gamma$ -ray spectrum is  $\pm 0.2$ .

### 5.10.2 Effects that Influence the Flux Reconstruction

The measurement of fluxes is subject to features of the detector which are not properly taking care of in the Monte Carlo simulation. Most of the below mentioned effects influence the trigger efficiencies and are strongest at the threshold of the experiment.

- Instable discriminator thresholds
- Temperature dependent signal propagation delays in the trigger logic
- Dead channels
- Gradually increasing light losses mentioned above result in a gradually increasing trigger threshold

Deficiencies can become visible as inhomogeneities in the response of the camera. For energies below 100 GeV, camera inhomogeneities are on the level 10%. Overall deficiencies can in part be estimated using different analysis methods. From the analysis of the Crab nebula (Chapter 6) the overall efficiency below 100 GeV is estimated to be uncertain by about  $\sim 30\%$ . The uncertainties reduce to  $\sim 10\%$  for higher energies.

## 5.11 Performance of the MAGIC Telescope

In the previous sections it was outlined how data recorded with the MAGIC telescope is analyzed. Crucial for the successful operation of any detector is the knowledge of benchmarks that reflect the capabilities of the instrument. For an air shower Cherenkov telescope the most important benchmarks are:

### 1. Sensitivity

---

<sup>6</sup>Positive intrinsic negative [diode]

2. Validity of the Monte Carlo simulations describing the recorded data
3. Stability and reliability of the telescope
4. Angular resolution and energy resolution

A general problem of air shower detectors of cosmic rays is the lack of a calibrated source, which can be used to address aforementioned topics. In particular the energy estimation is mostly dependent on Monte Carlo simulations and is subject to systematic uncertainties that are in the order of  $\sim 30\%$  (see previous section). An absolute calibration of the energy scale of an air Cherenkov telescope is only possible with the availability of a celestial object with an intrinsic line-like feature in its  $\gamma$ -ray spectrum<sup>7</sup>. This feature must be characterized e.g. with a space born detector that was calibrated on Earth. Furthermore, an overlap in the energy range of space and ground based experiments is required as well as a celestial object with a distinct spectral feature in the overlapping energy range. A prime  $\gamma$ -ray candidate for a calibration standard would be a pulsar with a sharp, well measurable cutoff in its  $\gamma$ -ray emission at a few tens of GeV.

Although the proposed method would be the ultimate calibration of the energy scale, the remaining questions of sensitivity, validity of MC, etc. have to be addressed in a different way. In the field of  $\gamma$ -ray astrophysics  $\gtrsim 100$  GeV this is commonly done by comparison with a strong and steady, over a wide range of energies emitting  $\gamma$ -ray point source. The prime candidate in the northern hemisphere and quasi calibration standard is the Crab nebula, the strongest known point source of steady VHE- $\gamma$ -ray emission.

I now discuss the sensitivity of the MAGIC telescope derived from observations of the Crab nebula. Afterwards I compare the distribution of image parameters of  $\gamma$ -rays extracted from data with Monte Carlo simulations. The stability of the telescope and the angular resolution of the telescope are implicitly discussed in Chapter 6. For the subsequent studies I used the same data as in the analysis of the Crab nebula in Chapter 6.

### 5.11.1 Sensitivity of the MAGIC Telescope derived from Observations of the Crab Nebula

The sensitivity describes the minimum flux level of a  $\gamma$ -ray source that can be detected within a unit time window. In the field of IACTs the sensitivity is typically given to be a  $\geq 5\sigma$  excess signal for a 50 hours long observation. The sensitivity for a steady state emitter scales with the square root of the observation time.

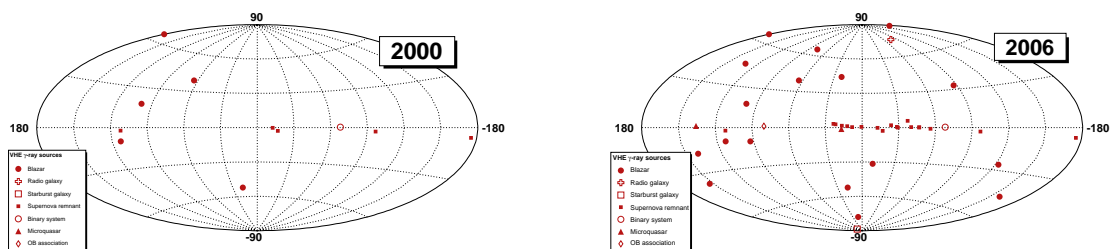


Figure 5.16: Only about 10 VHE  $\gamma$ -ray sources were known in 2000 (left figure). With the new generation of more sensitive IACTs, the number of detected sources increased to more than 40 in 2006 (right panel).

In a qualitative way Figure 5.16 illustrates how the sensitivity has improved from the first generation of imaging air Cherenkov telescopes like HEGRA and Whipple to the existing generation of telescopes such as e.g. MAGIC. VHE- $\gamma$ -ray sources with flux levels of  $\sim 1\%$  relative to the emission of the Crab nebula can be measured in less than 100 hours now. The lower energy threshold

<sup>7</sup>In principle a spectrum with an exponential cutoff could also be used

( $\sim 100$  GeV) of current telescopes is another big advantage to previous experiments, which allows one to study sources with soft spectra.

The sensitivity of IACTs is mostly background limited, influenced by:

- The power to separate  $\gamma$ -ray events from other events in the recorded data
- The acceptance of the detector, expressed in terms of the effective collection area
- The spectral shape of the  $\gamma$ -ray flux observed by an observer on Earth
- The angular resolution achieved in the reconstruction of the  $\gamma$ -ray origin
- Systematic effects that are introduced through instabilities of the detector

In the following I discuss the integral sensitivity of the MAGIC telescope for observations close to zenith.

### Integral Sensitivity

The integral sensitivity is derived by selecting only events above a given energy or as in this case above a certain SIZE-value<sup>8</sup>. The cut in SIZE and HADRONNESS was chosen such that the significance of the extracted signal from the Crab nebula is maximum. The optimization was done on the full Crab data sample taken on Oct. 10th 2005. The best SIZE-cut  $> 400$  phe and HADRONNESS-cut  $< 0.1$  was verified on the Crab data taken three months later on Dec. 31st 2005 and on the full data sample (s. Table 6.2). In addition to the SIZE-cut ( $> 400$  phe), HADRONNESS-cut ( $< 0.1$ ) and spark-cut<sup>9</sup> the following cuts were applied:

$$\begin{aligned}
 &0.4^\circ < \text{DIST} < 1.1^\circ \\
 &|\text{ALPHA}| < 7.5^\circ \\
 &\text{ONLY EVENTS WITHOUT ISLANDS} \\
 &\text{NUMBER OF CORE PIXELS} > 5 \\
 &\text{LEAKAGE} < 0.1 \\
 &\text{ZENITH ANGLE} < 20^\circ
 \end{aligned}$$

The optimal SIZE-cut  $> 400$  phe is a factor of four above the trigger threshold of MAGIC. This reflects the deterioration of the  $\gamma$ /hadron-separation power for lower SIZE, which is also found from simulations (cf. Figure 5.6). With the adopted image cleaning levels of 6 phe for core-pixels and 4 phe for boundary-pixels a SIZE  $> 400$  phe corresponds to a  $\gamma$ -ray energy of  $\gtrsim 250$  GeV.

The |ALPHA|-distribution shown in Figure 5.17 was obtained by applying the cuts to the full data sample. The signal is extracted for  $|\text{ALPHA}| < 7.5^\circ$  and the background is estimated by extrapolation from  $20^\circ < |\text{ALPHA}| < 85^\circ$ . The significance of the excess ( $74.9\sigma$ ) is calculated with Equation 5.12.

One possible way to derive the sensitivity per hour is to divide the significance by the square root of the observation time. For the effective observation time of 15.6 hours, the integral sensitivity  $> 200$  GeV for the Crab nebula emission is  $19.0 \sigma/\sqrt{\text{hr}}$ <sup>10</sup>.

---

<sup>8</sup>It should be pointed out again that the SIZE of an event is strongly correlated with its energy (cf. Figure 4.6)

<sup>9</sup>Spark-events are roundish and comprise only a few pixels. They are most likely caused by electric discharges in the camera.

<sup>10</sup>It should be noted that this is a conservative lower limit because the SIZE dependence of ALPHA is neglected.

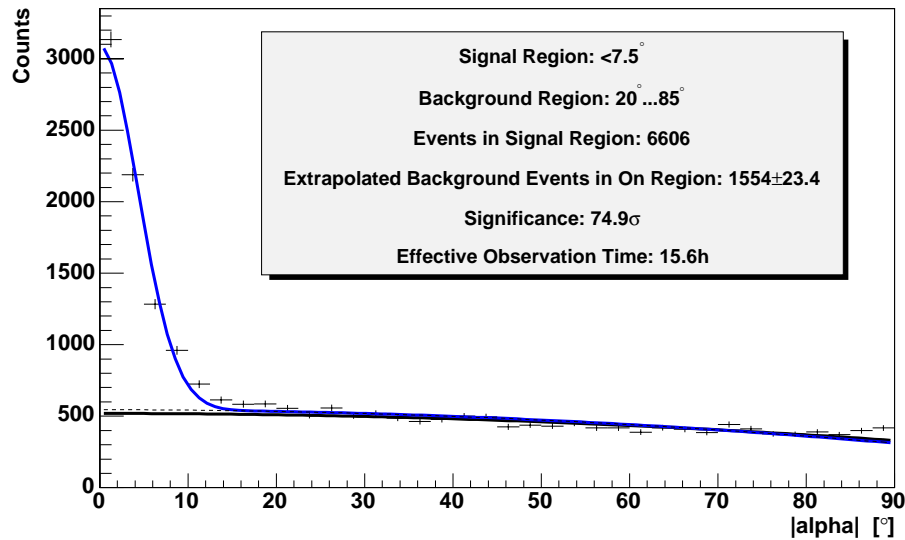


Figure 5.17: Alpha Plot of the total Crab data sample below  $20^\circ$  zenith angle.

Another commonly used way to express the sensitivity of a Cherenkov telescope is to evaluate the minimum flux of a source in units of the Crab nebula flux that can be detected with a  $\geq 5\sigma$  in 50 hours of observation. For this figure of merit the following definition of the significance  $S$  is used

$$S = \frac{N_{\text{Excess}}}{\sqrt{N_{\text{Background}}}} .$$

Applied to the full data sample it is found that a flux of 2.2% Crab can be detected within 50 hours.

### Integral Sensitivity Day by Day

Apart from deriving the sensitivity from the whole data sample it is instructive to calculate the sensitivity on a day by day basis. In this way one can learn something about the stability of the telescope. Table 5.1 gives the day to day sensitivities of the analyzed data sample in  $\sigma/\sqrt{\text{hr}}$  and % Crab (50hrs). In the last row the mean values of each column are quoted with their errors. The numbers in brackets give the root mean square (RMS) of the values of each column. The RMS indicates day by day fluctuations of the sensitivity on the level of 10%.

### Energy Dependency of the Integral Sensitivity

In the previous section the SIZE-cut was chosen that maximizes the significance of the  $\gamma$ -ray signal from the Crab nebula. Lowering the SIZE-cut does not result in a higher significance, because the  $\gamma$ /hadron separation power degrades and the spectral indices of the  $\gamma$ -ray emission and the recorded background are different.

In this context it is necessary to emphasize again that the sensitivity of the detector is tested against a specific source – the Crab nebula. The optimal analysis threshold will be shifted to obtain highest sensitivity for a source with a different spectral shape and absolute flux level. This was demonstrated in the extreme case of a  $\gamma$ -ray source with an exponential cutoff, which was discussed in Section 5.8.4.

The integral sensitivity was calculated for several analysis thresholds. The SIZE-dependent HADRON-NESS-cut (Equation 5.11) was used for  $\gamma$ /hadron separation and the ALPHA-cut was tightened with

	<b>time cleaning 6 4 absolute</b>	
<b>date</b>	<b>Significance</b> [ $\sigma/\sqrt{\text{hr}}$ ]	<b>Sensitivity</b> [% Crab, 50 hrs, $5\sigma$ ]
05.10.2005	18.1	2.4
12.10.2005	19.6	2.1
28.10.2005	19.9	2.1
29.10.2005	19.1	2.2
05.11.2005	19.4	2.2
10.11.2005	21.1	1.8
03.12.2005	23.6	2.0
05.12.2005	16.1	2.7
07.12.2005	18.9	2.2
09.12.2005	18.7	2.2
23.12.2005	19.1	2.3
25.12.2005	17.5	2.3
27.12.2005	18.0	2.3
31.12.2005	18.7	2.1
	$19.1 \pm 0.5$ (1.7)	$2.21 \pm 0.05$ (0.2)

**Table 5.1:** Integral sensitivities ( $> 250$  GeV) derived from the measurement of the Crab nebula; In the last row of the table the average values of each column are given. The numbers in brackets give the RMS of the values in each column.

increasing energy based on the optimal ALPHA-cut shown in Figure 5.9. The integral sensitivity for a 50 hours observations is 7.5% Crab at 110 GeV and continuously improves with the analysis threshold to about 2.2% above  $\sim 300$  GeV. Note that in the calculation of the integral sensitivity  $> 1600$  TeV the background is estimated from only 2 events, which results in an uncertainty of more than 70% on the integral sensitivity.

<b>Energy</b> [GeV]	<b> Alpha </b> <b>Cut</b>	<b>ON</b> <b>Events</b>	<b>OFF</b> <b>Events</b>	<b>Excess</b> <b>Events</b>	<b>Sensitivity</b> [% Crab, 50 hrs, $5\sigma$ ]
$> 110$	$< 10^\circ$	58600	49702	8898	7.5
$> 200$	$< 10^\circ$	11399	4960	6439	3.3
$> 400$	$< 7.5^\circ$	2866	348	2518	2.2
$> 800$	$< 5^\circ$	613	20	593	2.3
$> 1600$	$< 5^\circ$	43	2	41	1.0

**Table 5.2:** Integral sensitivities of the MAGIC telescope on the  $\gamma$ -ray emission of the Crab nebula for several analysis thresholds.

### 5.11.2 Comparison of Monte Carlo Data with real Data

As discussed above the sensitivity of the MAGIC telescope mostly depends on the power to suppress background events while keeping most of the  $\gamma$ -ray events. Monte Carlo simulations play a vital role in the analysis not only in  $\gamma$ /hadron separation but also in the:

- estimation of the energy of a  $\gamma$ -ray
- evaluation of the efficiency of the telescope (effective collection area)

It is evident that the validity of the Monte Carlo has to be checked. Here I restrict myself to the comparison of Monte Carlo simulated  $\gamma$ -rays with real data on the level of image parameters.

For the comparison a time-cleaning with cleaning levels of 6 phe and 4 phe is applied. A loose HADRONNESS-cut  $< 0.8$  rejects obvious background events. In the following the distribution of an image parameter (e.g. WIDTH) of the OFF-source sample is subtracted from the corresponding distribution of the Crab data sample after normalization (ON-OFF). The scaling factor of the OFF data was obtained from the  $|\text{ALPHA}|$  distributions of the ON and the OFF data at large  $|\text{ALPHA}|$  values. The comparison is done in bins of size between 100 phe and  $> 10,000$  phe.

Figures 5.18, 5.19, 5.20 and 5.21 show the comparisons for the image parameters DIST, CONC2, WIDTH and LENGTH respectively. The simulated distributions in blue are normalized to the ON-OFF subtracted distributions, given in black. Within errors the distributions obtained from data match reasonably well with the simulated distributions. Some peculiarities deserve further discussion.

Below SIZE 250 phe a comparison becomes impossible due to the large amount of background and comparative small  $\gamma$ -ray signal. The observed structures in the subtracted distributions at these SIZES are caused by inevitable tiny differences in the ON and OFF data sample, which are “carried” by the background events. As the background is much larger than the excess in the ON data sample the  $\gamma$ -ray signal is not more visible.

For SIZES  $> 2000$  phe a clear disagreement is visible between MC and real data in the image parameters WIDTH and LENGTH. The images of  $\gamma$ -rays are longer and broader in the data compared to the simulated  $\gamma$ -rays. The reason for the disagreement is not known. Possible reasons could be:

- wrongly simulated PSF ( currently a single Gaussian in X and Y )
- improperly simulated aberrations due to frame deformation (coma)
- the diffractive scattering caused by the diamond machined surface structure of the mirrors, which is not simulated

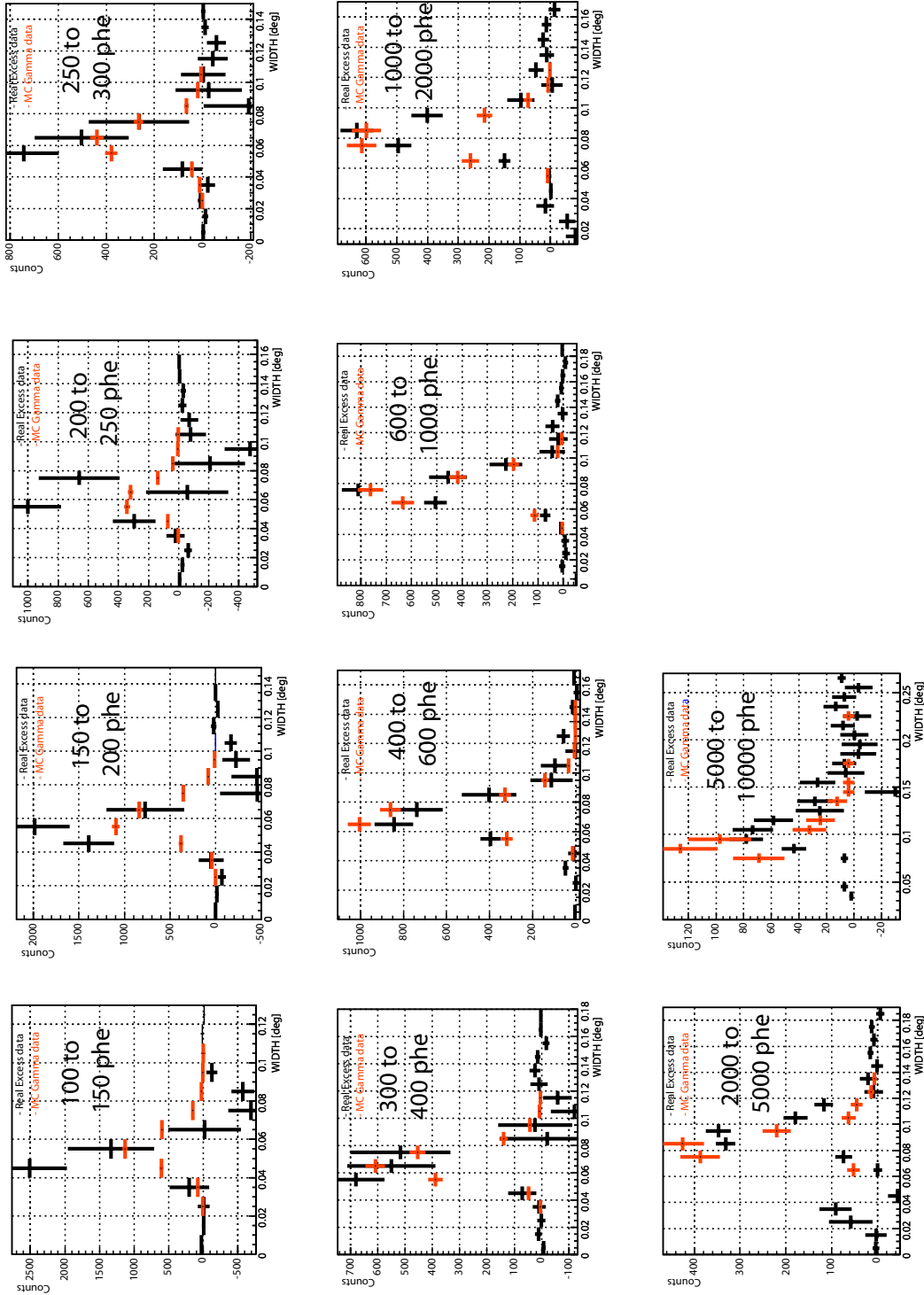


Figure 5.18: MC-Data Comparisons of the WIDTH parameter in bins of SIZE ( 6/4 cleaning)

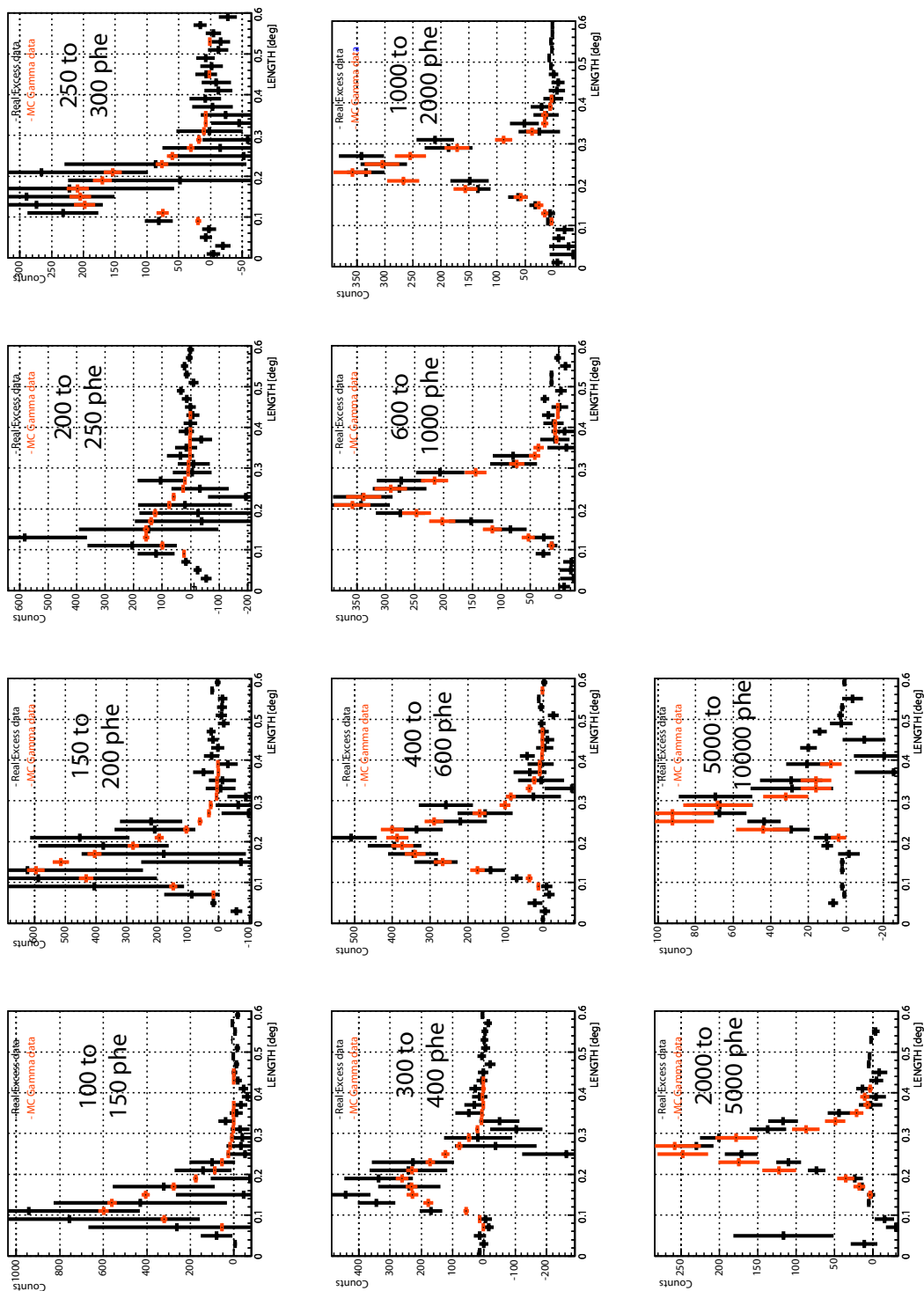


Figure 5.19: MC-Data Comparisons of the LENGTH parameter in bins of SIZE ( 6/4 cleaning)

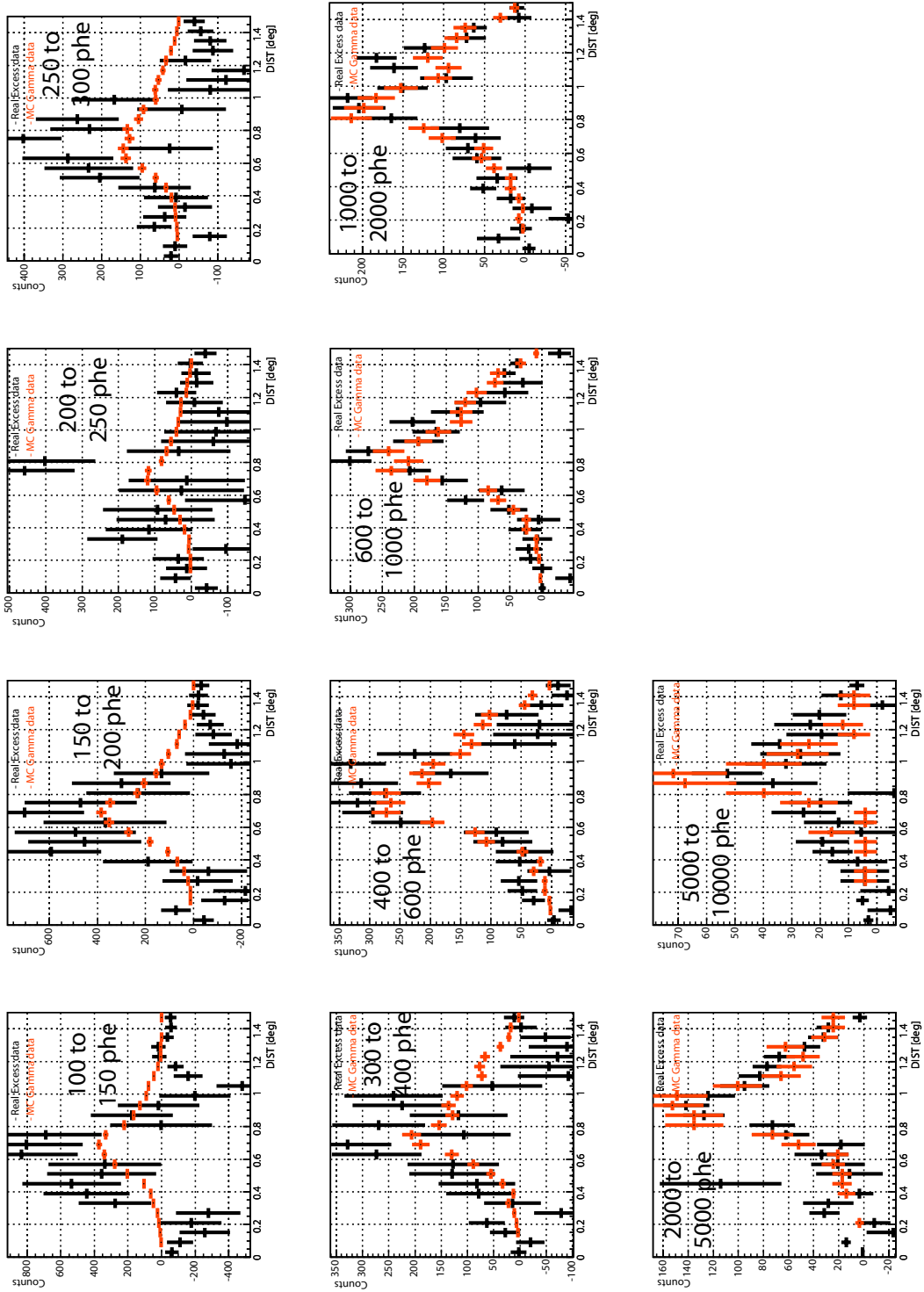


Figure 5.20: MC-Data Comparisons of the DIST parameter in bins of SIZE ( 6/4 cleaning)

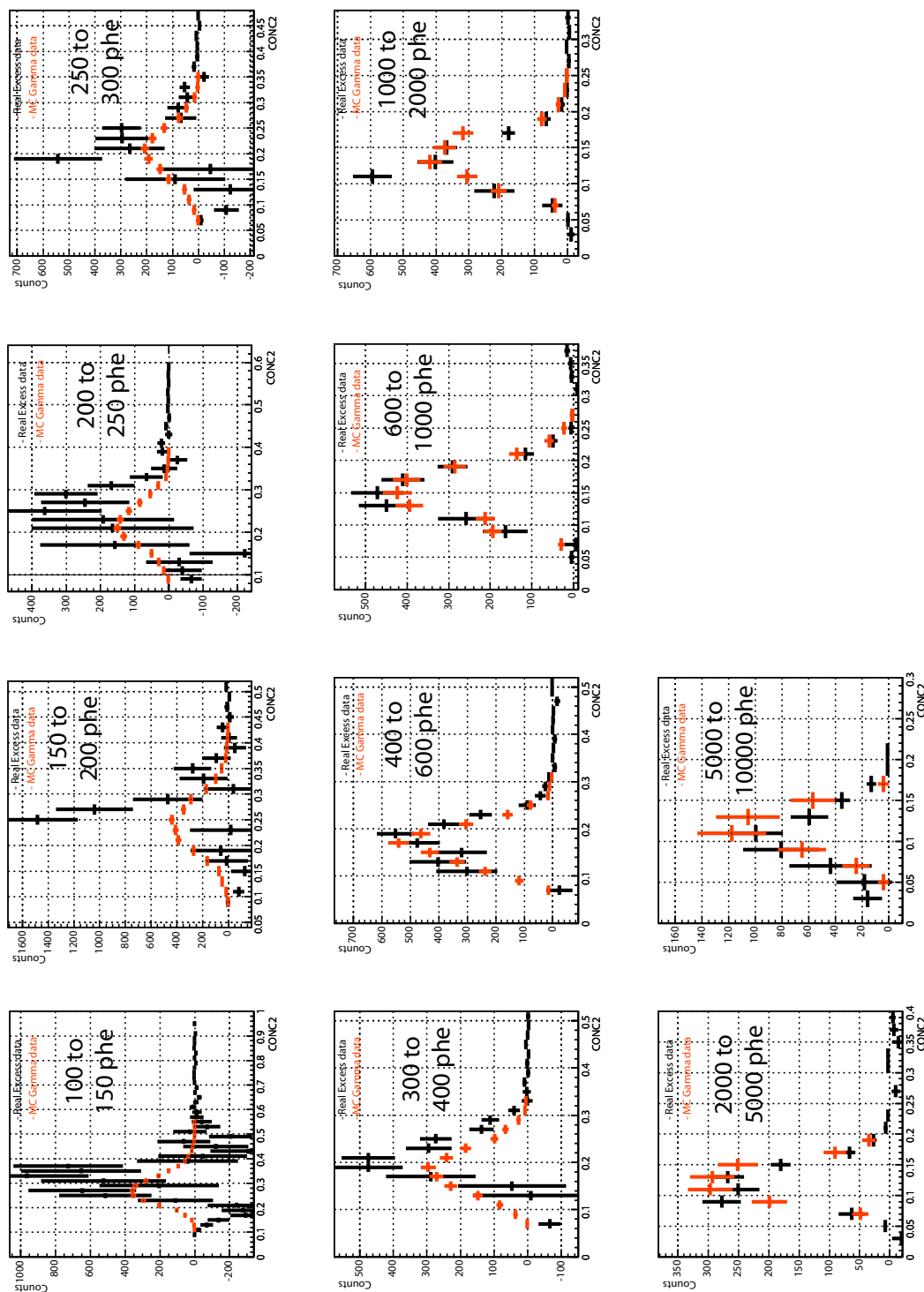


Figure 5.21: MC-Data Comparisons of the CONC2 parameter in bins of Size ( 6/4 cleaning)



## Chapter 6

# The Crab Nebula and Pulsar

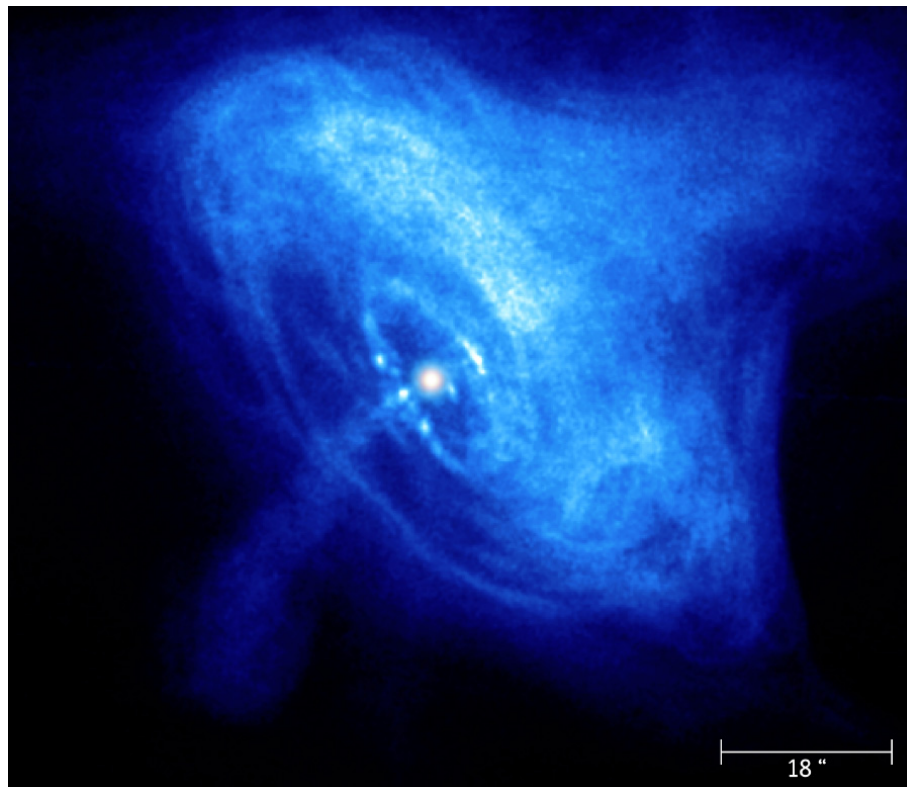


Figure 6.1: Dynamic rings, wisps and jets of electrons and positrons around the pulsar in the Crab Nebula. Observations in X-ray light by Chandra (1999). The inner ring is about one light year across.

### 6.1 Introduction

The Crab nebula and pulsar are leftovers of a supernova explosion of a star with  $8\text{--}10 M_{\odot}$  (e.g. Kitaura et al., 2006) in the constellation of Taurus close to  $\zeta$ -Tauri at a distance of  $\sim 2\text{ kpc}$ . The supernova was noted in the Song dynasty in early 1054 A.D. by Chinese astronomers who called the transient the “Tien-Kwian-guest-star”. According to bequeathed records, the supernova was

visible in daylight for 23 days, and 653 days to the naked eye in the night sky. The event was also observed in Japan, in North America and most likely in Europe too (Collins et al., 1999).

### 6.1.1 The Crab Nebula

The Crab nebula is one of the best studied and brightest objects of non-thermal emission in the Galaxy. The synchrotron emission of the nebula has been detected from radio wavelength throughout GeV- $\gamma$  ray energies (see Figure 3.11). The maximum power of the synchrotron emission is emitted in soft X-Rays. The maximum emitted power of  $10^{37}$  erg s $^{-1}$  corresponds to 10% of the pulsar's spin down luminosity. In 1989 the Crab nebula was the first astrophysical object detected at TeV energies (Weekes et al., 1989). The most commonly accepted explanation for the observed TeV  $\gamma$ -ray emission is inverse Compton upscattering of synchrotron photons by relativistic electrons that are also responsible for the synchrotron emission (Self Synchrotron Compton SSC) (e.g. De Jager and Harding, 1992; Gould, 1965, see also Section 3.5.1).

Since the first detection in TeV  $\gamma$ -rays detailed studies on the emission spectrum between several hundred GeV up to 80 TeV have been carried out (e.g. by Akerlof et al., 1990; Vacanti et al., 1991; Baillon and et al., 1991; Goret et al., 1993; Tanimori et al., 1998; Hillas et al., 1998; Amenomori et al., 1999; de Naurois et al., 2002; Majumdar et al., 2002; Aharonian et al., 2004, 2006a). The peak of the IC emission is expected between 10 GeV and  $\sim 400$  GeV. In this range observations are sparse. The STACEE collaboration reported an integral flux measurement above  $190 \pm 60$  GeV (Oser et al., 2001) and CELESTE with its lower threshold measured the integral  $\gamma$ -ray flux of the Crab nebula above 60 GeV (de Naurois et al., 2002).

### 6.1.2 The Crab Pulsar PSR B0531+21

The pulsar PSR B0531+21 was discovered in the Crab nebula by astronomers of the Arecibo Observatory 300-meter radio telescope in Puerto Rico on November 9, 1968 (Staelin and Reifenstein, 1968). The pulsar was the first one detected in the optical part of the spectrum by Cocke et al. (1969). In the visible light, the pulsar luminosity is of 16th apparent magnitude, which roughly corresponds to an absolute magnitude of +4.5 mag. This is about the same luminosity as that of the sun in the visible part of the spectrum! Some parameters of the pulsar are listed in Table 6.1. EGRET detected the Crab pulsar in  $\gamma$ -rays up to energies of 10 GeV with an indication of a cutoff in the spectrum in the highest energy bin at 6 GeV (Nolan et al., 1993; Fierro et al., 1998). Observations from ground at higher energies failed to detect pulsed emission despite various efforts (see e.g. Musquere, 1999; Lessard et al., 2000; de Naurois et al., 2002; Aharonian et al., 2004).

Table 6.1: Parameters of PSR B0531+21 (Manchester et al., 2005).

Parameter	Value
spin-down age	1240 years
surface magnetic flux density	$3.78 \cdot 10^{12}$ Gauss
spin-down luminosity	$4.6 \cdot 10^{38}$ erg/s
Energy flux at the sun	$1.2 \cdot 10^{38}$ erg/kpc $^2$ /s

### 6.1.3 Objectives of the Analysis

With its low energy threshold and high sensitivity, MAGIC is currently the only operating experiment that is able to measure the  $\gamma$ -ray emission of the Crab nebula down to 100 GeV and with

reduced sensitivity between 60 GeV and 100 GeV. Thus, for the first time, the Crab nebula can be measured with very high precision in the VHE-regime below 400 GeV.

Main objectives of the analysis:

- reconstruction of the IC  $\gamma$ -ray emission to the lowest accessible energies ( $\sim 60$  GeV)
- search for a possible variability in the  $\gamma$ -ray emission of the nebula on different times scales (months, weeks, days and minutes)
- search for an extended morphology of the  $\gamma$ -ray emission region at different energies
- detection of the pulsar in optical with the central pixel of the MAGIC camera; measurement of the phase difference between the position of the main peak in optical and radio wavelengths.
- search for pulsed  $\gamma$ -ray emission from the pulsar.

## 6.2 The Data Sample and related Information

In this section I describe the data sample and give the ephemerides used in the pulsed analysis.

### 6.2.1 Selection Criteria applied to the Data Sample

The following selection criteria were applied to the data aiming for the lowest possible analysis threshold:

**Zenith angle range:** Only data runs taken at zenith angles  $\lesssim 20^\circ$  were accepted for the analysis.

**Extinction coefficient:** A night on La Palma is considered good for photometry in “optical” astronomy if the average nightly extinction coefficient (EC) is less than 0.09 mag and varies less than 0.06 mag during the whole night. In the selected data sample the largest EC is 0.21 mag (cf. Table 6.2), which compared to an EC of 0.09 mag results in additional light transmission losses of about 10%. Losses of about 10% are acceptable and well in the range of the systematic uncertainties (cf. Section 5.10).

Runs affected by technical problems and bad weather were excluded. Nights with trigger rates fluctuating by more than 10% were also rejected. Table 6.2 lists the nights that survived all selection criteria. The second column of the table shows the nightly averaged event rate after applied image cleaning (cleaning levels of 6 and 4 photoelectrons). The third column shows the event rate after an additional cut in  $\text{SIZE} > 100$  photoelectrons and a filter cut to remove “spark events”<sup>1</sup>.

In total, data from 14 nights distributed over three months have been selected for the analysis. The total observation time amounts to 955 minutes or 16 hours. The data was obtained by directly pointing the MAGIC telescope to the position of the Crab pulsar (ON/OFF mode). The background is estimated from 19 hours of OFF-data. A  $\gamma$ -ray signal was detected with a significance of  $75\sigma$  and detailed performance studies of the telescope were done (see Section 5.11).

<sup>1</sup>These are events most likely produced by discharges close to the photocathodes.

Table 6.2: Some parameters of the selected data. The extinction coefficients for an effective photon wavelength of 625 nm are from public data available from the Carlsberg Meridian Telescope.

Date	Rates [Hz]	R. a. C. [Hz]	On Time [min]	Zd-Range [°]	Ext. Coef. [mag]	Sc. Ext. Coef. [mag]
05.10.2005	220	130	73	7...23	0.117	0.017
12.10.2005	170	115	100	7...19	0.122	0.025
28.10.2005	180	122	105	7...23	0.103	0.006
29.10.2005	160	105	61	8...20	0.101	0.010
05.11.2005	150	115	51	7...20	0.103	0.030
10.11.2005	130	95	50	7...20	0.212	0.093
03.12.2005	140	98	53	7...11	0.168	0.110
05.12.2005	140	105	48	7...10	0.104	0.007
07.12.2005	140	105	48	7...10	0.112	0.010
09.12.2005	150	108	50	7...14	0.138	0.020
23.12.2005	130	92	44	7...13	n.a	n.a.
25.12.2005	130	97	61	7...13	0.109	0.007
27.12.2005	140	100	107	7...14	0.101	0.010
31.12.2005	120	92	104	7...15	0.199	0.078
total observation time: 955 min						

## 6.2.2 Radio Ephemeris of the Crab Pulsar

The search for pulsed emission requires precise timing parameters of the Crab pulsar (cf. Section 5.8). Irregularities in the timing of the Crab pulsar requires a monthly update of the ephemeris. This service is provided by the pulsar group of the Jodrell Bank observatory, which monitors the Crab pulsar on a daily basis and releases updated ephemeris every month (Jodrell Bank Radio Telescope, 2006). The ephemerides of the Crab pulsar relevant for the analysis are listed in Table 6.3.

Table 6.3: Ephemerides of the Crab pulsar provided by the Jodrell Bank Radio Telescope (2006) relevant for the analysis. MJD is the reference day of the ephemeris and  $t$  is the time of appearance of the first main pulse after midnight on the reference day.

MJD	$t$ [sec]	Frequency ( $\nu$ ) [Hz]	Derivative ( $\dot{\nu}$ ) [ $10^{-15}$ Hz/s]
53597	0.029626	29.7798524524	-372992.36
53628	0.031767	29.7788534525	-372972.07
53658	0.022656	29.7778867428	-372950.45
53689	0.016803	29.7768878849	-372924.54
53719	0.026788	29.7759213143	-372886.52
53750	0.020341	29.7749226318	-372854.62
53781	0.006520	29.7739240139	-372823.70

## 6.3 Analysis of the $\gamma$ -Ray Emission from the Crab Nebula between 60 GeV and 9 TeV

In this section I present the analysis of the steady  $\gamma$ -ray emission from the Crab nebula above 60 GeV. In subsection 6.3.1 I discuss the energy spectrum. Time resolved measurements are presented in subsection 6.3.2. A study of the source morphology is discussed in subsection 6.3.3.

### 6.3.1 The Energy Spectrum

For the computation of the energy spectrum the data were processed in the following way:

- image cleaning with the time-cleaning algorithm (cf. Section 5.2.2) and cleaning levels of 6 and 4 phe for core- and boundary-pixels. The “time” coincidence parameters were set to  $\pm 3.3$  nsec.
- A minimum SIZE-cut  $> 100$  phe and minimum number of core-pixel-cut  $> 5$  strongly reduces differences between data and MC close to the threshold of the experiment.
- A SIZE-dependent upper DIST-cut was applied to reject events whose energy cannot be well reconstructed. The cut parameterization was found from Monte Carlo simulations, requesting that 75% of the  $\gamma$ -rays are kept. For the same reason of energy reconstruction a lower static DIST-cut of  $0.3^\circ$  was applied too.
- The HADRONNESS-cut was found from Monte Carlo simulations requesting that 90% of the  $\gamma$ -rays are kept.
- In an analogous manner the signal region in the |ALPHA| distributions (cf. Section 5.5) was found by means of Monte Carlo simulated  $\gamma$ -rays. The selected |ALPHA|-cuts retains 90% of the simulated  $\gamma$ -rays.

The cuts in |ALPHA| and HADRONNESS keep as many  $\gamma$ -rays as possible (“loose cuts”). This is in contrary to the cuts derived in Section 5.4.1 and Section 5.5.1, which aim for highest sensitivity. Loose cuts aim for a reduction of systematic effects due to MC-uncertainties, caused by e.g. the disagreement between real data and MC in some image parameters (see Section 5.11.2).

Figure 6.2 shows the differential energy spectrum after unfolding with the method by Bertero (1989). The differential flux for each energy point is quoted in Table 6.4. The influence of different core-pixel cuts, DIST-cuts and unfolding methods on the spectrum is shown by the yellow band. Apparent is the broadening to  $\pm 40\%$  below 100 GeV, due to the degradation of  $\gamma$ /hadron-separation (cf. Figure 5.6). The effect is illustrated by the |ALPHA|-distribution shown in Figure 6.3 for events with estimated energies between 80 GeV and 100 GeV. A small but nevertheless significant excess is visible on top of a huge background. The systematic error on the flux points in Table 6.4 was estimated assuming a 27% uncertainty on the energy scale and from the systematic uncertainties obtained from different analysis (yellow band in Figure 6.2).

The spectrum is parameterized with a power-law and a variable/curved power-law ansatz. The fit takes correlations between the spectral points into account, which are introduced in the unfolding procedure. A correlated fit with a power-law

$$\frac{dF}{dE} = f_0 \cdot \left( \frac{E}{300 \text{ GeV}} \right)^\Gamma, \quad (6.1)$$

provides a flux normalization  $f_0$  of  $(5.7 \pm 0.2_{\text{stat}}) \times 10^{-10} \text{ cm}^{-2} \text{ s}^{-1} \text{ TeV}^{-1}$  and a spectral index  $\Gamma$  of  $-2.48 \pm 0.03_{\text{stat}} \pm 0.2_{\text{syst}}$ . The  $\chi^2$  of the fit is 24 for 8 degrees of freedom, which disfavors a pure power-law behavior.

Table 6.4: Mean energy and differential flux of the spectral points shown in Figure 6.2.

<b>Mean Energy</b> [GeV]	<b>Differential Flux</b> [cm <sup>-2</sup> s <sup>-1</sup> TeV <sup>-1</sup> ]
77	$(1.14 \pm 0.27_{\text{stat}} \pm 0.70_{\text{syst}})10^{-8}$
127	$(3.65 \pm 0.38_{\text{stat}} \pm 2.15_{\text{syst}})10^{-9}$
210	$(1.41 \pm 0.09_{\text{stat}} \pm 0.88_{\text{syst}})10^{-9}$
346	$(4.37 \pm 0.23_{\text{stat}} \pm 2.9_{\text{syst}})10^{-10}$
570	$(1.32 \pm 0.07_{\text{stat}} \pm 0.90_{\text{syst}})10^{-10}$
940	$(3.55 \pm 0.23_{\text{stat}} \pm 2.45_{\text{syst}})10^{-11}$
1550	$(9.88 \pm 0.74_{\text{stat}} \pm 7.11_{\text{syst}})10^{-12}$
2554	$(2.69 \pm 0.29_{\text{stat}} \pm 2.01_{\text{syst}})10^{-12}$
4212	$(6.8 \pm 1.1_{\text{stat}} \pm 5.3_{\text{syst}})10^{-13}$
6943	$(1.15 \pm 0.53_{\text{stat}} \pm 0.93_{\text{syst}})10^{-13}$

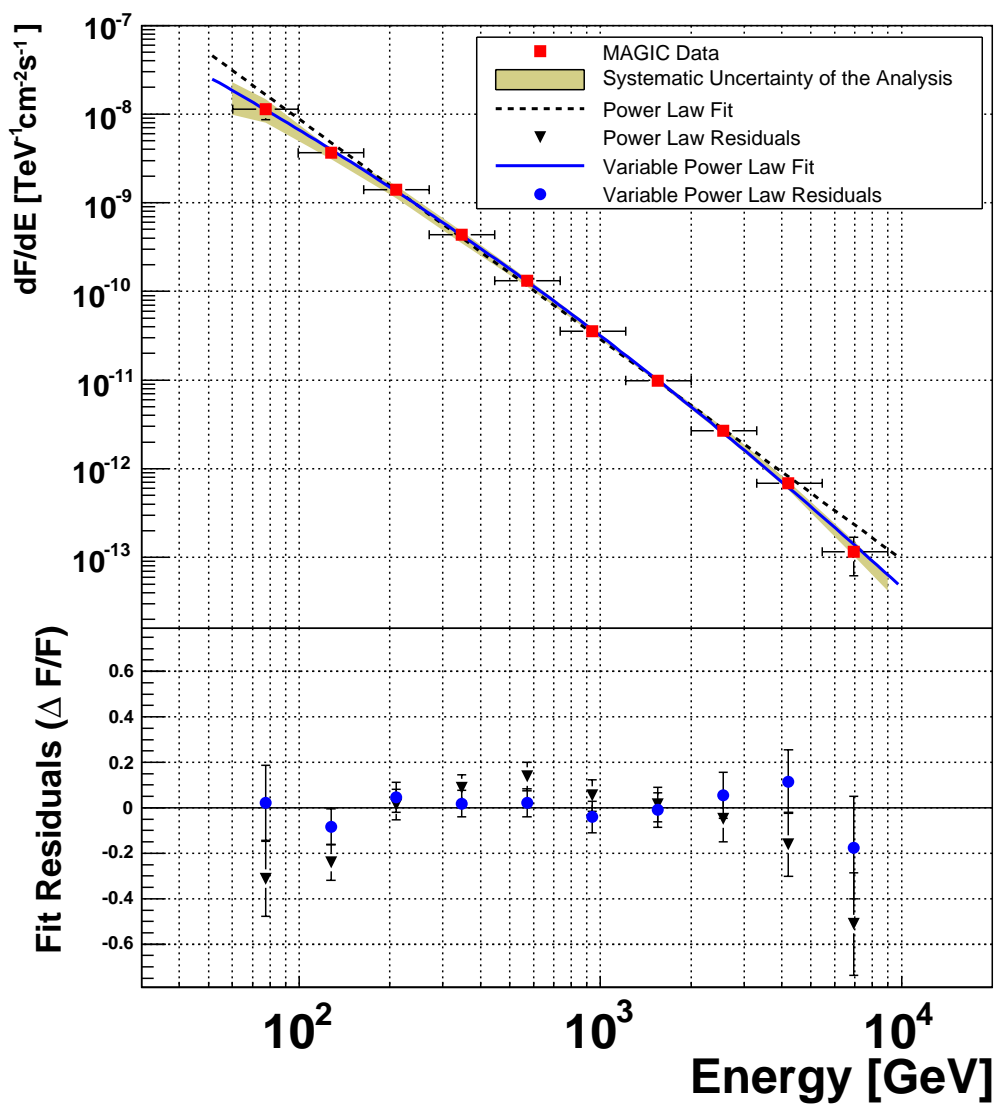


Figure 6.2: Differential energy spectrum of the Crab nebula between 60 GeV and 9 TeV. The spectrum was unfolded with the method by Bertero (1989). The upper part in the figure shows in addition to the unfolded data points also results of a power-law fit and a variable power-law fit. The lower panel shows the relative residuals between the fit results and the data points. A parameterization of the spectrum with a curved power-law is favored.

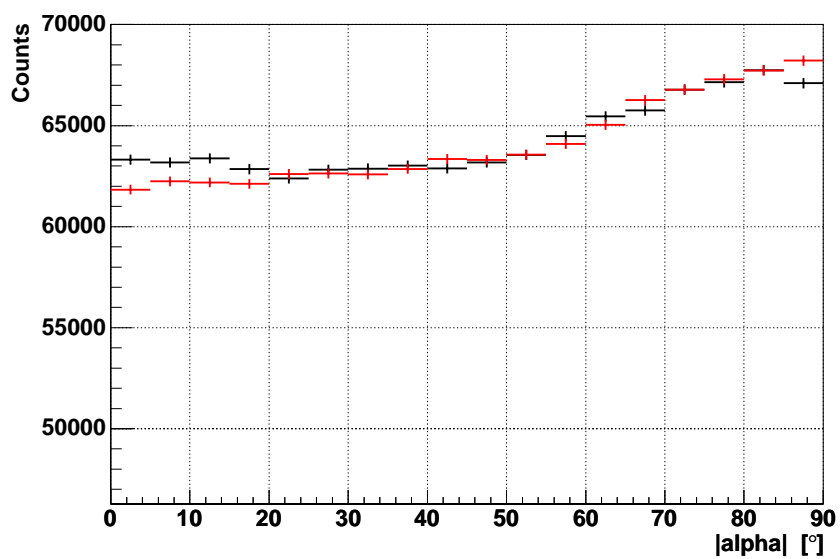


Figure 6.3:  $|\text{ALPHA}|$ -distribution for events with estimated energy between 80 GeV and 100 GeV. ON Events:  $292721 \pm 503$ , normalized OFF Events;  $248380 \pm 602$ , Excess Events;  $4341 \pm 784$ , Significance: 5.53, effective ontime: 58000 sec. Applied  $|\text{ALPHA}|$ -cut to extract the  $\gamma$ -ray signal  $< 20^\circ$ . The excess rate is  $4.5\gamma$ -rays per minute.

The data is better described with a variable power-law fit

$$\frac{dF}{dE} = f_0 \cdot \left( \frac{E}{300 \text{ GeV}} \right)^{(a+b \log(E/300 \text{ GeV}))} \quad (6.2)$$

with a flux normalization  $f_0$  of  $(6.0 \pm 0.2_{\text{stat}}) \times 10^{-10} \text{ cm}^{-2} \text{ s}^{-1} \text{ TeV}^{-1}$ ,  $a = -2.31 \pm 0.06_{\text{stat}} \pm 0.2_{\text{syst}}$  and  $b = -0.26 \pm 0.07_{\text{stat}}$ . The  $\chi^2$  of the fit is 8 for 7 degrees of freedom.

Figure 6.4 shows the same spectral points (filled blue circles) but multiplied by the energy squared so-called spectral energy density (SED). The Figure also shows data of  $\gamma$ -ray measurements of the nebula by other experiments. At energies  $> 500 \text{ GeV}$  the derived SED is in agreement with measurements by other air Cherenkov telescopes like Cangaroo (Tanimori et al., 1998), Hegra (Aharonian et al., 2004), H.E.S.S. (Aharonian et al., 2006a) or Whipple (Hillas et al., 1998). Striking is the difference with the result of the Tibet experiment (Amenomori et al., 1999), which uses a different experimental technique and is thus subject to different systematic uncertainties. Note also the large uncertainty on the spectral point measured by de Naurois et al. (2002).

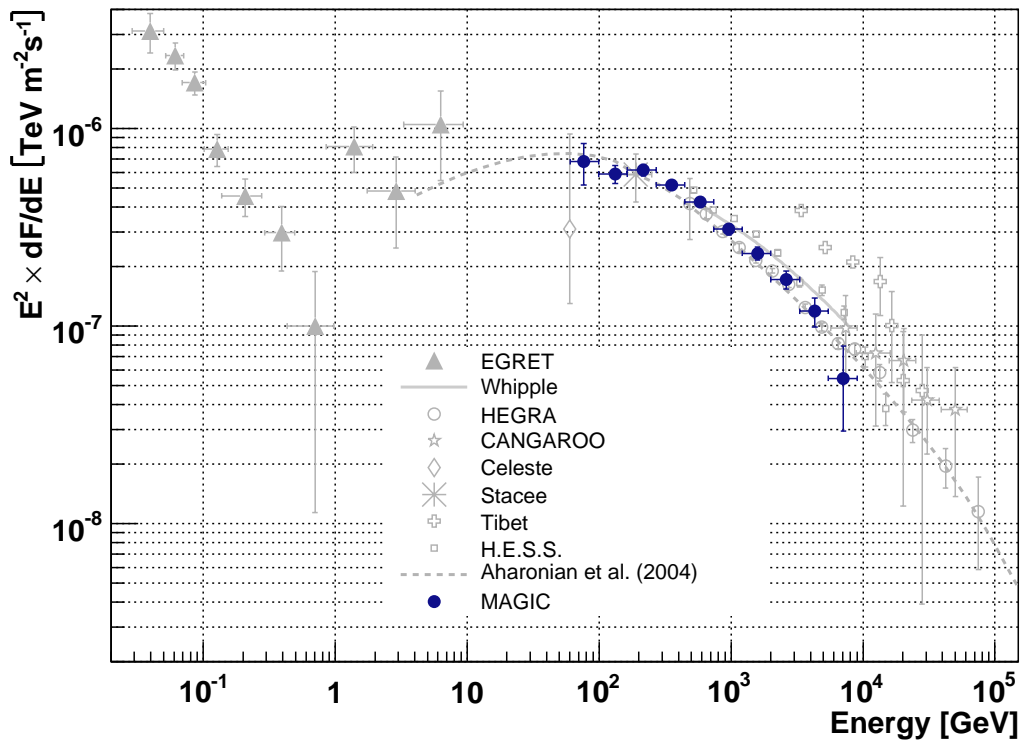


Figure 6.4: Compilation of different  $\gamma$ -ray measurements and one model of the Crab nebula. See text for discussion.

Above 1 TeV up to about 10 TeV the expected and measured energy spectrum is well described by a power-law behavior. Going to lower energies one expects a continuous hardening of the spectrum. However, this could not be demonstrated by earlier measurements. The change of the slope of the spectrum (spectral index)  $\Gamma'$  was tested for various points of the measured spectrum.  $\Gamma'$  is (see

also Equation 6.1).

$$\Gamma'(E) = \frac{d \ln(F)}{d \ln(E)} \approx \frac{\ln F_i - \ln F_j}{\ln E_i - \ln E_j} \quad (6.3)$$

$$E = \exp \left[ 0.5(\ln E_i + \ln E_j) \right], \quad (6.4)$$

where  $F_{i,j}$  is the differential flux measured at  $E_{i,j}$ . The four derived spectral indices at  $\sim 150$  GeV,  $\sim 300$  GeV,  $\sim 1$  TeV and  $\sim 2.5$  TeV shown in Figure 6.5 indicate a clear softening of the spectrum with increasing energy. The spectral index  $\Gamma'$  was also derived from the aforementioned results of the variable power-law fit<sup>2</sup>,

$$\Gamma' = a + 2b \log(E/300 \text{ GeV}) \quad (6.5)$$

and is shown by the solid black curve and the  $1\sigma$ -confidence interval by the dashed black curves. Within uncertainties the measured spectral index changes as predicted by Aharonian et al. (2004) (blue curve), who explain the VHE  $\gamma$ -ray emission as IC-scattering of relativistic electrons on several soft photon fields (synchrotron photons, mm-photons, CMB and far IR photons from dust and stars).

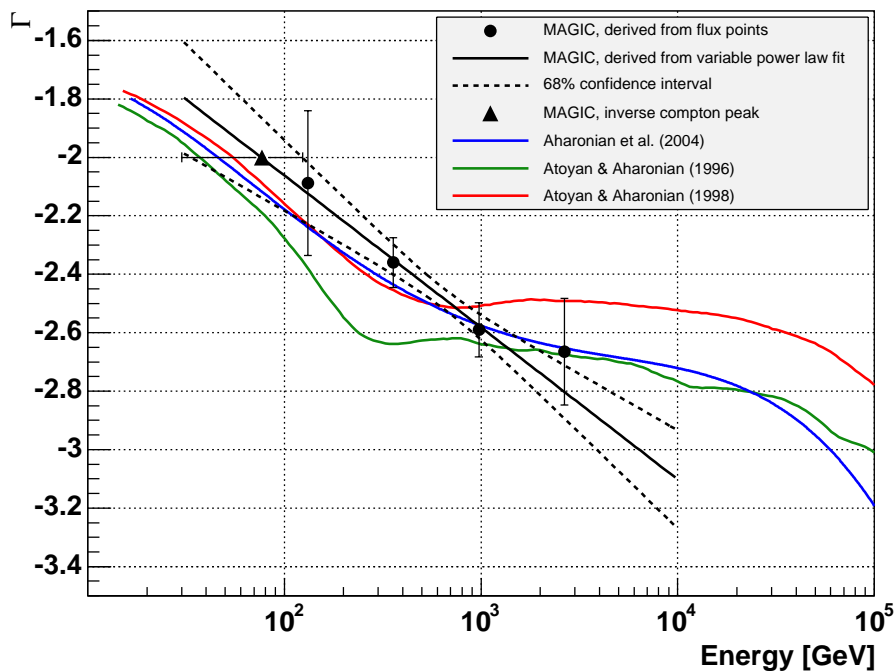


Figure 6.5: Measured spectral index derived from differential flux points (dots) and derived from the variable power-law fit (black solid line, the dashed line gives the  $1\sigma$  confidence interval); also shown are predictions by Aharonian et al. (2004) (blue curve), Atoyan and Aharonian (1996b) (green curve) and Aharonian and Atoyan (1998) (red curve).

EGRET observed at GeV energies a  $\gamma$ -ray flux a factor five above the flux predicted by the SSC-mechanism (De Jager et al., 1996). Atoyan and Aharonian (1996b) explain this  $\gamma$ -ray excess by an additional  $\gamma$ -ray component from Bremsstrahlung of electrons that are partially captured in filaments of the nebula. Such an extra component can significantly change the spectral slope at several hundred GeV compared to a pure IC-scenario (cf. blue and red curves in Figure 6.5), and

<sup>2</sup>Note that  $\Gamma'$  is not equivalent to the exponent of the variable power law. However in a pure power-law  $\Gamma'$  is equivalent to  $\Gamma$ .

results in an almost pure power-law behavior of the energy spectrum between  $\sim 100$  GeV and 10 TeV (constant  $\Gamma$ ). At 300 GeV, where the measurement is most sensitive, the measured slope (black curve and data point) is considerably harder than predicted by Atoyan and Aharonian (1996b). It is, therefore, unlikely that the  $\gamma$ -ray excess at GeV energies can be explained by Bremsstrahlung as proposed. Later predictions by Aharonian and Atoyan (1998) that also include the mentioned Bremsstrahlung mechanism, are in agreement with the presented measurement (red curve). In the prediction by Aharonian and Atoyan (1998) also a  $\gamma$ -ray component from  $\pi^0$ -decay is included, which results in a considerable harder spectrum above a few TeV compared to the pure IC-scenario (cf. Figure 6.5). However, given the limited statistics above 1 TeV one cannot exclude any prediction from the measurement.

The predicted GeV  $\gamma$ -ray emission has a peak in the SED-representation (see Figure 6.4). If one assumes that the energy spectrum around the peak can be described with a curved power-law, the position of the peak can be determined from the measurement of the spectral index obtained from the result of the curved power-law fit. A necessary condition for the peak in the SED is that the spectral index  $\Gamma'$  is -2. Using this condition in Equation 6.5, the peak is determined at  $77 \pm 47_{\text{stat}}^{+107} {}_{-46}^{\text{syst}}$  GeV (triangle in Figure 6.5)<sup>3</sup>. This is the first determination of the IC-peak.

### 6.3.2 Search for Flux Variabilities

In the community it is declared that the Crab is a constant and stable  $\gamma$ -ray source and can therefore be used as a quasi calibration standard. However, with more sensitive measurements it is required to check the stability of the  $\gamma$ -ray source.

Here I present a time-resolved measurement of the  $\gamma$ -ray flux, i.e. the light curve of the VHE  $\gamma$ -ray emission from the Crab nebula. Depending on the source strength and the analysis threshold, the time intervals can be as short as a few minutes. The extracted  $\gamma$ -ray signal is converted to flux by normalizing the  $\gamma$ -ray excess to the average effective collection area and the effective observation time.

I have calculated light curves in bins of 10 minutes from events with energies above 200 GeV. The light curves of all 14 nights are shown in Figure 6.6. Note that loose cuts are used for  $\gamma$ /hadron-separation, which reduces the sensitivity of the measurement. The probability that the light curve is described with a constant flux level is  $> 10\%$  in all except the first night where the fit probability is 0.8%. The average statistical uncertainty of the flux measurement per ten minute bin is  $\sim 20\%$ . Figure 6.7 shows the average flux of each night. The dashed line in the Figure denotes the average flux of all nights  $F_{>200 \text{ GeV}}$  and the shaded region is its statistical uncertainty:

$$F_{>200 \text{ GeV}} = (1.96 \pm 0.05_{\text{stat}}) \times 10^{-10} \text{ cm}^{-2} \text{ sec}^{-1} \quad . \quad (6.6)$$

The probability is 67% that the measured daily flux values are compatible with a constant flux. It can be concluded that, within statistical uncertainties, the reconstructed flux of the Crab nebula was constant over the entire observation period.

### 6.3.3 Morphology of the $\gamma$ -Ray Emission Region

The morphology of the  $\gamma$ -ray emission region was studied by generating skymaps in three energy bins above 100 GeV. The determination of the origin of an event was done by using the DISP-method (cf. Section 5.6). For the results presented here the following parameterization of DISP was used:

$$\text{DISP} = a(\text{SIZE}) + b(\text{SIZE}) \cdot \frac{\text{WIDTH}}{\text{LENGTH}} \quad , \quad (6.7)$$

<sup>3</sup>The systematic error is estimated from the systematic uncertainty on the spectral index, which is 0.2 (cf. Section 5.10)

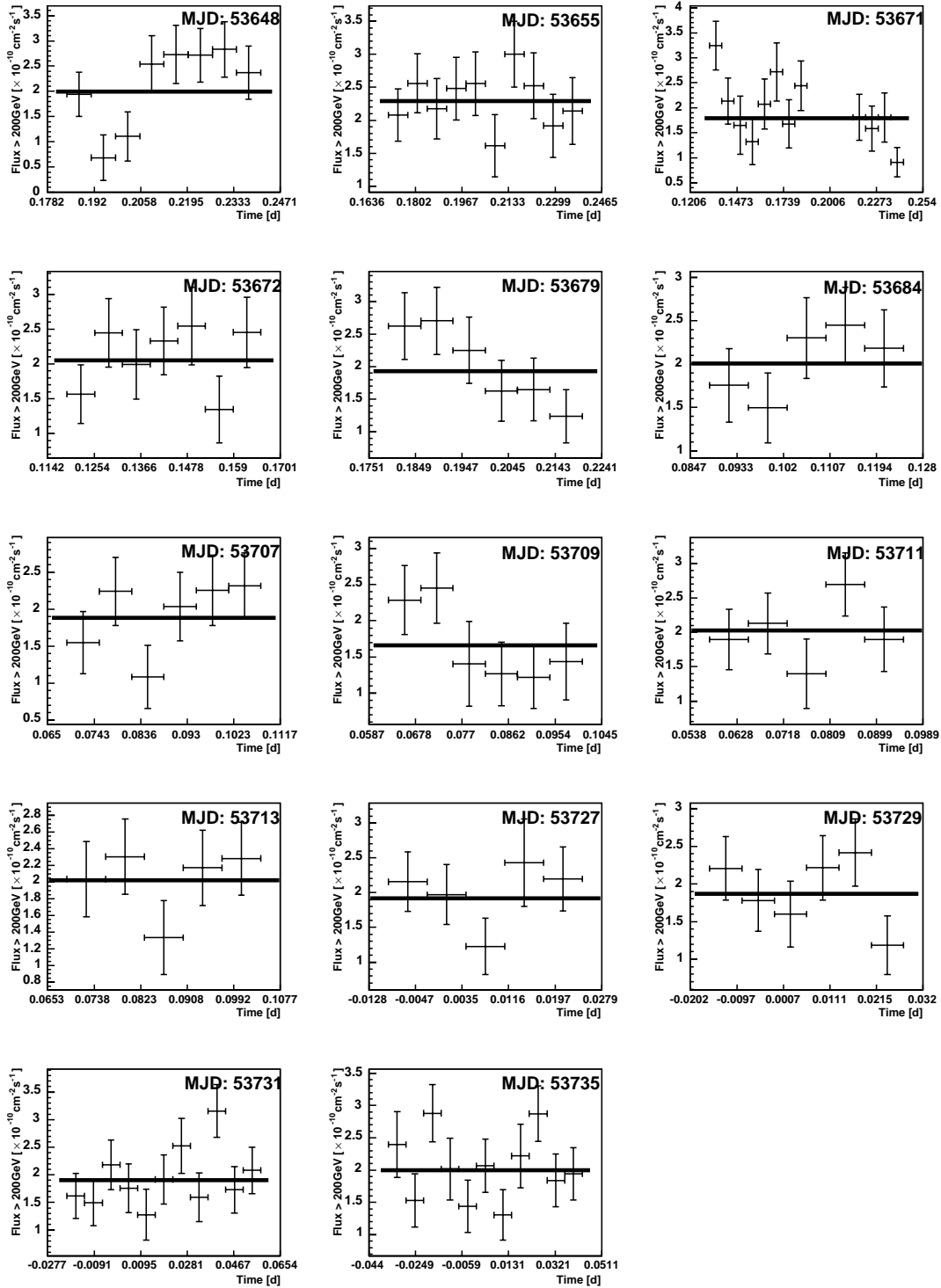


Figure 6.6: Light curves of the integral flux above 200 GeV from the Crab nebula for each of the 14 nights in a binning of 10 minutes. The black horizontal line in each light curve is the result of a fit of the light curve, assuming a constant  $\gamma$ -ray emission.

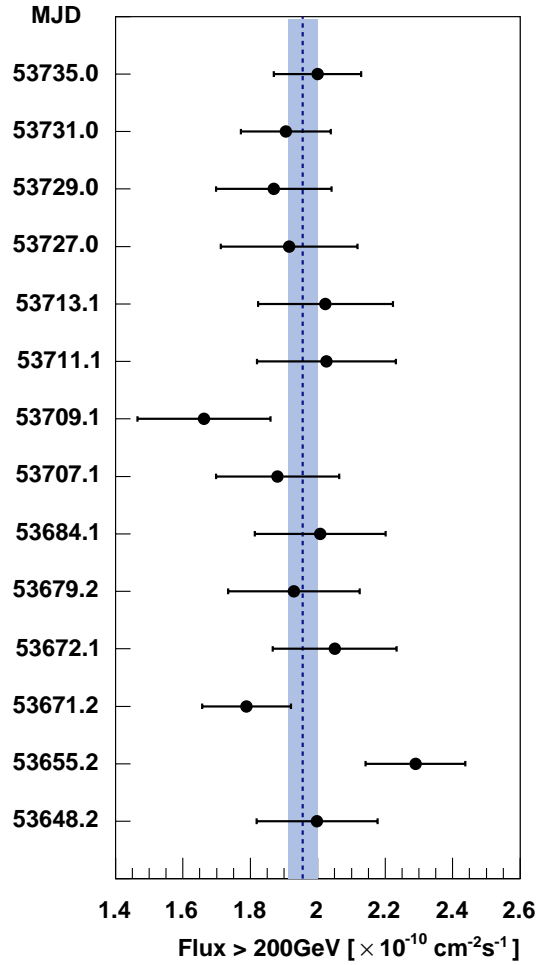


Figure 6.7: Average flux above 200 GeV of each observed night. The dashed blue line gives the average flux of all nights and the blue shaded region the statistical uncertainty of the average flux.

where  $a$  and  $b$  are second order polynomials found by fitting Monte Carlo simulated  $\gamma$ -ray showers (Domingo-Santamaria et al., 2005). Strong tail cuts of 10 and 8 photoelectrons were used in the image cleaning and a tight HADRONNESS-cut  $< 0.1$  was applied, providing a pure sample of  $\gamma$ -rays.

The reconstructed event origins were corrected for possible mispointing by using the information from the starguider camera (Wagner, 2006). Afterwards, 2D-histograms with bin sizes of  $(0.057^\circ \times 0.057^\circ)$  were filled with the corrected event origins (events with energies  $< 500$  GeV). For the skymap of the events with energies  $> 500$  GeV a four times finer binning was chosen than in the other skymaps. The OFF-skymap was subtracted from the ON-skymap. Both maps were normalized to each other at a radial distance between  $0.9^\circ$  and  $1.6^\circ$  from the center of the camera. Figure 6.8 shows the background-subtracted skymaps of excess events from the Crab nebula for  $\gamma$ -ray energies  $\sim 160$  GeV,  $\sim 250$  GeV and  $> 500$  GeV.

### Center of Gravity of the Emission Region

The center of gravity (cog) of the  $\gamma$ -ray emission was derived from the skymaps of excess events shown in Figure 6.8, by fitting them with a 2D-Gaussian of the form

$$F(x, y) = F_{\text{res}} + a \cdot \exp \left[ -\frac{(x - \bar{x})^2 + (y - \bar{y})^2}{2\sigma_{\text{data}}^2} \right], \quad (6.8)$$

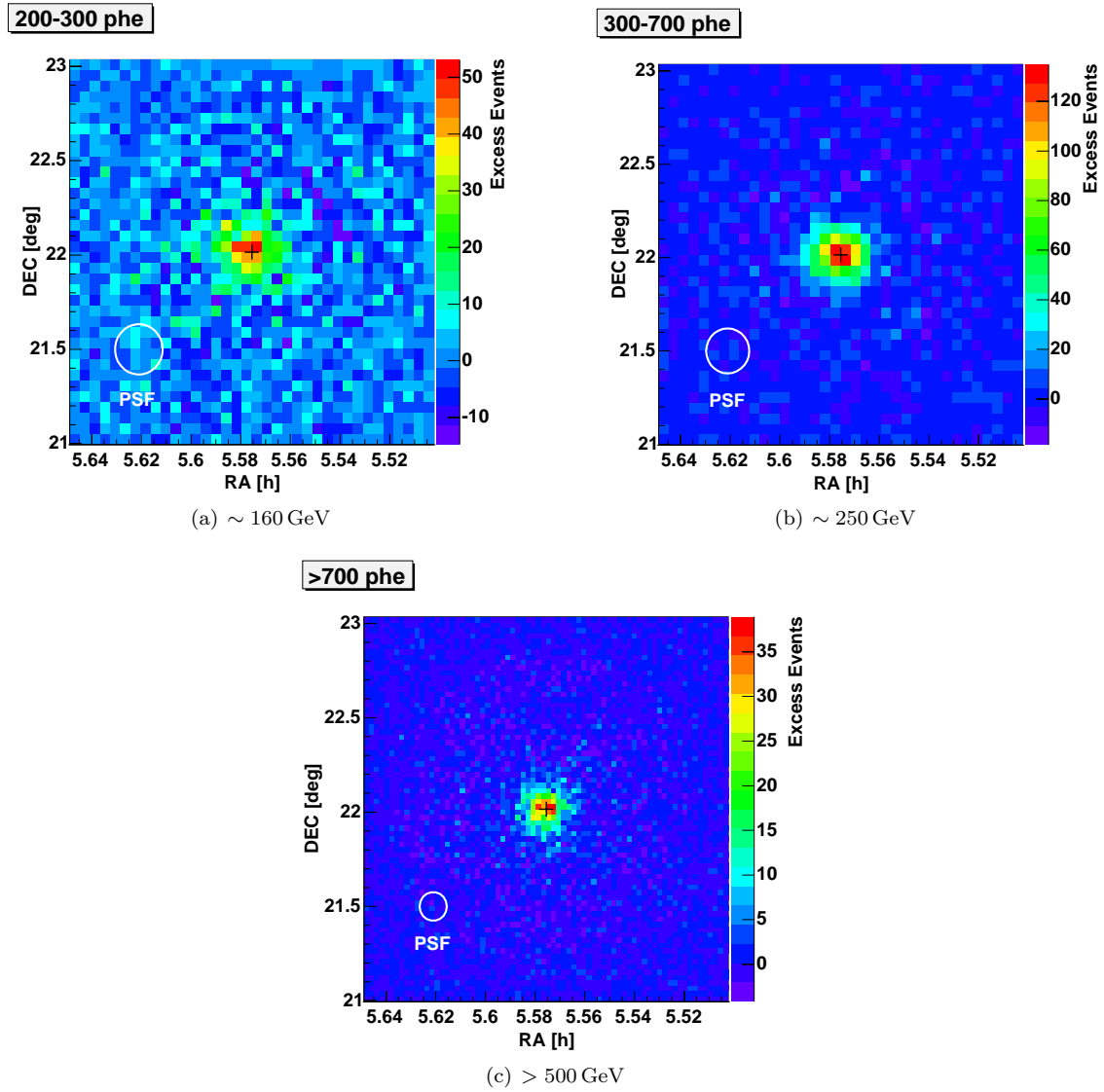


Figure 6.8: Sky-maps of excess events from the Crab nebula for different  $\gamma$ -ray energies ( $\sim 160$  GeV,  $\sim 250$  GeV and  $> 500$  GeV). The position of the pulsar is marked by the black cross and the angular resolution is indicated by the circle.

where  $F_{\text{res}}$  is introduced to account for a possible constant offset of the background subtracted sky-map. Note that in this definition of the 2D-Gaussian  $1\sigma_{\text{data}}$  is the 39% containment radius. It is assumed that the distribution of excess events is rotationally symmetric, i.e.  $\sigma_x = \sigma_y = \sigma_{\text{data}}$ . It is further assumed that  $\sigma_{\text{data}}$  is the convolution of the response of the detector  $\sigma_{\text{psf}}$  (hereafter point spread function) and the size of the  $\gamma$ -ray emission region  $\sigma_{\text{src}}$ :  $\sigma_{\text{data}} = \sqrt{\sigma_{\text{psf}}^2 + \sigma_{\text{src}}^2}$ . Note that here it is assumed that the  $\gamma$ -ray emission region follows the shape described by Equation 6.8, which is not necessarily the case (cf. Figure 3.10(b)).

The cogs obtained from the fitted  $\bar{x}$  and  $\bar{y}$  and their statistical uncertainties are listed in Table 6.5 and shown in Figure 6.9 superimposed on the combined image of optical, IR and X-ray observations of the Crab nebula. The three cogs are compatible with each other and coincide with the position of the pulsar. Note that the systematic uncertainty of the starguider calibration is  $\sim 1'$ .

**Table 6.5:** Center of gravity of the  $\gamma$ -ray emission of the Crab nebula obtained for different energies. In the first column the applied SIZE-cut is stated. The second column shows the corresponding  $\gamma$ -ray energies (peak value and full width at half maximum of the distribution of Monte Carlo  $\gamma$ -ray events). The last two columns give the position of the cog and the statistical uncertainty.

Size [phe]	Energy [GeV]	Right Ascension	Declination
> 700	> 500	5 <sup>h</sup> 5759 ± 0 <sup>h</sup> 0003	22 <sup>d</sup> 022 ± 0 <sup>d</sup> 003
300 ... 700	250 <sup>+130</sup> <sub>-80</sub>	5 <sup>h</sup> 5758 ± 0 <sup>h</sup> 0003	22 <sup>d</sup> 019 ± 0 <sup>d</sup> 004
200 ... 300	160 <sup>+80</sup> <sub>-50</sub>	5 <sup>h</sup> 5766 ± 0 <sup>h</sup> 0009	22 <sup>d</sup> 019 ± 0 <sup>d</sup> 011
Position of the Pulsar:		5 <sup>h</sup> 5755	22 <sup>d</sup> 015

### Search for a possible Extension of the Emission Region

A possible extension of the emission region was studied in two different ways. At first by means of skymaps and secondly on the basis of  $\theta^2$ -distributions. In both approaches the width of the distribution of excess events is compared to the expected point source spread derived from Monte Carlo simulations. The simulated distributions were verified by comparing them with data from Mrk421, an extragalactic  $\gamma$ -ray source that can be considered a point source for our purpose. The width of the  $\gamma$ -ray excess extracted from Mrk421 and the simulated width for a point source agree within statistical uncertainties.

**Study of the Extension of the Emission Region with Sky-maps:** In the first method the background subtracted sky-map of excess events is fitted with a 2D-Gaussian (Equation 6.8). The probability of the fit was in all three maps larger than 10%. The measured width ( $\sigma_{\text{data}}$ ) of the  $\gamma$ -ray excess from the Crab nebula is listed in Table 6.6 together the width obtained from the MC-simulated events ( $\sigma_{\text{psf}}$ ). In all three energy ranges, the real data and MC-simulated widths are compatible within statistical uncertainties. Upper limits on the 39% containment radius of the  $\gamma$ -ray emission (U.L.<sub>95%</sub>) are calculated following the procedure outlined in Yao et al. (2006) and under the assumptions made above about the source morphology.

$$\sigma_{\text{src}}^2 \text{U.L.}_{95\%} = \sigma_{\text{data}}^2 - \sigma_{\text{psf}}^2 + 2 \cdot x_{95\%} \cdot \sqrt{(\sigma_{\text{data}} \Delta\sigma_{\text{data}})^2 + (\sigma_{\text{psf}} \Delta\sigma_{\text{psf}})^2} \quad (6.9)$$

where  $\Delta\sigma_n$  are the statistical errors and  $x_{95\%}$  is 1.64 for a one sided 95% confidence interval. The upper limits are listed in Table 6.6.

Table 6.6: Measured and simulated widths of the  $\gamma$ -ray excess in the 2D-skymaps. In the last column upper limits on the 39% containment radius of the  $\gamma$ -ray emission region are given.

Energy [GeV]	Data $\sigma_{\text{data}} [^\circ]$	MC $\sigma_{\text{psf}} [^\circ]$	95% U.L. on $\sigma_{\text{src}}$
$> 500$	$0.080 \pm 0.008$	$0.076 \pm 0.003$	$2.3'$
$250_{-80}^{+130}$	$0.137 \pm 0.008$	$0.121 \pm 0.004$	$3.8'$
$160_{-50}^{+80}$	$0.12 \pm 0.02$	$0.13 \pm 0.01$	$3.0'$

**Extraction of the Size of the Emission Region from  $\theta^2$ -Distributions:**  $\theta^2$  is the angular distance squared between the reconstructed origin of an event and the assumed source position. In the following the average position of the cogs obtained from the three skymaps is assumed as  $\gamma$ -ray source position. Fixing the source position is the main difference of the  $\theta^2$ -method compared to the previously described one. The background subtracted  $\theta^2$ -distributions obtained for the three energy ranges are shown in Figure 6.10. Data and MC compare very well in all three bins of energy. An exponential function of the form

$$F(\theta^2) = a \cdot \exp\left[-\frac{\theta^2}{2\sigma^2}\right], \quad (6.10)$$

describes the expected distribution, where  $a$  is a normalization and  $\sigma$  is the same as in equation 6.8. Values for  $\sigma_{\text{data}}^2$  and  $\sigma_{\text{psf}}^2$  found by fitting the corresponding  $\theta^2$ -distributions with equation 6.10 are shown in table 6.7. Following the above outlined procedure, upper limits on the extension of the emission region were calculated with a confidence level of 95%.

$$\sigma_{\text{src}}^2 \text{U.L.}_{95\%} = \sigma_{\text{data}}^2 - \sigma_{\text{psf}}^2 + x_{95\%} \cdot \sqrt{(\Delta\sigma_{\text{data}}^2)^2 + (\Delta\sigma_{\text{psf}}^2)^2} \quad (6.11)$$

The limits are given in Table 6.7 and the upper limits for energies  $\sim 250$  GeV and  $> 500$  GeV are drawn in Figure 6.9.

Table 6.7: Results of the fit of the  $\theta^2$ -distributions with an exponential and thereof derived upper limits on the extension of the emission region (39% containment radius).

Energy [GeV]	Data $\sigma_{\text{data}}^2 [ \text{deg}^2 ]$	MC $\sigma_{\text{psf}}^2 [ \text{deg}^2 ]$	95% U.L. on extension
$> 500$	$0.0106 \pm 0.0012$	$0.0116 \pm 0.0006$	$1.6'$
$250_{-80}^{+130}$	$0.020 \pm 0.00170$	$0.0198 \pm 0.0006$	$2.4'$
$160_{-50}^{+80}$	$0.030 \pm 0.0056$	$0.0246 \pm 0.0012$	$5.2'$

### Concluding Remarks on the Morphology Studies

The presented morphology studies of the Crab nebula are the first of its kind in the energy range between 100 GeV and 1 TeV. In summary no hint for an extended emission region nor a significant offset of the cog from the position of the pulsar could be detected. This result is in agreement with the SSC-mechanism (De Jager and Harding, 1992, see also Section 3.5.1). The strong synchrotron cooling restricts the emission region to a few tens of arcseconds. A detection of an extended emission region is then only possible if sub-arcminute resolutions could be achieved, which is beyond the limits of the imaging technique. However, one should remember that a possible hadronic component in the pulsar wind could result in  $\gamma$ -ray production further out in the nebula, which can possibly be detected in the future.

Future improvements of the presented results is expected by taking several actions:

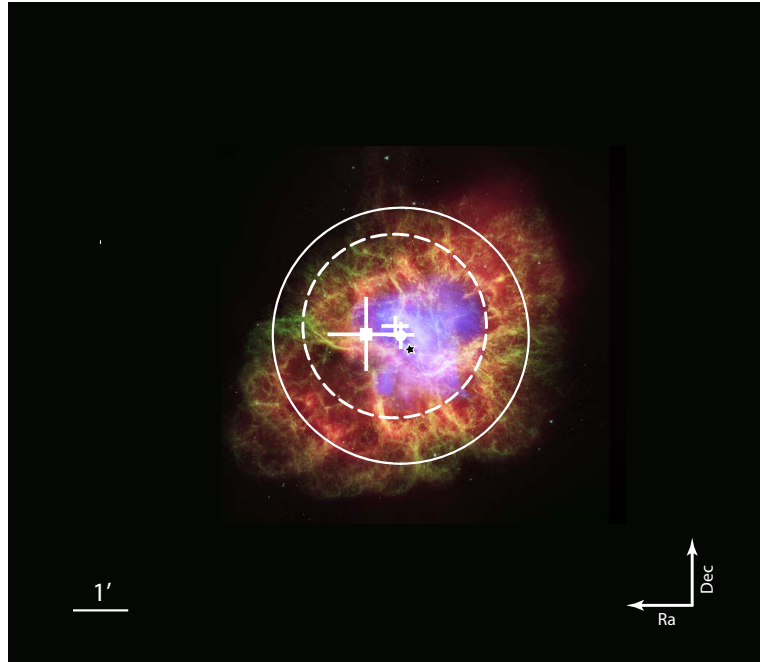


Figure 6.9: Emission of the Crab nebula in different energy bands. The position of the Crab pulsar is marked with a black star. The Chandra X-ray image is shown in light blue, the Hubble Space Telescope optical images are in green and dark blue, and the Spitzer Space Telescope’s infrared image is in red (picture from Chandra, 2006). Overlaid on top are the center of gravity of the  $\gamma$ -ray emission at different energies (simple cross  $> 500$  GeV; dot  $\sim 250$  GeV; square  $\sim 160$  GeV). The error bars indicate the statistical uncertainty in the position of the cog. The upper limits (95% confidence level) on the 39% containment radius of the  $\gamma$ -ray emission region that were derived from the  $\theta^2$ -distributions are indicated with circles (dashed  $> 500$  GeV; solid  $\sim 250$  GeV).

**Using a larger data sample:** The analyzed data sample includes about 16 hours of observation.

The integral observation time of the Crab nebula with MAGIC will increase to 100 hours within the next two years. With the larger data set the limit on the size of the emission region and the position of the cog of the  $\gamma$ -ray emission will improve by a factor of 2.5.

**A better understanding of systematic uncertainties:** With a refined calibration of the star-guider a systematic offset of  $< 25''$  can be expected in the future.

Improvement is also expected with stereo observations, when MAGIC II comes online. In stereo observations not only direct information about the origin of the  $\gamma$ -ray is inferred but — what is maybe even more important — the quality of the reconstruction of the impact point can be judged, as was pointed out by Aharonian et al. (2000).

## 6.4 Optical Observations of the Crab Pulsar with MAGIC

In the next two sections I discuss the non-thermal emission of the Crab pulsar. Optical observations of the Crab pulsar are presented in this section and the search for pulsed  $\gamma$ -ray emission in section 6.5.

The reason to study the optical emission of the Crab pulsar with MAGIC is twofold.

1. It allows to test the hardware and analysis chain that was set up to search for pulsed  $\gamma$ -ray emission (e.g. Lessard et al., 2000; de Naurois et al., 2002; Oña-Wilhelmi et al., 2004; Hinton

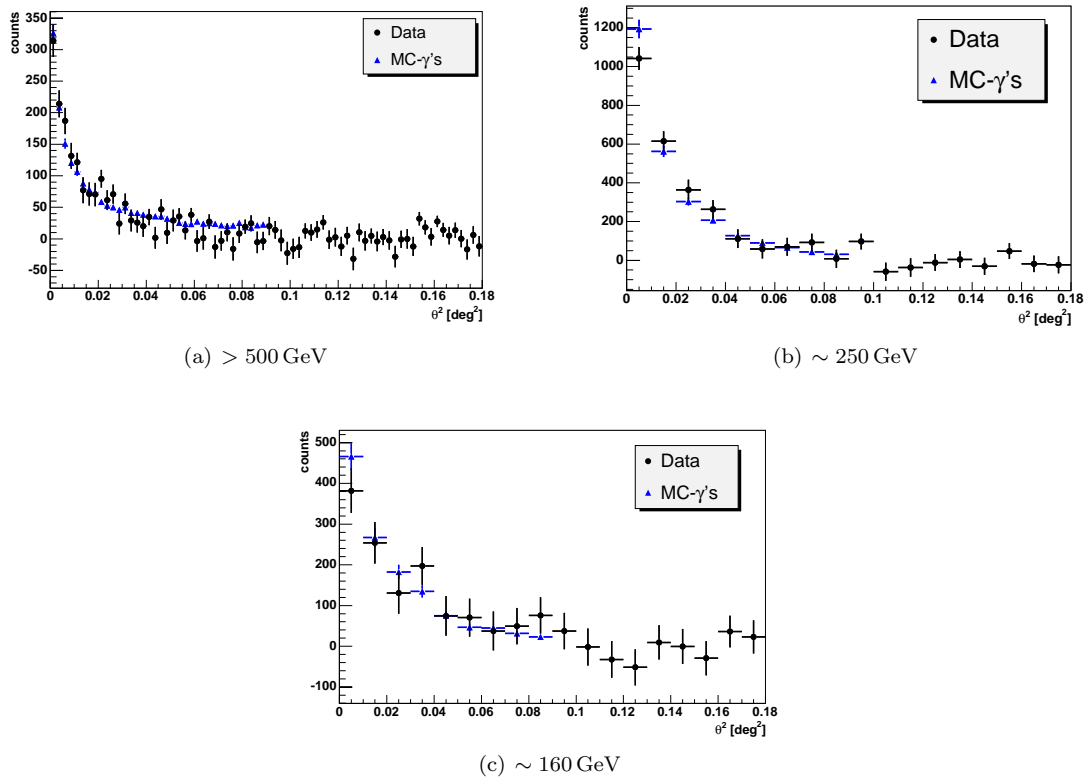


Figure 6.10: Background subtracted  $\theta^2$ -distributions produced with the DISP- method for different energies. See text for discussion.

et al., 2006). Details about the check of the analysis chain can be found in Appendix C.

2. The position of the main-pulse in the light curve is energy dependent. However, measurements of the position of the main-pulse in optical wavelengths are somewhat inconclusive (e.g. Oosterbroek et al., 2006). Some of the discrepancies can be attributed to the limited observation times of previous campaigns. Optical observations with MAGIC can be performed over several years. In this way one achieves an increase in accuracy in the measured quantities.

#### 6.4.1 Setup of the Central Pixel of the MAGIC Camera

The pixel in the center of the camera (hereafter Central Pixel or CP) was modified (Lucarelli et al., 2005) to perform optical observations with MAGIC. The modifications allow one to record optical fluctuations on timescales of a few hundred microseconds. In the standard configuration of the CP a separate, stand-alone data acquisition records the CP-signal. The angular acceptance of the CP is  $0.0079 \text{ deg}^2$  or  $28 \text{ arcmin}^2$ .

I modified the CP-readout in a way that the data acquisition of MAGIC digitizes and records the CP-signal every time the MAGIC-readout is triggered by a cosmic ray event. In this way it was possible to test the absolute accuracy of the system clock of MAGIC for the first time (cf. Appendix C). A disadvantage of this readout is the very low sampling fraction of the pulsar light curve ( $\sim 10^{-5}$ ).

For the modification (1) a new optical receiver<sup>4</sup> was designed with a differential output that fits to the dynamic range of the FADC of the MAGIC data acquisition and (2) on the corresponding FADC-channel the automatic baseline adjustment was disabled. Details of the modification can be found in Appendix C.

### 6.4.2 Data taken with the Central Pixel and reconstructed Light Curve of the Crab Pulsar

The Crab pulsar was observed with the modified CP-readout on nine nights between December 2005 and February 2006. The optical observations were performed in parallel to  $\gamma$ -ray observations of the Crab nebula. Two nights were rejected because of technical problems with the CP. The total observation time remaining for analysis is 12.5 hours. Note that the CP-signal is only recorded for 100 nsec once the readout is triggered by a cosmic ray event. Multiplying this with the average trigger rate of  $\sim 200$  Hz results in a duty cycle of  $2 \cdot 10^{-5}$ . Therefore, the effective observation time was only about one second. After correction of the event times (see section 5.8.1) and calculation of the event phases (see section 5.8.2) a light curve was calculated. Figure 6.11 shows the resulting profile histogram. The values given at each point are the mean amplitude of the CP-signal and the error on the mean amplitude.

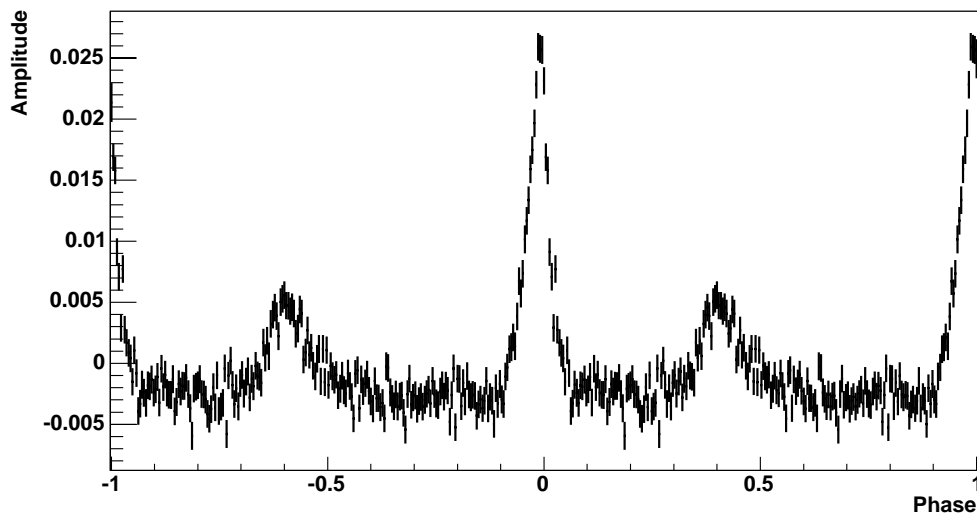


Figure 6.11: Optical light curve of PSR B0531+21 measured with MAGIC. The figure includes data obtained on seven nights between December 2005 and February 2006. The total observation time is 12.5 hours. However, the effective observation time is only  $\sim 1$  sec. For better visibility the light curve is shown twice.

### 6.4.3 Absolute Position of the Main Pulse in the optical Light Curve of the Crab Pulsar

The main- and inter-pulse of the light curve in Figure 6.11 are well resolved. The resolution is sufficient to estimate the offset of the peak position of the main-pulse from phase zero<sup>5</sup>. Close to the peak the rising and falling edge of the main-pulse can be described with a straight line (Straubmeier, 2001). The peak position is estimated by fitting the slope to the left and the

<sup>4</sup>The optical receiver is the electronics that converts the optical signal, which arrives from the telescope in the counting house, back into an electrical signal. See Appendix C for the schematics of the newly designed optical receiver.

<sup>5</sup>phase zero is the peak position of the main-pulse in radio

right side of the peak with a straight line. The peak position is then defined as the point of intersection of the extrapolated fit functions. The left side of the main-pulse is fitted in the range  $\phi = -0.03 \dots -0.011$  and the right side between  $\phi = -0.003 \dots 0.015$ . Figure 6.12 shows an expanded view of the main pulse and the result of the fit. The point of intersection of the two fitted lines is at  $\phi = -0.0075 \pm 0.0015$ .

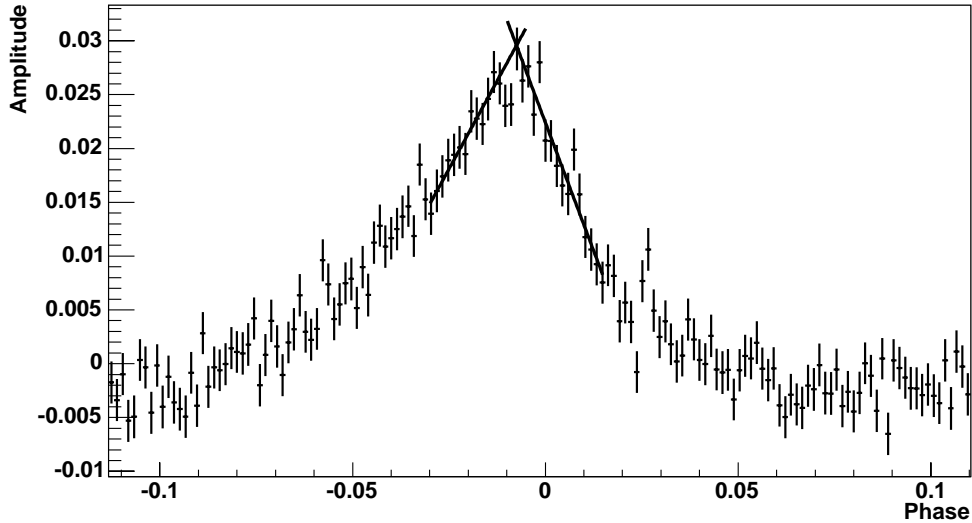


Figure 6.12: Expanded view of the main pulse of the Crab pulsar in optical. The different rise and fall times of the main-pulse are nicely resolved. The slopes of the main-pulse were fitted with two straight lines. The peak position of the main-pulse is given by the intersection of the two curves.

A physical interpretation of the offset of the peak position are different regions of the optical and radio emission, i.e. the optical emission comes from further out in the magnetosphere ( $\sim 75$  km above the origin of the radio emission in this measurement; assuming a non relativistic scenario). Another explanation is an offset between the optical and the radio beam of  $2.7^\circ$ .

### Comparison with other Measurements

In Straubmeier (2001) the point of intersection is at  $\phi = -0.0058 \pm 0.0002^6$ . The difference between both measurements is  $\Delta\phi = 0.0017$  or  $57 \mu\text{sec}$ , which can be explained by the statistical uncertainty of the measurement ( $50 \mu\text{sec}$ ) and the accuracy of the ephemerides ( $40 \mu\text{sec}$ ). An absolute offset of the system clock of MAGIC of less than  $57 \mu\text{sec}$  can be deduced. The measured peak position  $-252 \pm 64 \mu\text{sec}$ , is also in agreement with the contemporary measurement of  $-272 \pm 65 \mu\text{sec}$  by Oosterbroek et al. (2006).

It has to be stressed again that not all measurements of the peak position are in agreement (Oosterbroek et al., 2006). Shearer et al. (2003) and Hinton et al. (2006) give an offset of  $-100 \mu\text{sec}$ . Most likely this disagreement is caused by systematic effects. However, a temporal evolution of the offset cannot be excluded. MAGIC is a prime instrument to study a possible temporal evolution on time scales of years as many sources of systematic uncertainties can be excluded e.g. time differences due to different observatory locations and different experimental setups.

<sup>6</sup>The point of intersection is not explicitly mentioned in the thesis and had to be read from a figure

## 6.5 Search for pulsed $\gamma$ -Ray Emission from the Crab Pulsar

In this section I present the analysis results of a search for pulsed  $\gamma$ -ray emission from the Crab pulsar. The analysis comprises:

- A search for pulsed  $\gamma$ -ray emission in bins of estimated energy
- A search for pulsed  $\gamma$ -ray emission optimized for the lowest  $\gamma$ -ray energies accessible by MAGIC

### 6.5.1 Search for pulsed VHE $\gamma$ -Ray Emission in differential Bins of estimated $\gamma$ -Ray Energy

The search for pulsed emission in bins of estimated energy is motivated by the prediction of pulsed  $\gamma$ -ray emission at TeV energies (see Section 3.4.2 and Hirovani, 2001, 2006c,a). For this analysis I subdivided the energy range between 60 GeV and 10 TeV into five bins. The HADRONNESS-cut and |ALPHA|-cut are given by equation 5.11 and 5.13 respectively. After transformation of the event arrival times to the barycenter of the solar system (outlined in Section 5.8.1), the event-phases were calculated as described in Section 5.8.2. It was then searched for pulsed  $\gamma$ -ray emission with the tests described in section 5.8.3. No signature of pulsed emission was detected.

For each bin of estimated energy upper limits with 95% confidence level on the number of excess events were calculated from the result of the H-Test (see Section 5.8.3) and the pulse phase profiles. Using the H-Test I assume a duty cycle of the pulsed emission of 20%, corresponding to the duty cycle of the  $\gamma$ -ray pulse phase profile measured by EGRET (Nolan et al., 1993). Using the pulse phase profiles I assume that pulsed emission is expected in the same phase intervals where EGRET detected pulsed emission above 100 MeV (cf. Figure 3.6), i.e.  $-0.06 \dots 0.04$  and  $0.32 \dots 0.43$ , and calculate the upper limit on the number of excess events with the method of Rolke et al. (2005), additionally assuming a systematic error of 30% on the number of excess events. The limits derived from the pulse phase profiles are on average a factor of two better than those derived from the result of the H-Test, because the phase range where pulsed emission is expected has to be fixed in the pulse phase profiles. A constraint that is not made in the H-Test.

The upper limits on the number of excess events derived from the pulse phase profiles, were converted into flux limits. The collection area was calculated assuming a photon index of 2.6 for the  $\gamma$ -ray spectrum. The limits are shown in Figure 6.13 together with the upper limit on the cutoff energy, which is derived in the following subsection.

### 6.5.2 Upper Limit on the Cutoff Energy of the pulsed $\gamma$ -Ray Emission of the Crab Pulsar

Upper limits on the cutoff energy of the  $\gamma$ -ray spectrum of the pulsar were calculated as described in Section 5.8.4. In the procedure I used the parametrization of the pulsar spectrum  $< 10$  GeV by Fierro et al. (1998) but extended with an exponential cutoff:

$$F(E, E_{\text{Cutoff}}) = \left[ 7.0 \cdot 10^{-6} \left( \frac{E}{0.1} \right)^{-4.89} + 2.3 \cdot 10^{-5} \left( \frac{E}{0.1} \right)^{-2.05} \right] \cdot \exp \left( -\frac{E}{E_{\text{Cutoff}}} \right) \frac{\text{ph}}{\text{cm}^2 \text{s GeV}} \quad (6.12)$$

The analysis was done selecting events with a SIZE  $> 100$  phe and repeated with a cut selecting events with a SIZE  $< 300$  phe, which should result in the highest sensitivity in a search for pulsed emission (cf. Section 5.8.5). The pulse phase profiles of both analysis are shown in Figure 6.14.

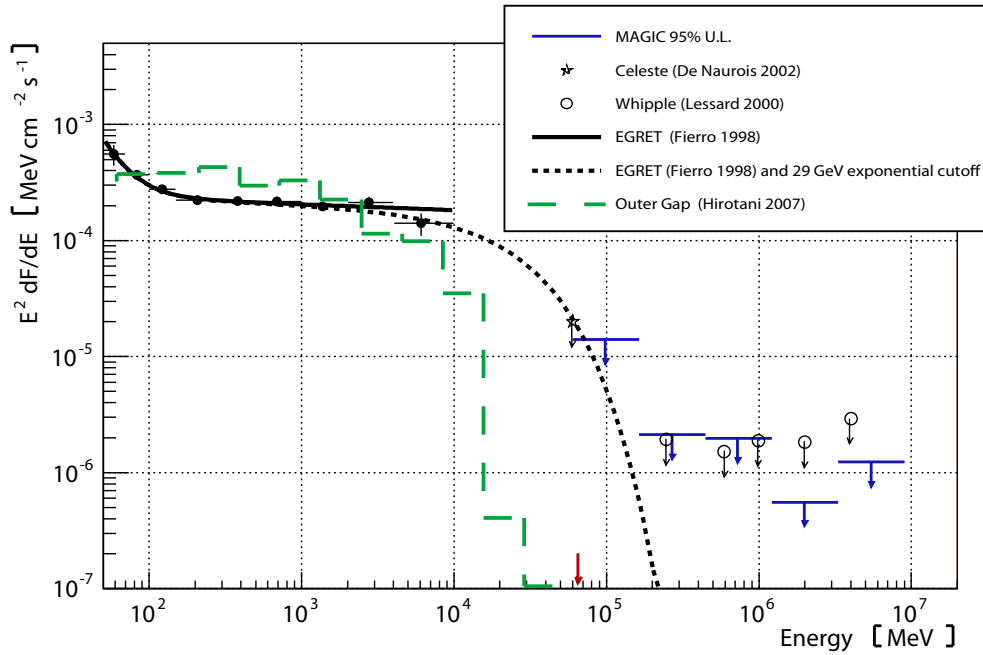


Figure 6.13: Upper limits on the pulsed  $\gamma$ -ray flux from the Crab pulsar; upper limits in differential bins of energy are given by the blue points. The upper limit on the cutoff energy of the pulsed emission is indicated by the dashed line. The red arrow indicates the analysis threshold when the upper limit on the cutoff energy was derived. It should be noted that the Celeste limit is based on a two times lower Crab flux than found by MAGIC.

### Results of the Analysis after Selection of Events with Size > 100 photoelectrons

In the analysis of the events with SIZE > 100 phe the result of a  $\chi^2$ -Test applied to the pulse phase profile is 21.0 with 10 degrees of freedom (d.o.f.). This corresponds to a significance of  $2.32\sigma$  for deviating from a uniform distribution. The result of the H-Test is 10.71, corresponding to a significance of  $2.46\sigma$  for deviating from a uniform distribution. The test of Gregory and Loredo (1992) results in a (Bayesian) probability of  $5.5 \cdot 10^{-3}$  that pulsed emission is present in the data.

Upper limits on the cutoff energy  $E_{\text{Cutoff}}$  of the pulsed emission were calculated from 95% confidence level upper limits on the number of pulsed excess events obtained from the result of the H-Test and the pulse phase profiles. Values of 45 GeV and 37 GeV were obtained for  $E_{\text{Cutoff}}$ . Differential and integral flux upper limits were calculated as outlined in Section 5.9 (see Table 6.8).

Table 6.8: Analysis results for a cut selecting events with SIZE > 100 photoelectrons

Method	H-Test	Rolke
Test result	10.71	n.a.
Significance	$2.46\sigma$	n.a.
$2\sigma$ U. L. on excess events	2090	1606
U. L. on the Cutoff Energy [GeV]	45	37
$2\sigma$ Integral U. L. on Flux Level [ $1/\text{cm}^2 \text{sec}$ ]	$5.0 \cdot 10^{-11}$	$8.9 \cdot 10^{-11}$
$2\sigma$ Differential U. L. on Flux Level [ $1/\text{cm}^2 \text{sec GeV}$ ]	$4.8 \cdot 10^{-12}$	$6.6 \cdot 10^{-12}$
Analysis Threshold [GeV]	71	

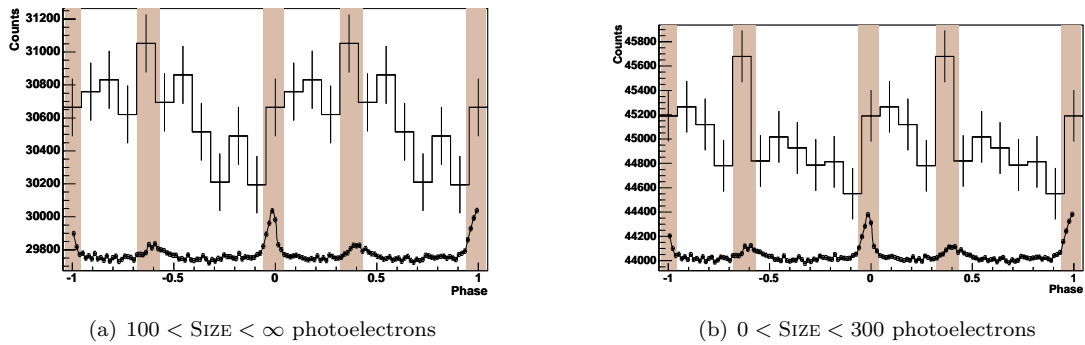


Figure 6.14: Pulse phase profiles obtained after applying SIZE dependent HADRONNESS-cuts (Section 5.4.1) and  $|\text{ALPHA}|$ -cuts (Section 5.5.1) for two different SIZE-cuts. The optical light curve of the Crab pulsar is shown in the bottom of the pulse phase profiles. Indicated by the vertical bars are the regions where EGRET detected pulsed emission above 100 MeV (cf. Figure 3.6)

### Results of the Analysis after Selection of Events with Size < 300 photoelectrons

In the analysis of events with  $\text{SIZE} < 300$  phe the result of the  $\chi^2$ -Test is 13.1 with 10 degrees of freedom (d.o.f.) ( $1.23\sigma$  deviation from a uniform distribution). The result of the H-Test is 3.92 ( $1.26\sigma$ ). The test by Gregory and Loredo (1992) results in a probability of  $4.1 \cdot 10^{-4}$  that pulsed emission is present in the data.

In the pulse phase profile a tentative excess is visible at the position of the inter-pulse, i.e. the peak in the light curve with the smaller amplitude at lower energies. If one defines the phase regions where EGRET detected pulsed emission (shaded regions in the pulse phase profile) as signal region and the remaining phase intervals as background region one calculates a  $2.9\sigma$  significance of the excess. Note that the pulse phase profile is shown twice for better visibility.

To get a feeling whether the excess is a fluctuation or not, additional pulse phase profiles with different upper SIZE-cuts were calculated (with  $\text{SIZE} < 80$  phe,  $< 100$ ,  $< 200$ ,  $< 400$ ). The profiles are shown in Figure 6.15 together with the pulse phase profile of the Crab pulsar measured by EGRET above 5 GeV. Striking is that the EGRET data seem to indicate that the  $\gamma$ -ray emission from the interpulse dominates the  $\gamma$ -ray emission above 5 GeV and that the observed excess shows the same behavior. The significance of the excess is about  $3\sigma$  in all pulse phase profiles except for the  $\text{SIZE} < 80$  phe one where the significance is lower ( $1.9\sigma$ ), which is also expected (cf. Section 5.8.5). With increasing upper SIZE-cut the number of excess event in the phase range between 0.32 and 0.43 continuously increases from 200 to 300 to 700 to 850, which is also expected if a signal would be present.

It has to be pointed out that a significance of  $3\sigma$  in a pulsed analysis is a strong indication that periodicity is present. The search for periodicity is performed among event arrival times, which are more reliable and more stable than image parameters. Image parameters are easily affected by instrumental artifacts, which is the reason why in a standard analysis that searches for steady  $\gamma$ -ray emission a detection can only be claimed if the significance reaches  $5\sigma$ . In summary, the data indicate a signature of pulsed emission. However, a detection cannot be claimed as the conventional detection limit in the field, i.e. a significance of  $5\sigma$ , is not reached.

The analysis threshold for a SIZE-cut  $< 300$  phe is 60 GeV, which is the reason why the upper limits obtained on the cutoff energy (27 GeV and 34 GeV respectively) are lower than in the analysis where the events with  $\text{SIZE} > 100$  phe were analyzed. A summary of the results and differential and integral flux limits are given in Table 6.9.

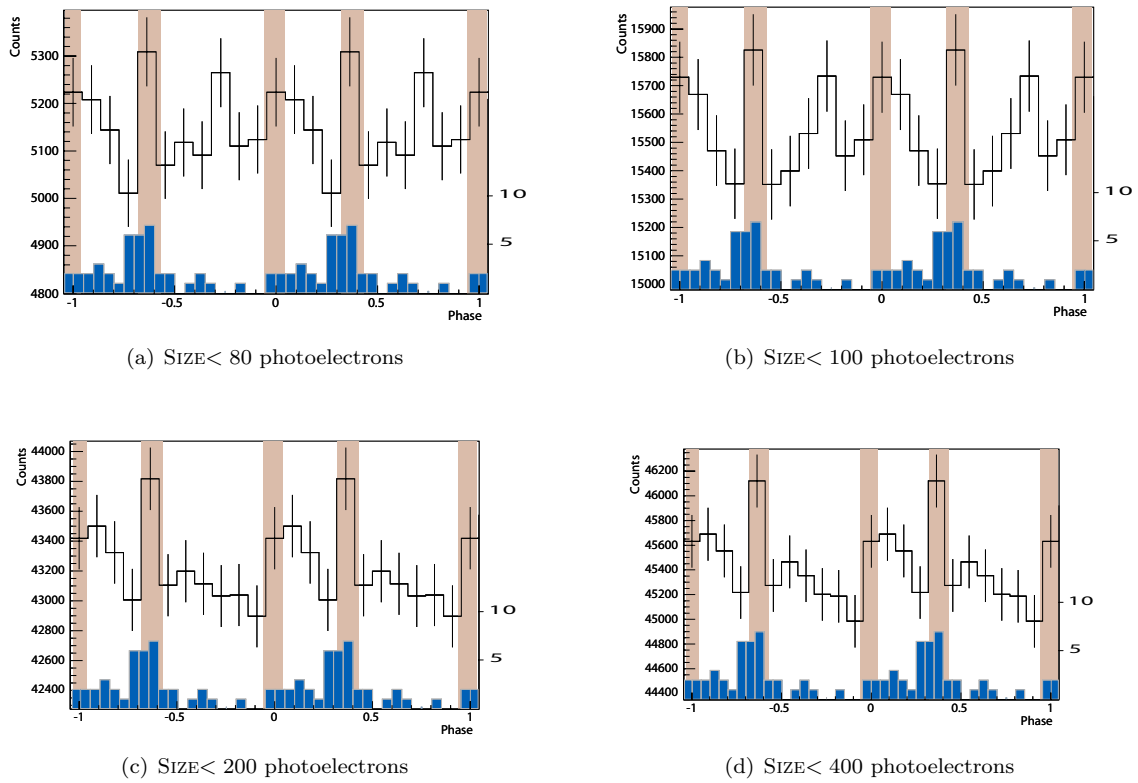


Figure 6.15: Pulse phase profiles obtained after applying SIZE dependent HADRONNESS-cuts (Section 5.4.1) and  $|\text{ALPHA}|$ -cuts (Section 5.5.1) for four different upper SIZE-cuts. The EGRET data above 5 GeV are given in blue and the corresponding scale is shown on the right side (cf. Figure 3.6). In all profiles an excess is visible in the VHE- $\gamma$ -ray data at the position of the interpulse (phase range between 0.32 and 0.43) in coincidence with the EGRET data. The excess in this phase range is monotonically increasing with increasing upper SIZE-cut.

Table 6.9: Analysis results for a cut selecting events with  $\text{SIZE} < 300$  photoelectrons

Method	H-Test	Rolke
<b>Test result</b>	3.92	n.a.
<b>Significance</b>	$1.26\sigma$	n.a.
<b><math>2\sigma</math> U. L. on excess events</b>	1635	3198
<b>U. L. on the Cutoff Energy [GeV]</b>	27	34
<b><math>2\sigma</math> Integral U. L. on Flux Level [<math>1/\text{cm}^2 \text{ sec}</math>]</b>	$2.5 \cdot 10^{-11}$	$7.9 \cdot 10^{-11}$
<b><math>2\sigma</math> Differential U. L. on Flux Level [<math>1/\text{cm}^2 \text{ sec GeV}</math>]</b>	$4.5 \cdot 10^{-12}$	$8.9 \cdot 10^{-12}$
<b>Peak Energy MC [GeV]</b>	60	

## 6.6 Discussion

The Crab data sample presented here was so far the largest analyzed within the MAGIC collaboration. My analysis focused on data of the lowest energies accessible by MAGIC. It was possible to detect with high significance  $\gamma$ -rays with energies down to 60 GeV. Below 400 GeV the results outperform measurements by converted solar tower experiments. This proves that the imaging technique is far superior to the method used in converted solar tower experiments. Many studies were done for the first time e.g. the determination of the IC-peak, the measurement of the spectral index, the search for flux variabilities at 200 GeV or the morphology studies  $< 1$  TeV.

The energy spectrum of the Crab nebula was measured between 60 GeV and 9 TeV. A description of the energy spectrum with a curved power-law is clearly favored. Model predictions by Aharonian et al. (2004) that explain the VHE- $\gamma$ -ray observed from Crab as inverse Compton scattering are in agreement with the measured spectrum and the observed energy dependent spectral slope.

At GeV energies EGRET measured a  $\gamma$ -ray flux about a factor five above the predicted IC- $\gamma$ -ray flux. Atoyan and Aharonian (1996b) are able to explain the observed GeV-excess with Bremsstrahlung of electrons that are partially trapped by filaments of the nebula. However, they predict a spectral index at 300 GeV that clearly deviates from the measured index. In a later prediction the same authors predict an energy spectrum in agreement with the measured photon index (Aharonian and Atoyan, 1998).

At the highest energies, say above 10 TeV, a possible hadronic component would influence the spectral shape. This could not be studied due to insufficient statistics at these energies.

From the measurement of the spectral slope, the peak of the  $\gamma$ -ray emission in the SED-representation could be determined at  $77 \pm 47_{\text{stat}}^{+107} {}_{-46}^{\text{syst}}$  GeV. This is the first determination of the IC-peak.

For the first time the morphology of the Crab nebula was studied in the energy range between 100 GeV and 1 TeV. Within the angular resolution of the MAGIC telescope, the  $\gamma$ -ray emission from the Crab appears to be from a point like source also at the lowest tested energies. The upper limit derived on the source extension restricts the  $\gamma$ -ray emission to originate from within the optical synchrotron nebula. Model calculations in VHE- $\gamma$ -rays (e.g. Gould, 1965; De Jager and Harding, 1992) predict a decreasing size of the emission region with increasing  $\gamma$ -ray energy. This is naturally expected as lower energy electrons can diffuse further out in the nebula before they are cooled by synchrotron radiation to energies below the production threshold of VHE- $\gamma$ -rays by IC-scattering. If the magnetic field is distributed as expected from MHD calculations (Kennel and Coroniti, 1984b), De Jager and Harding (1992) showed that the surface brightness of the nebula at energies  $< 500$  GeV falls to 50% of the peak intensity at a radial distance of  $30''$  from the pulsar. Assuming a faster decaying field configuration ( $B \propto 1/r$ ) the emission region could extend up to  $\sim 80''$ , which is about the size that is constrained by the upper limits obtained in this work.

X-ray observations indicate variabilities in the acceleration and cooling times of electrons on timescale of months (e.g. Hester et al., 2002). However, the measured light curve  $> 200$  GeV is consistent with that of a steady source on all studied time scales. The stability of the integral flux is better than 10%.

The Crab pulsar was detected in optical wavelengths with high significance by feeding the CP-signal into a free channel of the MAGIC DAQ. With this setup the first verification of the system clock of MAGIC could be carried out. The study of the position of the main peak showed a shift of  $-0.0075 \pm 0.0015$  in phase with respect to the position of the main peak in radio. The measured offset is in agreement with most other experiments. However, not all measurements come to the same conclusion (e.g. Hinton et al., 2006). The disagreement can be likely attributed to systematic differences between experiments. A temporal effect intrinsic to the pulsar cannot be excluded and requires further studies with MAGIC over a larger period of time.

In a search for pulsed VHE- $\gamma$ -ray emission with optimized cuts an excess was found in the pulse phase profile at the same position where EGRET detected pulsed emission above 5 GeV. The significance of the excess is  $2.9\sigma$  if the phase regions where EGRET detected pulsed emission are chosen as signal regions and the remaining phase intervals as background regions. The similarity of the distribution of excess events in the EGRET and MAGIC data and the monotonic increase of the number of excess events with increasing upper SIZE-cut are strong indications that the observed excess is not a random fluctuation. However, a detection can not be claimed as the conventional  $5\sigma$  detection limit is not reached. Further investigations with a larger data set (about 3 times longer observation time) are needed to verify or discard the observed excess.

With the optimized cuts and the result of the H-Test an upper limit on the cutoff energy of 30 GeV was derived, assuming that the power-law spectrum of the pulsar at GeV energies is attenuated by an exponential cutoff. The current data (EGRET and MAGIC) leave only a small window open where the cutoff can reside. However, if the cutoff has a super-exponential shape a cutoff energy almost as high as the analysis threshold ( $\sim 60$  GeV) cannot be excluded.

Another interesting pulsar study is the search for VHE- $\gamma$ -ray emission in correlation with the appearance of giant pulses (GP). GPs are transients observed at radio wavelengths with a duration of a few microseconds. They are on average 100 times more intense than the average intensity of individual pulses. As a matter of fact the Crab pulsar was detected by virtue because of GPs, which appear at an average rate of 0.1 Hz. An increase of the optical emission ( $\sim 3\%$ ) during GPs was found (Shearer et al., 2003), however, a correlated increase at X-ray energies was not found (Lundgren et al., 1995). For a similar study in  $\gamma$ -rays a Cherenkov telescope clearly outperforms satellite experiments as one profits from a more than  $10^4$  times larger collection area and thus from a  $10^4$  times higher sensitivity. Note that the measurement with a Cherenkov telescope is quasi background free if one requires a small coincidence window ( $\sim 10 \mu\text{sec}$ ) between the appearance of a GP in radio and the correlated VHE- $\gamma$ -ray emission.

A GP-study with simultaneous radio and  $\gamma$ -ray observations was not done before. However, first, simultaneous observations of the Crab with MAGIC and the Giant Meterwave Radio Telescope (GMRT) in Pune, India were done in late 2006. The data are currently being analyzed and results will be reported elsewhere.

## Chapter 7

# Study of the Pulsar PSR B1951+32 and associated Pulsar Wind Nebula

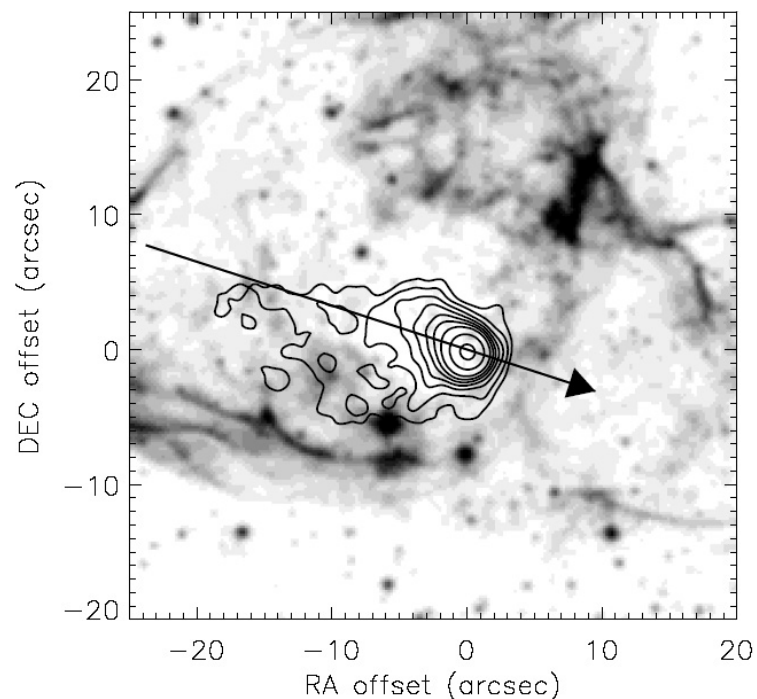


Figure 7.1:  $H\alpha$  emission around PSR B1951+32 (grey) and X-ray emission (contours) that can be associated to the pulsar wind nebula that is powered by PSR B1951+32. The arrow shows the direction of the proper motion of the pulsar. A striking difference to Crab is that PSR B1951+32 has a much higher proper motion (240 km/s), which results in the formation of a bow shock. Picture from Moon et al. (2004).

## 7.1 Introduction

### 7.1.1 The Pulsar PSR B1951+32

PSR B1951+32 was detected at first at radio frequencies by Kulkarni et al. (1988a), and is one of the six rotational-powered pulsars whose GeV emission was detected by EGRET (Ramanamurthy et al., 1995). Among  $\gamma$ -ray pulsars, PSR B1951+32 is the only source observed to emit up to 20 GeV with no cutoff being evident in the differential energy spectrum. The spectrum shows a hard spectral index of 1.74 between 100 MeV and 20 GeV. The pulsar has an apparent high efficiency ( $\sim 0.4\%$ ) of converting its rotational spin down luminosity,  $3.7 \times 10^{36}$  ergs s $^{-1}$ , into  $\gamma$ -rays  $> 100$  MeV (assuming a distance between Earth and the pulsar of 2.5 kpc). The  $\gamma$ -ray luminosity at  $\sim 10$  GeV is comparable to the Crab pulsar (Ramanamurthy et al., 1995).

Inferred from its rotational parameters the age of PSR B1951+32 is  $\sim 10^5$  years (Manchester et al., 2005), i.e. about 100 times older than the Crab pulsar. The magnetic field strength of  $4.9 \cdot 10^{11}$  G (Manchester et al., 2005) is lower than in most rotational-powered pulsars. Based on some models (e.g. Harding et al., 1997) it is expected that the screening of  $\gamma$ -rays due to pair production in the magnetosphere of PSR B1951+32 is reduced and the cutoff of the high energy emission subsequently shifts to higher energies. Based on these arguments, the pulsar PSR B1951+32 is a prime candidate for observation by ground based  $\gamma$ -ray detectors with low energy thresholds such as the imaging air Cherenkov telescope MAGIC.

### 7.1.2 The Interaction of the Pulsar with its surrounding Medium

The pulsar is located in the core of the radio nebula CTB 80, which is thought to be physically associated with the pulsar. In X-rays the nebula shows a cometary shape (Moon et al., 2004; Li et al., 2005), being confined by a bow shock that is produced by the pulsar's high proper motion of  $240 \pm 40$  km/s (Migliazzo et al., 2002) (s. Figure 7.1). Bednarek and Bartosik (2005b) predict a  $> 200$  GeV flux from the nebula at a level of  $\sim 4.4\%$  Crab flux, if high energy leptons can accumulate for long periods of time.

The current tightest constraint on the  $> 100$  GeV emission from the pulsar and its nebula, obtained by the Whipple collaboration (Srinivasan et al., 1997), puts a 75 GeV upper limit on the cutoff energy of the pulsed emission. On the steady emission  $> 260$  GeV they obtain an upper limit,  $\leq 1.95 \times 10^{-11}$  cm $^{-2}$ s $^{-1}$ . The latter limit is a factor  $\sim 2$  within the prediction of Bednarek and Bartosik (2005b).

In this chapter I present upper limits on the cutoff energy of the pulsed emission from the pulsar, as well as on the steady and pulsed VHE fluxes from the region associated with the radio nebula, resulting from MAGIC telescope observations that were performed in July throughout September 2006. The chapter has the following structure: After a short summary of the observations, I report about the search for steady and pulsed emission from PSR B1951+32. The chapter finishes with a discussion of the implications of the results.

## 7.2 Selection and Processing of the Data Sample

### 7.2.1 Summary of the Data Sample

In 2006 PSR B1951+32 was observed by MAGIC for a total of 17 nights between July 4<sup>th</sup> and September 17<sup>th</sup>. The observations were performed in the ON/OFF mode, i.e. the source was observed by directly pointing to it (ON) — in this case by pointing to the position of PSR B1951+32. The background was estimated by observing at the same zenith angle range a suitable region in

the sky where no  $\gamma$ -ray source was expected (OFF). Three nights were rejected because of unstable trigger rates due to bad weather. In total 30.7 hours of ON data remained for analysis. The zenith angle range of the observation was between  $5^\circ$  and  $25^\circ$ , guaranteeing the lowest possible energy threshold. A summary of the observation gives Table 7.1. This table also includes atmospheric extinction coefficients of all nights, provided by the Carlsberg Meridian telescope, which is located at the same site as MAGIC.

Table 7.1: Summary of the observation of PSR B1951+32 with MAGIC. The extinction coefficients are taken from public available data of the Carlsberg Meridian Telescope that is located on the same site as MAGIC. The extinction coefficient is for an effective wavelength of 625nm.

Date	Rates [Hz]	On Time [min]	Ext. Coef. [mag]	Sc. Ext. Coef. [mag]	selected
04.07.2006	164	130	0.099	0.017	yes
05.07.2006	164	136	0.100	0.011	yes
06.07.2006	167	105	0.088	0.014	yes
07.07.2006	176	62	0.091	0.011	yes
03.08.2006	151	95	0.161	0.009	yes
04.08.2006	n.a.	n.a.	0.266	0.045	no
23.08.2006	175	168	0.079	0.017	yes
24.08.2006	158	105	0.088	0.014	yes
25.08.2006	165	138	0.142	0.029	yes
26.08.2006	135	148	0.168	0.044	no
27.08.2006	167	124	0.140	0.042	yes
28.08.2006	n.a.	n.a.	0.249	0.056	no
13.09.2006	147	83	n.a	n.a	yes
14.09.2006	139	155	0.105	0.016	yes
15.09.2006	156	102	0.091	0.017	yes
16.09.2006	147	125	0.095	0.013	yes
17.09.2006	149	89	0.094	0.060	yes

## 7.2.2 Processing of the Data

The data were processed following the scheme outlined in Chapter 5 and Chapter 6. After calibration of the recorded PMT-signals with the F-factor method, the events were cleaned with two different sets of tail-cuts. For most of the presented results the events were cleaned with the time image cleaning procedure with absolute cleaning levels of 6 and 4 photoelectrons respectively. For the generation of skymaps with the DISP-method the events were cleaned with cleaning levels of 10 and 8 photoelectrons.

After the image cleaning and image parameter calculation the HADRONNESS of each event was determined. The random forests were trained with the image parameters DIST, WIDTH, LENGTH and SIZE. In the analysis with cleaning levels of 10 and 8 photoelectrons, the parameter DIST was not used in the training of the random forests but the parameters CONC5 and CONC7.

## 7.3 Search for steady $\gamma$ -Ray Emission from the Pulsar Wind Nebula

### 7.3.1 Steady $\gamma$ -Ray Emission from the Location of the Pulsar

With different analysis thresholds between 140 GeV and 2.6 TeV it was searched for  $\gamma$ -ray emission assuming a point source coinciding with the position of PSR B1951+32. Figure 7.2 shows on the right hand side the  $|\text{ALPHA}|$ -distribution that includes events with energies  $\gtrsim 280$  GeV. An excess due to  $\gamma$ -ray emission from PSR B1951+32 should be visible in the figure for  $|\text{ALPHA}| < 7.5^\circ$ . The background subtracted  $\theta^2$ -distribution that includes events of similar energies is shown on the left side. An excess due to  $\gamma$ -ray emission is expected for  $\theta^2 < 0.1$  degrees<sup>2</sup>. The results of this analysis (from the  $|\text{ALPHA}|$ -distribution) and analysis with other thresholds are summarized in Table 7.2. As no significant signal ( $> 5\sigma$ ) of  $\gamma$ -rays was found, upper limits were calculated on the number of excess events with a confidence level of 95% by using the method of Rolke et al. (2005). In the calculation of the limits a systematic uncertainty on the flux of 30% was taken into account. The upper limits on excess events were converted into upper limits on the integral flux as outlined in Section 5.9 by assuming a spectral index of 2.6 for the calculation of the effective collection areas. The limits on the integral flux of  $\gamma$ -rays shows Figure 7.3 together with the measurement by Srinivasan et al. (1997) and the predictions by Bednarek and Bartosik (2003).

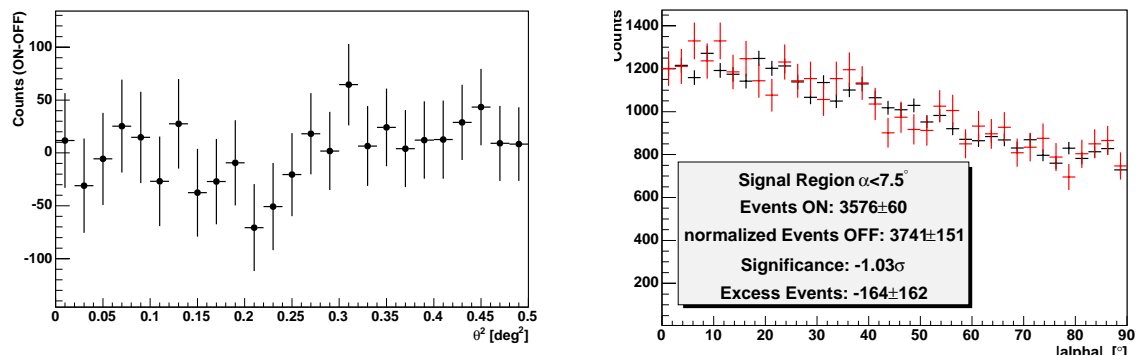


Figure 7.2: The left panel shows the  $\theta^2$ -distribution after background subtraction. The right panel shows the  $|\text{ALPHA}|$ -distribution of ON-events (black) and OFF-events (red). In both cases no hint of a signal is visible. The cuts are chosen in both cases such that the energy threshold of the analysis is 280 GeV

Table 7.2: Results from an analysis of steady emission from PSR B1951+32.

Analysis Threshold [GeV]	ON Events	OFF Events	Excess Events	Significance [ $\sigma$ ]	Upper Limit Excess Events 95% C.L.	Flux Upper Limit [ $\text{cm}^{-2}\text{s}^{-1}$ ]
> 140	37869	$37933 \pm 381$	-64	-0.15	792	$1.52 \times 10^{-11}$
> 280	3576	$3740 \pm 150$	-164	-1.03	196	$2.66 \times 10^{-12}$
> 530	712	$777 \pm 42$	-65	-1.31	54	$6.95 \times 10^{-13}$
> 800	232	$231.5 \pm 22$	0.5	0.02	55	$7.00 \times 10^{-13}$
> 1060	101	$90.6 \pm 14$	10.4	0.61	45	$5.84 \times 10^{-13}$
> 1400	58	$49.5 \pm 10.8$	8.5	0.64	35	$3.88 \times 10^{-13}$
> 2600	17	$26 \pm 10$	-9	-0.93	14	$2.51 \times 10^{-13}$

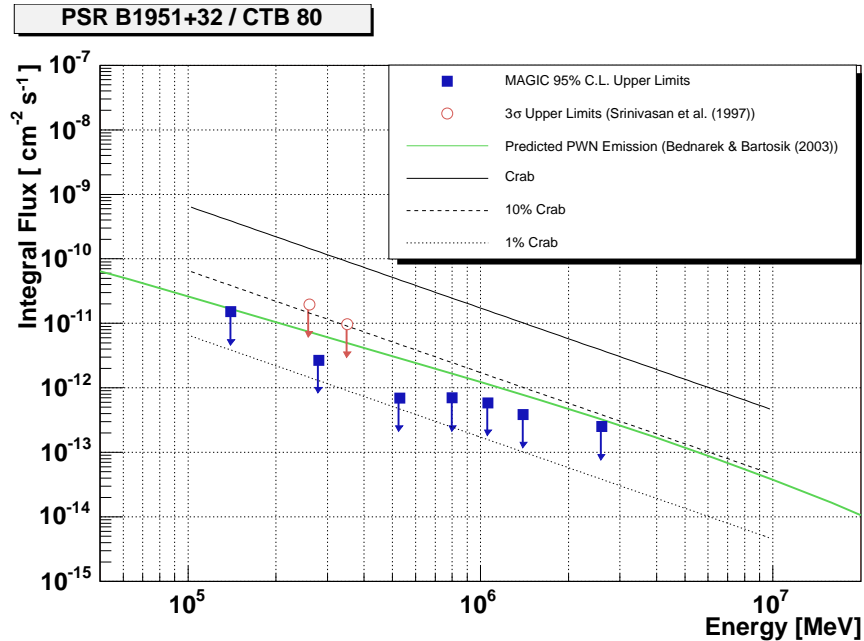


Figure 7.3: Integral upper limits (95 % Confidence Level) on the steady emission from the direction of PSR B1951+32. For comparison, the  $\gamma$ -ray flux of the Crab nebula (Wagner et al., 2005) is also indicated.

### 7.3.2 Search for $\gamma$ -Ray Emission in the Vicinity of PSR B1951+32

The region in the sky around the position of the pulsar was searched for a possible extended and/or dislocated emission region of  $\gamma$ -rays. The latter is a likely scenario due to the high proper motion of the pulsar. For this study the DISP-method was employed (cf. Section 5.6). Sky maps were produced in different bins of energy. Figure 7.4 shows some maps. Note that the maps are smoothed with a Gaussian kernel of  $\sim 0.1^\circ \sigma$ , i.e. a similar width as the point spread function. In none of the maps  $\gamma$ -ray emission was found within the reconstructed field of view of  $\sim 0.6^\circ$  radius.

The map in Figure 7.5 shows the significance calculated in bins of  $(0.1 \times 0.1)$  degrees<sup>2</sup> for events with energies  $\gtrsim 300$  GeV. Figure 7.6 shows a map of the calculated upper limits (95 % Confidence Level) on the integral flux for the same events. Following this study one can exclude steady  $\gamma$ -ray emission  $> 200$  GeV on the level predicted by Bednarek and Bartosik (2003), which would have been detected if a) the emission had been originating from within a circle of radius  $\approx 0.1^\circ$  centered on the position of the pulsar, and b) the apparent emission region had been restricted to less than  $\sim 0.4^\circ$  in diameter.

## 7.4 Search for $\gamma$ -Ray Emission from the Pulsar

Before I searched for pulsed  $\gamma$ -ray emission from the pulsar, the arrival times were transformed to the barycenter of the solar system with the TEMPO timing package (Taylor et al., 2000). Afterwards, the corrected arrival times  $t_j$  were folded to the corresponding phase  $\phi_j$  of PSR B1951+32 as described in section 5.8. A contemporary ephemeris of PSR B1951+32 was provided by Lyne (2006). The values of the ephemeris are given in Table 7.3.

A search for pulsed  $\gamma$ -ray emission from PSR B1951+32 was performed in 5 differential bins of reconstructed energy between 100 GeV and 2 TeV. To test for periodicity the Pearson- $\chi^2$ -test, the H-Test (De Jager et al., 1989) and the test by Gregory and Loredo (1992) were applied (cf. section 5.8.3). No signature of pulsed emission was found in any of the energy intervals. As an example I

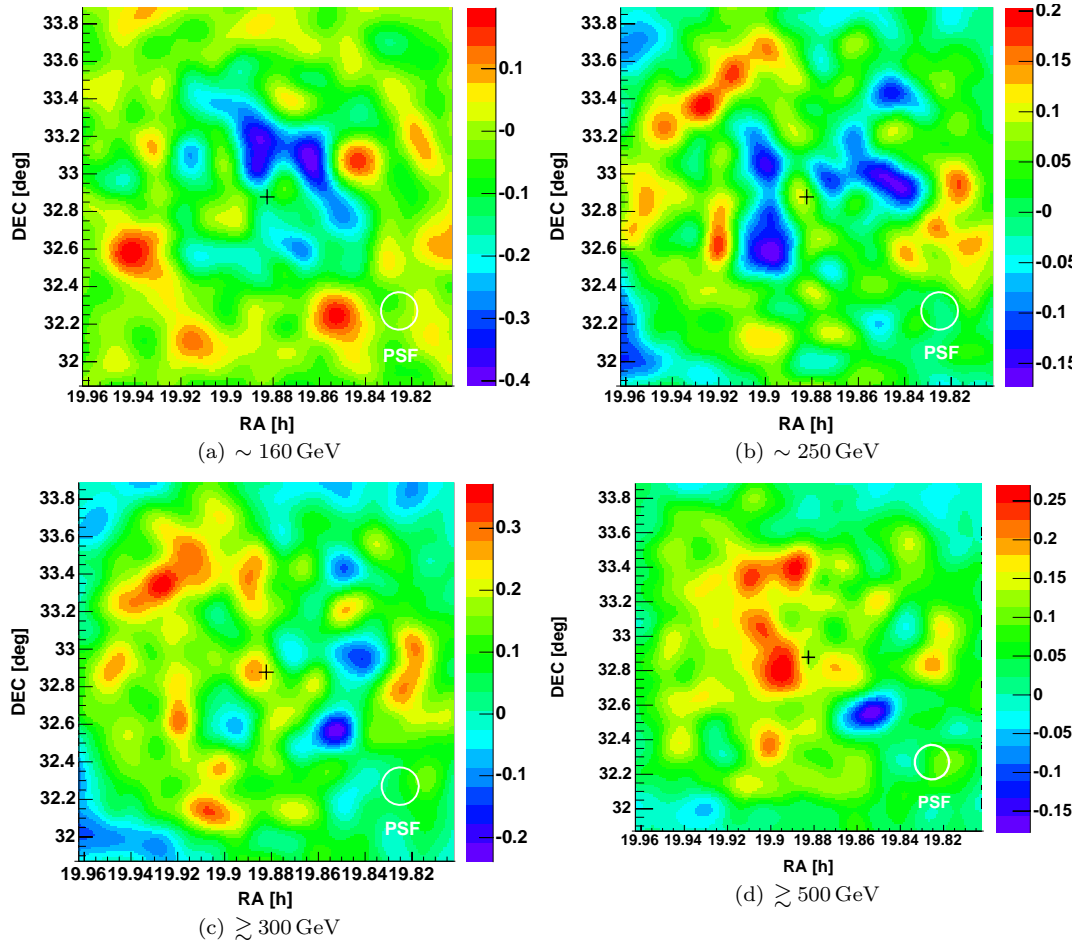


Figure 7.4: Sky maps of excess events in the region around PSR B1951+32 smoothed with a Gaussian kernel of  $0.1^\circ$ .

give the results of the H-Test, which yielded significances of 0.3, 2.3, 0.6, 0.2 and  $1.4\sigma$  respectively with increasing energy. The corresponding 95% confidence level upper limits on pulsed emission are shown in Figure 7.7. The limits were calculated from the results of the H-Test (De Jager, 1994), assuming a duty cycle of the pulsed emission of 36%. This corresponds to the duty cycle of PSR B1951+32 at energies  $> 100$  MeV (Ramanamurthy et al., 1995). A spectral slope of 2.6 was assumed in the calculation of the collection area.

In a second analysis, I searched for pulsed emission by selecting events with a  $\text{SIZE} > 100$  phe, i.e. events with energies  $\gtrsim 75$  GeV. Again, no hint of pulsed emission was found. The H-Test yielded 1.4, and a  $\chi^2$ -Test a  $\chi^2$  of 7.2 with 11 degrees of freedom. The test by Gregory and Loredo (1992) gave a probability for pulsed emission of  $2.4 \cdot 10^{-4}$ .

From the result of the H-Test I computed an upper limit on the number of excess events (s. Table 7.4) and derived an upper limit on the cutoff energy of the pulsed emission as described in section 5.8.4. For the spectrum of the pulsar I have adopted the parametrization by Fierro (1996). The expected number of excess events were matched to the upper limit on the number of pulsed excess events at a cutoff energy of 32 GeV. The spectrum of PSR B1951+32 with an exponential cutoff of 32 GeV is depicted as solid red line in Figure 7.7. The analysis threshold of 75 GeV is marked with a red square.

The same analysis was repeated this time by selecting all events with a  $\text{SIZE} < 300$  photoelectrons. The resulting light curve shows Figure 7.8. The analysis resulted in a slightly better upper limit

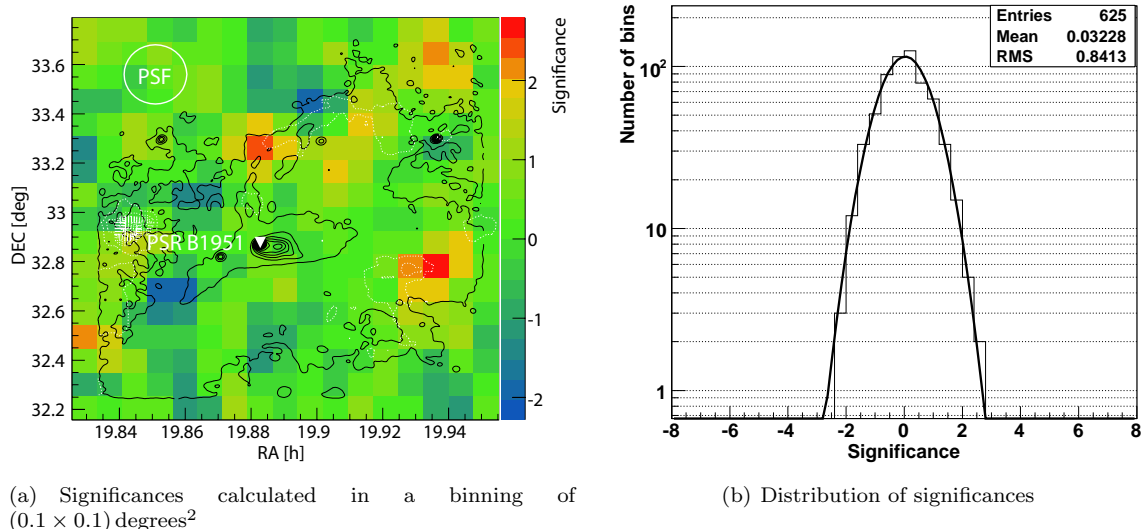


**Figure 7.5:** Significance of VHE  $\gamma$ -ray emission from the region around PSR B1951+32. Left side: calculated significance of VHE  $\gamma$ -ray emission  $\gtrsim 300$  GeV in bins of  $(0.1 \times 0.1)$  degrees<sup>2</sup>. Overlaid in black are contours of radio observations (Castelleti et al., 2003) and in white contours of IR observations (Fesen et al., 1988). Right side: distribution of significances. The distribution has a mean of 0.03 and a RMS of 0.84, compatible with randomly distributed data. Figures provided by E. Aliu.

on the cutoff energy of 28 GeV. In this case the analysis threshold was 60 GeV.

A search for periodicity was done by changing the frequency of the radio pulsar in a small range around the frequency of the ephemeris and selecting events with a  $\text{SIZE} < 300$  photoelectrons. This scan was performed with an oversampling factor of 30. The results of the H-Test and  $\chi^2$ -Test at each sampled frequency point are shown in Figure 7.9. The results of the Bayesian-test by Gregory and Loredo (1992) are shown in Figure 7.10. Within the scanned frequency range no signature of periodicity was found in any of the tests.

## 7.5 Discussion

Theoretical predictions and experimental evidence had been quite favorable for a possible MAGIC detection of  $\gamma$ -ray emission from PSR B1951+32 or its nebula. Despite the higher sensitivity of

Table 7.3: Ephemeris of PSR B1951+32 from Lyne (2006). Uncertainties are given in brackets.

<b>Position Epoch</b>	50227.9144 MJD
<b>Right Ascension</b>	19 <sup>h</sup> 52 <sup>m</sup> 58 <sup>s</sup> .27568995
<b>Declination</b>	32°52'40"6824033
<b>Pulsar Epoch</b>	53931.224208 MJD
$\nu$	25.29516019929(63) Hz
$\dot{\nu}$	$-3.72818(33) \cdot 10^{-12}$ Hz/s
$\ddot{\nu}$	$-1.15(25) \cdot 10^{-21}$ Hz/s <sup>2</sup>

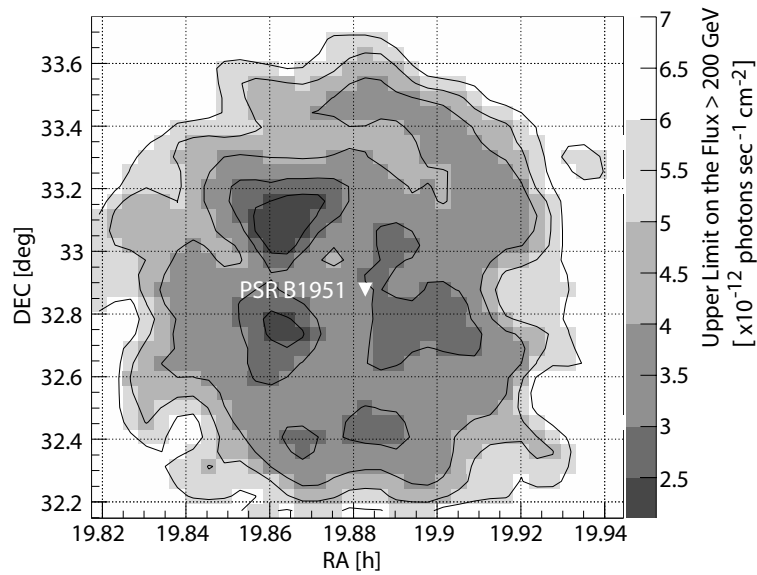


Figure 7.6: Upper limits (95 % Confidence Level) on the integral  $\gamma$ -ray emission  $> 200$  GeV, calculated in bins of  $(0.05 \times 0.05)$  degrees<sup>2</sup>. Figure provided by E. Aliu.

Table 7.4: Results of the analysis for periodicity within the PSR B1951+32 data sample.

	H-Test				$\chi^2$	Bayesian
	H	Significance	$2\sigma$ U.L. Excess Events	$2\sigma$ Flux U.L. [ $\text{cm}^{-2}\text{s}^{-1}$ ]		
SIZE $> 100$ phe	1.38	$0.27\sigma$	2188	$4.32 \cdot 10^{-11}$	7.15	$2.4 \cdot 10^{-4}$
SIZE $< 300$ phe	3.21	$1.08\sigma$	3388	$4.98 \cdot 10^{-11}$	10.65	$3.6 \cdot 10^{-4}$

this observation compared to previous ones, no  $\gamma$ -ray emission was detected.

The upper limits in Figure 7.3 on the steady  $\gamma$ -ray emission from the PWN surrounding PSR B1951+32 are below the  $\gamma$ -ray flux that was predicted by the time dependent model of Bednarek and Bartosik (2003, 2005a). Although their model takes into account the temporal evolution of the nebula (but not the spatial evolution), the acceleration of leptons and therefore also the equilibrium spectrum of leptons inside the nebula still depends on a few free parameters, which are usually not well known. These parameters, e.g. the density of the medium surrounding the PWN, the acceleration efficiency of leptons, or the magnetization parameter of the pulsar wind at the shock region, need reasonable guesses in order to estimate the  $\gamma$ -ray flux.

Concerning the magnetization parameter, i.e. the ratio of the magnetic energy flux to the particle energy flux, Li et al. (2005) have recently estimated the magnetic field strength of the compact X-ray nebula around PSR B1951+32 to be  $\sim 300 \mu\text{G}$ . As this is larger than the value assumed by Bednarek and Bartosik, it is clear at present that the value of the magnetization parameter  $\sigma$  of the pulsar wind has to be much larger than the value of  $\sigma = 10^{-3}$  assumed by Bednarek and Bartosik. As a result, the cooling of electrons by synchrotron radiation is faster and the IC  $\gamma$ -ray flux is suppressed. A hadronic  $\gamma$ -ray component, as is predicted in some models (Bednarek and Bartosik, 2003; Horns et al., 2006) would dominate if the acceleration efficiency of leptons were low (Bednarek, 2006) but the  $\gamma$ -ray flux would be below the sensitivity of the observation.

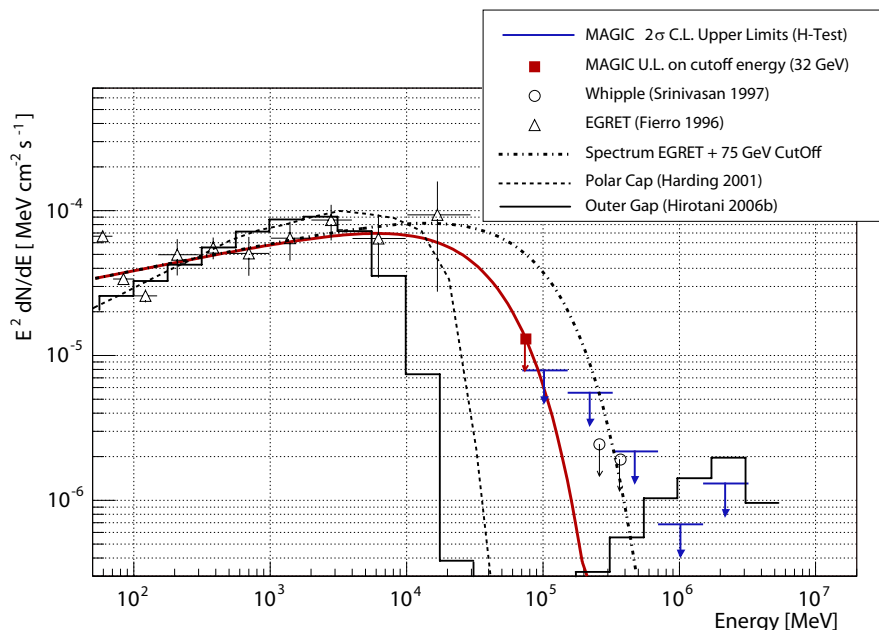


Figure 7.7: Results of the analysis in search for pulsed emission from PSR B1951+32. Upper limits are given for a 95 % confidence level. The red curve shows the spectrum measured by Fierro (1996) but extended by an exponential cutoff of 32 GeV.

Another aspect is that the model of Bednarek and Bartosik deals with PWNe, which are well confined by the external medium, and pulsars, which are assumed to slowly move through the interstellar medium (the prototype of such a nebula is the Crab nebula). Only in such a scenario a well localized  $\gamma$ -ray nebula should be expected, whereas, when the pulsar is moving very fast, the  $\gamma$ -ray emission will be distributed over a larger volume. In the case of PSR B1951+32, which moves with an apparent velocity of  $240 \pm 40 \text{ km s}^{-1}$  (Migliazzo et al., 2002), the  $\gamma$ -ray flux estimated by Bednarek and Bartosik (2005b) will be smeared over an area with a diameter of at least  $\sim 0.5$  degrees (assuming an age of the pulsar of  $7 \times 10^4$  years), which reduces the detection probability with MAGIC. In this context it is interesting to note that extended TeV  $\gamma$ -ray sources associated with displaced pulsars, were recently detected by the H.E.S.S. Collaboration (e.g. the Vela pulsar (Aharonian et al., 2006b) or PSR B1823-13 (Aharonian et al., 2005)).

Regarding the  $\gamma$ -ray emission from the pulsar, I could constrain the cutoff of the pulsed emission to  $< 32 \text{ GeV}$  assuming that the  $\gamma$ -ray spectrum is attenuated by an exponential cutoff. Taking into account that large uncertainties govern the last spectral point measured by EGRET it follows that the allowed energy region where the cutoff resides can be constrained to  $10 \dots 30 \text{ GeV}$ . The narrow allowed range does not leave much freedom for models. The upper limit on the cutoff energy as well as the upper limits from the search in differential bins of energy are compared in Figure 7.7 with theoretical predictions from the polar-cap and the outer-gap model. In the figure, the dotted line represents the spectrum obtained in a polar-cap model (Harding, 2001) that was renormalized to the points of the EGRET spectrum. The thin solid line shows the spectrum of a latest outer-gap model (Hirotani, 2006b).

The polar-cap model predicts a cutoff in the curvature radiation, which is within the allowed region whereas the outer-gap model seems to marginally underestimate the cutoff energy. It has to be emphasized that in all pulsar models the spectral cutoff sensitively depends on model parameters and assumptions. These have to be made because of insufficient experimental constraints as well as incomplete theories about the pulsar magnetosphere. In order to resolve the longstanding question about the cutoff in the curvature spectra, upcoming measurements are needed with higher statistics around  $10 \text{ GeV}$ , e.g. by GLAST or measurements by future ground based experiments with lower

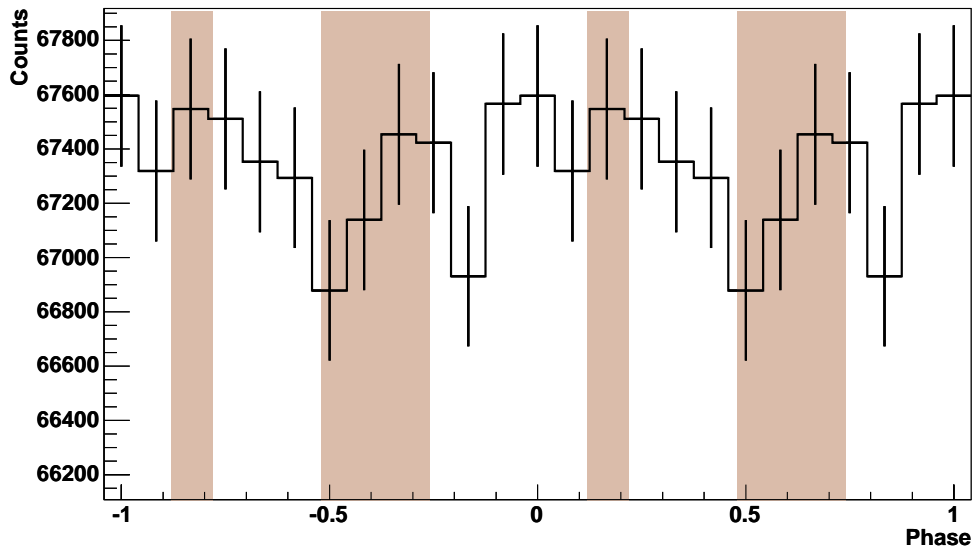


Figure 7.8: Pulse phase profile obtained after selecting events with a SIZE < 300 photoelectrons. The shaded areas indicate phase regions where PSR B1951+32 is emitting at low GeV energies (Ramanamurthy et al., 1995). See also Figure 3.6.

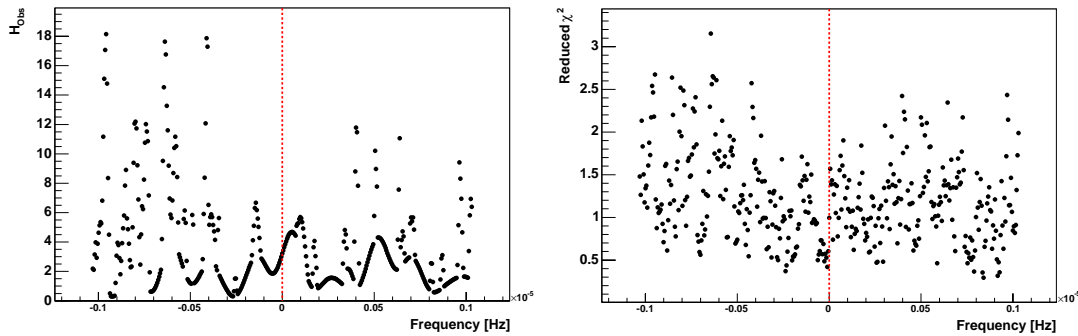


Figure 7.9: Scan around the frequency of the radio ephemeris. An upper size cut of 300 photoelectrons was adopted for this analysis. The left figure shows the result of the H-Test, the right figure shows the result of the  $\chi^2$ -Test.

thresholds than MAGIC, e.g. MAGIC II or CTA, a planned future array of about 100 Cherenkov telescopes.

The predicted inverse-Compton (IC) flux at TeV-energies in the outer-gap model appears to be inconsistent with the derived upper limits. The IC-flux is obtained by assuming that all the magnetospheric soft photons illuminate the equatorial region in which the gap-accelerated positrons are migrating outwards. Therefore, the predicted IC-flux specifies an upper boundary of the possible pulsed TeV emission. The poloidal magnetic field lines could be more or less straight near the light cylinder, as the solution of the time-dependent force-free electrodynamics of an oblique rotator indicates (Spitkovsky, 2006). If this is the case, soft photons from the magnetosphere will not be efficiently upscattered and the IC flux will be significantly reduced. This problem will be solved in future when the self-consistent gap electrodynamics (Hirota, 2006a,b) and the three-dimensional force-free electrodynamics will be combined.

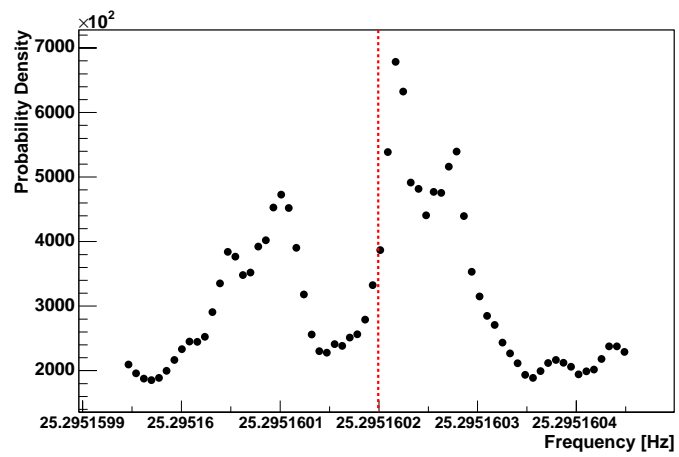


Figure 7.10: Results of the test by Gregory and Loredo (1992) from a scan around the frequency of the radio ephemeris. For this analysis an upper size cut of 300 photoelectrons was used.



## Chapter 8

# The Black Widow Pulsar PSR B1957+20

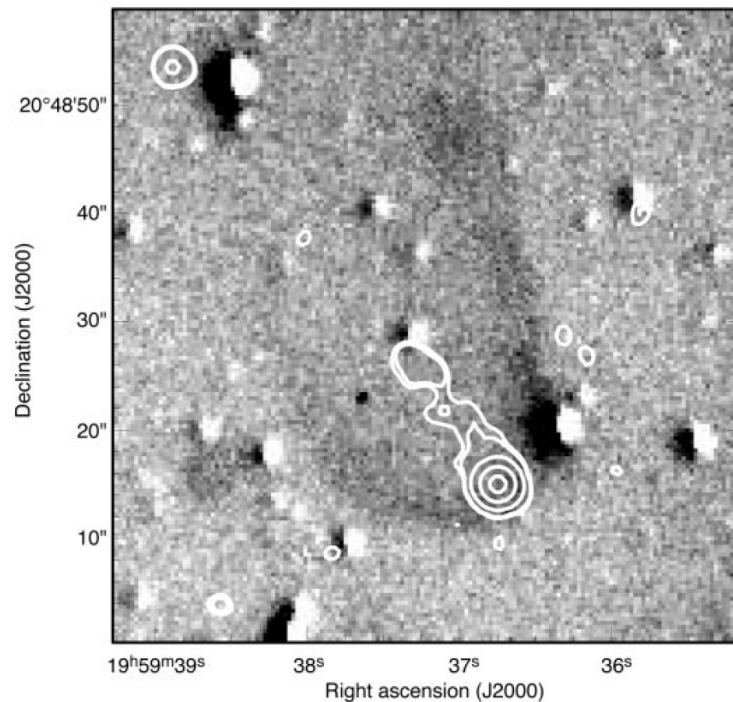
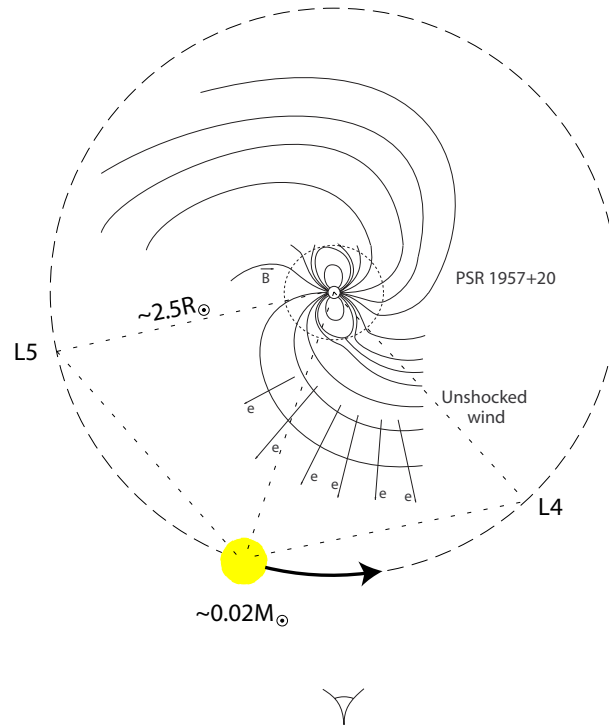


Figure 8.1: X-Ray data from Chandra smoothed to a resolution of 5'' (contours) and overlaid on an H $\alpha$  image obtained from Taurus Tunable Filter service mode observations on the Anglo Australian Telescope on 3rd of August 2000. The x-ray tail is located well inside the boundaries of the H $\alpha$  emission and also close to its symmetry axis. The x-ray contour levels are shown at 0.9, 1.2, 5.3, 35.0, and 78.8% of the peak x-ray surface brightness. The optical residuals correspond to incompletely subtracted stars. Picture and Caption from Stappers et al. (2003).

### 8.1 Introduction

PSR B1957+20 is a “recycled” millisecond pulsar with a spin-down luminosity of  $1.6 \cdot 10^{35}$  ergs/s and in many aspects different to Crab and PSR B1951+32. The period of the pulsar is 1.6 ms

(second shortest known) and has been discovered at first by Fruchter et al. (1988b). PSR B1957+20 is the massive component of a binary system, where a companion star with a mass of  $0.025 M_{\odot}$  orbits the pulsar in 9.17 hr (see Figure 8.2). During 10% of the orbit the radio emission of the pulsar is eclipsed by the companion star. A commonly accepted interpretation of this observation is that the system is viewed almost edge on and that most of the eclipsing material lies outside the companion's Roche lobe, which is constantly replenished by the stellar wind from the companion star (Fruchter et al., 1990). The stellar wind is driven by the energy of the pulsar, thus slowly evaporating the companion. This is the reason why PSR B1957+20 is also called the "black widow" pulsar. Another effect of the pulsar wind is that it is heating the surface of its companion to a few thousand K, making it optically visible (Kulkarni et al., 1988b; Fruchter et al., 1988a).



**Figure 8.2:** Schematic view of the binary system with the pulsar PSR B1957+20. The dimensions of the companion star and the distance between the star and the pulsar are shown in the correct proportions. The magnetic field configuration is magnified for better visibility.

A shock may be formed between the pulsar wind and the ablated wind from the companion where  $e^{\pm}$  pairs with energy  $> 1$  TeV will be cooled by synchrotron emission and inverse Compton scattering. The result may be a TeV  $\gamma$ -ray flux of  $9 \cdot 10^{-11}$  photons  $\text{cm}^{-2} \text{s}^{-1}$  (Harding and Gaisser, 1990). And indeed a tentative detection (significance  $3.7\sigma$ ) of VHE  $\gamma$ -ray emission from PSR B1957+20 at the position of the L4 Lagrange point was reported by Brink et al. (1990). They measured an integral flux  $> 2.7$  TeV of  $1.6 \cdot 10^{-10}$  photons  $\text{cm}^{-2} \text{s}^{-1}$ . Acharya et al. (1990) on the other hand did not detect  $\gamma$ -ray emission and report upper limits  $> 4.3$  TeV of  $1.9 \cdot 10^{-10}$  photons  $\text{cm}^{-2} \text{s}^{-1}$  at the position of the L4 Lagrange point.

Due to the age of the pulsar the strength of the magnetic field is rather low ( $1.67 \cdot 10^8$  G). The effect of photon-photon pair creation and thus the screening of  $\gamma$ -rays in the magnetosphere is reduced with respect to canonical (young) pulsars. Bulik et al. (2000) predict a curvature radiation component that is extending beyond 100 GeV at a detectable flux level for MAGIC. The detection of this pulsed component is complicated a) by the short period of the pulsar of 1.6 ms and b) by signal propagation delays within the binary system. The latter one is particularly severe as the orbital parameters of the system show irregularities on time scales of month, which have to be taken into account in the analysis.

## 8.2 Selection and Processing of the Data Sample

Data on PSR B1957+20 was taken with MAGIC in the year 2004 and 2005. 7.4 hours of data were rejected due to bad weather. 13.08 hours remained for analysis. A summary of the data is given in Table 8.1.

The data sample was processed as outlined in Chapter 5. The F-factor method was used for calibration of the data and the events were cleaned with the time image cleaning procedure with absolute cleaning levels of 6 and 4 photoelectrons. For the generation of sky maps the cleaning levels have been increased to 10 and 8 photoelectrons.

Table 8.1: Summary of the observation of PSR B1957+20 with MAGIC. The extinction coefficient was taken from public data available from the Carlsberg Meridian Telescope. The coefficient provides the extinction for an effective wavelength of 625 nm. A night is considered to have a good photometric quality in optical astronomy if the extinction coefficient (Ext. Coef.) is 0.09 mag and if the scatter of the extinction coefficient (Sc. Ext. Coef.) over the whole night is below 0.06 mag.

Date	Rates [Hz]	On Time [min]	Ext. Coef. [mag]	Sc. Ext. Coef. [mag]	selected
07.10.2004	198	25	0.106	0.011	yes
08.10.2004	200	11	0.113	0.021	no
10.10.2004	202	33	0.116	0.016	yes
16.10.2004	196	41	0.172	0.019	no
31.07.2005	174	131	0.088	0.013	yes
02.08.2005	174	58	0.092	0.013	yes
04.08.2005	181	117	0.084	0.006	yes
08.08.2005	154	102	0.172	0.034	no
10.08.2005	171	53	0.096	0.015	yes
12.08.2005	172	24	0.090	0.015	yes
27.08.2005	125	59	n.a.	n.a.	no
04.09.2005	146	70	0.337	0.032	no
06.09.2005	165	76	0.243	0.029	no
23.09.2005	171	38	0.109	0.011	yes
25.09.2005	165	87	0.104	0.006	yes
27.09.2005	164	70	0.114	0.021	yes
29.09.2005	173	69	0.143	0.031	yes
30.09.2005	146	83	0.211	0.042	no
03.10.2005	168	80	0.125	0.068	yes

## 8.3 Search for steady $\gamma$ -Ray Emission

PSR B1957+20 is part of a binary system. A search for steady  $\gamma$ -ray emission was performed a) on the full data sample and b) by performing an orbital-phase resolved analysis.

### Search for $\gamma$ -Ray Emission in the full Data Set

The full data set was searched for a steady  $\gamma$ -ray flux from the direction of PSR B1957+20 using different analysis thresholds. The results of this analysis are summarized in Table 8.2.

Above 100 GeV and above 200 GeV an excess was observed in the |ALPHA|-distribution with a significance of  $4.88\sigma$  and  $2.29\sigma$  respectively. In the complementary analysis with the DISP-method no signal was found in the  $\theta^2$ -distributions. Moreover, the excess is only observed in the data from 2005. A closer inspection of the 2005 data revealed a hot spot in the distribution of shower images in the camera, probably produced by sparks. Therefore the observed excess in the ALPHA-distribution is likely to be attributed to an instrumental artefact.

Upper limits on the number of excess events have been calculated with the method by Rolke et al. (2005) (95% confidence level). Corresponding limits on the flux have been computed as outlined in Section 5.9, assuming a spectral slope of 2.6. The limits are listed in Table 8.2 and depicted in Figure 8.3.

Table 8.2: Results from an analysis of steady emission from PSR B1957+20 averaged over all observed orbital phases.

Analysis Threshold [GeV]	ON Events	OFF Events	Excess Events	Significance [ $\sigma$ ]	Upper Limit Excess Events 95% C.L.	Flux Upper Limit [ $\text{cm}^{-2}\text{s}^{-1}$ ]
> 100	25178	24143	1034	4.88	2644	$1.79 \times 10^{-10}$
> 200	1922	1790	132	2.29	385	$2.08 \times 10^{-11}$
> 400	301	305	-4.2	-0.18	50	$2.45 \times 10^{-12}$
> 600	97	103.2	-6.2	-0.47	25	$1.11 \times 10^{-12}$
> 800	40	45.9	-5.9	-0.67	15.09	$8.60 \times 10^{-13}$
> 1000	24	24.9	-0.9	-0.14	15.7	$9.36 \times 10^{-13}$
> 2000	3	0.3	2.7	2.19	9.9	$6.29 \times 10^{-13}$

### Search for $\gamma$ -Ray Emission in the Vicinity of the PSR B1957+20

Using the DISP-method (cf. Section 5.6) I have produced maps of the region of the sky around PSR B1957+20. Two maps smeared with a Gaussian kernel of  $0.1^\circ$  are shown in Figure 8.4. The maps have been computed for events with energies  $\sim 160$  GeV and for events with energies  $> 280$  GeV. No significant excess is visible in the maps.

### Orbital Phase resolved Search for $\gamma$ -Ray Emission

Motivated by a possible variable  $\gamma$ -ray flux due to a modulation by the interaction of the pulsar wind with the stellar wind, the  $\approx 9$  hour orbit has been divided in ten equally spaced bins. No signal was found for different analysis thresholds. For the searches at energies  $> 200$  GeV and  $> 400$  GeV respectively light curves as well as upper limits on the integral flux are given in Figure 8.5. Note that the light curve for energies  $> 200$  GeV is offset from zero. The reason is the previously discussed instrumental artefact, which produces a fake signal in the |ALPHA|-distribution.

With a  $\chi^2$ -test it has been tested whether any variability was present in the light curves. The light curve  $> 200$  GeV is constant with a probability of 7%. With a probability of 29% the light curve  $> 400$  GeV shows a somewhat better agreement with the zero hypothesis.

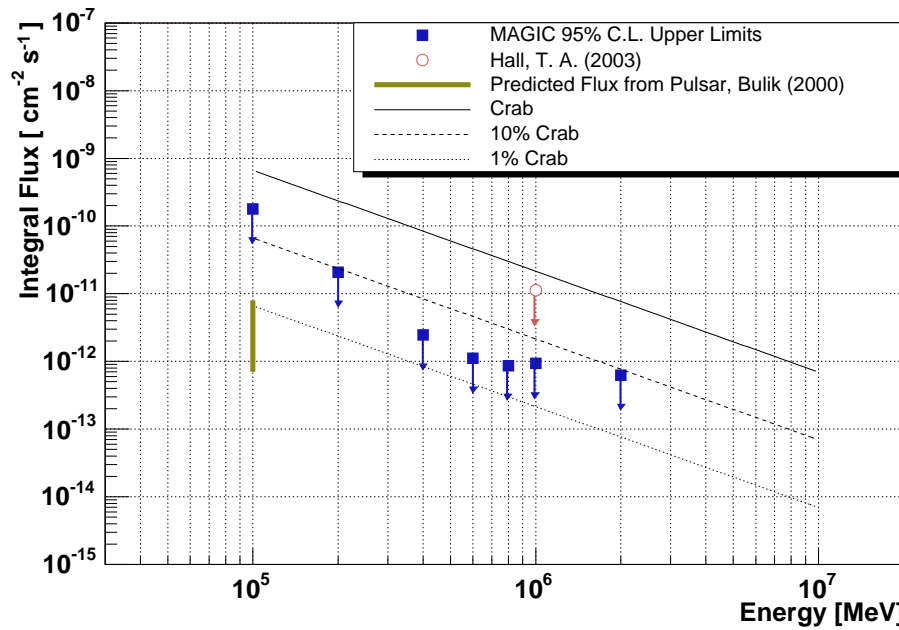


Figure 8.3: Integral upper limits (95 % Confidence Level) for the steady emission from the direction of PSR B1957+20

Judging from the orbital phase averaged upper limits in Figure 8.3 and the light curves in Figure 8.5  $\gamma$ -ray emission  $> 2.7$  TeV on the level of  $1.6 \cdot 10^{-10}$  photons  $\text{cm}^{-2} \text{s}^{-1}$  as claimed by Brink et al. (1990) can be clearly excluded to originate from the direction of PSR B1957+20 at the position of the Lagrange point L4.

## 8.4 Search for $\gamma$ -Ray Emission from the Pulsar

An analysis for pulsed emission could not be performed on the data set as no valid ephemeris of the pulsar and the binary system were available. Parallel observations in radio have been done on PSR B1957+20 with the Giant Meter Radio Telescope in Pune, India but it was not possible to extract accurately enough ephemeris from the recorded data.

## 8.5 Discussion

The observation of PSR B1957+20 with MAGIC did not result in the detection of a  $\gamma$ -ray signal, neither by analyzing the full data sample nor by subdividing the data sample into 10 equally distributed bins over the orbit of the binary system. Despite an instrumental effect, which fakes a signal in the data, one can firmly exclude the tentative reports of a positive detection by Brink et al. (1990). The flux upper limit  $> 400$  GeV at the Lagrange point 4 is on the level of  $5 \cdot 10^{-12}$  photons  $\text{cm}^{-2} \text{sec}^{-1}$  or  $\lesssim 6\%$  Crab.

An analysis for pulsed emission could not be made. The predictions for pulsed emission by Bulik et al. (2000) cannot be constrained with the observation presented here.

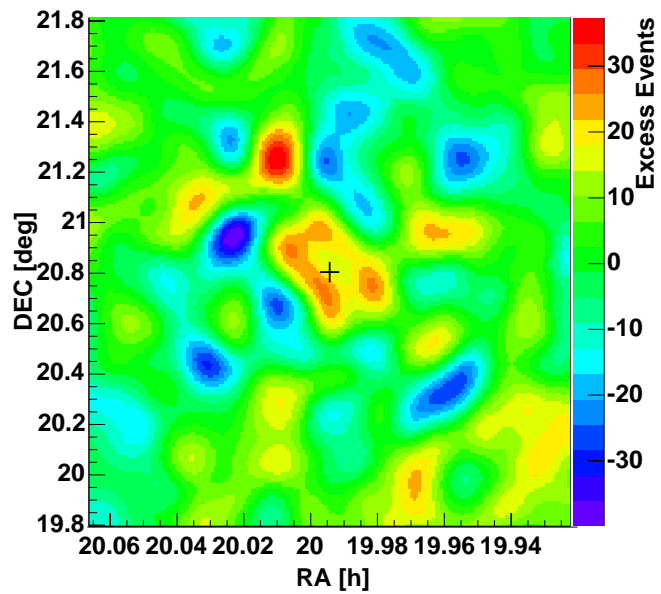
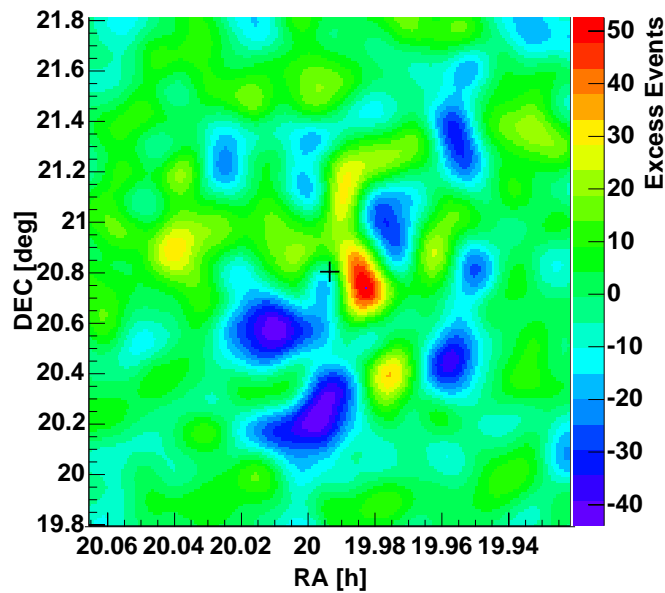
(a)  $\sim 160$  GeV(b)  $> 280$  GeV

Figure 8.4: Sky maps of the region around PSR B1957+20. The skymaps are smoothed with a Gaussian kernel of  $0.1^\circ$ . The position of the pulsar is marked with a cross.

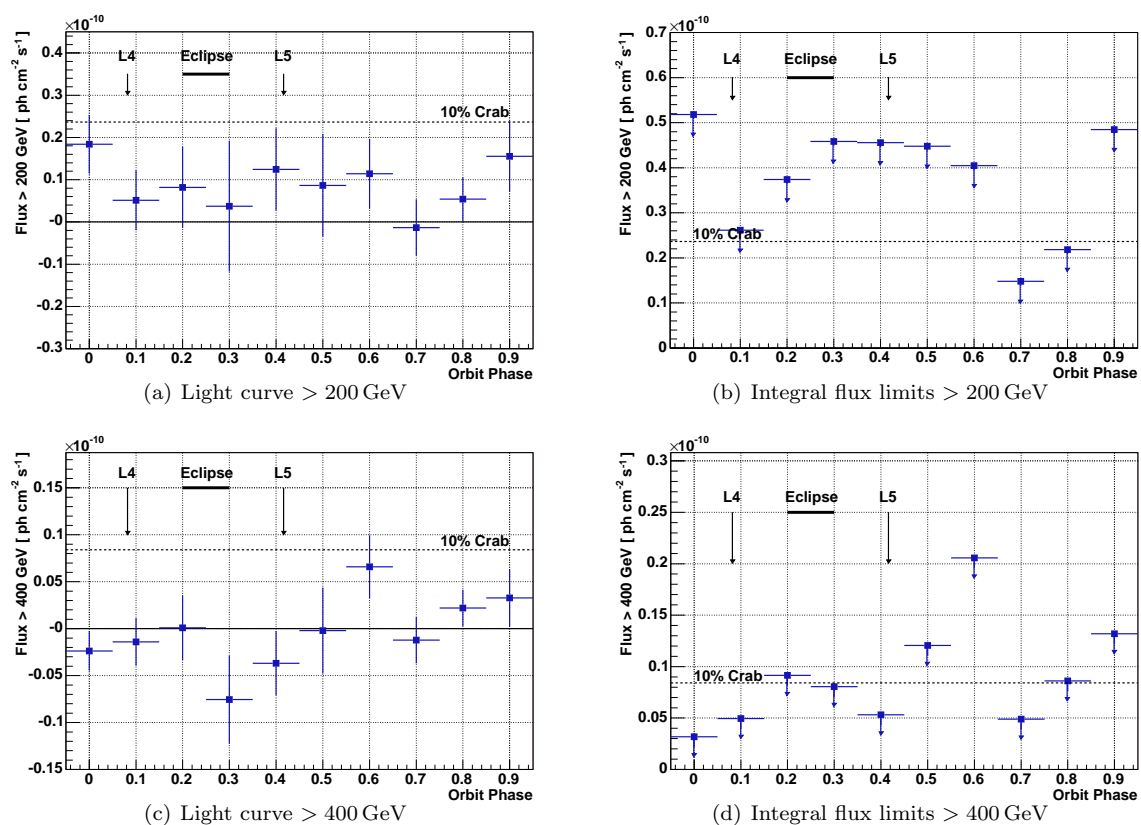


Figure 8.5: Flux measurements of PSR B1957+20 in phase bins of the binary orbit. Upper row: for energies  $> 200$  GeV; lower row: for energies  $> 400$  GeV. On the left side the measured flux is given whereas in the right panels the 95% confidence level upper limits on the flux are shown. The position of the eclipse of the radio emission as well as the positions of the Lagrange points L4 and L5 are also indicated.



## Chapter 9

# A novel Photon Detector Concept for Experiments in High Energy Physics

### 9.1 Need for new Photon Detectors for VHE $\gamma$ -Ray Astronomy

Most of today's high energy astroparticle physics experiments rely on efficient photon detectors, which must also often have single photon response, respectively single photoelectron response (SER). Ground-based examples are air shower fluorescence detectors, imaging air shower Cherenkov telescopes (IACTs), neutrino detectors in ice or water. Space-based examples are planned satellites for the study of the highest energy cosmic rays  $\gtrsim 10^{19}$  eV.

Up to now only PMTs are used as photon detectors. PMTs have, except a few prototypes, a peak QE around 25%. It is obvious that in IACTs the peak QE (around 25%) and the average QE (of 12%-15%) are the key limiting elements to convert the Cherenkov photons into analyzable electric signals.

Basically two objectives drive the development for better instruments in ground-based  $\gamma$ -ray astronomy:

- Improvement of the sensitivity of experiments by one order of magnitude
- Lowering of the threshold energy down to 10 GeV both on the trigger- and if possible, also on the analysis-level

The lowering of the threshold energy is needed in order to observe high red shift  $\gamma$ -ray sources such as distant extragalactic sources e.g. active galactic nuclei (AGNs), sources with soft spectra and  $\gamma$ -ray pulsars in our own Galaxy.

At  $\gamma$ -ray energies  $> 100$  GeV where the classical  $\gamma$ /hadron-separation is working well, the sensitivity can be improved by either increasing the effective collection area of the experiment or by recording finer details of the shower development such as by stereo observations or by collecting more Cherenkov photons and increased photon to photoelectron conversion. The straightforward way to increase the collection area by one order of magnitude is to distribute 100 telescopes over an area of  $1 \text{ km}^2$ . To increase the number of recorded photoelectrons requires large diameter mirrors and better photon detectors similarly as for the lowering of the threshold.

At trigger level one gains access to lower  $\gamma$ -ray energies by increasing the recorded Cherenkov signal of each telescope. This can be accomplished by:

1. Enlarging the reflector surface of the telescope
2. Reduction of losses of photons in the optical system such as by low reflectivity, large angles scattering or transmission losses
3. A higher conversion efficiency from Cherenkov photons to photoelectrons

The latter option is the most promising one, but is more challenging as it implies the development of new, more sensitive photon detectors<sup>1</sup>. With new high sensitive photon detectors smaller telescopes could be constructed, such avoiding the mechanical instabilities and financial limitations of a reflector well beyond the size of MAGIC. Secondary advantages of smaller telescopes are a faster positioning in case of gamma-ray burst (GRB) observations or less wind load in case of strong storms. Reflectivity losses are already fairly small and no more big gain can be achieved. Also costs rise disproportionately.

At the analysis level one of the main problems is the suppression of the background at lower energies. In Figure 5.6 it is illustrated that below  $\sim 150$  GeV the ability to differentiate between  $\gamma$ 's and background in MAGIC is rapidly deteriorating. High efficient photon detectors with ultra fast timing and single photon resolution may be able to provide the ultimate information needed to perform the task of better suppressing the background (Mirzoyan et al., 2006).

## 9.2 Photon Detector Requirements for Imaging Air Cherenkov Telescopes e.g. as for a MAGIC Type Telescope

In the following I summarize the requirements of photon detectors for Imaging Air Cherenkov Telescopes. Some requirements are telescope dependent, e.g. the sensor size. In such a case specifications for the MAGIC telescope are quoted. Topics discussed are:

- sensitive wavelength range
- single photoelectron count rate capability
- photon detector intrinsic dark rate
- dynamic range
- event rate capability
- mechanical and operational constraints

**sensitive wavelength range:**  $\sim 280 \dots \sim 600$  nm; The lower wavelength limit is given by transmission losses of Cherenkov photons in the atmosphere (cf. Figure 4.5), primarily by the ozone cutoff and secondarily by Rayleigh scattering (particularly for large zenith angle observations). Towards larger wavelengths the intensity of Cherenkov photons decreases proportional to  $1/\lambda^2$  (cf. section 4.1.3). At the same time the intensity of the NSB is increasing (Benn and Ellison, 1998). Optimal signal  $S$  (Cherenkov light) to background ( $NSB$ ) is found by restricting the sensitivity to wavelengths where

$$\frac{\Delta S}{\sqrt{\Delta NSB}} = \int_{280 \text{ nm}}^{\lambda_{\text{max}}} \frac{S(\lambda)}{\sqrt{NSB(\lambda)}} d\lambda \quad (9.1)$$

---

<sup>1</sup>Besides increasing the effective QE of the photosensors one has also the option to improve the mirror focusing and the mirror reflectivity and the light catcher reflectivity. The potential gain of these improvements is much lower.

is maximum, e.g.  $\lambda_{\max} = 700 \text{ nm}$ . The precise value of the upper boundary very much depends on the actual response of the detector and the zenith angle.

**single photoelectron count rate capability: 1 phe per  $\mu\text{sec}$  per  $\text{mm}^2$  sensor area;** The minimum required single photoelectron count rate capability depends besides on the mirror area also on the region of sky (galactic/extragalactic) that is observed as well as on the angular acceptance, the sensitive wavelength range and the QE of the photon detector. The angular acceptance of the Winston cone that is attached to each PMT in MAGIC is  $\sim 26^\circ$ , i.e. the accepted solid angle per pixel is 0.66 steradian. The resulting average background (NSB) count rate in MAGIC is 1 photoelectron per 10 nanoseconds per pixel ( $\equiv 1 \text{ phe}/\text{mm}^2/10 \mu\text{sec}$ ). If the telescope is equipped with more efficient photon detectors ( $\text{QE} \gg 20\%$ ) they have to have a single photoelectron count rate capability of  $\sim 1$  photoelectron per  $\mu\text{sec}$  per  $\text{mm}^2$  sensor area.

**limit of the intrinsic dark rate of the photon detector:  $< 10^5$  counts per sec per  $\text{mm}^2$  sensor area;** The maximum allowed intrinsic dark rate of the photon detector is closely linked to the NSB, which sets the ultimate non suppressible background. An average dark count rate of 25% of the NSB level is considered acceptable.

**required dynamic range:  $\sim 100$  phe per  $\text{mm}^2$  sensor area;** To correctly reconstruct the energy of  $\gamma$ -rays  $> 10 \text{ TeV}$  a dynamic range of  $\sim 100$  phe per  $\text{mm}^2$  sensor area within a few nanoseconds is necessary, if one assumes a size of the reflector similar to that of MAGIC and a photon detection efficiency close to 100%.

**mechanical and operational constraints;** Beside the above mentioned physics requirements additional operational requirements have to be taken into account. These are either essential for a successful operation of the experiment or simplify the operation of the telescope and the analysis of the data.

- The size of the photon detector building blocks (pixels) should be at least  $5 \times 5 \text{ mm}^2$ , or better  $10 \times 10 \text{ mm}^2$ . Otherwise it will become difficult to overcome the dead area between individual photon detectors with light concentrators. Small pixels are in principle no problem for the readout as the outputs of individual pixels can be combined to form a single readout channel.
- In future one will aim to operate a telescope for about 10 years with as little access for maintenance as possible. This requires robust, long living, non aging and stable photon detectors. Stability and reliability become more important than in today's IACTs.
- Fluctuations of the parameters (in particular the photon detection efficiency) between photon detector elements must be kept to a minimum already at the production level. This is particularly important for future large experiments where a careful selection of individual photon detector elements becomes unrealistic due to the huge demand for photon sensors.
- The current high price of photon detectors used in IACTs is a major factor when building the telescope(s). Cost reduction would be envisaged.

## 9.3 The Concept of the Silicon Photomultiplier

In the nineties a novel semiconductor photon detector concept (Bisello et al., 1995; Golovin and Saveliev, 2004; Buzhan et al., 2003) was developed that in principle could meet all the requirements that have been mentioned in the previous section. It is also a promising candidate for the photon detector in other experiments in astroparticle physics and high energy physics (Otte, 2006; Otte et al., 2006). Currently, the detector is still in its development phase.

Due to many parallel developments many different names exist for basically the same concept: Metal Resistive layer Semiconductor (MRS-APD), Silicon Photomultiplier (SiPM), Multi Photon Pixel Detector (MPPD), Micro-Cell APD, Geiger APD, Digital Pixel Photo Diode (DPPD), . . . , etc. . Hereafter I will use SiPM as a synonym of the many different types making use of basically the same principle.

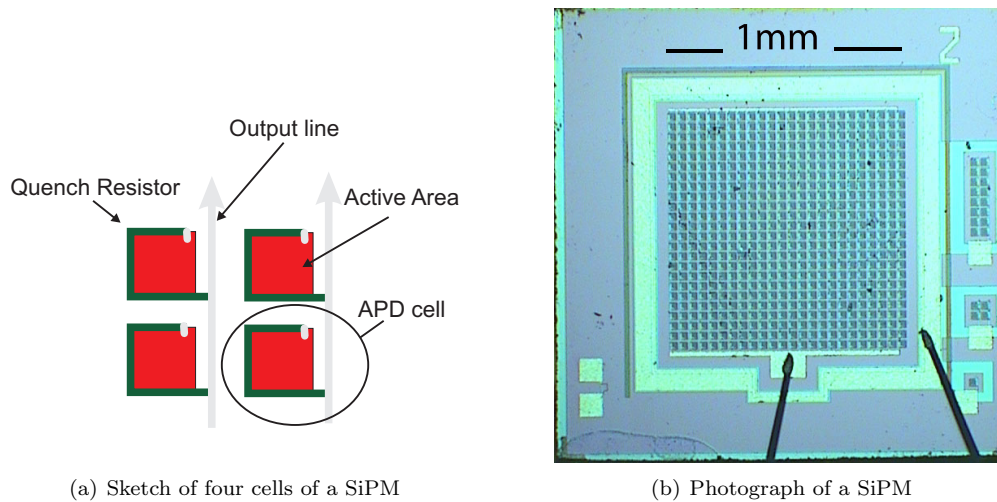


**Figure 9.1:** The silicon photomultiplier; The left picture shows four cells of a SiPM and the right photograph a prototype SiPM comprising 576 cells. The device was developed and produced by MEPhI and Pulsar enterprize.

Figure 9.1(b) shows a prototype SiPM that was produced in MEPhI<sup>2</sup> and Pulsar enterprize, Moscow in 2003. The device has an active area of  $(1 \times 1) \text{ mm}^2$  inside which 576 avalanche photo diodes, hereafter called cells, are implanted on a silicon chip.

Each cell operates in the limited Geiger mode, i.e. each cell is biased via an integrated resistor to a voltage slightly above breakdown. In this mode an electrical breakdown of the reversely biased junction can be triggered by a single photoelectron. The breakdown results in a well measurable output signal. A drawback but also an advantage is that the output signal is standardized i.e., independent of the number of photons that have been absorbed in the cell. The concept of the SiPM bypasses this problem by dividing the detector area into many cells, which are small enough to ensure that in case of low light level signals at most only one photon is hitting and absorbed by one cell.

All cells of a SiPM are connected to a common anode bus. Each cell is independently operating from the other ones as a large ( $\sim \text{M}\Omega$ ) resistor is connected in series to each cell (s. Figure 9.1(a)). Apart from decoupling the cells from each other the resistor also ensures that the current that flows through the cell during breakdown is limited. Thus the breakdown quenches in a very short time (within a few nsec).

The signals from all cells are added up on the bus and thus the output signal of a SiPM is the summed up signal of all coinciding in time "fired" cells. An information which cells fired is not available.

The SiPM has two terminals, one for the bias voltage and another one for the output signal. Care has to be taken that the output terminal is DC coupled to the ground.

After this rather short introduction of the SiPM, I will describe in more detail some characteristics. At first I will elaborate briefly on the now classical linear mode avalanche photodiode (APD),

<sup>2</sup>Moscow Engineering Physics Institute (State University)

then on the principle of small area APD operating in the limited Geiger mode and finally on characteristics specific to SiPMs.

## 9.4 Characteristics of the Silicon Photomultiplier

### 9.4.1 The Principle of the Geiger Avalanche Diode

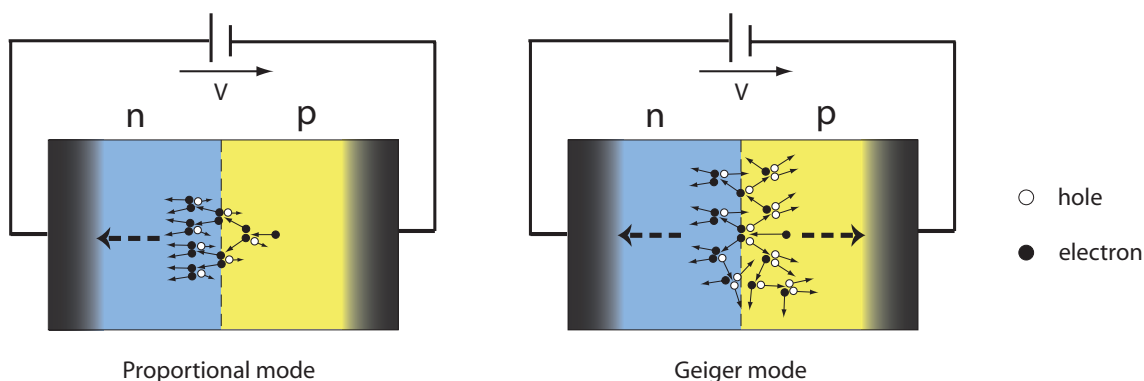


Figure 9.2: Left figure: Sketch of the multiplication process in an avalanche diode that is reverse-biased slightly below breakdown voltage—multiplication only by electrons (proportional mode). Right Figure: Multiplication process in an avalanche diode that is reverse-biased above breakdown voltage—multiplication by electrons and holes (Geiger mode). In Geiger mode the avalanche diverges, whereas in proportional mode the avalanche stops automatically as the avalanche “propagates” only in one direction.

#### The classical APD

Avalanche Photo Diodes (APDs) in proportional mode are semiconductor photon detectors with very high detection efficiencies, with a large dynamic range and internal gain ranging between 10 to a few hundred, in rare cases up to a few 1000. The  $pn$ -junction of an APD is reversed biased, slightly below the breakdown voltage (Figure 9.2). APDs have an excess noise factor<sup>3</sup>  $F^2 \geq 2$  due to the statistical nature of the multiplication process. At high gains the excess noise factor can easily rise to very large values ( $F^2 \gg 2$ ). The large excess noise factor prevents to separate the individual photoelectron peaks from each other as well the single photoelectron peak from the pedestal.

For illustration of this effect a simulated pulse height distribution of the output signal of a proportional APD is shown in Figure 9.3. In this Monte Carlo simulation the multiplication (avalanche) has been generated 10,000 times for several cases of signals from 1 to 4 photoelectrons. In this toy avalanche model the multiplication process might occur at 1000 discrete steps. In each step an electron is accelerated by the high electrical field in the  $pn$ -junction and can generate an electron-hole pair by losing its gained kinetic energy (impact ionization). This process has a certain probability  $< 1$ . In my toy model I assume that holes, drifting in the opposite direction are unable to participate in the pair production (an important requirement for the linear mode APD, see Figure 9.2). In each new step the kinetic energy of all electrons is set to zero, regardless if an electron has generated a new electron-hole pair or not. In the next step the process can repeat. The

<sup>3</sup>The excess noise factor is the ratio of the actual noise to that existing if the multiplication process in the APD were noiseless.

probability for multiplication has been chosen such that on average in each avalanche 1000 secondary electrons are generated. The simulated pulse height distribution reproduces the expected exponential behavior for the distribution of the output signal in the case the input signal is always one photoelectron. Only in case of  $\geq 2$  photoelectrons the distributions are clearly separated from zero. In case of a large number of photoelectrons  $N$  the signal distribution approaches a Gaussian with a  $\sigma \propto \sqrt{F \cdot N}$ ,

In reality the situation is worse because also holes participate (with lower probability) in the multiplication process. Also, because of the small signal, noise and pickup can become critical.

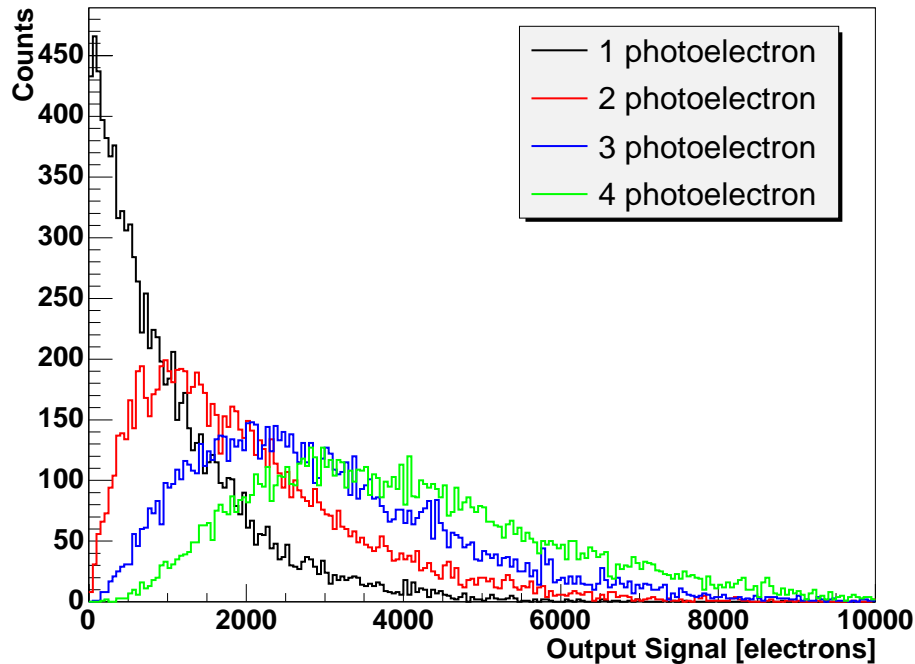


Figure 9.3: Simulated pulse height distribution of output signals of an APD operating in proportional mode for different input signals. The average gain is 1000 per initial photoelectron.

APDs operated at high gain, i.e. close below breakdown, show a strong dependence of the gain on temperature and bias voltage (e.g. 3% change in gain per one volt difference in bias supply and -2.2% change in gain per one degree temperature difference both at a nominal gain of 50 (Grahl et al., 2003). This is a specific example. In general the voltage and the temperature effects are strongly device dependent. However, very good temperature and bias voltage stability are generally required. Another limiting factor is the rather low gain of proportional mode APDs ( $< 1000$ ), which requires high quality, low noise amplifiers, restriction in operation bandwidth and special precautions to prevent pickup.

Besides electron(-hole pairs) generated by photon absorption also thermally generated electrons in the depletion layer of the  $pn$ -junction can initiate avalanches. In large area APDs this can become a serious background, particularly if one raises the bias voltage close to the breakdown voltage. Just below breakdown hole multiplication sets in, which makes the entire multiplication process unstable.

### Small Area APDs operated in the limited Geiger Mode

Limitations in gain and most of the gain stability problem can be avoided in small area APDs when operating them in the limited Geiger mode instead of in the proportional gain mode, i.e. by increasing the bias voltage slightly (10%–20%) above breakdown voltage (see Figure 9.2). If

the active volume is small it can be kept free for prolonged times of free electrons/holes. In this mode, a single free electron or hole can trigger a diverging avalanche multiplication process. In contrast to the proportional mode, where by constructive means basically only electrons generate additional electron hole pairs, the avalanche in the limited Geiger mode is diverging because both electrons and holes actively participate in the multiplication process (see Figure 9.2). A high current can flow through the junction. If the current is limited to below a critical value, the current flow is disrupted (quenched) a certain time (between picoseconds and nanoseconds) after the breakdown has started, due to statistical fluctuations. A simple method to achieve quenching is by adding a high ohmic resistor (integrated or external) in series to the diode. After quenching, the resistor prevents an instantaneous recharge of the diode capacitance up to the initial bias voltage. Depending on the resistor the bias voltage is typically reset in a few 100 nsec. Due to the diverging nature of the multiplication, any information about the primary signal (i.e. the number of initially generated photoelectrons) that initiated the breakdown is lost. The device operates in a binary mode. Therefore, it is strictly speaking incorrect to talk about gain if one addresses the output charge of such a device.

The quenching of the breakdown can also be achieved by a dedicated electronic circuit that is triggered by the breakdown and that lowers the bias voltage below the breakdown voltage for a certain period of time until the breakdown is quenched.

The limited Geiger mode is only useful for very small area avalanche diodes because besides free electrons being generated by the photoeffect, electron-hole pairs are constantly generated thermally. In silicon at room temperature (20°) a thermal generation rate as low as  $6 \times 10^8$  pairs per second per  $\text{cm}^2$  can be achieved in  $450\mu\text{m}$  thick fully depleted material. Without cooling only small volumes can be free of thermally generated electron-hole pairs for prolonged time periods. Traps filled during the breakdown and releasing the trapped charge carriers after the diode is reset are another source of triggers. In combination with the recovery time of the diode these effects set an upper limit to the area of the diode/cell.

Small area APDs operated in the Geiger mode have the advantage of large, well defined output pulses ( $10^5 \dots 10^7$  electrons, depending on the overvoltage and diode capacitance) per breakdown, and can be used for "single photon counting". Such single cell APDs are often referred to as Single Photon Avalanche Counters (SPADs). The concept of SPADs has been developed already more than 30 years ago (e.g. Oldham et al., 1972; Ingerson et al., 1983; Lacaíta et al., 1993; Kindt and van Zeijl, 1998) and these devices are commercially produced but have not achieved widespread use. In fact, SPADs are only found in applications that require low rate, single photon counting, and where a small size detector is sufficient (typically 100 to 10,000  $\mu\text{m}^2$  sensitive area). Due to their inability to resolve the number of primary photons, respectively photoelectrons, SPADs can, e.g. not be used in calorimetry. A more detailed discussion about the physics, quenching methods and history of APDs in Geiger mode can be found e.g. in Cova et al. (2004).

The next step to overcome the SPAD single cell structure was to combine many but very small cells to a single unit, the silicon photomultiplier, which was already introduced earlier (page 119). With the SiPM it is now possible to retain an information about the number of photoelectrons as long as the average number of photoelectrons per cell is  $\ll 1$  per unit recovery time.

I will now elaborate on specific characteristics of SiPM. A small signal model of the SiPM is discussed as well as the photon detection efficiency, optical crosstalk and the dynamic range.

#### 9.4.2 A Small Signal Model of the Silicon Photomultiplier

Figure 9.4 shows the small signal model that I have developed to characterize the output signal of the SiPM. In the model the small signal properties of a cell are described by the part of the circuit that is emphasized in the shaded region.

A cell consists of a diode and the quenching resistor  $R_q$ . The diode has a parallel capacitance  $C_d$

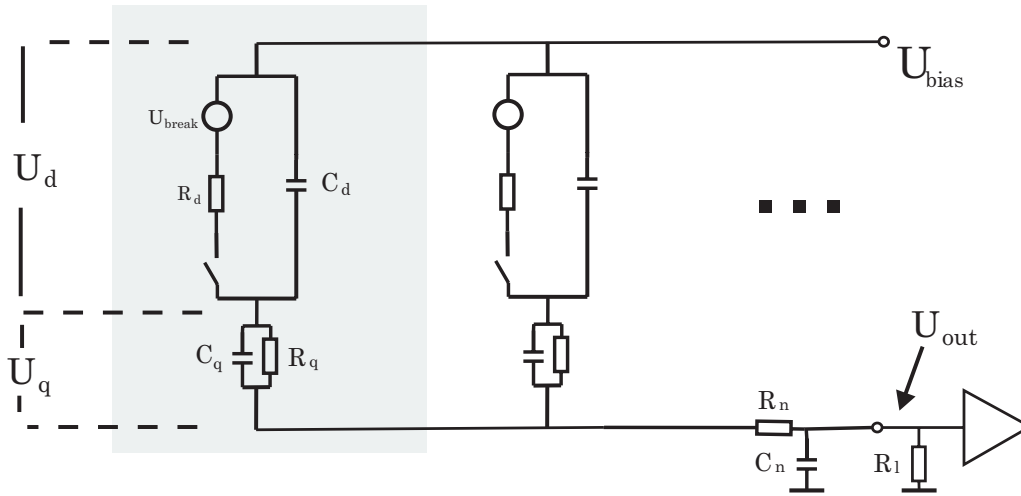


Figure 9.4: Small signal replacement circuit of a SiPM. To the left the replacement circuit of two SiPM-cells is shown. The characteristics of the output network is described with a RC-low-pass filter. Connected to ground is the load resistor, which is followed by an amplifier.

that is typically  $\sim 10$  fF. During breakdown the junction is low ohmic with a varying conductivity and is behaving like a voltage source  $U_{break}$ . For simplicity it is assumed that the conductivity  $1/R_d$  and the output of the voltage source are constant during breakdown. Typical values for  $R_d$  found in the literature and in simulations are 10 k... 100 k $\Omega$ .

The breakdown develops for  $\sim 10$  psec (Lacaita et al., 1993), i.e. much faster than any other time constant in the system. Therefore, it is sufficient to describe the onset of the breakdown as a switch that is being closed and opened again at quenching. The condition for quenching is satisfied once the current that flows through the junction drops below a critical value of  $\sim 10 \mu A$ .

The measured output signal is the displacement current that flows during breakdown and after quenching through  $C_q$  and  $C_d$ . On top of the displacement currents is adding the current that flows in parallel through the quenching resistor and the junction resistance.

The characteristics of the low ohmic network that connects all cells is described in the model by a low-pass network ( $R_n$  and  $C_n$ ).  $R_n$  is a small series resistor and  $C_n$  a parasitic parallel capacitance.  $R_l$  is the load resistor, which is either the input resistance of the preamplifier the SiPM is connected to or any other combination of parallel resistors, connected in series between the output of the SiPM and ground. Typically a value of 50  $\Omega$  is chosen for  $R_l$ .

In this model the potentials across  $R_l$  ( $U_{out}$ ),  $R_q$  ( $U_q$ ) and the diode ( $U_d$ ) are jointly connected by means of three coupled differential equations during breakdown<sup>4</sup>:

$$\dot{U}_d = (U_{break} - U_d) \cdot \frac{1}{R_d \cdot C_d} - (U_d + U_{out} + U_q - U_{bias}) \cdot \frac{1}{R_n \cdot C_d} \quad (9.2)$$

$$\dot{U}_{out} = -U_{out} \cdot \frac{1}{R_l \cdot C_n} - (U_d + U_{out} + U_q - U_{bias}) \cdot \frac{1}{R_n \cdot C_n} \quad (9.3)$$

$$\dot{U}_q = -U_q \cdot \frac{1}{R_q \cdot C_q} - (U_d + U_{out} + U_q - U_{bias}) \cdot \frac{1}{R_n \cdot C_q} \quad (9.4)$$

$$(9.5)$$

<sup>4</sup>Note that  $U_{out}$ ,  $U_q$  and  $U_d$  are time dependent;  $\dot{U}_{out}$ ,  $\dot{U}_q$  and  $\dot{U}_d$  are the corresponding time derivatives.

where  $U_{bias}$  is the bias voltage across the SiPM. The same equations without the first term on the right hand side of equation 9.2 describe the return of the potentials to their original values after the breakdown is quenched. The initial conditions are  $U_d(0) = U_{bias}$ ,  $U_{out}(0) = U_q(0) = \dot{U}_d(0) = \dot{U}_{out}(0) = \dot{U}_q(0) = 0$ .

### Application of the Model

The differential equations have been numerically solved for  $U_{out}$  in Figure 9.5. The parameters used in this specific case have been:

$$R_d = 10 \text{ k}\Omega, \quad C_d = 2 \text{ fF}, \quad R_n = 1 \text{ m}\Omega, \quad R_l = 50 \Omega, \quad C_n = 50 \text{ pF}, \quad R_q = 500 \text{ k}\Omega, \\ C_q = 100 \text{ fF}, \quad U_{bias} = 37 \text{ V}, \quad U_{break} = 35 \text{ V}$$

The breakdown is quenched if the current flowing through  $R_d$  drops below  $20 \mu\text{A}$ . The time of quenching is marked by the vertical line in the Figure.

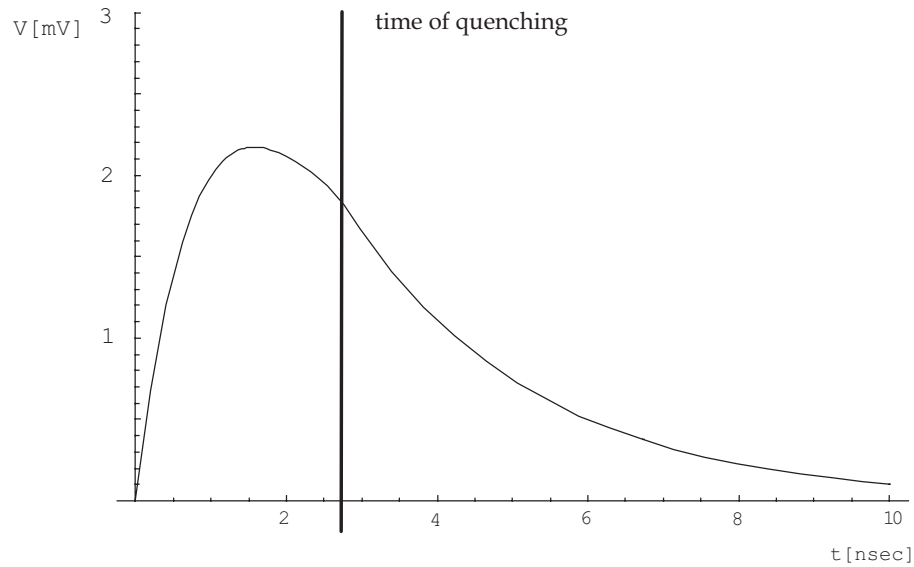


Figure 9.5: Simulated output pulse of a SiPM. See text for details.

### 9.4.3 The Photon Detection Efficiency of SiPMs

The photon detection efficiency (PDE) of a SiPM is usually quoted to describe the sensitivity of the device. This is in contrast to e.g. the characterization of PMTs, where usually the quantum efficiency of the photocathode is quoted and additional losses are neglected<sup>5</sup>. The PDE of a SiPM is a combination of several contributions, see also Figure 9.6 for an  $n$ -on- $p$  structure.

1. partial light losses due to back reflection on the surface (5 in the Figure)
2. photon absorption in the conductive semiconductor top layer (highly doped  $n^{++}$ ) (4 in the Figure)
3. generation of electron-hole pairs in the depleted silicon before the  $p$ - $n$  multiplication zone; important as UV-photons are absorbed within a few hundred nanometers. (4 in the Figure)

<sup>5</sup>e.g. the non perfect collection of photoelectrons onto the first dynode and low multiplication in the first dynode of the PMT

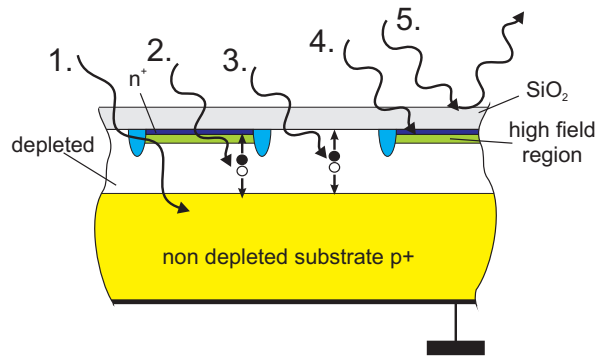


Figure 9.6: Different scenarios that can occur when a photon hits a SiPM: 1. Absorption of the photon in the non depleted substrate; 2. Absorption in the depleted region and subsequent drift of the photoelectron into the high field region; 3. Absorption between two cells; 4. Absorption in the SiO<sub>2</sub> or non depleted implantation below the surface; 5. Reflection on the surface

4. alternatively generation in the  $p$ - $n$  junction or the depletion  $n$ -zone behind the junction (2 in the Figure)
5. or electron-hole pair generation in the non-depleted  $p^+$ -bulk (1 in the Figure)
6. active area fraction (3 in the Figure)
7. efficiency to generate a breakdown (different for electrons and holes)

In first order the PDE is a product of the QE times the breakdown efficiency. In second order the details of the above listed effects have to be taken into account, in third order also the dead time effects from recharging after a breakdown have to be taken into account. Some of the effects are discussed in the following:

**The Quantum Efficiency (QE)** is defined as the average number of electron-hole pairs created by conversion of one photon in the depleted layer of a semiconductor<sup>6</sup>. For photon energies above the band gap of the semiconductor (1.1eV in silicon) the QE is unity and rises above unity if the energy of the photoelectron is sufficient for impact ionization (photon energies >3.6eV in silicon). Photons of shorter wavelengths (<400nm) will mostly be absorbed just beneath the silicon surface within less than 100 nm. If the absorption takes place in the highly doped top implantation layer below the surface, the generated electron/hole pair is most probably lost due to the very short recombination times. The fabrication of very shallow  $p^{++}$  ( $n^{++}$ ) top layers is one of the challenges when producing blue, respectively UV sensitive photon detectors. If, on the other hand, the photon energy is too low (red, respectively IR light), the photon penetrates deeply into the silicon and is mostly absorbed in the non-depleted bulk, or traverses the detector without interaction. Therefore, red, respectively IR sensitive photon sensors need thick depletion layers.

**Losses at the Entrance Window** due to reflection and absorption. Reflection losses  $R$  for vertical incident light on the detector surface are described by the Fresnel formula

$$R = \left( \frac{n - 1}{n + 1} \right)^2 \quad (9.6)$$

where  $n$  is the index of refraction. These losses can be minimized by proper engineering of the entrance window, e.g. by the use of optically pure materials and appropriate layers of

<sup>6</sup>For short wavelength UV light  $\geq 2$  photoelectrons can be generated in case the photon energy exceeds 3.6 eV

intermediate refraction indices. More than 90% transmission can be achieved with a  $\text{Si}_3\text{N}_4$ -layer in between the top  $\text{SiO}_2$ -layer and the Si-detector.

**The effective Area**, i.e. the total area multiplied by the fraction of the sensitive area, is less than unity as the physical separation of cells requires considerable dead space. Current devices have effective area ratios, ranging from 25% up to 60%. Effective areas as high as 80% seem feasible in the foreseeable future. Illumination of the device from the back side might circumvent the limitations of a small effective area (see Chapter 10).

**The Breakdown Probability** is the probability for a single electron (hole) to trigger a breakdown. This depends very much on the electrical field strength in the junction. As saturation of the PDE is observed with increasing overvoltages, it is commonly believed that breakdown probabilities  $\sim 100\%$  can be achieved for photo-generated charge carriers generated in front of the high field region (Oldham et al., 1972). The probability of a breakdown also depends on the type of charge carrier (electron/hole) that enters the high field region. As holes can also initiate the avalanche breakdown it is not mandatory to have e.g. a *p-on-n* structure for blue (UV) sensitive devices.

**The Recovery Time** e.g. defined as the period of time until a cell is again fully sensitive after a breakdown<sup>7</sup>, also has an influence on the detection efficiency for the following reason. After a cell has experienced a breakdown it needs a certain time  $\lesssim \mu\text{sec}$  to recharge to full sensitivity. Triggered by dark noise and background light, typically 0.1%...1% of all cells are always in a state of recovery, which reduces the effective area of the sensor by the same fraction. The decrease in PDE is normally negligible for low light level applications ( $\mathcal{O} 1\%$ ). It should be mentioned that the recovery of individual cells is frequently misinterpreted as a recovery of the whole device. The situation is different in case of intense light flashes or high rate applications when the average time between consecutive events becomes comparable to the recovery time.

Among all mentioned effects, currently the biggest impact on the PDE is the limited effective area. This holds generally true for devices that are composed of many cells with individual quenching resistors. Electrical separation between cells requires a few micrometers dead space. The highest reported PDEs are about 40% (Dolgoshein, 2006a). This is slightly below the geometrical occupancy of these devices times the QE of silicon. In back side illuminated SiPMs (see Chapter 10) dead space is not an issue anymore. Therefore, very high PDEs ( $> 80\%$ ) can be hoped for in such a device.

The measurement of the PDE is not an easy task. Often SiPMs are compared to a photomultiplier with known quantum efficiency (but of unknown photoelectron collection efficiency). In Appendix B I present a method, which allows one to measure the PDE of SiPMs without the use of photomultipliers.

#### 9.4.4 Optical Crosstalk

A well known process in semiconductors is photon emission associated with the avalanche multiplication process (s. Figure 9.7). The origin of this emission is not fully understood (e.g. Villa et al., 1995, and references therein). The situation is complicated by partially contradictory measurements e.g. Lacaita et al. (1993); Swoger and Kovacic (1993); de Kort et al. (1993). Lacaita et al. can describe their measured emission spectrum above 1.7 eV with a Maxwellian curve with an effective temperature of 4000 Kelvin. The same authors have measured the efficiency of photon

<sup>7</sup>Note that the recovery time for a SiPM is different than the recovery time for a proportional mode APD. Because of the quasi digital nature of operation the recovery of a SiPM is conveniently defined as the recovery of a single cell of the SiPM, as the time that is needed until the amplitude of a consecutive signal is at least 90% of the previous pulse.

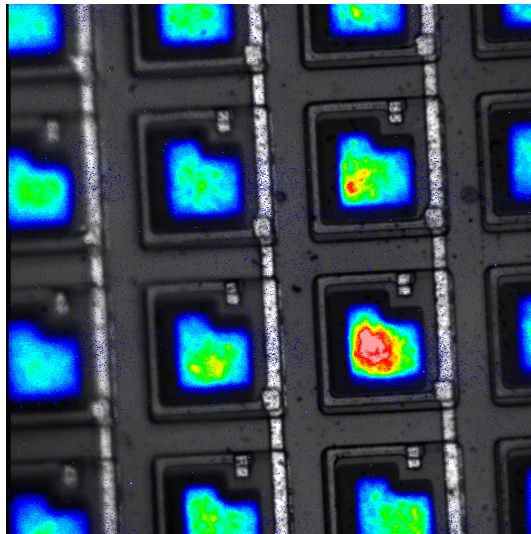


Figure 9.7: Two photographs are overlaid on top of each other. The lower one shows the surface structure of a SiPM. Shown on top is the light intensity that is emitted from the avalanche cells. The SiPM (from MEPhI and Pulsar enterprise) was operated at 50V. The light emission was integrated for 300sec. The colors give the intensity of the emitted light. Photo from C. Merck.

emission with energies  $> 1.14\text{ eV}$  to be  $3 \times 10^{-5}$  photons per charge carrier crossing the junction during breakdown. In Swoger and Kovacic (1993) the measured spectrum is steeper and the emission more intense.

In SiPMs, the hot carrier luminescence gives rise to an effect called optical crosstalk. Optical crosstalk appears when the luminescence photons can propagate mostly unhampered within the device and may be absorbed in the sensitive volume of a different cell, thus triggering an additional breakdown. Depending on the gain and number of already fired cells, additional cell can be further triggered.

The crosstalk effect is well demonstrated from noise count studies shown in Figure 9.8(a). A single noise induced breakdown can trigger a multiple number of cells in a very short time ( $\ll 1\text{ nsec}$ ).

Luminescence photons can also trigger a neighboring or a distant cell if the conversion of the photon takes place in the non-depleted detector volume and the electron or hole diffuses into the depleted volume of a cell. In most applications this case is of minor importance, as most of the generated electron hole pairs are lost due to their too short lifetimes in the non-depleted volume.

### Measures to be taken to suppress Optical Crosstalk

Optical crosstalk can be reduced by limiting the number of charge carriers crossing the junction., i.e. by reducing the gain of the SiPM. In turn, one reduces the production of secondary photons. One obvious way to achieve a lower gain is by lowering the bias voltage of the device. Although easy, this has the unwanted side effect that the breakdown probability will also be reduced.

The amount of charge flowing during breakdown can also be limited by reducing all parasitic capacitances associated with the cell ( $pn$ -junction, quenching resistor,...).

A third approach is to etch trenches between individual cells, thus acting as optical barriers. This method has been applied previously on linear arrays of SPADs (e.g. Kindt, 1999) and has been successfully implemented in the SiPM production process at MEPhI recently (Dolgoshein, 2006a).

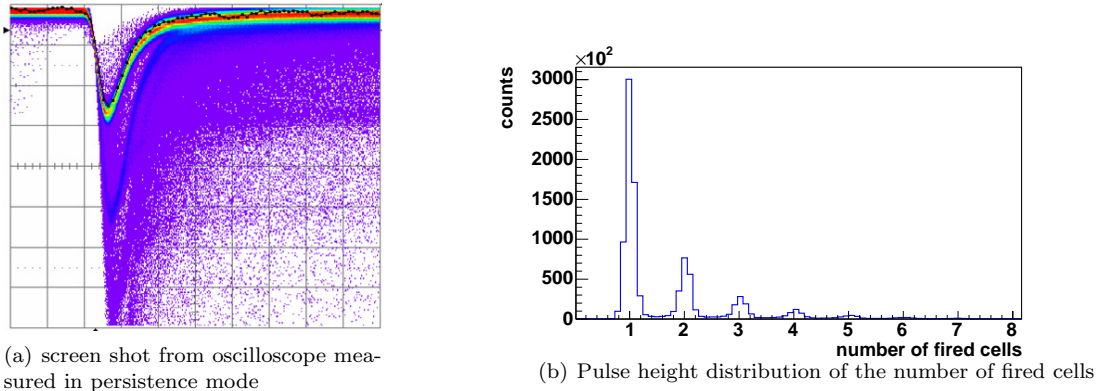


Figure 9.8: The left picture shows an oscilloscope screen shot of many overlaid SiPM noise pulses (2 nsec division in time and 2 mV in amplitude). Most of the time, only one cell of the SiPM shows a signal. With lower probability, 2, 3, or even more cells can fire simultaneously due to optical crosstalk. The right panel shows the pulse height distribution of the output of a SiPM integrated for 4 nsec after one cell has fired on a dark count. The signal shows nicely the quasi digital output as a function of the simultaneously fired cells.

#### 9.4.5 Dynamic Range Limitation

From the SiPM concept it follows immediately that the output signal cannot be strictly proportional to the number of photoelectrons  $N_{\text{phe}}$ . Only in case  $N_{\text{phe}} \ll N_{\text{cells}}$  one can expect approximate proportionality. If  $N_{\text{phe}} \sim N_{\text{cells}}$  saturation will set in. Figure 9.9 shows a self-explanatory example of the correlation of fired cells with the number of photoelectrons. Analytically the response can be derived by calculating the average number of cells that give a signal if the sensor is flashed with a pulsed light source:

$$N_{\text{fired}} = N_{\text{available}} \left[ 1 - e^{-\frac{N_{\text{phe}}}{N_{\text{available}}}} \right] \quad (9.7)$$

Where  $N_{\text{fired}}$  is the average number of cells that trigger if on average  $N_{\text{phe}}$  photoelectrons are generated in a device with a total number of  $N_{\text{available}}$  cells. From the equation it follows that the output signal is deviating by more than 20% from linearity if the number of photoelectrons is exceeding 50% of the available cells on the SiPM. The reason is a steadily increasing probability that a cell is hit by more than one photon. It is noteworthy that the relation only holds for very fast signals, i.e. all photons arrive within a time window that is much smaller than the recovery time of a cell. For signals spread in time, late arriving photons can trigger already hit cells again (e.g. for slowly decaying scintillators in PET applications).

At first glance the saturation effect seems to be of disadvantage for large dynamic range requirements but at second glance it can be of advantage in some applications. Often one uses log-amplifiers to compress the dynamic range of a signal. In SiPMs logarithmic compression is intrinsic.

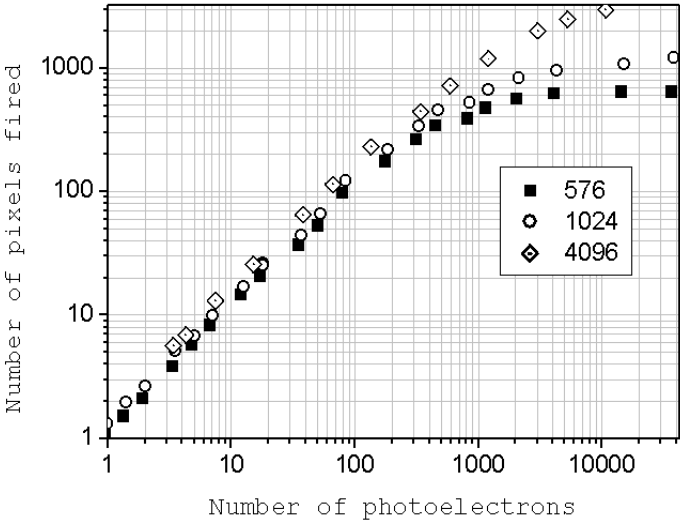


Figure 9.9: Response of three different SiPM with 576, 1024 and 4096 cells as a function of photoelectrons in the active area (from Dolgoshein, 2006b)

## Chapter 10

# Development and Evaluation of an Avalanche Structure for a Back Side illuminated Silicon Photomultiplier

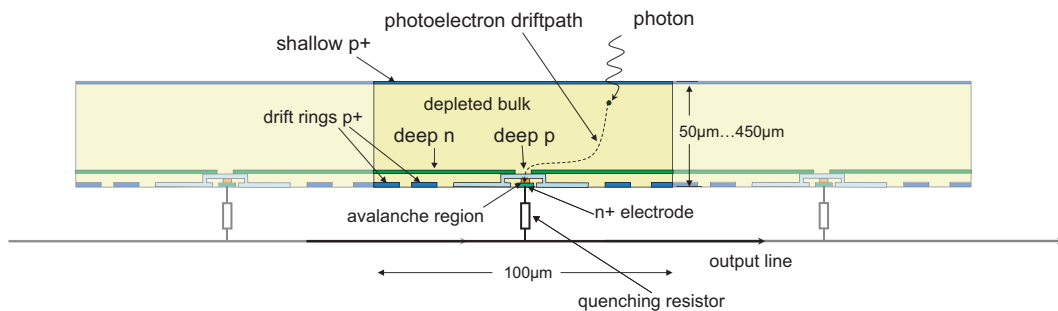


Figure 10.1: Side profile of three cells of a back side illuminated SiPM. Note that the drawing is not to scale.

### 10.1 The Back Side illuminated Silicon Photomultiplier

The aim to enhance the sensitivity of SiPMs by illuminating them from the back side can be regarded as a next logical step in the development. This idea (Lutz et al., 2006) is now pursued in the semiconductor laboratory (HLL). Here I will describe my contribution to the development of a back side illuminated SiPM (hereafter BaSiPM).

When starting this work the BaSiPM only existed as a general concept. Since then R&D has progressed up to the point of evaluation of test structures of the avalanche region (late 2006). I made major contributions to the R&D:

- Developing and simulating an avalanche structure that can be used in a BaSiPM
- Taking part in setting up a technology that was used to produce the simulated structure in the HLL

- Designing test structures that are compatible with the defined technology
- Evaluating some of the test structures with respect to their later use in the BaSiPM
- Development of an instrument to measure the PDE of a SiPM

In the following I will address these activities in more detail. Special emphasis has been put on the study of the impact of the optical crosstalk in BaSiPMs. By means of a Monte Carlo simulation I could demonstrate that optical crosstalk can be a serious drawback in high gain BaSiPMs.

### 10.1.1 Principle

The basic idea of the BaSiPM is that photons are entering the detector from the back side, while the avalanche zone is located at the front side. Figure 10.1 shows a side profile of three cells of such a photon detector. Photons enter the detector from the back side through a specially designed entrance window that is optimized for high photon transmission. After having passed the shallow and uniform implantation of the back side cathode (shallow  $p^+$ ) the photons are mostly absorbed in the high ohmic and fully depleted detector volume (depleted bulk).

A drift field guides the photoelectrons into a small avalanche region at the opposite side of the detector. Upon entering the high field avalanche region a photoelectron induces a localized Geiger breakdown.

### 10.1.2 Characteristics

The main advantage of illuminating the back side is a 100% active area of the detector. The low geometrical efficiency of current SiPMs (typically 40%...60%) is the major factor limiting the photon detection efficiency of this type of photon detector (cf. Section 9.4.3). As a side effect of the large active volume, the BaSiPM will suffer from:

- high dark count rates due to electrons, which are thermally generated in the active volume. Cooling and reduction of the detector volume by thinning will be mandatory for a successful operation.
- timing properties will be degraded due to the dependence of the drift time on the origin of the electron within the detector volume.
- The detector will have a higher sensitivity in the IR than standard SiPMs. This can have some disadvantages for some applications. For example, in air Cherenkov telescopes a cutoff in the sensitivity of the photon detector is required for photon wavelengths  $\gtrsim 700$  nm where the NSB light is rapidly increasing (cf. Section 4.1.4 and Section 9.2).
- Another disadvantage of the huge active detector volume is its sensitivity to crosstalk photons, which unhamperedly travel through the detector and are with high probability absorbed in the active volume of a neighboring cell .
- Also inclined charged particles can fire quite a few cells<sup>1</sup>

---

<sup>1</sup>This so-called nuclear counter effect is much less harmful than in linear mode APDs and PiN-photodiodes

## 10.2 Design and Simulation of one Cell

### 10.2.1 Requirements of an Avalanche Structure for a BaSiPM

When designing an avalanche structure for a BaSiPM several requirements have to be simultaneously fulfilled.

- The electric field in the avalanche region has to be homogenous and above the critical field strength for breakdown
- Special care has to be taken that the maximum of the field is in the central region and not at the edges of the avalanche region
- It must be possible to embed the avalanche structure into a drift detector structure and electrons that are generated at any location in the drift structure must drift into the (small) avalanche region

Apart from the above mentioned requirements, which can be studied by means of simulations, the final performance of the avalanche structure very much depends on the technology (experience) used to produce the device. In the following I describe the avalanche structure that was found after some iterations and optimizations. The presented studies concentrated on the electron collection properties, timing properties and the behavior of the avalanche structure during breakdown.

### 10.2.2 Simulated and Evaluated Avalanche Structures

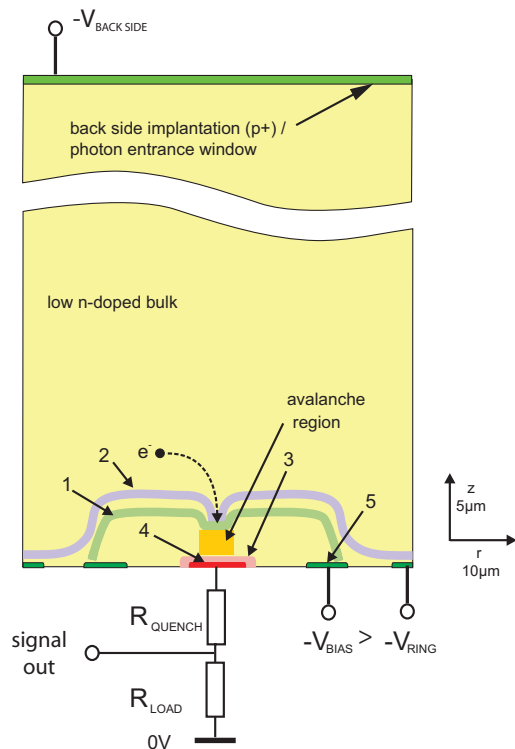
After many iterations and different approaches a structure was found that in principle can meet all the above mentioned specifications. A sketch of this structure is shown in Figure 10.2.

The BaSiPM desing is based on high ohmic  $n$ -type bulk material. The avalanche diode structure is made up by a deep boron  $p^+$  implant (1) - the anode, and a highly doped Arsenic  $n^{++}$  implant (4) - the cathode of the diode. The signal can be decoupled from either (4) or (5). The deep boron implant is modulated such that the distribution of the electric field exhibits a global maximum in the center of the avalanche region. In this way a breakdown at the rim of the cathode implant is suppressed, which would otherwise cause instabilities during operation. The cathode implant is embedded into a well of Phosphorus (3), which is depleted during operation and smoothes the gradient of the potential further.

During operation a reverse bias is applied to the contacts (4) and (5) of the avalanche diode and the anode implant is depleted in the center. The electrical field in the center is defined by the dose of the anode implantation. A depletion of the anode is necessary in order to allow electrons to drift from the bulk into the avalanche region. The anode-implant establishes the transfer between the avalanche-structure and the drift-structure.

The distribution of the potential in the drift-structure is such that holes are emitted from the deep boron implant and drift to the back side of the drift-structure (punch through), which causes an unwanted leakage current. This unwanted property is avoided by a weakly doped deep  $n$ -implant (2) that shifts the potential maximum away from the anode into the drift structure. In addition the implant is modulated in the center such that no potential minimum for electrons is formed in front of the avalanche structure.

Implantation doses, energies and lateral extensions have been carefully tuned by means of simulations with the software package TOSCA (Gajewski et al., 1992), to achieve a homogenous electric field in the avalanche region, good electron collection efficiencies and to avoid punch through between the anode and the back side of the device. In the simulations the rotational symmetry of the cell was used, as it is sufficient to reduce the general 3D structure to a 2D problem  $(r, z)$ , where



Implantation Nr.	Dopant	Type	Dose [1/cm <sup>2</sup> ]
1	Boron	$p^+$	$3 \cdot 10^{12}$
2	Phosphorus	$n$	$5 \cdot 10^{11}$
3	Phosphorus	$n^+$	$3 \cdot 10^{12}$
4	Arsenic	$n^{++}$	$1 \cdot 10^{15}$
5	Boron	$p^{++}$	$1 \cdot 10^{15}$

Figure 10.2: Cross section of the designed cylindrical avalanche structure that can be embedded into a drift structure. Free electrons drift into the center of the structure as indicated by the dashed arrow. The potential is shaped by appropriate voltages applied to the back side implantation and two drift rings on the front side of the device. The first drift ring is indicated in the lower corners of the figure. The different implantations are marked with numbers. The doses and type each implantation is given in the table.

the simulated area extends in lateral direction from the center of the avalanche structure to the border of the cell while in  $z$ -direction the simulated area extends over the full depth of the device. Room temperature has been assumed in the simulations.

### 10.2.3 Study of the Electron Collection Properties

The electron collection properties were studied by simulating one cell of a back side illuminated SiPM. In the simulations the cell is assumed to be cylindrical with a depth of  $450 \mu\text{m}$  and a radius of  $50 \mu\text{m}$ . The center of the cathode of the avalanche structure is located at the front side in the middle of the cell at  $r, z = (0, 0)$ . Two drift rings are placed at a distance of  $r = 30 \dots 35 \mu\text{m}$  and  $r = 45 \dots 50 \mu\text{m}$  from the center of the cell, respectively.

In the example that is shown in Figure 10.3 the anode is biased to  $-60 \text{ V}$  and the rings to  $-100 \text{ V}$  and  $-120 \text{ V}$ , respectively. The back side is biased to  $-400 \text{ V}$  and the cathode is connected via a  $500 \text{ k}\Omega$  resistance to ground. The distribution of the electrical potential is indicated in the figure by lines of equipotential (grey lines). The isolines are parallel until close above the avalanche zone, i.e. at a depth of  $\sim 50 \mu\text{m}$ . For the simulations a substrate was chosen with an intrinsic doping concentration of  $10^{12} \text{ holes/cm}^3$ .

### Photoelectron Collection Efficiencies

In the specific simulation, shown in Figure 10.3, 10,000 electrons have been generated at  $r = 40 \dots 45 \mu\text{m}$  and  $z = 448 \mu\text{m}$ . The different colored blobs are snapshots of the drifting electron cloud

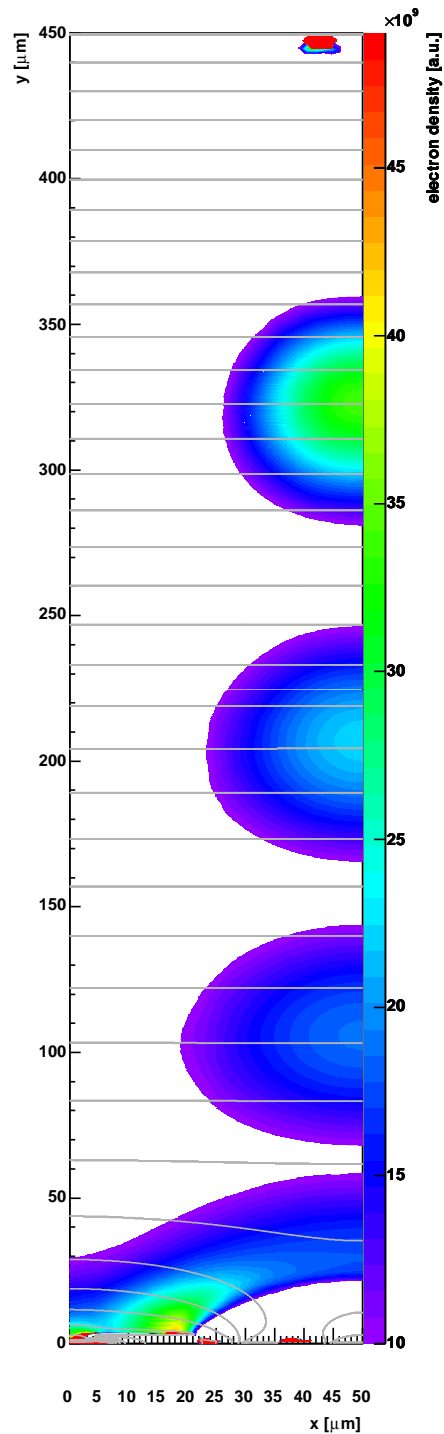


Figure 10.3: Simulation of a drifting electron cloud in a back side illuminated SiPM cell. The charge was generated at  $r=40 \dots 45 \mu\text{m}$ ,  $z=448 \mu\text{m}$  (the smallest blob in the top of the figure). The picture shows the location of the drifting electrons in time steps of 2 nsec. Note the difference in notation  $r=x$  and  $z=y$ .

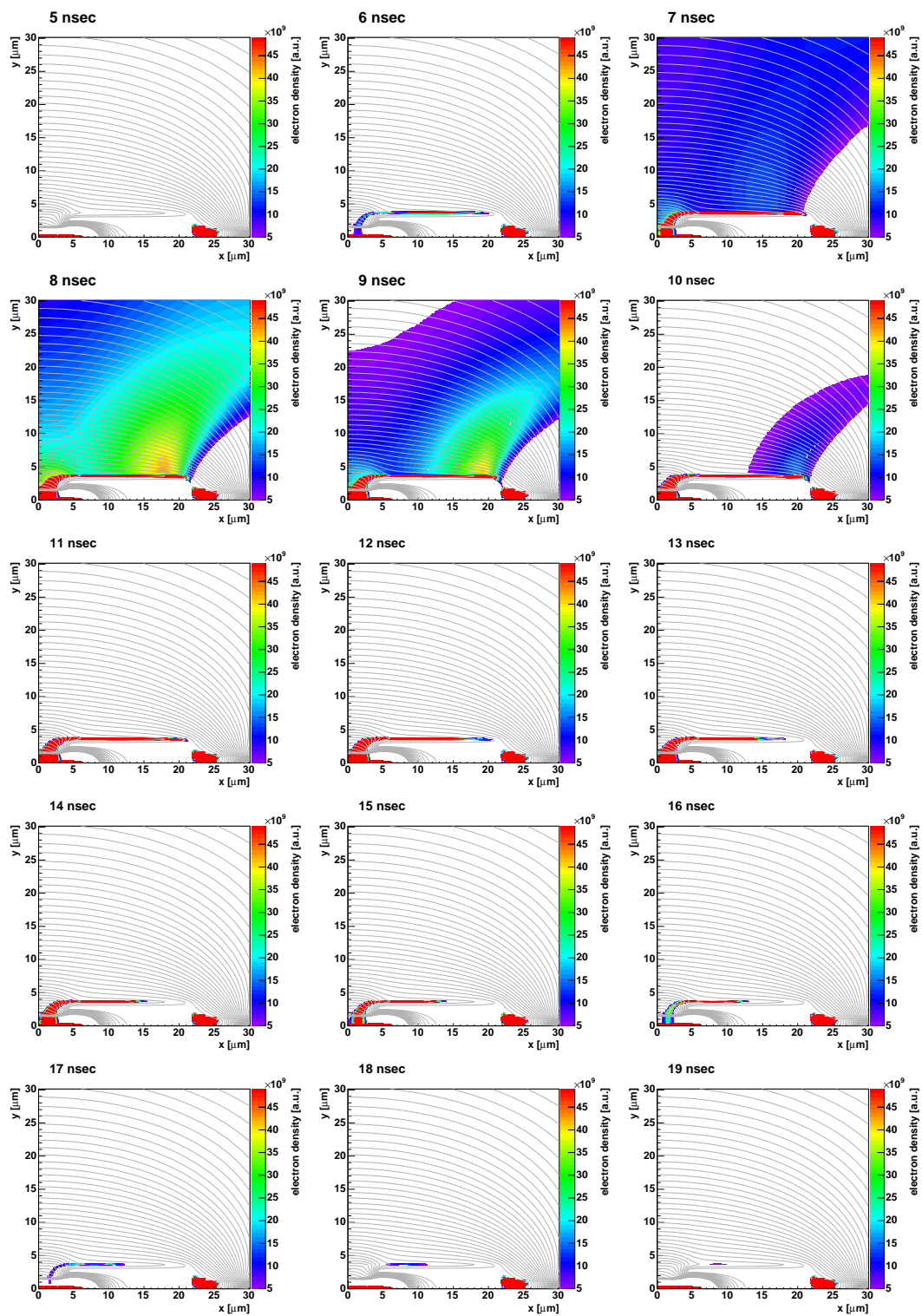


Figure 10.4: Expanded view of the avalanche region of the simulated cell shown in Figure 10.3. The charge is completely collected in the avalanche region ( $r=0 \dots 5 \mu\text{m}$  and  $z=0 \dots 2 \mu\text{m}$ ) 20 nsec after its generation. Note the difference in notation  $r=x$  and  $z=y$ .

in time steps of 2 nsec. The first snapshot (red spot) shows the electron distribution directly after its generation. After 8 nsec most of the electrons have arrived at the front side above the avalanche zone (bottom in the Figure). The average drift velocity of the charge cloud is approximately 50% of the saturation velocity of electrons in silicon, which is  $\sim 10^7$  cm/sec at room temperature (Beadle et al., 1984).

Figure 10.4 shows an expanded view of the avalanche region in the same simulation. The electron density is given in time steps of 1 nsec, starting at a time of 5 nsec and stopping at 19 nsec after the electron generation. After 11 nsec all electrons have gathered in front of the avalanche structure from where they drift much slower into the avalanche structure. 19 nsec after their generation all electrons have reached the avalanche region.

These “movies” give a rather qualitative impression of the charge collection capabilities. The charge collection is studied in a more quantitative way by measuring the charge that flows through the avalanche region as a function of time<sup>2</sup>. For this purpose electrons were generated at three different positions at  $r = 2.5 \mu\text{m}$ ,  $32.5 \mu\text{m}$  and  $42.5 \mu\text{m}$  in a depth of  $z = 448 \mu\text{m}$  and the electron density in the avalanche region recorded as a function of time.

The result of this simulation shows Figure 10.5. The charge is generated at  $t=0$ . The integral over time of any of the depicted curves gives the total collected charge. The integrals vary by 5%, which shows a good collection efficiency for electrons generated anywhere close to the back side of the device. Note that efficiency losses due to the recombination of electrons during the drift can be neglected as recombination times are much longer ( $\mathcal{O} \sim \text{ms}$ ) than the average drift time of the electrons into the avalanche region.

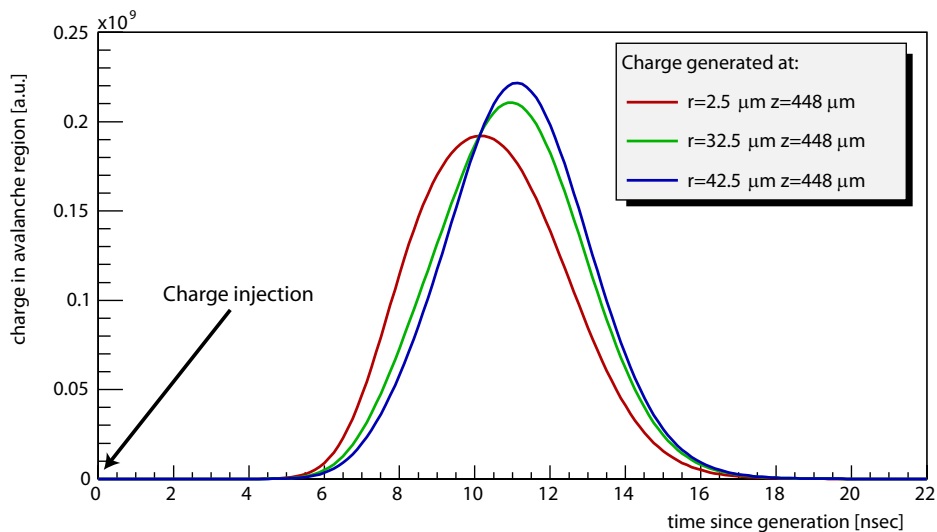


Figure 10.5: Temporal evolution of the electron density in the avalanche region. For this simulation electrons have been generated at three different locations in the cell at time  $t=0$ .

### Timing Properties

Figure 10.5 can also be used to judge the timing properties of the device such as the total drift time and drift time differences of the photoelectrons.

The peaks of the curves give the average drift time, 10.5 nsec for electrons generated in the center of the cell back side just below the surface and  $\sim 11$  nsec if the electron is generated in the corner of a cell.

<sup>2</sup>while the avalanche mechanism is turned off in the simulation

For the later application of the BaSiPM, drift time differences (similar to the transit time spread in photomultiplier tubes) are more important than the total drift time of the electrons. One contribution to the drift time differences comes from the different locations of electron generation (center of the cell or closer to the border of a cell). The magnitude of this effect can be inferred from the different positions of the peaks in Figure 10.5. The effect is  $< 1$  nsec and rather small, if compared to the contribution coming from the diffusion.

Diffusion is the random walk (thermal motion) of the charge carriers which adds on top of their drift motion. Diffusion causes a dispersion of the simulated charge cloud and manifests in the width of the curves shown in Figure 10.5. In principle the influence of the diffusion can be directly read from the widths of the curves. However, this is not possible, as TOSCA does not correctly simulate the diffusion process. From experience and estimates (cf. Equation 10.6) one knows that the simulated dispersion is too high. Therefore, the simulated dispersion  $\sigma \sim 2$  nsec can only be considered as an upper limit on the true dispersion. With appropriate test structures the diffusion-model in TOSCA can be tuned to obtain more realistic values, which should be less than 1 nsec.

### 10.2.4 The predicted Electric Field in the Avalanche Region

For a properly shaped high field region, the choices of the exact dimensions as well as implantation doses in the avalanche structure require particular attention. This was already outlined in Section 10.2.2 when the avalanche structure was introduced.

Figure 10.6 shows for the final structure the electric field distribution inside the avalanche region when the anode is biased to  $-60$  V and the cathode put to ground. A bias voltage of  $-60$  V is an extreme case. In principle a bias voltage of  $-40$  V is sufficient to achieve electric fields high enough for breakdown ( $> 30$  V/ $\mu$ m).

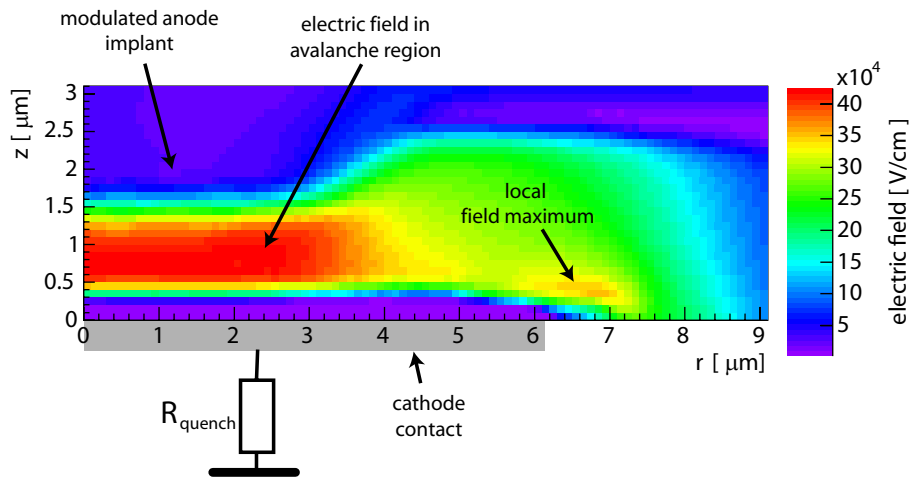


Figure 10.6: Electric field in the avalanche region before breakdown. Bias voltage  $-60$  V.

The simulation shows that for a bias voltage of  $-60$  V the maximum of the electric field remains in the middle of the avalanche structure where the field is defined by the space charge of the depleted anode implant (1 in Figure 10.2). An increase of the bias voltage beyond the value required for depletion ( $\sim 40$  V) has no influence on the electric field in the middle of the structure. Instead the electric field at the rim of the cathode implant ( $r \sim 6.5$   $\mu$ m) is enhanced. The high field zone is homogenous up to lateral extensions of  $\sim 3$   $\mu$ m from the center of the avalanche structure, coinciding with the modulation of the anode.

The local electric field maximum at the rim of the cathode can cause edge breakdown. However,

the effect is largely suppressed as the global field maximum resides in the center of the avalanche structure.

### 10.2.5 Simulated Characteristics during Breakdown

The TOSCA simulation package includes the possibility to simulate avalanche processes. The parameters of the avalanche model (Selberherr, 1984) have to be tuned in order to properly reflect reality. This was not possible due to the lack of appropriate test structures. The avalanche model has no quenching mechanism included. Despite these deficits, simulations of avalanches were performed using the standard parameters of the avalanche-model. The idea was to obtain a qualitative picture of the performance of the structure during breakdown.

Figure 10.7 shows the current (black) and voltage (red) at the cathode contact during breakdown. In the simulation the anode is biased to  $-40$  V and the cathode is connected via a resistor of  $500$  k $\Omega$  to ground. A capacitance of  $100$  fF is used in parallel to the resistor.

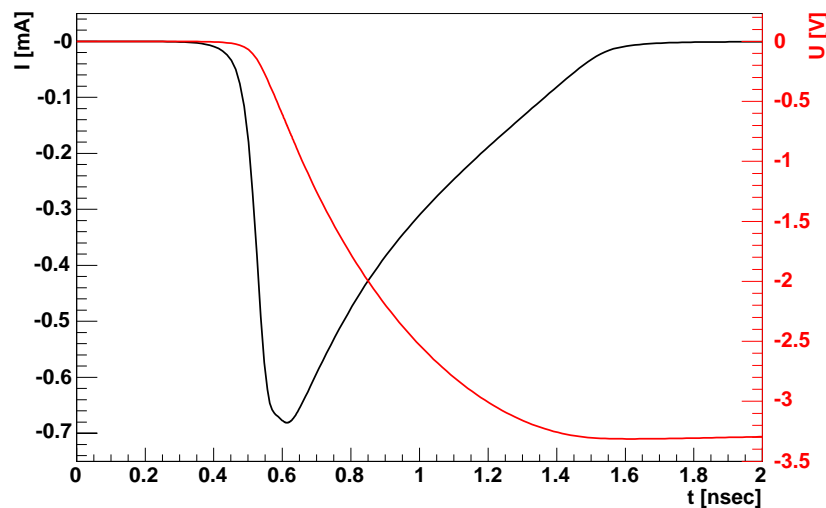


Figure 10.7: Current and electric potential at the cathode during breakdown. In this simulation the avalanche structure is biased to  $-40$  V. The cathode is connected via a  $500$  k $\Omega$  resistor to ground. A  $100$  fF capacitance is connected in parallel to the resistor.

The sharp onset of the current reflects the short timescale, over which the avalanche develops (Lacaita et al., 1993). After the avalanche has fully developed the current decreases again due to the charge up of the  $100$  fF capacitance. The charge up results in a drop of the potential at the cathode.

The capacitance is charged up until the potential across it has reached the difference between the breakdown voltage and the bias voltage. At that point the current that flows in the junction is equal to the current that flows in the external resistor.

If one assumes that the resistance of the junction does not change during the breakdown one can estimate the resistance from the charge-up time of the capacitance ( $100$  fF) and finds  $\sim 4$  k $\Omega$ .

## 10.3 Test Structures

The simulations have demonstrated that the characteristics of the device can in principle meet the requirements for photo sensors in air Cherenkov telescopes. However, several aspects of the device

performance cannot be studied with the simulation tools at hand, e.g. afterpulsing, long term stability, breakdown characteristics, etc. . The simulations also ignore any limitations imposed by the production of the structure. Therefore, it was necessary to show that the simulated structure can be realized. In the following I describe the technology that was developed to produce test structure of the avalanche region.

### 10.3.1 Technology for the Production of the simulated Avalanche Structure

Figure 10.8 shows the sequence of eight production steps of the test structure. The top of the silicon substrate is at  $z = 0$  and the wafer extends to negative values. The center of the avalanche region is at  $r = 0$ .

In this sequence the deep  $n$ -implant is not included, which is required to avoid emission of holes from the anode to the back side (cf. Section 10.2.2). The implant could be omitted for the time being as the avalanche structure is not operated within a drift structure.

The first production step inserts the deep  $p^+$ -implant of the anode into the semiconductor. The reason to choose this implant first was that the implantation process produces the most severe damage to the silicon lattice, because of the high boron dose and implantation energy. The damage is repaired by an appropriate annealing, which would influence already existing implantations.

Before the implantation of the deep  $p^+$ , a thermal oxide with a thickness of 230 nm is processed on the wafer surface followed by a 30 nm thick deposit of nitride. The nitride serves as etch stop at a later step of the production. For the modulation of the deep  $p^+$  in the middle of the avalanche structure a low temperature oxide (LTO) with a thickness of  $1.2 \mu\text{m}$  is deposited on top of the Nitride. A  $6 \mu\text{m}$  thick photosensitive lacquer layer shields the substrate from the implant outside of the future area for the external contact of the anode ( $r > 13 \mu\text{m}$ ). Figure 10.8(a) shows the situation just before the deep  $p^+$  is implanted.

After the deep  $p^+$  has been implanted the LTO is etched away and the silicon wafer is annealed (Figure 10.8(b)).

In the next step the nitride is removed and the oxide in the cathode region etched down to a thickness of  $\sim 65 \text{ nm}$ . Before the  $n^+$ -implant (implant 3 in Figure 10.2) is inserted lacquer is processed on the surface that shields the rest of the substrate (Figure 10.8(c)).

In the production of the test structures it was not foreseen to produce quenching resistors made from poly-silicon. Instead resistors are realized with a boron implant with a dose of  $10^{12} \text{ cm}^{-2}$  (the resistor implant is shown in the very right of Figure 10.8(d)). Before the structure is annealed a 400 nm thick LTO layer is deposited on top of the wafer (brownish layer on top of the silicon in Figure 10.8(d)).

After annealing, the oxide in the cathode area is etched to a thickness of 60 nm (Figure 10.8(e)) and the arsenic cathode is implanted. The arsenic implant is fully absorbed in the LTO anywhere except in the area where the LTO is 60 nm thick. The implantation is followed by another annealing process (Figure 10.8(f)).

Before the anode contact (5 in Figure 10.2) is implanted the oxide above the future contact is etched to a thickness of 50 nm (Figure 10.8(g)). Note the lacquer, which shield the remaining substrate from the boron implantation.

In the last step before metallization the oxide above the anode and cathode contacts is removed (Figure 10.8(h)).

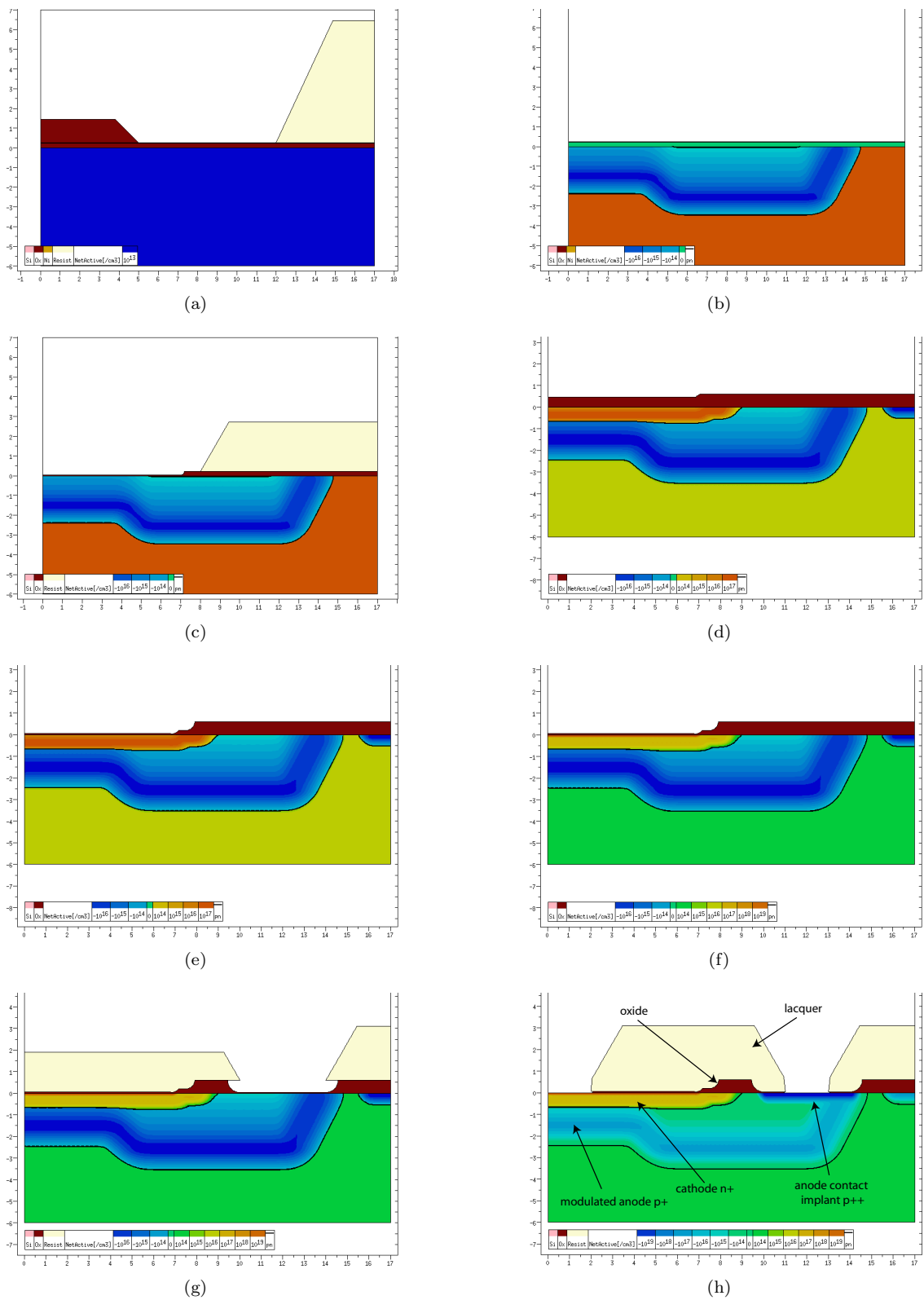


Figure 10.8: Snapshots of the technology at eight steps in the production. The dimensions of the  $x$ - and  $z$ -axis are micrometers. The implantation doses are given in units of dopants per  $\text{cm}^3$ . The pictures have been compiled by Rainer Richter with the technology simulation Dios.

### 10.3.2 Designed Test Structure

By means of the technology described in the previous section I designed avalanche test structures of different diameters and shapes. Some of them are displayed in Figure 10.9. The cathode areas in the larger structures are not covered by aluminum. In this case it is possible to study the homogeneity of the avalanche region with a microscope, which detects the light emission from the avalanche.

Another aspect that I wanted to study was the necessary condition for quenching. For this purpose test structures were designed with a parallel RC-combination in series to the avalanche structure. Figure 10.10 shows one of such a structure. In this particular case I have chosen 50 fF for the capacitor and 500 k $\Omega$  for the resistor.

In addition I designed test structures for the study of the optical crosstalk. In this case a set of two avalanche diodes are placed with different distances to each other.

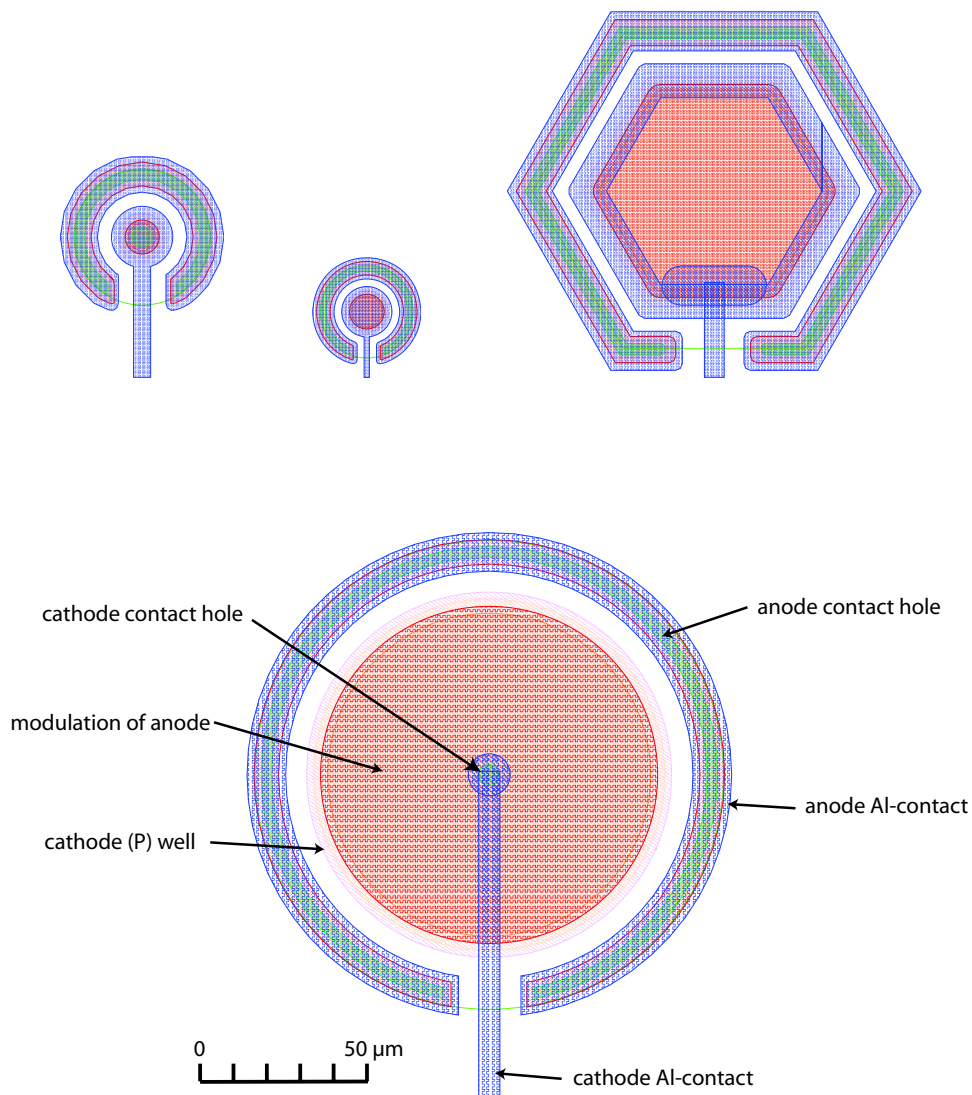


Figure 10.9: Four different examples of avalanche test structures designed for the technology outlined in Section 10.3.1. The diameters of the avalanche regions are 10  $\mu\text{m}$ , 18  $\mu\text{m}$ , 70  $\mu\text{m}$  and 100  $\mu\text{m}$ , respectively.

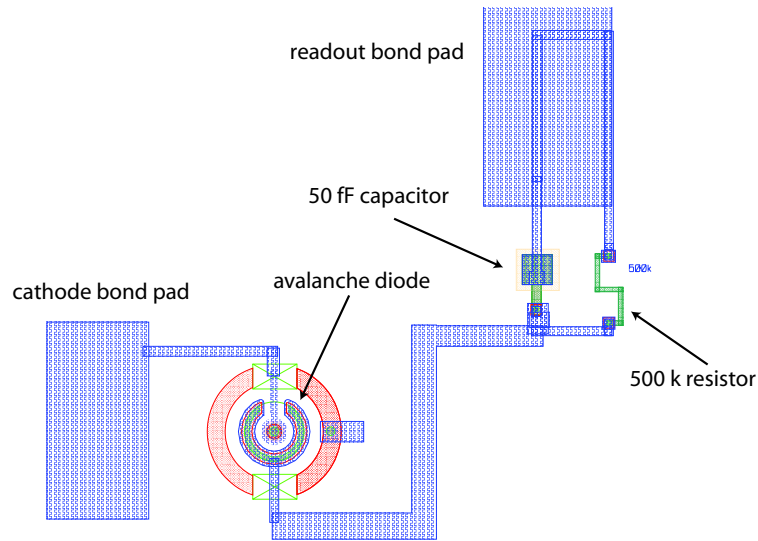


Figure 10.10: Avalanche structure with a  $500\text{ k}\Omega$  resistor and  $50\text{ fF}$  capacitance combination connected in series with the anode contact. The avalanche region has a diameter of  $10\text{ }\mu\text{m}$ .

## 10.4 Evaluation of the Test Structures

The production of the test structures was quite time consuming ( $\sim 1$  year). Therefore, most of the designed and produced structures could not be evaluated within the time window of my thesis. The results presented here were obtained with only one type of diode with a diameter of  $10\text{ }\mu\text{m}$ . The analyzed structures are from the same wafer. Thus studies about the influence of different doping concentrations, annealings, etc. on the performance of the avalanche structure could not be carried out.

The layout of the investigated structures is similar to the one presented in Figure 10.10. The design values of the RC combinations are  $500\text{ k}\Omega/50\text{ fF}$ ;  $1\text{ M}\Omega/100\text{ fF}$ ;  $2\text{ M}\Omega/100\text{ fF}$  and  $2\text{ M}\Omega/200\text{ fF}$ , respectively.

All measurements presented hereafter were done at room temperature. Figure 10.11 shows the readout board that was especially designed for the evaluation of the test structures. The chip with the test structures is placed in the socket in the middle of the board. Two test structures can be studied at the same time. The output signal of a test structure is amplified by a MMIC-amplifier type MAR-8ASM from Mini-Circuits. The bandwidth of the amplifier is  $500\text{ MHz}$ .

### 10.4.1 Dependence of the Signal Charge and Amplitude on Bias

Figure 10.12 right shows the dependence of the signal-charge<sup>3</sup> vs. the bias voltage and Figure 10.12 left the dependence of the signal amplitude vs. the bias voltage of the four analyzed structures. In all measurements the signals are amplified by a custom made, high bandwidth preamplifier of gain 23. In the figures the gain of the preamplifier is taken out.

In the small signal model of Section 9.4.2 a linear dependence of the signal-charge as a function of the bias voltage is expected due to the charging of the capacitances during breakdown. This behavior is in general reproduced up to bias voltages a few volt above breakdown voltage. Beyond a certain bias voltage the characteristics deviate from this behavior and the signal-charge increases

<sup>3</sup>the area enclosed by the signal and the baseline

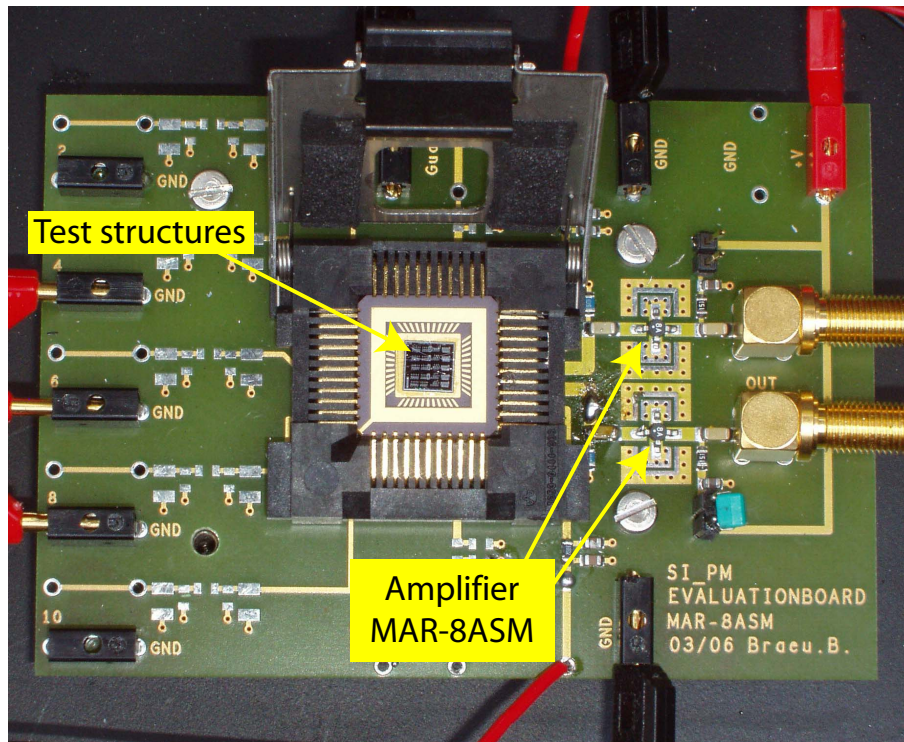


Figure 10.11: Evaluation board that was especially designed for the readout of the test structures. The signal of a test structure is amplified by a broadband (Monolithic Microwave Integrated Circuit) MMIC-amplifier type MAR-8ASM from Mini-Circuits.

stronger than expected. The signal-charge is highest for the structure with the highest capacitor and goes up to  $2.8 \cdot 10^7$  electrons for a bias voltage ten Volts above breakdown.

The value of the capacitances  $C$  can be inferred from the slope of the signal-charge vs. bias voltage at small bias voltages ( $C = \Delta Q / \Delta U$ ) and are listed in brackets in the legend of the left panel in Figure 10.12. The capacitances found differ significantly from the design value. The differences are not systematically above or below the design value, thus indicating a strong influence of the layout.

The breakdown-voltage of the diode is found by a linear extrapolation of the  $Q$  vs.  $U$  dependence to zero signal-charge or amplitude, respectively. In all tested structures a similar breakdown voltage of  $(39.8 \pm 0.2)$  V is found, which is within 10% of the simulated value.

#### 10.4.2 Recovery of the Electric Field in the Avalanche Region after Breakdown

After a breakdown is quenched, the electric field in the avalanche region needs a certain time to return to its original value. The time constant for this process is determined by the capacitance of the diode, the capacitor of the RC-combination and the quenching resistor that discharges the capacitances. Note that the recovery time  $\tau$  is defined here as the time that is needed until the output signal reaches again 63% of the original amplitude. In this way it is easier to compare the measured recovery time with the expected recovery time from the values of the RC-combination.

The recovery time was measured by recording the time and the amplitude of the output signal of subsequent breakdowns triggered by dark counts. Figure 10.13 shows one such measurement that was done with a digital LeCroy oscilloscope LC 554DL operating in persistence mode.

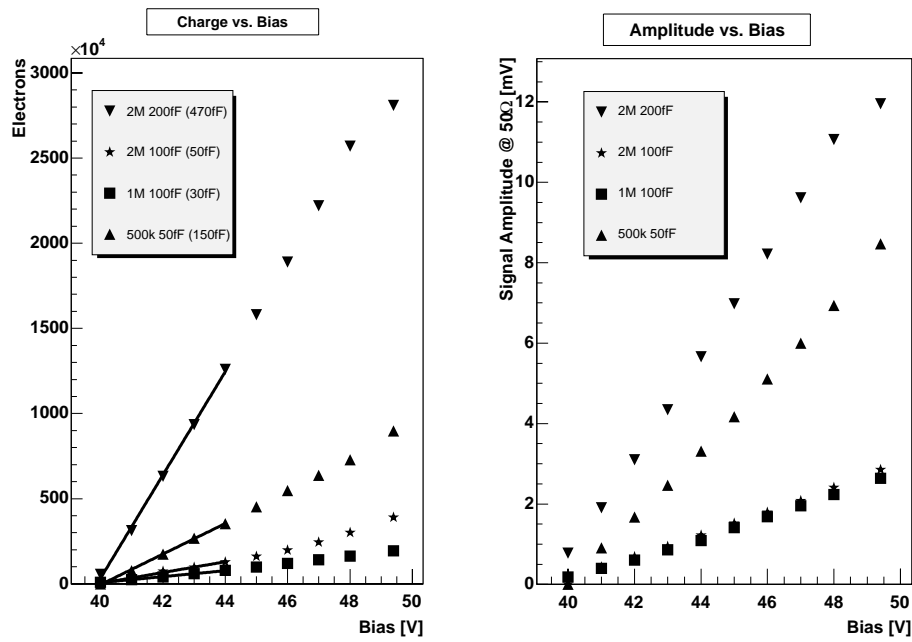


Figure 10.12: Signal charge and amplitude dependence as a function of the bias voltage for four different RC-combinations. The values of the capacitors obtained from the slope of the signal-charge vs. bias voltage are given in brackets.

After waiting a sufficiently long time ( $\sim 20$  min) enough triggers have been accumulated to read the recovery time from the screenshot in the following way. After measuring the time needed until the signal-amplitude reaches 92% of the original amplitude the recovery time  $\tau$  is calculated from

$$1 - e^{-\frac{t}{\tau}} = 0.92 \quad \Rightarrow \quad \tau = \frac{t}{-\ln(1 - 0.92)} \quad . \quad (10.1)$$

In this way one obtains a recovery time of 253 nsec at a bias of 49.5 V for the structure with 1 M $\Omega$  and 100 fF (the measurement is shown in the figure). This is a factor of 2.5 above the value derived from the design values of the RC-combination (1 M $\Omega$  · 100 fF = 100 nsec). On the other hand if one uses the value of the capacitance that was found from the signal-charge vs. bias measurement in the previous section (30 fF) one expects a recovery time of 1 M $\Omega$  · 30 fF = 30 nsec. In this case the discrepancy to the measured value is even higher (factor 8.2). The discrepancy can be explained if the true value of the resistor is  $\sim 8$  M $\Omega$ .

The recovery times of all measured structures is systematically above the expected value (at a bias voltage of 49.5 V):

$$\begin{aligned} 2 \text{ M}\Omega / 100 \text{ fF} &\rightarrow \tau = 435 \text{ nsec} \\ 2 \text{ M}\Omega / 200 \text{ fF} &\rightarrow \tau = 8300 \text{ nsec} \end{aligned}$$

Moreover, the recovery time depends on the bias voltage. In the structure with 500 k $\Omega$ /50 fF a recovery time of 158 nsec is measured at 49.5V but only 119 nsec at 41V. Such a strong deviation from the expected behavior is not observed in the signal-charge vs. the bias voltage measurement. This leads to the conclusion that the implanted resistor increases its value with increasing bias voltage due to partial depletion of the resistor implantation, whereas the capacitor value does not change.

Figure 10.13 shows another interesting aspects worth mentioning. The density of the secondary breakdowns is higher immediately after the triggering breakdown despite the low probability that

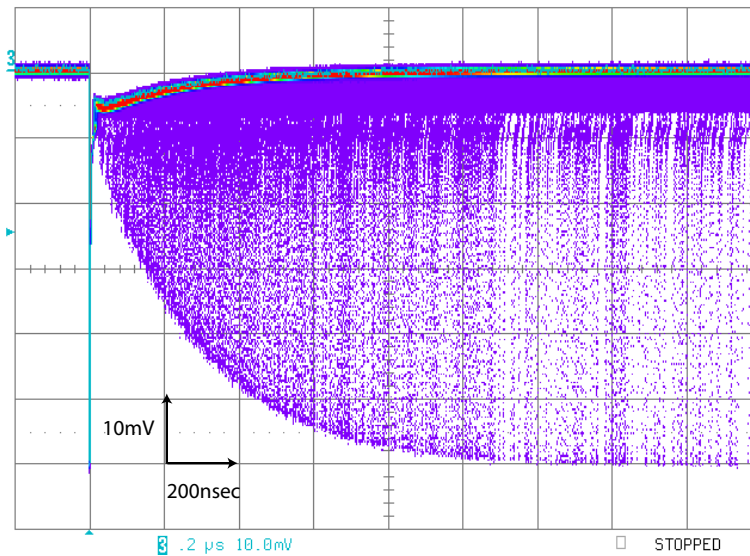


Figure 10.13: Multiple triggers of dark counts for the structure with  $1\text{ M}\Omega$  and  $100\text{ fF}$  and a bias voltage of  $49.5\text{ V}$ .

a charge can initiate a second breakdown because of reduced Geiger probability. The observed behavior is because of trapping of charges during breakdown, which are released again after a certain time. These so-called afterpulses are discussed in more detail in Section 10.4.6.

### 10.4.3 Shape of the Output Signal

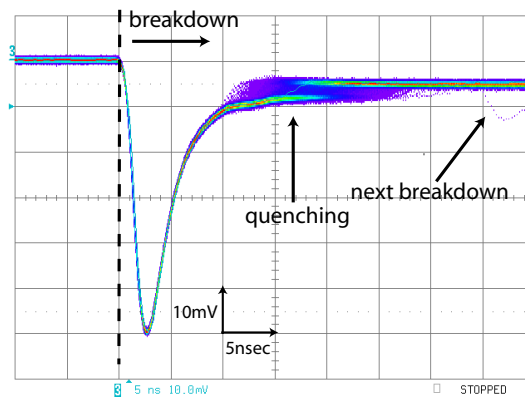


Figure 10.14: Signal shape in case of the structure with the RC-combination  $1\text{ M}\Omega$  and  $100\text{ fF}$  biased at  $49.5\text{ V}$ .

Figure 10.14 shows the output signal of the avalanche structure with the RC-combination of  $1\text{ M}\Omega$  and  $100\text{ fF}$  at a bias voltage of  $49.5\text{ V}$ . The signal is amplified by a factor of 23 with a  $500\text{ MHz}$  bandwidth voltage amplifier MAR-8ASM from Mini-Circuits.

The screenshot from the oscilloscope shows an overlay of several breakdowns. Visibly is a fuzzy behavior in the tail of the pulse when the quenching occurs. The time when the quenching takes place is not constant, which reflects the statistical nature of the quenching process.

The output signal depends on the RC-combination attached to the diode. Figure 10.15 shows the output signal at a bias voltage of  $49.5\text{ V}$  of four investigated structures, each with a different

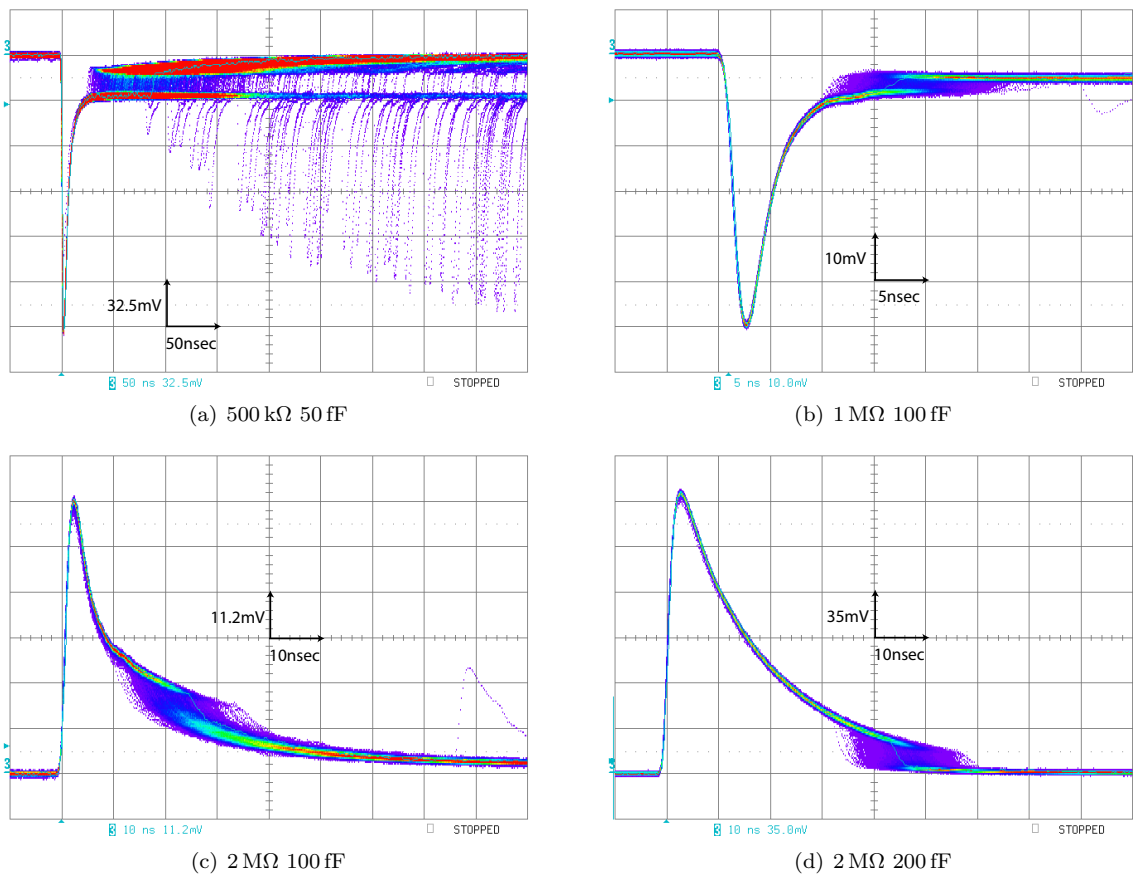


Figure 10.15: Output signal shapes for different RC-combinations connected in series to the avalanche diode structure. The bias voltage is in all cases 49.5V. The signal amplitude is positive in the lower two figures because the signal was tapped from the cathode and not from the anode. Note that an inverting amplifier was used and that the time scales as well as amplitude scales are different in each figure.

RC-combination. Figure 10.16 shows how the signal shape for the structure with 500 k $\Omega$  and 50 fF changes for different bias voltages. At the lower bias voltage the breakdown quenches about 12 nsec after the onset whereas at the higher bias voltage the breakdown quenches between  $\sim$  50 nsec and  $\sim$  100 nsec after the onset of the breakdown. The observed increase of the quenching time with increasing bias voltage is explained a) with the time constant by which the capacitances are charged and b) with the absolute current level at which the breakdown is quenched. Due to the exponential time characteristics of the capacitor charging it takes longer to reach the current level for quenching at a higher bias voltage.

#### 10.4.4 Comparison of the Output Signal with the small Signal Model

I used the small signal model of the SiPM (Section 9.4.2) to describe the output signal of the structure with the RC-combination of 1 M $\Omega$  and 100 fF. It should be noted that the AC-coupling<sup>4</sup> of the preamplifier is not taken into account when modelling the signal. Therefore some small differences are expected when comparing the predictions with measured data.

Figure 10.17 shows four modelled pulse shapes, on top of the superposition of many real pulses. The gain of the amplifier of 23 is taken into account in the modelled pulse shapes. The breakdown

<sup>4</sup>On the readout board the output of the test structure is connected via a 5 k $\Omega$  resistor to ground and coupled via a 1  $\mu$ F capacitor to a MAR-8ASM amplifier.

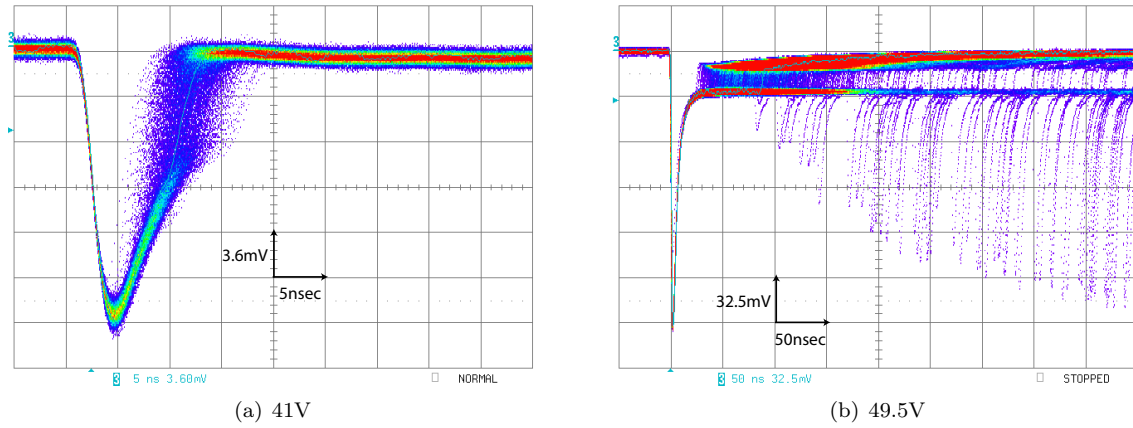


Figure 10.16: Output signal shapes of the avalanche diode structure with  $500\text{ k}\Omega/50\text{ fF}$  connected in series, at different supply voltages. Note that both the time and amplitude scales are different in both screenshots.

voltage is  $39\text{ V}$  in the model, i.e. the same value that was measured (cf. Section 10.4.1). The bias voltage of  $49.5\text{ V}$  in the model is identical to the bias voltage of the test structure. The  $50\ \Omega$  load resistance in the model is identical to the input impedance of the amplifier. The capacitance of the diode of  $2\text{ fF}$  was derived from simulations with TOSCA. The other model parameters are listed in Table 10.1.

For all four simulated pulse shapes the capacitance of  $C_q$  is similar to the one measured from the signal-charge vs. bias voltage characteristics (cf. Section 10.4.1). The rise time of the modelled signal is determined by the bandwidth of the readout. It is tuned in the model by changing  $C_n$  of the low-pass network. Thus the only free parameters in the model are the resistance of the quench resistor  $R_q$  and the resistance of the diode during breakdown,  $R_d$ , as well as the current level at which the breakdown quenches  $I_{quench}$ .

In the first three models  $R_q$  was chose to be  $1\text{ M}\Omega$ , i.e. the design value of the resistor. Good agreement with the measured shape is obtained with values of  $R_d \lesssim 100\text{ k}\Omega$ . The only remaining free parameter the quenching current  $I_{quench}$  is found to be close to  $10\ \mu\text{A}$ .

In model 4 the value of  $R_q$  is set to  $8\text{ M}\Omega$ . This is the value derived from the measurement of the recovery time (cf. Section 10.4.2) under the assumption that  $C_q$  is  $30\text{ fF}$  (as it was found from the signal-charge vs. bias voltage characteristics). The best agreement with the measured pulse shape is obtained when choosing  $R_d \sim 100\text{ k}\Omega$  and a quenching current of  $\sim 2\ \mu\text{A}$ .

In summary the models describe the measured signal shape reasonably well. The quenching current of the analyzed test structure is a few micro Ampere and the resistance of the diode during breakdown is about  $100\text{ k}\Omega$ .

Table 10.1: Parameters of the modelled pulse shapes that are shown in Figure 10.17

Model	$R_q$	$C_q$	$R_d$	$C_d$	$R_n$	$C_n$	$R_l$	$I_{quench}$
1	$1\text{ M}\Omega$	$20\text{ fF}$	$70\text{ k}\Omega$	$2\text{ fF}$	$1\text{ m}\Omega$	$25\text{ pF}$	$50\ \Omega$	$10\ \mu\text{A}$
2	$1\text{ M}\Omega$	$30\text{ fF}$	$70\text{ k}\Omega$	$2\text{ fF}$	$1\text{ m}\Omega$	$35\text{ pF}$	$50\ \Omega$	$10\ \mu\text{A}$
3	$1\text{ M}\Omega$	$30\text{ fF}$	$100\text{ k}\Omega$	$2\text{ fF}$	$1\text{ m}\Omega$	$25\text{ pF}$	$50\ \Omega$	$11\ \mu\text{A}$
4	$8\text{ M}\Omega$	$30\text{ fF}$	$100\text{ k}\Omega$	$2\text{ fF}$	$1\text{ m}\Omega$	$30\text{ pF}$	$50\ \Omega$	$2\ \mu\text{A}$

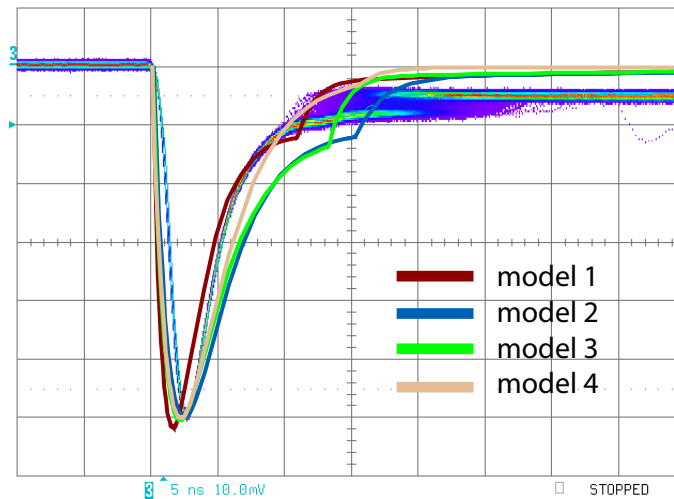


Figure 10.17: Measured pulse shape of the structure with  $1\text{ M}\Omega$  and  $100\text{ fF}$  and four different model pulse shapes. (s. text for details)

#### 10.4.5 The Dark Count Rate

The dark count rate of the structure with the  $500\text{ k}\Omega/50\text{ fF}$ -combination was measured at room temperature in dependence of the bias voltage. The result is shown in Figure 10.18. The rate rises from 300 counts per second at  $43\text{ V}$  bias voltage up to 5000 counts per second at a bias of  $9\text{ V}$  above breakdown. Note that the diameter of the avalanche structure is  $10\text{ }\mu\text{m}$  ( $\sim 80\text{ }\mu\text{m}^2$  area). Thus normalized to the area the rate increases from about  $4 \cdot 10^6$  counts per second per  $\text{mm}^2$  to  $6 \cdot 10^7$  counts per second per  $\text{mm}^2$ . The rate was constantly monitored during 300 hours of operation (fixed bias voltage and constant temperature). The rate was stable on the level of  $\pm 2\%$ , which indicates stable characteristics of the developed avalanche structure.

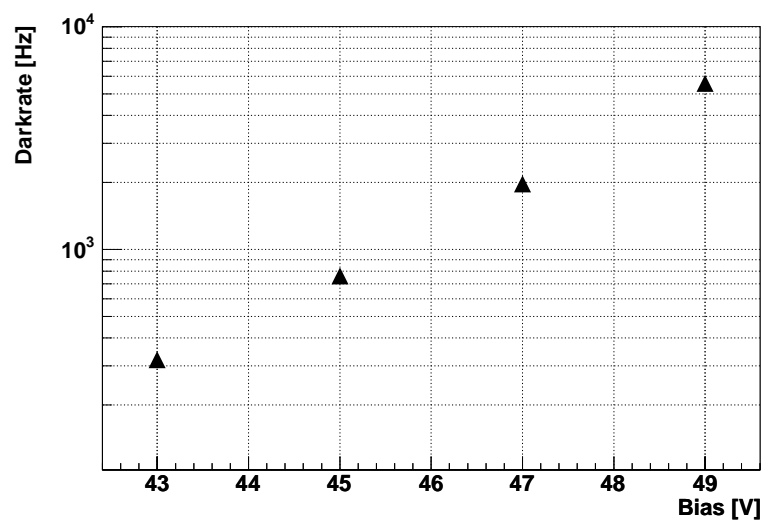


Figure 10.18: Dark count rate as a function of the bias voltage.

### 10.4.6 Afterpulsing

Afterpulsing is caused by electrons or holes, which are trapped in the avalanche region during breakdown and are released again after a certain time. Traps are created e.g. by defects in the semiconductor crystal, introduced during the production.

The probability  $P_{\text{after}}$  that an afterpulse will take place at a time  $t$  after quenching is proportional to an exponential function<sup>5</sup> (Cova et al., 1991).

$$P_{\text{after}} \propto \exp\left(-\frac{t}{\tau}\right) \quad , \quad (10.2)$$

The average trapping time  $\tau$  is determined by the energy level of the trap, the number of traps of the same kind that exist within the avalanche region and the probability that a trap is filled during the breakdown. In reality the situation is more complicated as traps with different energy levels exist and each type of trap has its own characteristic time constant  $\tau_i$ . Therefore,  $P_{\text{after}}$  is the sum of several exponential functions

$$P_{\text{after}} = A_1 \cdot \exp\left(-\frac{t}{\tau_1}\right) + A_2 \cdot \exp\left(-\frac{t}{\tau_2}\right) + \dots A_i \cdot \exp\left(-\frac{t}{\tau_i}\right) \quad , \quad (10.3)$$

The effect of afterpulsing was studied by recording the time periods between consecutive breakdowns and filling the recorded times in a histogram. Figure 10.19 shows the result of one such measurement. On the X-axis is given the time difference  $\Delta t$  between two consecutive breakdowns. On the Y-Axis is shown the probability per unit time that a consecutive breakdown will take place at a time  $\Delta t$ . Note that the measurement was done such that the smallest  $\Delta t$  recorded is  $1 \mu\text{sec}$ . The probability was found by normalizing the number of events in each bin to the total number of recorded events and dividing by the width of the corresponding bin. The histogram can be well described with equation 10.3 if three different time constants are taken into account. The probability of afterpulsing  $P_i$  from one kind of trap is then given by the product

$$P_i = A_i \cdot \tau_i \quad (10.4)$$

The probability of afterpulsing was calculated for each type of trap from measurements with three different bias voltages at room temperature: 43 V, 46 V, and 49 V. The results are listed in Table 10.2. The measurement at a bias voltage of 43 V was repeated with similar outcome after 13 days of continuous operation of the test structure. As one can see, the afterpulsing probabilities (first and second component) increase with increasing bias voltage as traps are more likely populated with more charge flowing through the junction. The third component is due to thermal generated dark counts and, as expected, its relative contribution decreases with increasing bias voltage. Note that the summed probability of all three components does not add up to 100% because no such constraint was enforced in the fit.

**Table 10.2:** Results of the afterpulsing measurements at three different bias voltages at room temperature. Note that the sum of the  $P_i$ 's in each row is more than 100%. This is because no condition was imposed during the fit, which enforces an overall probability of 100%.

Bias	$A_1$ [sec <sup>-1</sup> ]	$\tau_1$ [μsec]	$P_1$	$A_2$ [sec <sup>-1</sup> ]	$\tau_2$ [μsec]	$P_2$	$A_3$ [sec <sup>-1</sup> ]	$\tau_3$ [msec]	$P_3$
43 V	$3.3 \cdot 10^4$	4.0	13%	8500	15	13%	360	3.5	130%
46 V	$7.4 \cdot 10^4$	3.4	25%	$2.2 \cdot 10^4$	11	24%	410	1.7	70%
49 V	$2.2 \cdot 10^5$	3.3	73%	$3.9 \cdot 10^4$	9.2	36%	190	0.9	17%

<sup>5</sup>The probability is constant that a trapped carrier is released in an infinitesimal small time  $\delta t$

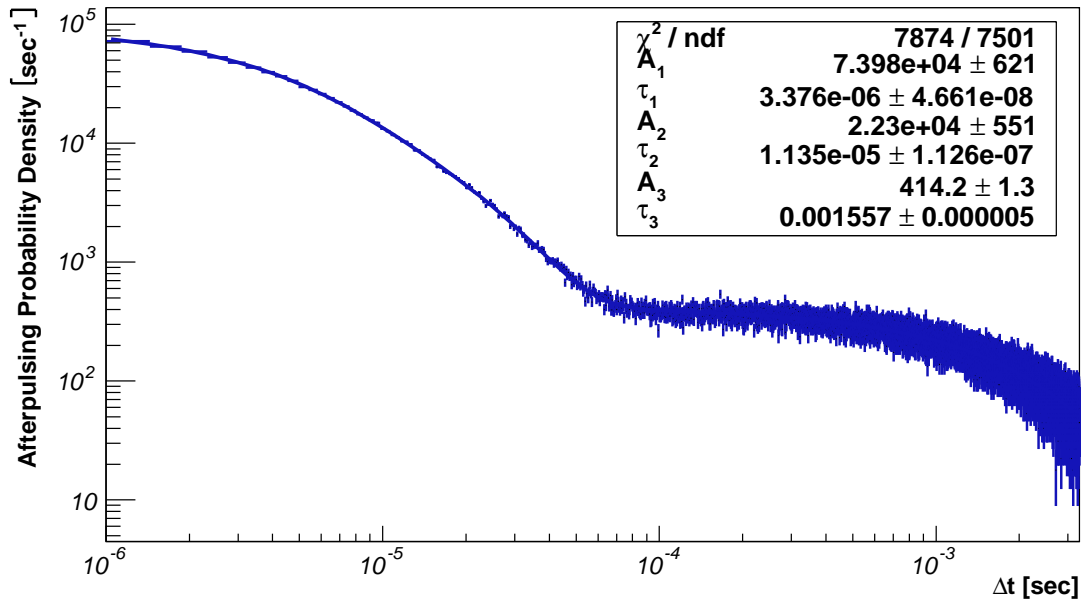


Figure 10.19: Afterpulsing measurement of the 500 k $\Omega$ /50 fF-structure at a bias voltage of 46 V.

In the tested structure (500 k $\Omega$ /50 fF) afterpulsing is the dominating source of background triggers if operated above 46 V, i.e. more than 20% above breakdown voltage at room temperature. Remember that a bias voltage of  $\gtrsim 10\%$  above breakdown voltage is needed to achieve  $\sim 100\%$  breakdown probability.

The contribution of afterpulsing is suppressed without reducing the breakdown probability if the total capacitance of the device is reduced. Another possibility is to introduce appropriate gettering processes in the production of the avalanche structure, which reduce the number of traps (Sciacca et al., 2003).

## 10.5 Influence of Optical Crosstalk in Back Side illuminated SiPM

Optical crosstalk (cf. Section 9.4.4) is an intrinsic feature of SiPM. It is unique in the sense that other photon detectors with internal amplification are not affected by a similar effect. In “conventional” SiPMs optical crosstalk can be largely suppressed by trenches between cells due to the thin depth of the active volume. In BaSiPMs the active volume basically extends over the whole depth of the detector without insensitive volume between cells. Therefore, BaSiPMs are prone to optical crosstalk and obvious measures to suppress optical crosstalk in these devices are:

- A reduction of the number of emitted photons during a breakdown - this can be done by reducing the amount of charge that flows through the avalanche region, e.g. by lowering the gain.
- Designing BaSiPMs with small avalanche regions and large cell diameters, such that the produced photons are absorbed in the same cell.

I studied the effectiveness of these actions by means of a Monte Carlo simulation. The free parameters in the simulation were tuned by comparing simulated crosstalk spectra with measured ones. Doing so I was able to estimate the photon production efficiency in avalanches for photons with energies  $\sim 1.2$  eV.

In the following I describe at first the sequence of the Monte Carlo simulation, then I present the results from the simulation and finally conclude on the optical crosstalk behavior in BaSiPMs.

### 10.5.1 Simulation of Optical Crosstalk in Silicon Photomultipliers with the Simulation Code “SiSi”

To study the effect of optical crosstalk in SiPMs I have developed a 3D Monte Carlo (MC) simulation of a SiPM, the **Silicon photomultiplier Simulator SiSi**<sup>6</sup>. The modular, object oriented structure of SiSi allows also easy implementation of effects like afterpulsing and dark counts. These effects can be ignored for the time being, because for the comparison of the simulated optical crosstalk effect with real data a time window was simulated of only up to 40 nsec. Nevertheless, SiSi simulates in its current state most of the basic characteristics of a SiPM because the geometrical structure of a SiPM is fully implemented in the code.

#### Geometry of the simulated Silicon Photomultiplier

Figure 10.20 shows a cross section of the geometry of the SiPM that is implemented in SiSi. The sizes of all regions except the depth of the avalanche region can be freely chosen. The avalanche region is assumed to be infinitesimally thin and it is located directly beneath the front side of the detector. However, the lateral size of the avalanche region can be freely chosen.

The simulated geometry consists of two non-depleted volumes, one at the back side of the detector and another one below the front side (orange regions in the figure). Note that the figure shows the structure of a front side illuminated SiPM, i.e. the large non-depleted volume, which extends from the back side is the low-ohmic and about  $\sim 400 \mu\text{m}$  thick substrate of the detector. In the simulation of the BaSiPM the thickness of this volume reduces to  $< 1 \mu\text{m}$ , i.e. to the thickness of the non-depleted implantation below the entrance window. Electrons/holes generated in non-depleted regions are subject to a random walk and have limited lifetimes (i.e. experience faster recombination than in depleted volumes). In the depleted volumes (yellow and green) free electrons/holes will experience a drift field. In the case of the BaSiPM this volume extends almost over the full thickness of the wafer ( $\sim 400 \mu\text{m}$ ). Between two cells a region can be defined (green region) within the depleted volume, where free electrons/holes do not drift into the avalanche region, i.e. they are not detected. In the following I only talk about electrons, as in the discussed structures almost only electrons drift into the avalanche region and cause a breakdown.

#### Flowchart of a simulated Breakdown

Within the described geometry several processes are simulated when an avalanche starts. Figure 10.21 shows the flowchart of these processes, which will be explained in the following.

Once a cell is fired, SiSi simulates the amount of photons produced, the energies of the photons and the directions into which they are emitted. Each photon is tracked while it propagates through the SiPM until it either leaves the SiPM or is absorbed. The wavelength dependent absorption lengths (see Figure 10.22) are taken from the EMIS Datareviews Series, No. 4 (1988). Some of the possible and simulated fates of a photon are shown in Figure 10.20. I now describe the scenarios, which cause the breakdown of another cell.

In the case the photon is absorbed in non-depleted detector volume (3 and 4 in the figure) a diffusion process of the generated photoelectron sets in. This process is described later in this section. If the electron diffuses within its lifetime into the depleted detector volume (3 in the

---

<sup>6</sup>Elisabeth “Sis(s)i” von Wittelsbach was the empress consort of Emperor Franz Joseph of Austria. She was born 1837 in Munich, Bavaria and murdered 1898 in Geneva, Switzerland

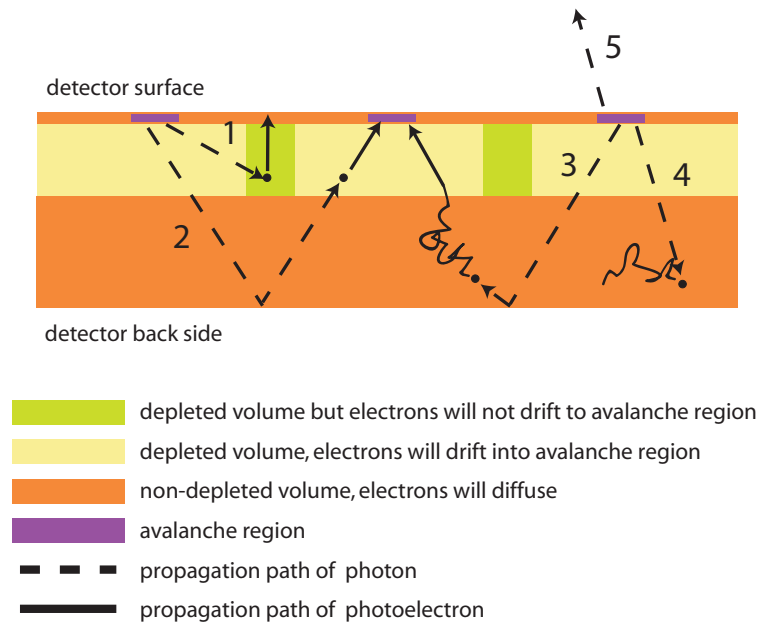


Figure 10.20: Cross section of the geometry of the SiPM that is simulated in SiSi. Also indicated are five different possible fates of photons, which are simulated: 1. Absorption of the photon in the depleted volume of a cell but the photoelectron will not drift into the avalanche region. 2. Reflection of the photon from any surface of the detector and subsequent absorption in the depleted and sensitive volume of a different cell (can start another avalanche). 3. Absorption of the photon in the non-depleted volume of the detector and subsequent diffusion of the electron in the depleted and sensitive volume of a cell. (can start another avalanche) 4. Absorption of the photon in the non-depleted volume of the detector and absorption of the generated photoelectron. 5. Transmission of the photon through any surface of the detector.

figure), the photoelectron is treated like a photoelectron that was produced by absorption of a photon in depleted detector volume. This is discussed next.

In the event the photon is absorbed in the depleted detector volume (1 and 2 in the figure) the photoelectron experiences a drift field. If the photoelectron drifts into the avalanche region of the cell (2 in the figure) and the cell did not experience a breakdown before, an avalanche will be initiated with a given probability.

### Production of Crosstalk Photons in SiSi

The production process of the photons is not simulated in detail in SiSi. It is assumed that the differential energy distribution of the photons is described by black-body radiation of a given temperature and that for each charge carrier crossing the avalanche region a photon is emitted with a given probability. The photons are emitted uniformly distributed within the avalanche region and the emission direction is assumed to be isotropic.

### Simulation of the Random Walk in SiSi

On the microscopic level an electron performs a random walk in non-depleted detector volume. If the electron does not enter the depleted detector volume during its lifetime it recombines and is lost.

The random walk is easy to implement in the simulation code but also requires a lot of computing power. Instead of a full random walk its simpler macroscopic description, i.e. diffusion, is imple-

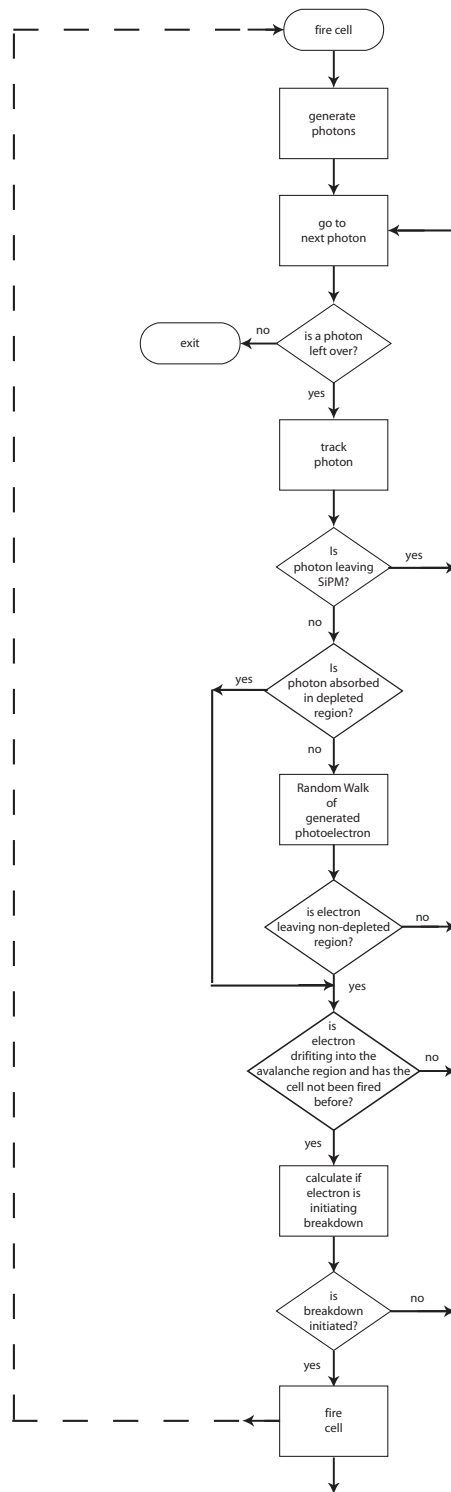


Figure 10.21: Flowchart of the SiSi Monte Carlo program that is simulating optical crosstalk in SiPM.

mented to keep simulation times in SiSi to an acceptable level. Diffusion is simulated in three steps:

1. The lifetime  $t$  of the electron is simulated from the probability distribution

$$\frac{dP}{dt'} = e^{-t'/\tau} \quad , \quad (10.5)$$

where  $\tau$  is the average lifetime ( $\sim 100$  nsec) of an electron in non-depleted detector volume.

2. The direction into which the electron moves is simulated by picking a random point on the unit sphere (Marsaglia, 1972).
3. The distance  $r$  that the electron moves during its lifetime  $t$  away from its origin is simulated by assuming a radial position probability density that is Gaussian ( $r \propto \exp(-r^2/2\sigma^2)$ ) with

$$\sigma = \sqrt{2 \cdot \frac{k \cdot T}{q} \cdot \mu(T) \cdot t} = 8.4 \text{ cm} \cdot \sqrt{t [\text{sec}]} \quad , \quad (10.6)$$

where  $k$  is the Boltzmann constant,  $T$  is the absolute temperature,  $q$  is the electron charge and  $\mu$  is the electron mobility. For the later presented results a mobility of  $1350 \text{ cm}^2/\text{V sec}$  was used in the simulations.

After the distance of the diffusion  $r$  and the direction of the electron is evaluated it is checked whether the electron leaves the non-depleted volume during its lifetime. This assumes that the electron moves straight, which is not true but justified by the short lifetimes of the electrons in the non-depleted volume. In the case that the electron enters the depleted volume the electron experiences a drift field, which eventually guides it into the avalanche region.

### 10.5.2 Study of the Production Efficiency and the effective spectral Temperature of the Photons produced in Avalanches

In the above described simulation code three physical parameters can be freely chosen:

- The temperature of the black body radiation that is assumed for the energy spectrum of the emitted photons and which is not known
- The probability that an electron/hole in the avalanche emits a photon
- The lifetime of electrons in the non-depleted detector volume, which is device dependent

The production mechanism of photons in the avalanche is most likely device independent as it was shown e.g. by Lacaita et al. (1993) and references therein. The same authors showed that the total photon intensity is in first order proportional to the reverse current that flows in the junction. No consensus exists about the energy spectrum nor the intensity of the emitted photons (e.g. Lacaita et al., 1993; Swoger and Kovacic, 1993; Akil et al., 1999). The lifetime of electrons/holes in the non-depleted volume is device dependent; e.g. it depends on the purity of the semiconductor substrate and the production processes.

The spectral shape as well as the efficiency of photon emission can be fixed in the simulation from experimental results, under the assumptions that they are device independent. For the purpose of measuring the photon characteristics dedicated test-structures were designed and fabricated but it was not possible to evaluate them due to the limited time available for my studies. Instead I have chosen a different approach to study the photon emission and to fix the free parameters in the simulation. In this approach the crosstalk behavior of a prototype SiPM was measured and the result compared with simulations. The unknown parameters were tuned in SiSi until the simulation results were matching the measurements.

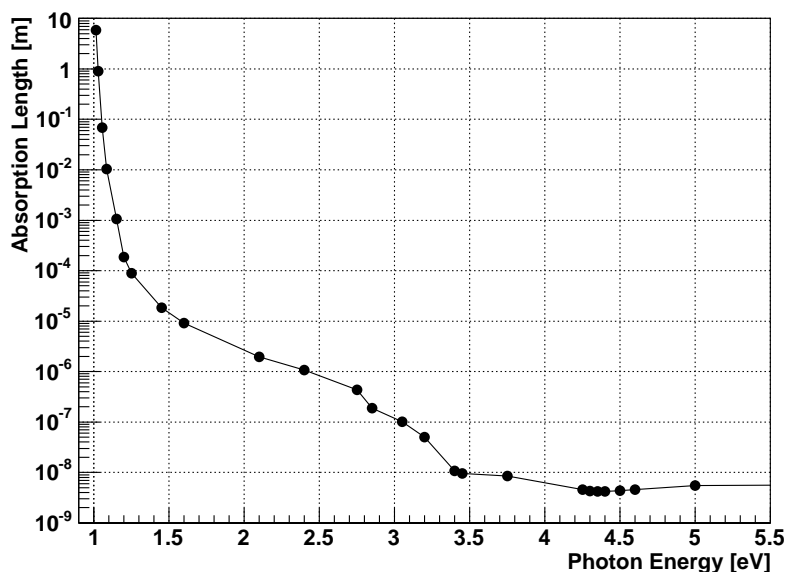


Figure 10.22: Absorption lengths of photons in silicon. Data from EMIS Datereviews Series, No. 4 (1988).

### Parameters of the SiPM used in the Comparison with Measurement

The SiPM for the comparison with measurement was designed and produced at MEPhI and Pulsar enterprise in Moscow. A photograph of the device is shown in Figure 9.1(b). It comprises 576 cells within an area of  $(1 \times 1) \text{ mm}^2$ . The pitch between cells is  $42 \mu\text{m}$  and the edge length of the active area of one cell is  $21 \mu\text{m}$ . The depleted region has a thickness of  $2.5 \mu\text{m}$  and the wafer is  $380 - 400 \mu\text{m}$  thick (Popova, 2004). These dimensions were used in the simulation. In the simulation it is assumed that an electron or hole can initiate a breakdown with a probability of 90%.

The device operated at a *gain* of  $(1 \dots 2) \cdot 10^6$ , i.e. during a breakdown  $(1 \dots 2) \cdot 10^6$  electron/hole pairs were flowing in the junction. For a conservative, lower estimate of the photon production efficiency I adopted a gain of  $2 \cdot 10^6$  in the simulations.

### Study of the Temperature of the Emission Spectrum and the Efficiency of Photon Production in the Avalanche

For the above described device the crosstalk was characterized by recording dark count events where multiple cells fire simultaneously (cf. Figure 9.8(a)). The measurement was done by integrating the signal of the SiPM for 4 nsec. The integration gate is centered on the peak amplitude of the first fired cell and the width of the gate was chosen such that it contains the full signal of one fired cell. In this way mostly events are recorded where crosstalk photons are absorbed in the fully depleted and sensitive volume (case 2 in Figure 10.20). The slower contribution to optical crosstalk that is caused by photoelectrons generated in the non-depleted volume and which first have to diffuse into the active volume of a cell (case 3 in Figure 10.20) can be neglected. For this reason the life time of the electrons is set to zero for the time being. Figure 9.8(b) shows the measured pulse height distribution. The same distribution was simulated with SiSi after choosing a value for the photon production efficiency and the temperature of the emission spectrum.

The agreement between the measured and the simulated crosstalk distribution is quantified by means of a  $\chi^2$ -Test up to the case when 8 cells fire simultaneously. This includes the randomly fired first cell. Figure 10.23 shows three simulated distributions each with a different set of model

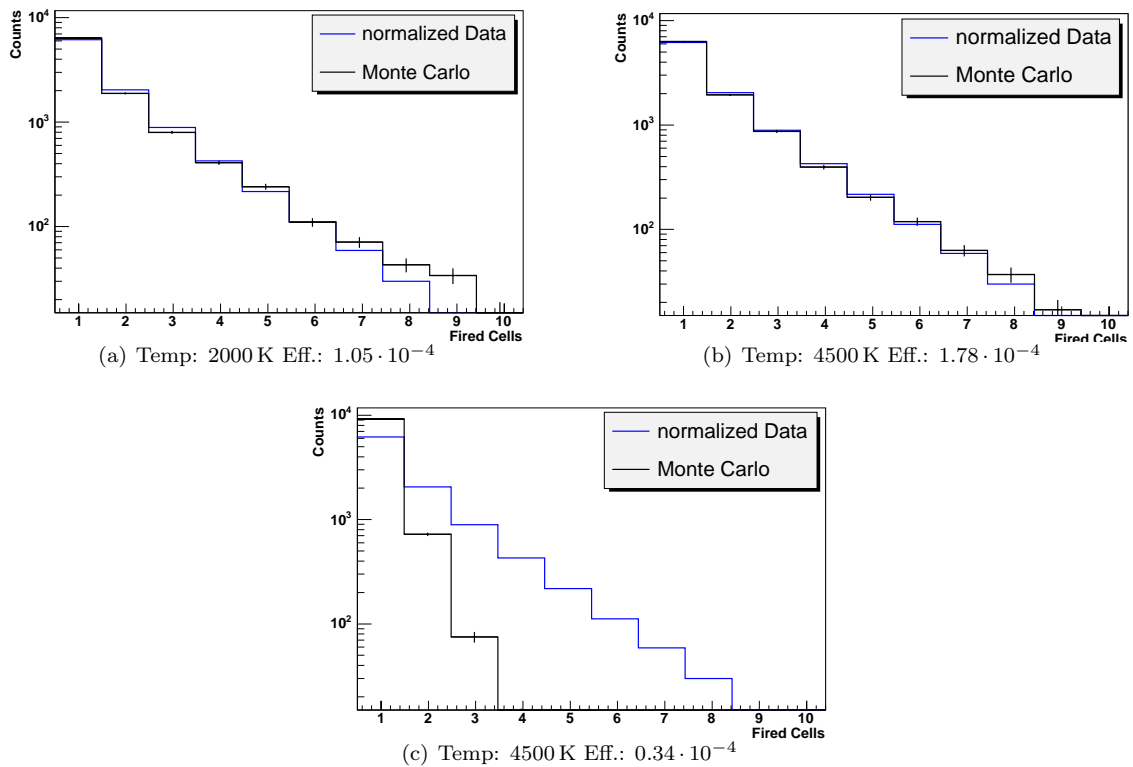


Figure 10.23: Distribution of the number of cells, fired by optical crosstalk if one cell of the SiPM fires at random. The upper row shows the simulated distributions (black) for two sets of temperature and efficiency parameters, which result in a good agreement with the measured distribution (blue). In the lower plot the parameters from Lacaita et al. (1993) were used in the simulation. The efficiency is given in units of emitted photons with energies  $> 1.015\text{eV}$  per charge carrier in the avalanche. The errors on the measured distribution can be neglected and thus are not shown.

parameters. In the upper two figures the simulated distributions are in good agreement with the measured one. In the upper right figure the measured and simulated distribution are matching with a probability of 53%. The disagreement in the lower figure is obvious.

The displayed cases are three examples of a scan in the temperature of the photon spectrum and the efficiency of the photon production. Figure 10.24 shows for each scanned choice of parameters the result of the  $\chi^2$ -test (note the logarithmic color scale). The efficiency of photon production is given in units of emitted photons with energy  $> 1.015\text{eV}$  per charge carrier in the avalanche. The figure shows that for each assumed temperature of the emission spectrum only one value for the photon production efficiency exists where the measured and the simulated distributions are in very good agreement. If, at a given temperature, the efficiency is higher the optical crosstalk is over-predicted and correspondingly under-predicted if the photon production efficiency is lower.

This study shows that choices of parameters exist, for which very good agreement is obtained with the measured distribution. The choice of parameters is not unambiguous. The reason will become clear when I discuss the energy distribution of the photons causing optical crosstalk.

For the “best fit” photon production efficiency at a temperature of 4500 K two simulated events are shown in Figure 10.25 where seven and ten cells fire in addition to one randomly fired cell. The different colors give the “generation” of the fired cell. Generation zero is the randomly fired first cell. The cells marked generation one are those fired by photons coming from cell zero. Generation two are the cells fired by photons of the cells of the first generation... . The probability that more than 7 cells fire due to crosstalk is less than one percent for the SiPM under study (cf. Figure

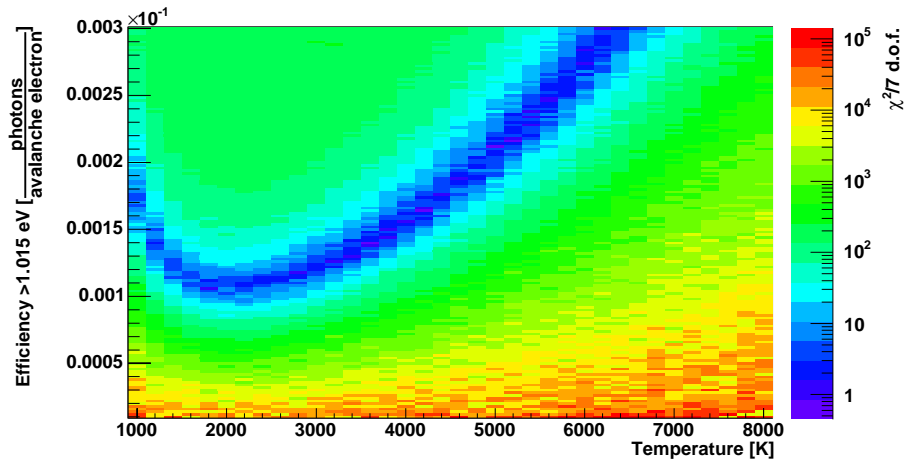


Figure 10.24: Result of a  $\chi^2$ -test between the simulated and the measured crosstalk-distribution from a scan in the parameters temperature of the photon spectrum (X-axis) and efficiency of photon production in the avalanche (Y-axis).

10.23(b)).

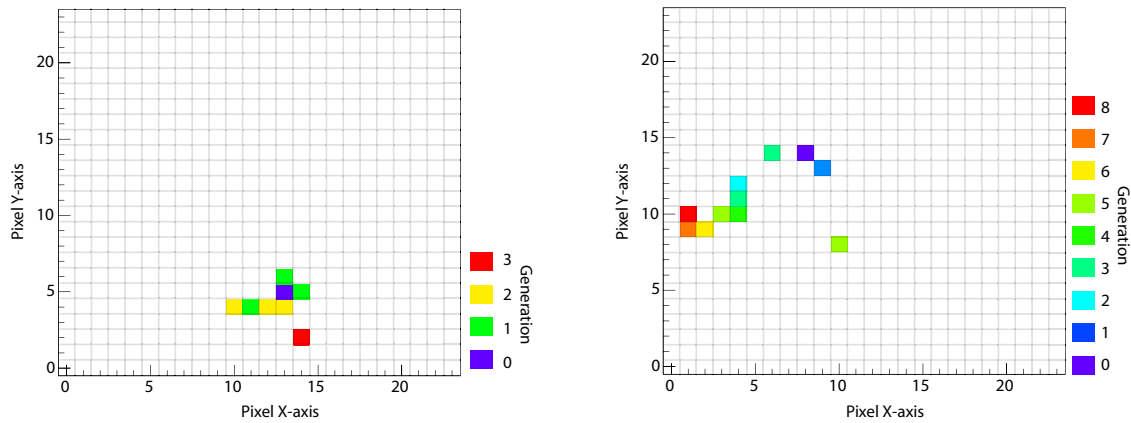


Figure 10.25: Two simulated events where additional cells are fired due to crosstalk.

### Influence of a finite Electron Lifetime in the non-depleted Detector Volume on the Optical Crosstalk

In the previous simulation the diffusion of electrons was not taken into account. I will now discuss the influence of a finite electron lifetime in the non-depleted detector volume on the optical crosstalk.

Assuming different electron lifetimes in the simulation the simulated crosstalk distributions are compared by means of a  $\chi^2$ -Test with the measured distributions as in the preceding section. Two scenarios are simulated, one scenario with an integration gate of 4 ns and another scenario with a 18 nsec long integration gate. Each of the two simulated scenarios is compared with the corresponding measurement and the result of the two  $\chi^2$ -Tests is summed up to give one figure of merit.

Figure 10.26 shows the result of a scan in photon production efficiency (X-axis) and electron lifetime (Y-axis) for two different assumed spectral temperatures of 4500K (left panel) and 2000K

(right panel). It is obvious from the simulation that the photon production efficiency reduces by about 30% compared to the previous simulation to obtain a quantitatively good match with the measured distribution. This means that up to 30% of the crosstalk in the SiPM, used in this study, is produced by photons absorbed in non-depleted detector volume.

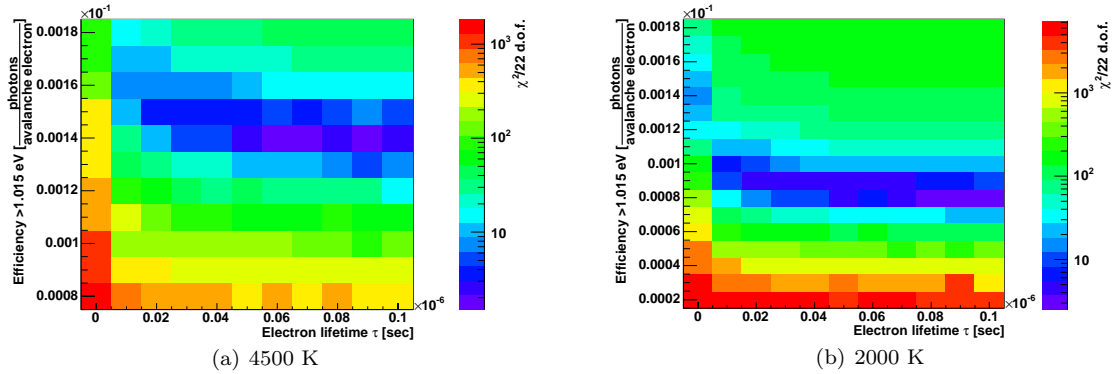


Figure 10.26: Result of a  $\chi^2$ -test between the simulated and the measured crosstalk distribution. Each bin gives the  $\chi^2$  value obtained for one simulated pair of photon production efficiency (X-axis) and electron lifetime in the non-depleted detector volume (Y-axis). A spectral temperature of the emitted photons of 4500K is assumed in the left panel and a temperature of 2000K in the right panel.

In the figures one sees that the best fit photon production efficiency stays constant for assumed electron lifetimes larger than 50 nsec. Therefore, the best fit photon production efficiency at large assumed electron lifetimes can be considered as a solid lower limit of the true photon production efficiency. One can also derive a lower limit of about 50 nsec for the electron lifetimes in the non-depleted volume of the device under study.

### A Comparison between one simulated and one measured Crosstalk Distribution

It is interesting to note that in the previous section the simulation with an assumed black body emitter with a temperature of 4500 K is in better agreement with the measurement than the simulation with a black body temperature of 2000 K (6% fit probability vs. 0.01%).

Figure 10.27 shows in the left panel the measured crosstalk distribution obtained with a signal gate of 18 nsec. For the simulated crosstalk distribution a temperature of the photon spectrum of 4500 K, a photon production efficiency of  $1.45 \cdot 10^{-4}$  and an electron lifetime of 60 nsec was assumed. The right panel in Figure 10.27 shows the residuals between both distributions. The X-axis is given in units of cells that fired in addition to the randomly selected first one. For large numbers of additionally fired cells the data is well represented by the simulation (zero residuals). For small numbers of additionally fired cells (1 and 2) the residuals indicate an excess in the data that is not explained by the model.

The excess seen in the residuals can be explained by thermally generated dark counts, which are not simulated in SiSi. The excess is well described by a Poisson distribution with a mean of  $0.18 \pm 0.14$  additionally fired cells per measured event (black line). Taking into account that the signal gate was 18 nsec the average rate is  $0.18/18 \text{ nsec} = (10 \pm 7) \cdot 10^6$  counts per second. This is in agreement with the measured dark count rate of the device. One has to point out that in this estimate one neglects that the dark counts themselves are subject to optical crosstalk but given the large uncertainties of the fit the estimate is good enough.

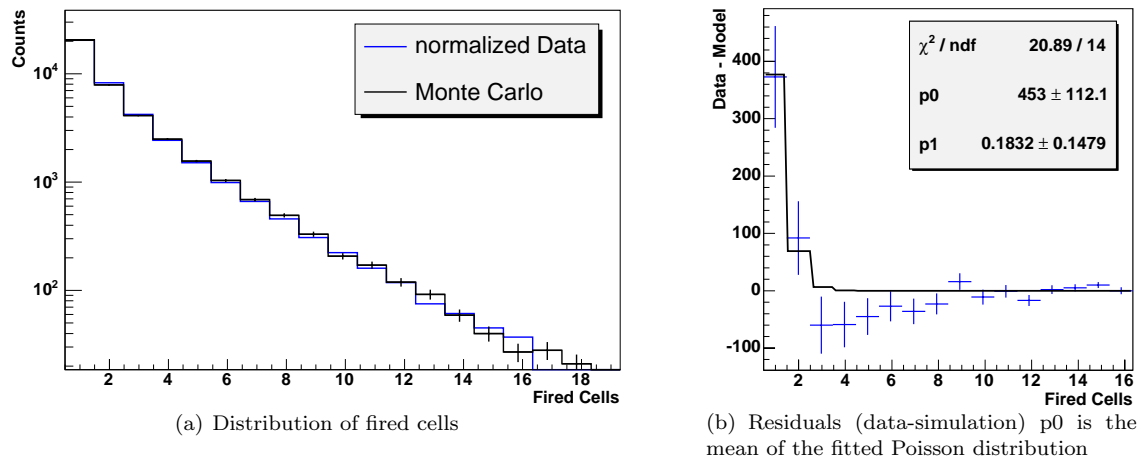


Figure 10.27: Simulated and measured distribution of crosstalk events. The residuals can be explained as dark counts, which are not simulated. Parameters in the model have been a photon temperature of 4500 K, a photon production efficiency of  $1.45 \cdot 10^{-4}$  and an electron lifetime in the bulk of 60 nsec.

### The Energy Distribution of Photons, giving rise to Optical Crosstalk

Whether or not a “crosstalk”-photon can fire another cell is strongly correlated with its energy. If the energy of the photon is too low the photon will not be absorbed in the detector. If, on the other hand, the photon energy is too high the photon will most likely be absorbed in the same cell where it is emitted. Figure 10.28(a) shows the simulated energy distribution of the photons that fired additional cells. The simulation was done with the two sets of parameters discussed in the previous section and which resulted in a good agreement with the measured crosstalk behavior.

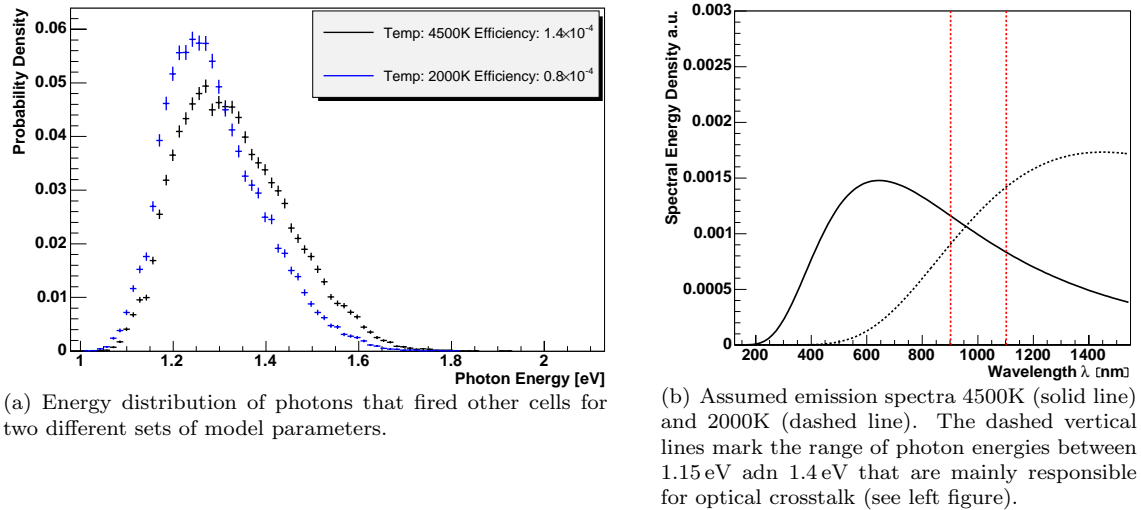


Figure 10.28: The left panel shows two simulated energy distributions of photons that were produced in a breakdown and caused a breakdown of another cell. The right panel shows the photon emission spectra that were assumed in the simulation. Despite the very different emission spectra of 2000K and 4500K one finds an almost identical crosstalk behavior.

The distributions have their maximum at 1.25 eV (2000K) and 1.28 eV (4500K) respectively with widths of only 0.21 eV (2000K) and 0.27 eV (4500K) FWHM, respectively. The widths and the peak positions are well in agreement with each other despite the very different emission spectra

of 2000K and 4500K (cf. 10.28(b)). Such a narrow distribution is expected because of the strong dependence of the absorption length on the energy of the photon (cf. Figure 10.22).

The absolute photon production efficiency in this small energy range during breakdown can be estimated from the integral photon production efficiency that is used in the simulation for photon energies  $> 1.015$  eV. In this way one obtains that photons of energies between 1.15 eV and 1.42 eV are produced with an efficiency of  $2.94 \cdot 10^{-5}$  emitted photons per charge carrier crossing the junction during breakdown. Similarly, one obtains for the simulation with an assumed temperature of 2000 K an efficiency between 1.15 eV and 1.36 eV of  $2.77 \cdot 10^{-5}$ . In both cases the energy range is the FWHM of the distributions shown in Figure 10.28(a). The measured intensity is uncertain by a factor of two due to uncertainties in the geometrical configuration of the implantations in the studied SiPM.

Given the result it is evident that the energy spectrum of the emitted photons does not need to be precisely known over a large range of photon energies. To study the effect of optical crosstalk in a BaSiPM, it is sufficient to use the above discussed model parameters that fit best to the measured data.

### 10.5.3 Prediction of Optical Crosstalk Behavior of a Back Side illuminated Silicon Photomultiplier

I showed above that only photons within a small band of the emission spectrum are responsible for optical crosstalk. A precise knowledge of the emission spectrum is not necessary, for a study of optical crosstalk effects. The measured crosstalk distributions are well reproduced by SiSi after tuning the parameters photon production efficiency, temperature of the emission spectrum and the electron lifetimes in the non-depleted bulk.

In the following I study the effect of optical crosstalk in BaSiPMs with two choices of parameters that reproduce the crosstalk characteristics of the SiPM used in the previously presented studies:

1. A temperature of 2000 K and a photon production efficiency  $> 1.015$  eV of  $0.8 \cdot 10^{-4}$  photons per charge carrier in the avalanche
2. A temperature of 4500 K and an efficiency of  $1.4 \cdot 10^{-4}$  photons per charge carrier in the avalanche

Note that in a BaSiPM basically the full detector is depleted, i.e. non-depleted regions can be neglected. Therefore, I adopt the scenario that photons absorbed anywhere in the detector produce an electron/hole pair, from which either the hole or the electron drifts into the avalanche region.

#### Geometry of the simulated BaSiPM

A geometry of a BaSiPM (see Figure 10.29) was simulated, which meets the dynamic range requirements of an air Cherenkov telescope (cf. Section 9.2). The diameter of a cell is  $100 \mu\text{m}$ , which is the maximum allowed diameter concerning the dynamic range requirements but is also the most favorable geometry concerning the suppression of optical crosstalk. The avalanche region is located in the center of the cell at the front side and has a diameter of only  $10 \mu\text{m}$ . Photons with absorption lengths of  $< 50 \mu\text{m}$  that are emitted in the avalanche are thus most likely absorbed in the same cell. The detector is assumed to have a thickness of  $400 \mu\text{m}$ . In fact the thickness of the detector does not influence the outcome of the simulation as reflection losses on the front and back side of the detector are small and therefore are not simulated with SiSi. The non-depleted region at the back side of the detector (top of the figure) is  $1 \mu\text{m}$  thick and  $0.2 \mu\text{m}$  thick at the front side. A device of  $24 \times 24$  cells was simulated.

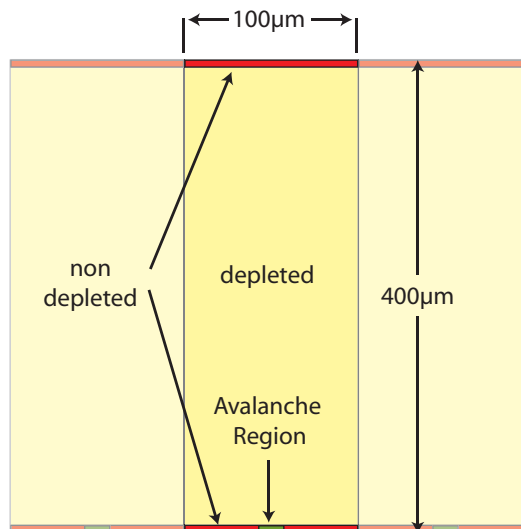


Figure 10.29: Geometry of the simulated BaSiPM

### Effect of Optical Crosstalk in the simulated BaSiPM

The effect of optical crosstalk was simulated in the above described geometry for the two choices of crosstalk parameters. Figure 10.30 shows as a function of gain the probability that at least one additional cell fires due to crosstalk if a randomly picked cell of the device has fired. The simulated distributions are remarkably well in agreement for both assumed spectral temperatures (2000 K and 4500 K). For comparison, the simulated crosstalk probability of the SiPM that was used in the previous crosstalk studies is also shown (dots and stars).

If the studied front side illuminated SiPM is operated at a gain of  $> 10^7$  the probability for optical crosstalk reaches 100%. An optical crosstalk probability of 100% implicates that if one cell of the device fires basically all the remaining cells of the device will fire due to optical crosstalk. The simulated optical crosstalk characteristics of the simulated BaSiPM are more dramatic. The crosstalk probability is 100% for gains  $> 2 \cdot 10^5$  and only approaches 10% if the device gain is lowered to  $10^4$ . If operated at a gain  $5 \cdot 10^4$  the probability for optical crosstalk will be 50%.

Figure 10.31 shows the crosstalk distribution of the simulated BaSiPM for three different gains ( $10^4$ ;  $5 \cdot 10^4$ ;  $10^5$ ). For comparison the measured distribution (blue) of the SiPM that was used in the studies presented in the previous sections is also shown. Note that in this case the gain was set to  $\sim 2 \cdot 10^6$ .

## 10.6 Discussion

### 10.6.1 About the Development of an Avalanche Structure for a BaSiPM

In this chapter I presented and discussed the back side illuminated SiPM. The BaSiPM is an extension of the SiPM concept and was invented by Lutz et al. (2006) with the intention to overcome the limitations of the PDE of “normal” SiPMs by increasing the active area to 100% with the back side illumination principle.

I presented the development of an avalanche structure for a BaSiPM. With extensive simulations a structure was found that can be embedded into a drift structure. The simulated characteristics promise good charge collection efficiencies of  $> 95\%$  and time resolutions for single photons of  $\sim 1 \dots 2$  nsec.

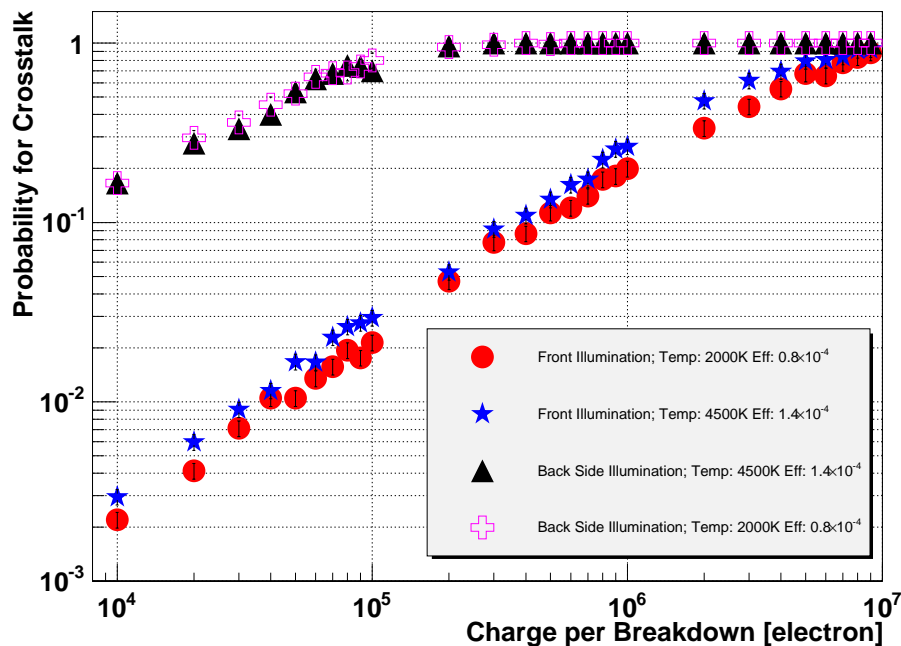


Figure 10.30: Probability for optical crosstalk as a function of gain for a front side illuminated SiPM (stars and dots) and a BaSiPM (crosses and triangles)

Based on the simulations test structures were produced and evaluated. The output signal of one test structure was modelled with a small signal model. Good qualitative agreement was obtained between the model and the measurement. In these comparisons it was found that the breakdown is quenched once the current flowing in the junction drops below  $2 \dots 10 \mu A$ . This has to be taken into account when choosing the quenching resistors for the first full prototype detectors in the next development cycle of the BaSiPM.

It was shown that afterpulsing is the dominating source of dark counts in the analyzed structure, if operated at gains exceeding  $5 \cdot 10^6$ . The afterpulsing probability is proportional to the number of traps in the semiconductor and thus proportional to the area of the device. Structures with two times smaller area than the studied one can be produced. The strongest reduction of afterpulsing is achieved by lowering the gain of the device. This can be done without changing the breakdown probability by reducing the capacitances. The capacitance of the analyzed structure is about 150 fF. A reduction to  $< 20$  fF is possible. Combining a smaller structure and a lower readout capacitance in the next iteration an afterpulsing probability  $< 5\%$  can be achieved at room temperature. In turn an amplification of the smaller signal might be necessary. This amplifier might be integrated very close to the anode directly onto the silicon chip.

## 10.6.2 About Optical Crosstalk

In the last part of the chapter I presented SiSi, a SiPM simulator. I used SiSi to study the characteristics of photons, which are emitted in the avalanche and give rise to optical crosstalk. It was found that only photons in a very narrow range of energies between 1.2 and 1.4 eV are responsible for optical crosstalk. This is explained by the dramatic decrease of the absorption length with increasing photon energy in this energy interval. Photons with energies below 1.2 eV are mostly not absorbed in the device. Photons with energies above 1.4 eV are absorbed in the same cell. The measured photon intensity in the energy interval between 1.2 and 1.4 eV is about  $2.8 \cdot 10^{-5}$  emitted photons per charge carrier crossing the junction during breakdown. This is about a factor of five higher intensity than the previously measured value by Lacaita et al. (1993)

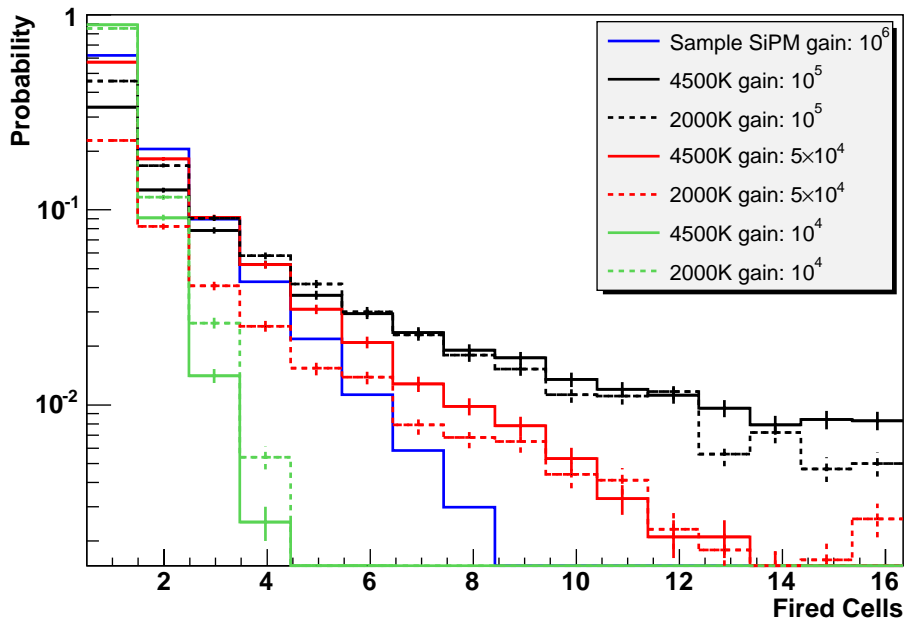


Figure 10.31: Probability distribution that  $X$  additional cells fire due to crosstalk in a BaSiPM for three different gains. The blue distribution was measured with a front side illuminated SiPM and is shown for comparison.

in the same energy interval. The intensity found is uncertain by a factor of two due to geometrical uncertainties of the implantations in the studied SiPM.

With the best fit photon production efficiencies for two different emission spectra (2000 K and 4500 K) the optical crosstalk behavior of a BaSiPM was studied. I found that the simulated structure cannot be operated if the gain is larger than  $3 \cdot 10^5$ , because then practically all cells of the SiPM will fire once one cell randomly fires. The probability for optical crosstalk will drop to below 10% if the gain of the device is lower than  $10^4$ .

The operation at gains lower than  $10^4$  implicates difficulties in the readout. A necessary requirement in air Cherenkov telescopes is the preservation of the short, a few nanosecond long signals. This can only be achieved by an ultra-fast readout (bandwidth  $\sim 500$  MHz). In such fast readouts appropriate signal-to-noise ratios are obtained for signals consisting of more than  $10^4$  electrons. Therefore, in order to resolve signals down to the single photoelectron level an intrinsic gain of the photon detector in the order of  $10^4$  seems to be at the lowest acceptable limit (see also comment about reduced Geiger efficiencies at the end).

It has to be pointed out that no study was performed up to now that quantifies the maximum acceptable level of optical crosstalk in air Cherenkov telescopes. In the following I motivate why optical crosstalk of a few percent will be acceptable in air Cherenkov telescopes. The most stringent constraint comes from the requirement to lower the trigger threshold of the experiment. The requirement is fulfilled if the accidental trigger rate of the experiment is not dominated by crosstalk events.

In order to give a specific example for the case of a MAGIC type telescope (photon detection efficiencies of about 20%), I assume that the accidental trigger rate of the telescope is dominated by NSB fluctuations and the trigger threshold of one pixel in the camera is set to 4 to 5 photoelectrons. With a four fold coincidence between next neighbors (coincidence window of 10 nsec) this configuration results in an accidental trigger rate of  $< 1$  kHz. Note that 1 kHz is about the maximum rate the data acquisition can handle. The probability that 4 or more photoelectrons from NSB arrive in one pixel of the MAGIC camera within a trigger window of 10 nsec is about

2%. This is similar to the probability that 3 or more cells are fired by optical crosstalk if one NSB photoelectron is detected in a BaSiPM operating at a gain of  $\sim 10^4$  (cf. green curves in Figure 10.31). Therefore, the simulated BaSiPM can be used in a Cherenkov telescope if it has a PDE of  $\sim 20\%$  and is operated at a gain  $\sim 10^4$ .

If it is possible to increase the PDE of the BaSiPM to 100% the recorded flux from NSB will increase by a factor of five. In order to limit the accidental trigger rate of the telescope to below 1kHz, the trigger threshold for each pixel has to be raised to about 9 phe. In this case the gain of the BaSiPM can be increased to about  $5 \cdot 10^4$ , before the contribution from optical crosstalk dominates the accidental trigger rates.

In the two examples discussed above it is assumed that the accidental trigger rates due to NSB and optical crosstalk are about equal. The acceptable total probabilities for optical crosstalk are 15% and 30% respectively (see Figure 10.30). These are acceptable experimental conditions. However, one would aim to reduce the contribution from optical crosstalk to the accidental trigger rate to the level of 10%. This condition is fulfilled, if the probability for crosstalk does not exceed a few percent.

From the discussion it is clear that the BaSiPM has to operate at a gain of a few  $10^4$  to allow for a sufficient suppression of optical crosstalk and sufficient large output signals. However, it was mentioned already several times before that the PDE is a strong function of the applied bias voltage (see e.g. Figure B.6). If the BaSiPM is operated at a lower bias voltage, the gain and thus optical crosstalk but in turn also the PDE will be considerably reduced, which is obviously not desired. One way out of this dilemma would be to reduce the capacitance of one cell and the capacitance in parallel to the quenching resistor, as both determine the gain. However, it will be difficult to reduce the capacitances below the required level as I will show now. Geiger probabilities of  $\sim 100\%$  are obtained for bias voltages of about 10% above breakdown voltage. Assuming a rather low breakdown voltage of 20 V and a gain of  $5 \cdot 10^4$  the total capacitance  $C$  of one cell has to be less than

$$C \leq \frac{\Delta Q}{\Delta U} \leq \frac{5 \cdot 10^4 \times 1.6 \cdot 10^{-19} \text{ C}}{2 \text{ V}} \leq 4 \text{ fF} \quad , \quad (10.7)$$

which is difficult to achieve.

One possibility to reduce optical crosstalk in BaSiPMs are trenches with a depth of a few tens of micrometers close to the avalanche region. This is a major technological challenge because no practical solution for producing such deep trenches is known. I did not study how large the suppression of crosstalk would be.

Considering the above discussed restrictions of the BaSiPM it seems more promising to follow the conventional approach of a front side illuminated SiPM with small active volumes and trenches in between cells to reduce optical crosstalk. The active area in these devices can be increased up to 80%, which is only slightly less than the projected 100% active area of the proposed BaSiPM.



# Chapter 11

## Concluding Remarks

VHE- $\gamma$ -ray astronomy is leaving its infancy and evolves into a mature field of astrophysics. Currently about 45 VHE  $\gamma$ -ray emitting sources are known; of which all except one were discovered by the IACT-technique. Most sources were found in the last three years. This was possible by the use of larger diameter telescopes of lower threshold and a steady improvement of the imaging analysis method. Typical detection limits ( $5\sigma$ ) of the new instruments are about 1% Crab flux for 50 hours of observation.

In the future an improvement in sensitivity for energies  $\gtrsim 1$  TeV can best be achieved by increasing the collection area by a factor of ten e.g. with an array of 100 telescopes distributed over an area of  $10^6$  m<sup>2</sup> or with experiments that have a large field of view.

At lower energies the situation is more complicated. Above 100 MeV EGRET detected 271 sources, which is in contrast to the number of sources detected at multi-GeV to TeV energies despite the higher sensitivity of ground based experiments. This shows that most  $\gamma$ -ray sources have a steep intrinsic cutoff in an intermediate energy range between 10 GeV and 100 GeV. An example of such a source class are pulsars. In this work the presence of strong spectral cutoffs could be confirmed for the Crab pulsar and PSR B1951+32. The cutoff of both pulsars could be constrained to be below 30 GeV, assuming an attenuation of the  $\gamma$ -ray spectrum by exponential cutoff.

The GLAST satellite with its higher sensitivity and a higher upper energy limit compared to the precursor satellite experiment EGRET will measure the energy spectra of several pulsars in the cutoff region up to 100 GeV with great precision and will answer many open questions related to the acceleration mechanisms in pulsars. However, the advantage of ground based experiments, i.e. a large collection area of order  $10^4 - 10^5$  m<sup>2</sup> is out of reach for satellite experiments. Only with ground based experiments it is, therefore, possible to study potentially interesting transient phenomena of low intensity or short time scales, e.g. giant pulses of pulsars, search for radio quiet pulsars, fast flaring of AGN, ... .

A detection of selected  $\gamma$ -ray pulsars by ground based experiments is likely in the future if one is able to lower the energy threshold of experiments from currently 60 GeV to 30 GeV. This can be achieved with a higher photon collection efficiency, by using either larger mirror surfaces and/or new, high efficient photon detectors. One promising photon detector candidate for future ground based  $\gamma$ -ray experiments is the SiPM. The development of the conventional, front side illuminated SiPM is quite advanced. Blue sensitive devices became available with peak PDEs of 60% and sensitive areas of  $3 \times 3$  mm<sup>2</sup> just at the time of the final write-up of this thesis. Compared to classical photomultiplier tubes these SiPM are 3 times more sensitive to Cherenkov light from air showers but still suffer from too small sensor areas. Nevertheless, with these devices it was already possible, for the first time, to record genuine Cherenkov light from air showers.

Apart from lowering the energy threshold in future experiments it will be a major challenge to

improve the sensitivity below 100 GeV. At present the sensitivity of MAGIC is at the limit of measuring the energy spectrum of the Crab nebula down to 60 GeV. The presented 16 hour long observation is sufficient to fulfill this aim with a systematic and statistical uncertainty of about 40% each. An increase in sensitivity and thus reduced systematic uncertainties around and below 100 GeV is only possible with improved background suppression and better angular resolution of the experiment. ALPHA is currently the most effective parameter to separate background and  $\gamma$ -ray events below 100 GeV.

The other issue is to reduce significantly the systematic errors in the energy determination. The large uncertainty has far reaching consequences on the determination of the cut-off energy of pulsars to the cutoff of the acceleration processes of most sources and the absorption cutoffs of high red-shift AGNs.

It is beyond this thesis to study reasons why the  $\gamma$ /hadron-separation by means of the Hillas-analysis degrades below around 150 GeV and basically fails completely below 60 GeV. Solutions that solve these problems cannot be given. However, some conclusions can be drawn. Recorded and analyzed shower images below 100 GeV and impact parameters below 120 m contain at least 100 phe when observed by MAGIC. In telescopes like HEGRA, which have smaller mirror surfaces and subsequently higher energy thresholds than MAGIC, event SIZES of 100 phe or more are normally sufficient to perform excellent  $\gamma$ /hadron-separation. Insufficient signal reconstruction is, therefore, unlikely the reason why  $\gamma$ /hadron-separation fails below 100 GeV in MAGIC.

One reason might be that the larger mirror surface of MAGIC collects enough light from a single high altitude ( $> 5$  km above the telescope) track, e.g. a muon or their hadronic parent particles, which fulfills the trigger condition and imitates a very narrow  $\gamma$ -ray shower. This event class can in principle be distinguished with fast timing and digitization, as currently prepared with new 2 GHz FADCs. Another reason for the background could be an increase in the number of events at lower energies in which a single  $\pi^0$  carries a large fraction of the initial energy, while all the other tracks inside the FOV are below the Cherenkov threshold or are not well reconstructed.

## Appendix A

# A Test of Silicon Photomultipliers as Readout for PET

At the time when I started this thesis the SiPM available could not be used in very demanding astro-particle experiments due to several reasons. The photon detection efficiency was very low and the sensitivity peaked in the “red” because the devices had an *n-on-p* structure, dark count rates were too high and the available sensor sizes too small.

I considered it very important to prove that the SiPM can already be used at a very early stage of the development in applications, which are not as demanding as in high energy physics or astroparticle physics experiments. For this reason I have demonstrated the feasibility of SiPM as readout elements in scintillator based Positron Emission Tomography (PET). It should be mentioned that this study was the very first proof for PET application although the idea was mentioned already as a possibility by a few colleagues in the PET community. The publication that resulted from this study (Otte et al., 2005) was the first of its kind. The results of this study are presented in this chapter.

In the study I use as scintillator the newly developed LYSO crystals, which has similar characteristics as LSO. With the arranged setup I measured an energy resolution of about 22% and a time resolution of a single crystal element of  $(1.51 \pm 0.07)$  nsec, both full width at half maximum. A significant improvement in time resolution could be achieved by triggering on the first photoelectron in the signal. I also present the coincidence rate of two detector channels vs. the position of a small point-like  $^{22}\text{Na}$  positron source.

### A.1 Introduction

Positron emission tomography (PET) scanners are powerful tools for the study of physiological processes in vivo. Current developments aim to build smaller, more compact and less expensive devices with improved resolution and a simpler mode of operation. In case of higher spatial resolution, respectively finer structures one has to take into account the body movements to make the correct correlation with anatomical structures. It might be of advantage to combine a PET scanner with an NMR scanner in order to simultaneously acquire information about the morphological structure and physiological processes<sup>1</sup>. To comply with these requirements, a reliable and cheap photon detector is needed, which is insensitive to magnetic fields and pickup as well as causing minimal interference with the NMR detector’s front end signal pickup.

---

<sup>1</sup>The world largest PET producer CTA/Siemens has decided to develop such a system just a few months ago

First suggestions to use SiPMs as photon sensor in PET applications can be found in e.g. (Akindinov et al., 1997), but no specific study had been performed that time. The main advantages of SiPMs compared to linear (classical) APDs, which are widely used are:

- Standardized output pulses for single photoelectrons
- Low sensitivity for pickup, respectively EMI
- Large intrinsic gain,  $10^5$ – $10^6$
- No need for sophisticated and expensive preamplifiers
- Fast pulse risetime
- Significantly lower operating voltages (20–200 V) compared to that for classical APDs or PMTs
- More stable operation conditions compared to those of classical APDs, e.g. less stringent requirements for temperature and bias stabilization
- The costs are expected to be rather low because of simple production techniques

Another reason why SiPM can be used in PET is that the high dark rate at room temperature is uncritical, as one is interested in signals that exceed the one-photoelectron level by a large margin while the integration window is only a few tens of nanoseconds for fast scintillators.

This chapter has the following structure. Firstly, I discuss the setup and present experimental results on energy, time and position resolution. Finally I conclude on the prospects of SiPMs in PET and discuss some special issues and advantages of the SiPM as readout element.

## A.2 The SiPM used in the Test Setup

For the studies I used a  $(1 \times 1)$  mm<sup>2</sup> prototype SiPM developed at MEPHI and PULSAR enterprises. It is the same device that was also used in the characterization of the optical crosstalk in section 10.5.2. The main features of the device are summarized again in Table A.1. The device has an *n-on-p* structure and is therefore less sensitive to the blue part of the emission spectrum of the LYSO scintillator to which the SiPM is coupled.

Table A.1: Specifications of the SiPM used in this study.

Parameter	Value
Sensor area	$(1 \times 1)$ mm <sup>2</sup>
Number of individual cells	576
Active area fraction of the sensor	25%
Peak PDE (at 540 nm)	10% to 15%
Bias voltage	52 V – 60 V
Breakdown voltage	50 V
Gain	$10^4$ – $5 \cdot 10^6$
Typical dark count rate at room temperature	$10^6$ counts/mm <sup>2</sup> /s

## A.3 Experimental Setup

### A.3.1 Mechanics

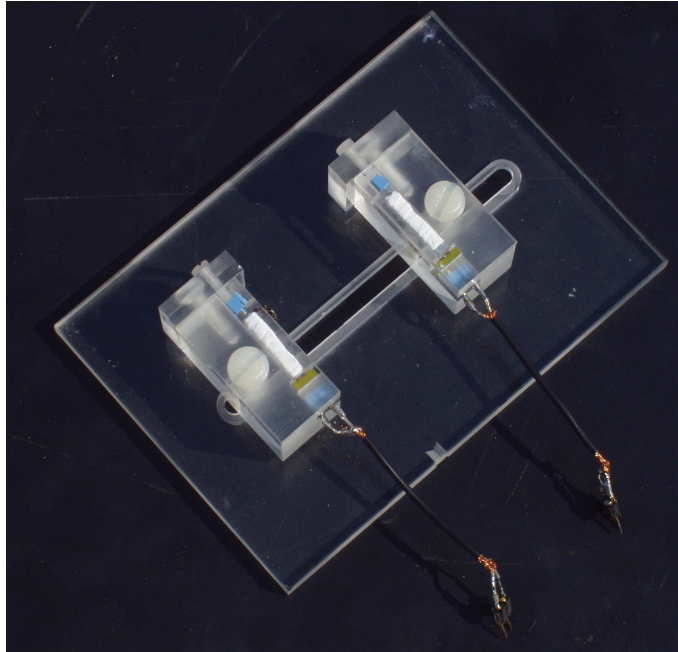


Figure A.1: Photograph of the detector setup used in this study. For details see text.

A simple mechanical support from Lucite was constructed for a good fixation and coupling of the crystal and photon detector combination (see Figure A.1). In between the two crystals a small  $^{22}\text{Na}$ -source was placed that faked a point-like positronium source. The distance between the two detectors was 5 cm.

As scintillator crystals I used LYSO, which was provided by the company Saint Gobain. The crystals have polished surfaces and dimensions  $(2 \times 2 \times 15) \text{ mm}^3$ . LYSO has a high light yield of 32000 photons/MeV and a fast decay time of 40 nsec (Saint Gobain, 2004). Each crystal is wrapped in a dielectric mirror foil from 3M to assure good light collection. The reflectivity of this prototype foil is shown in Figure A.2. The same foil with a  $(1 \times 1) \text{ mm}^2$  hole is used for an aperture and is placed between the end face of the scintillator and the photon detector. This is necessary to compensate for some of the large area mismatch between the sensitive area of the silicon photomultiplier ( $1 \text{ mm}^2$ ) and the four times larger end face of the scintillator. The light coupling between crystal and photon detector was improved by optical grease BC630 from Saint Gobain (refractive index 1.463).

### A.3.2 Signal Readout

For the explanation of the electrical signal readout I refer to Figure A.3. For most of the tests an additional passive RC-integrator ( $\sim 1 \dots 10 \text{ nsec}$ ) was used that is located at the SiPM in order to shape the signal. The shaped signal is routed via a thin Belden 50 Ohm coaxial cable to a preamplifier MAN-1LN from Mini Circuits. No special care was taken to further optimize the signal shape or to suppress noise.

After shaping and amplification the signal is split by a passive divider and routed to an LC554DL oscilloscope and to the input of a discriminator. The oscilloscope is used to determine the magni-

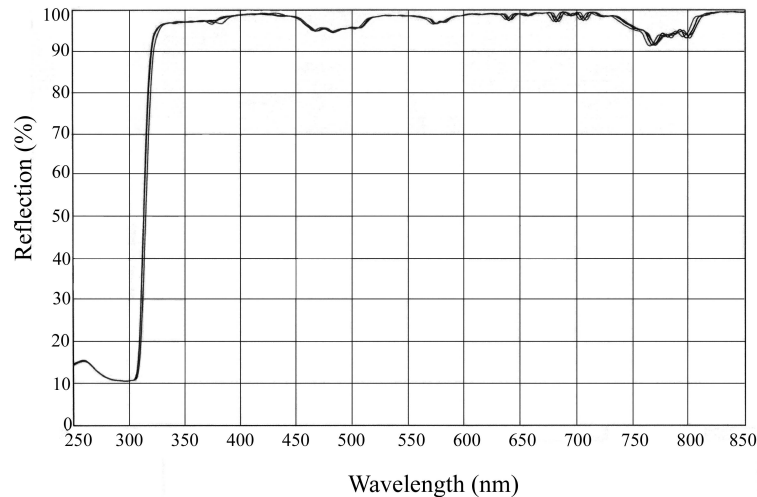


Figure A.2: Reflectivity of the dielectric foil by 3M measured at four different positions on a sample.

tude of the signal by measuring the area under the signal trace (charge) for about 300 nsec for most of the measurements. The output of the discriminator is fed into another input of the LC554DL and provides a time information. For further analysis the time information and signal magnitude are sent via a General Purpose Interface Bus (GBIP) to a PC.

The scope was triggered by the coincidence of the two discriminators with a threshold of  $\sim 250$  mV corresponding to a few photoelectrons.

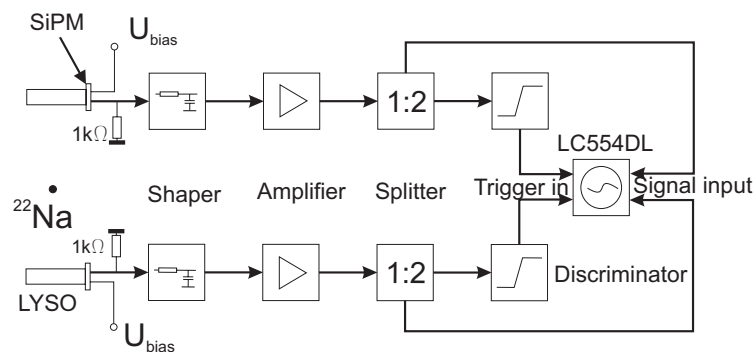


Figure A.3: Block diagram of the electronics used in this test.

## A.4 Energy Resolution and Calibration

Figure A.4(a) shows the pulse height distribution of the  $\gamma$ -spectrum from the  $^{22}\text{Na}$  source when triggering on coincidence events. The spectrum was measured with the source placed half way between the LYSO crystals. The spectrum shows the photopeak of the 511 keV- $\gamma$ 's fully absorbed in the LYSO crystal and a contribution from Compton scattered events (Compton continuum). Due to the discriminator levels the Compton continuum is partially suppressed and the valley between the Compton edge and the photopeak is nearly invisible, despite the system resolution (see later). Figure A.4(b) shows the  $^{22}\text{Na}$  spectrum in a self-triggered mode. In this case the Compton contribution is much higher and the backscatter peak well visible. For the determination of the energy resolution I fitted the photopeak in Figure A.4(a) by a single Gaussian and ignored

the contribution from the Compton edge. I found for the photopeak a full width at half maximum (FWHM) of about 22%, which is close to the 15% FWHM reported by (Pichler et al., 2001) for the LSO read out by classical APDs. Note that the used APD had a sensitive area covering most of the scintillator surface and that the QE of the APD is about four times higher than the PDE of the SiPM.

In addition I measured the energy dependent resolution as well as the energy response by measuring also the pulse height distribution of a  $^{133}\text{Ba}$ - and a  $^{137}\text{Cs}$ -source.  $^{133}\text{Ba}$  and  $^{137}\text{Cs}$  emit  $\gamma$ 's with energies of 356 keV and 662 keV, respectively (Yao et al., 2006). The resulting spectra are shown in Figure A.5.

The spectra around the photopeak have been fitted by a Gaussian to determine the resolution. In Figure A.6 the peak values are plotted versus the known energy. Despite the limited number of SiPM-cells, the correlation between the measured signal and the incident energy is well described by a linear function.

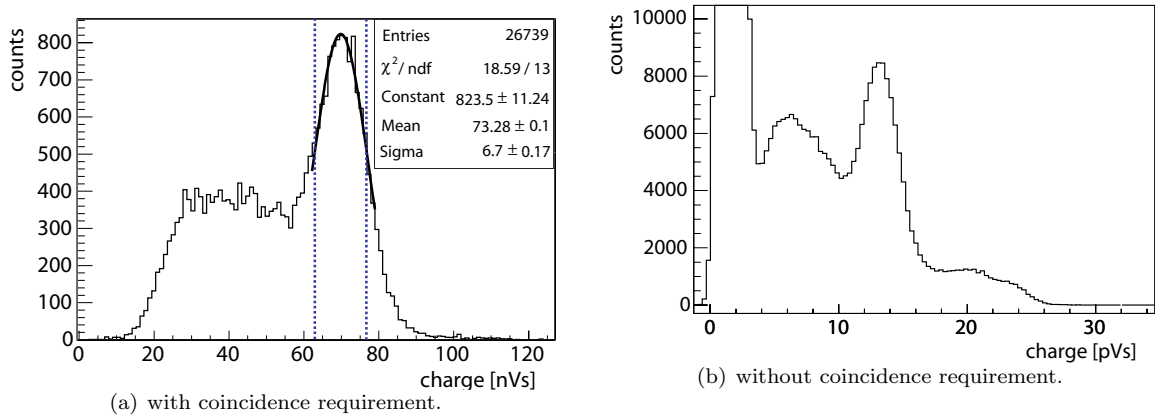


Figure A.4:  $\gamma$ -pulse height distributions of a  $^{22}\text{Na}$  positronium source. The distribution on the left side was measured by triggering on a coincidence of the two channels. The dashed vertical lines indicate the cuts applied in order to restrict the analysis of the time resolution to the photopeak signal. For the distribution on the right a minimum amplitude in the detector channel was required. The 511 keV peak as well the 1.275 MeV shoulder are clearly visible. Note that for the right hand picture no amplifier was used and that the signal was attenuated (18dB).

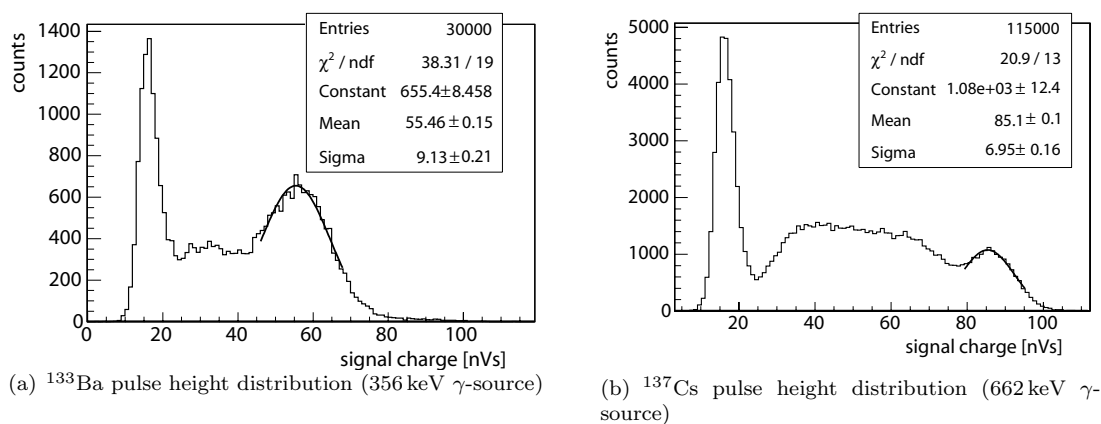


Figure A.5: Pulse height distributions of  $^{133}\text{Ba}$  and  $^{137}\text{Cs}$ . The peaks at lower energy are caused by dark counts where, due to optical crosstalk, many standardized signals are produced within  $\ll 1$  nsec and the summed up signal is high enough to pass the discriminator threshold.

The gain calibration of a SiPM is carried out by analyzing the pulse height distribution of dark

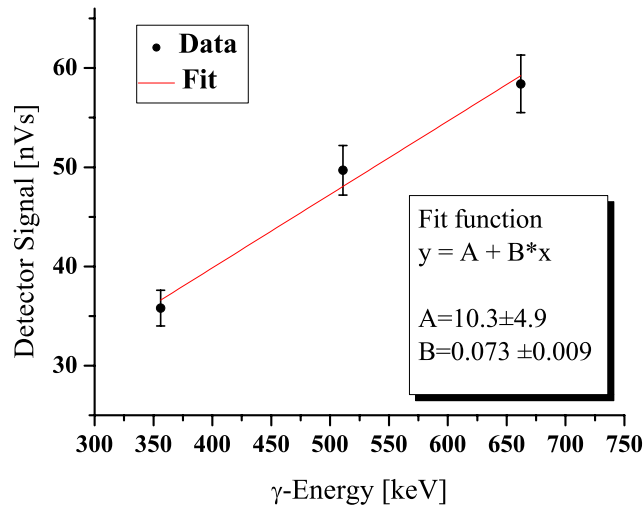


Figure A.6: Correlation between  $\gamma$ -ray energy and signal height (in units of charge, respectively number of fired cell).

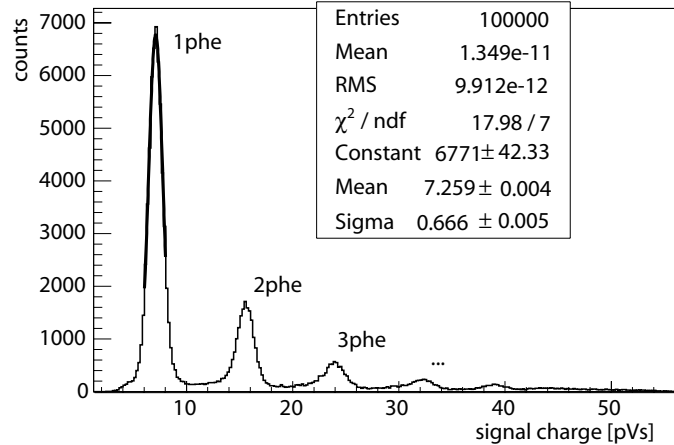


Figure A.7: Spectrum of dark count pulses in the used SiPM. Each peak corresponds to a different number of cells fired per event. The distribution was measured without any preamplifier but the passive splitter (1:2) still included. The insert box lists the fit result for the first peak.

counts (see Figure A.7). The integration window for this measurement was reduced to 10 nsec. As the output amplitude of a cell is standardized the number of fired cells can be derived in first order from the pulse height distribution of the dark count spectrum. I measured the gain by determining the positions of the peaks. The slope of a linear fit to the peak positions in electrons vs. the number of fired cells gives the gain. For the present configuration I found a gain of  $(2.1 \pm 0.16) \cdot 10^6$ .

Together with the gain of the SiPM and the preamplifier ( $21.1 \pm 0.1$ ) I also determined the number of cells that fired on average if one 511 keV- $\gamma$  was fully absorbed in the crystal. From the  $^{22}\text{Na}$  pulse height distribution in Figure A.4(a) I calculated that the peak position corresponds to  $413 \pm 20$  fired cells. Therefore, the signal should already in part be affected by saturation effects as the used SiPM comprises only 576 cells. This conclusion is based on the assumption that the SiPM has a recovery time that is significantly larger than the gate time for the charge collection.

The dependence of the SiPM signal  $N_{\text{SiPM}}$  (number of fired cells) on the number of photoelectrons  $N_{\text{phe}}$  is given by

$$N_{\text{SiPM}} = p \cdot \left( 1 - e^{-\frac{N_{\text{phe}}}{p}} \right), \quad (\text{A.1})$$

where  $p$  is the number of cells of the SiPM (cf. Section 9.4.5).

It has to be stressed again that this formula is based on the assumption that the recovery time of the fired cells is much longer than the optical decay time of the scintillator and recovery effects can therefore be neglected.

From equation A.1 we calculate for 413 fired cells at the photopeak a mean number of  $\sim 730$  phe. This number includes both primary photoelectrons generated by scintillation photons as well as electrons generated by optical crosstalk photons (cf. Section 9.4.4). By using a simple Monte Carlo simulation (neglecting recovery effects of the cells) I corrected for the optical crosstalk. The simulation code is different from the one presented in Section 10.5 in a sense that crosstalk is implemented as a probability distribution, following the pulse height distribution of the dark counts similar to the one depicted in Figure 9.8(b). The geometry of the SiPM is not simulated. Instead, the SiPM is simulated as a boolean array with 576 entries; one entry for each cell, which is sufficient to describe the dynamic behavior of the SiPM. Once a cell of the SiPM is fired it is evaluated in the simulation how many more cells will fire due to crosstalk. In a second step these cells are randomly picked among the 576 cells of the SiPM and fired if possible. This process is repeated in a loop until no more cells are fired by optical crosstalk. A recovery of a pixel once fired was not taken into account in the Monte Carlo.

One outcome of that simulation was that the number of primary photoelectrons should have been around 520. This is in fairly good agreement with a simple estimate based on a scintillation light yield of 16650 photons for a 511 keV- $\gamma$ , a typical light collection onto the SiPM of around  $25 \pm 5\%$  and a mean PDE of around 12% with an estimated error of 3% (due to the spectral mismatch), which results in  $(500 \pm 180)$  photoelectrons.

Monte Carlo simulations predict an energy resolution of 7% FWHM assuming an ideal scintillator with a Gaussian like light distribution over time with fluctuations proportional to  $\sqrt{N_{\text{phe}}}$ . Even for optimal light collection one commonly finds for high light yield scintillators that the resolution does not strictly follow the  $\sqrt{N_{\text{phe}}}$  rule (Moses, 2002). It can be concluded that the 22% resolution has its origin either in crystal scintillation non-uniformities or non-uniform light collection due to the aperture and the large area mismatch. Further studies are needed for the clarification of the 22% resolution<sup>2</sup>.

## A.5 Influence of the Recovery Time on the measured Spectrum

Figure A.4(b) shows, besides the prominent 511 keV peak, indications of the 1.275 MeV line and the corresponding Compton edge (note that the photo efficiency of LYSO around 1200 keV is already highly suppressed). Using the above calibration it is found a number of fired cells exceeding 576. This can only be explained by partially recovered cells firing a second time within the gating time due to late emitted photons from the LYSO.

Further tests are needed but complex recovery effects have to be considered when scintillation light is spread in time exceeding partial recovery. Naively speaking, the 413 fired cells are based on the assumption of standardized cell pulses. Due to partial recovery resulting in lower cell amplitudes the number of fired cells must be considerably larger than 413 and in turn the number of detected photoelectrons must also be larger than 520.

---

<sup>2</sup>In later studies with SiPMs that match to the scintillator end face, energy resolutions of 12.5% have been achieved.

## A.6 Time Resolution

An important parameter to reduce accidental signals in PET is a good time resolution. For the measurement of the time resolution I only accepted events within the one sigma limit around the photopeak in each channel (see vertical lines in Figure A.4(a)). The selection of accepted events was done offline.

A series of tests were performed with a constant fraction (CF) discriminator triggering on the rising edge of the signal. Between the SiPM output and the preamplifier input I inserted a passive element to shape the signal. The time constant of the shaping element and the delay of the constant fraction discriminator was varied. The best time resolution for one detector channel of  $(2.24 \pm 0.03)$  ns FWHM was achieved without shaping and a delay of 7 nsec. I did not correct for the time resolution of the electronics, which was 200 psec and thus can be neglected.

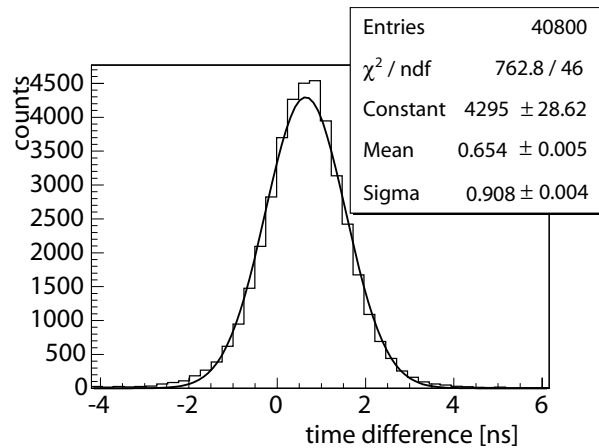


Figure A.8: Distribution of time differences of the two detector channels. For this measurement the time was measured by triggering on the first photoelectron of each signal with a leading edge discriminator.

I also tried a different timing method by triggering on half height of the first photoelectron in the detector signal with a normal leading edge discriminator (LeCroy 621AL). Because of the well defined single photoelectron signal of the SiPM this is a very promising and cheaper method compared to a CF-discriminator, which is not so simple to realize as an integrated circuit (IC). As an additional trigger condition we required a minimum signal amplitude of a few tens of photoelectrons. In this way data recording was triggered only on  $\gamma$ 's. With this setup I achieved a 39% improvement in time resolution compared to the constant fraction method. The distribution of the time differences between the two channels is plotted in Figure A.8. From the distribution I derive a time resolution for a single detector channel of  $(1.51 \pm 0.07)$  ns FWHM. This is comparable to the CF timing in classical APD-LSO combinations in PET (Pichler et al., 2004). The very similar resolution with a SiPM where one detects even less than 20% of the photoelectrons compared to an APD can be explained by the fact that one triggers in SiPMs on the well shaped, standardized signal of the first photoelectron.

## A.7 Position Resolution of a Point Source

The sensitivity of the detector setup on the position of the  $^{22}\text{Na}$   $\gamma$ -source was tested by measuring the coincidence rate versus the displacement of the  $\gamma$ -source. For this test the distance between the two crystals was set to 5 cm and the pointlike radioactive sample was placed in between. Then the  $^{22}\text{Na}$  sample was moved perpendicular to the long side of the crystals. The result is shown in Figure A.9. One expects a linear rise and fall of the coincidence rate as the source moves through the setup. The expected behavior is well reproduced by the measurement. The full width at half

maximum of the position dependent coincidence rate is 1 mm, i.e. only limited by the 2 mm width of the crystals.

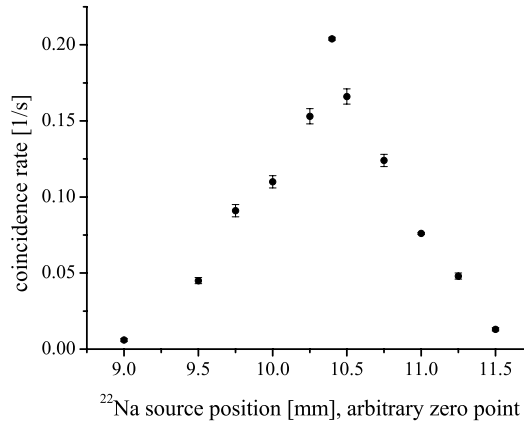


Figure A.9: Coincidence rate as function of the  $^{22}\text{Na}$   $\gamma$ -source position.

## A.8 Conclusions and Discussion of the Results

In this study the predicted prospects for using SiPMs as new photon detectors in PET have been confirmed.

In detail the following conclusions can be drawn from the studies:

1. The 511 keV- $\gamma$  energy resolution of about 22% FWHM was found to be somewhat worse compared to that achieved with larger size classical APDs with a 1:1 coupling to small crystals. The achieved energy resolution is remarkable, as the scintillator was coupled to a SiPM, which is four times smaller than the end-face of the crystal, and the 511 keV- $\gamma$  signal corresponds on average to about 500 photoelectrons. There remains a discrepancy between the resolution predicted by Monte Carlo simulations and the observed value. This can be mainly explained by either
  - a non-uniform light yield of the tested crystals originating in part from the inhomogeneous cerium doping in the crystals
  - some uneven light collection at the end close to the SiPM
  - possibly a contribution of the dead time recovery effects.

The first deficiency can be improved by growing crystals at different parameters while the second problem can normally be solved by a mix of diffuse and specular reflectors and a larger SiPM. In recent measurements (Britvich et al., 2006) an energy resolution of 12.5% (FWHM) has been achieved with  $2 \times 2 \times 12$  mm LYSO crystals coupled to  $3 \times 3$  mm devices made by Z. Sadygov.

2. The impact of the recovery process is not fully understood and needs more studies. Due to the recovery the signals from a previously fired cell after a few decades of nanoseconds are not as large as the standardized ones. The probability of a second avalanche breakdown is reduced in the early phase of recovery<sup>3</sup>. The impact of recovery and the dependence of gain and avalanche breakdown as function of delay need further studies and a better understanding

<sup>3</sup>From our measurements we concluded initially that about 420 cells have fired for a  $\gamma$  of 511 keV. Due to the above described recovery and the smaller amplitudes we conclude that in reality more cells fired and the number of photoelectrons is significantly larger than 500.

for the light detection when the scintillator emission decay time is comparable to the recovery time. This effect does not at all prevent the use of SiPMs in PET applications.

3. Provided one can tolerate some degradation of the optimal energy resolution, the use of SiPMs of much smaller area than the crystal end faces offers room for easy wiring in case of large matrices of pixels. The use of the aperture defining end reflector results only in a small loss of photons. Obviously one should choose a SiPM with a number of cells significantly exceeding the number of expected photoelectrons (possible disadvantages are an increased dead area and in turn a lower PDE. Thus optimization is required).
4. Quite some improvement in the resolution should also be possible when using *p-on-n* structures with a better matched spectral sensitivity to LYSO and higher PDE in the blue wavelength region.
5. The reduction in dead area between cells might result in a higher crosstalk rate. This is uncritical for the use in PET.
6. As mentioned above, the high noise rate is irrelevant for PET applications. Even for a SiPM providing 1 MHz/mm<sup>2</sup> dark count rate a signal of a few hundred fired cells within, say, 100 nsec, is not at all influenced. Cooling for noise reduction is unnecessary.
7. The high intrinsic gain of  $10^5 - 10^6$  is a big advantage for PET applications. As a result of the high gain, the detector will be much less sensitive to pickup. Compared to devices using classical APDs the noise immunity is typically 2–4 orders of magnitude better. Therefore, the shielding requirements are much less demanding. This is of quite some importance when installing a PET detector inside an NMR detector where space is at a premium and where conductive installations should be avoided. It should be possible to install only the crystals and SiPMs inside the NMR magnet and connect them to the outside located electronics by thin coax cables carrying both the bias voltage and the fast signals. The high gain of the SiPMs might also be sufficient to drive low power Vertical Cavity Laser Diodes (VCSEL) and transmit the analog signals by thin optical fibers to the outside electronics.
8. When using simple leading edge discrimination on the first photoelectron, the achieved timing resolution of 1.5 nsec FWHM for a 511 keV- $\gamma$  matches that achieved with linear mode APDs triggering a constant fraction discriminator. As mentioned, a leading edge discriminator is much easier to realize as an IC than a constant fraction discriminator. In principle a sub-nanosecond time resolution should be possible in case SiPMs with a larger number of pixels and a higher PDE are used. It should be stressed again that efficient leading edge triggering is possible due to the large standardized signals of single cells.
9. In this test I studied the 1:1 coupling of small crystals to small SiPMs. In principle it should be possible to read out also 'block' detectors by means of larger area SiPMs. But the lower costs for the "1:1" detectors and the simpler electronics offset very much gains achieved in a lower number of larger SiPMs and a more complex analysis procedure.

In summary it can be concluded that the SiPM is a photon detector concept, which, although still in its prototype phase, can already fully replace classical APDs and conventional PMTs in PET. For the combination of PET with NMR the SiPM has the advantages of:

- insensitivity to magnetic fields
- easy gain calibration due to single cell resolution
- low sensitivity to pickup
- compactness
- need of minimal electronics inside the magnetic field.

Moreover, the production costs of SiPMs are already much lower compared to other photon detectors thus a significant price reduction for PET devices is expected.

The apparent drawbacks such as modest photon detection efficiency, high dark count rates and optical crosstalk only play a minor role in PET.



## Appendix B

# A new Method to measure the Photon Detection Efficiency of Photon Detectors with Single Photon Resolution

### B.1 Introduction

In Cherenkov telescopes and many other applications of photon detectors one needs to know the absolute number of photons incident on the detector. Thus an absolute calibration of the device is necessary.

The overall conversion factor from photons to the number of detectable photoelectrons is called photon detection efficiency (PDE). The major effects that contribute to the PDE of SiPMs have been outlined in Section 9.4.3 and will not be repeated here. One has to point out that the PDE of SiPMs depends on operation parameters like background rate, bias voltage and others whose interplay is difficult to estimate. Therefore, it is mandatory that the PDE of a SiPM is measured under the same conditions under which it will operate in the application. In many PDE measurements of SiPMs a photomultiplier tube of known QE is used as a reference but the collection efficiency of the photoelectrons onto the first dynode is only poorly known and is frequently ignored. This gives rise to a systematic overestimation of the PDE of a SiPM.

In this chapter I present a new method that has been primarily developed to measure the PDE of SiPM but can also be used to measure the PDE of other photon detectors with single photon counting capabilities.

### B.2 Measurement Principle

When measuring a signal different from zero with a SiPM one cannot directly deduce the number of photoelectrons. The reason is the optical crosstalk phenomenon because of which additional cells fire (cf. Section 9.4.4). Disentangling the optical crosstalk contribution from the signal is rather difficult. If not done correctly it apparently results in a too high measured PDE. The dependence of the output signal on the input signal is non linear (cf. Section 9.4.5). These problems can be bypassed if the SiPM is illuminated with short low intensity light flashes ( $\sim 10$  nsec) and the triggers  $N(0)$  are counted where no photoelectron was detected by the SiPM. As one normally knows the

total number of flashes  $N_{total}$ , one can calculate the mean number of detected photoelectrons  $\mu$  per flash if one assumes a Poisson distribution for the number of detected photoelectrons per light pulse

$$P(0) = e^{-\mu} = \frac{N(0)}{N_{total}} \quad (\text{B.1})$$

$$\Rightarrow \mu = -\ln \frac{N(0)}{N_{total}} \quad (\text{B.2})$$

where  $P(0)$  is the probability that no photoelectron is detected if the SiPM is illuminated by one light flash. In this way the task of determining the mean number of photoelectrons is reduced to a counting experiment that only depends on how well one can separate a signal from the background. This condition is very well satisfied in the case of SiPMs where one can almost unambiguously identify on an event by event base the “zero”-signal events. This is illustrated in Figure B.1, which shows the distribution of signal amplitudes of a SiPM during a measurement of its PDE.

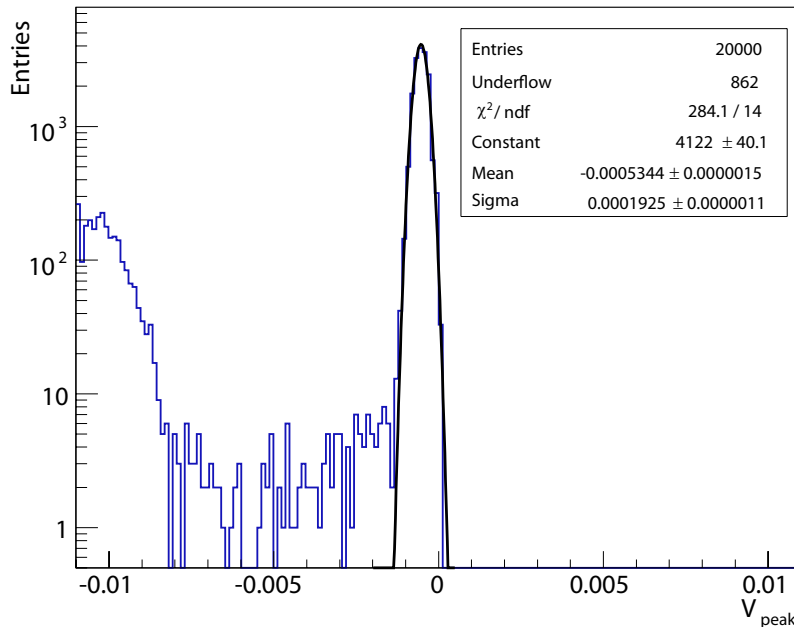


**Figure B.1:** Pulse height distribution of a SiPM during a measurement of the PDE. Pedestal events can be very well separated due to the large and standardized output signals of the SiPM. Note the logarithmic scale of the y-axis and that the output signal of the SiPM is negative.

If in a second measurement the mean number of incident photons can be separately determined, one can infer the PDE. I have built an apparatus for such a study that is described in more detail in the following section. In this apparatus each light flash illuminates a PiN diode<sup>1</sup> in parallel to the SiPM. From the signal of the PiN diode one can calculate the mean number of photons ( $\overline{N}_{photons}$ ) at the position of the SiPM as will be explained later and finally obtain the PDE:

$$\text{PDE} = \frac{\mu}{\overline{N}_{photons}} \quad (\text{B.3})$$

<sup>1</sup>As a gain 1 device the photodiode is a perfect device to measure the light pulse intensity even in the pulsed mode. The only requirement is that the light pulse must be significantly larger than the noise of the readout system.

## B.3 Measurement Procedure

In the following I describe the mechanical setup that is used to determine the average number of photons hitting the SiPM. I explain how the setup is calibrated and how a measurement of the PDE is carried out.

### B.3.1 Mechanical Setup

The mechanical setup consists of a small integrating sphere (a so-called Ulbricht sphere), which is actually approximated by a cylinder closed with two caps. The sphere has been made from sintered Teflon powder, a diffuse high reflectivity material (Pichler et al., 2000) (c.f. Fig. B.2). The wall of the cylinder is 25 mm thick, and the inner diameter of the cylinder is 40 mm. The cylinder has two orthogonal viewing ports of 2 mm and 10 mm diameter, respectively.

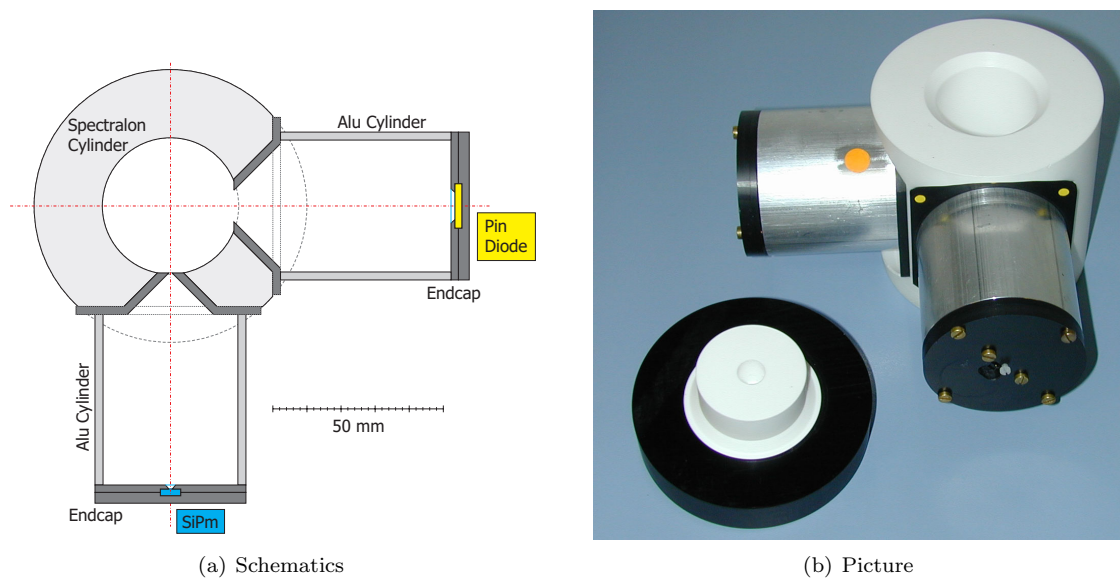


Figure B.2: Left side: Horizontal cut through the mechanical setup used for the measurement of the PDE. Right side: Photograph of the mechanical setup with the opened cap. A pulsed LED emits light into the sphere through the hole in the cap. The setup guarantees a fixed light splitting ratio between the reference detector (PiN diode) and the photon detector under investigation.

In the measurement of the PDE a monochromatic LED illuminates the sphere through a small inlet port in the upper cap of the integrating sphere (Figure B.2(b)). From Monte Carlo simulations it had been concluded that a photon is on average 100 times diffusely reflected within the integrating sphere before it gets absorbed or exits through one of the viewing ports. Thus the decay time of the light intensity inside of the sphere is well below 20 nsec. The integrating sphere in combination with the viewing ports is acting as an optical splitter, where the splitting ratio is given by the areas of the two viewing ports.

Mounted behind each viewing port is a small aluminum cylinder that is closed with a precision diaphragm. This geometry guarantees a highly uniform and parallel light beam at the position of the diaphragm. The inner wall of the aluminium cylinders are covered by black fleece to avoid any stray light.

The diaphragms have a diameter of 0.8 mm and 8 mm respectively. Behind the larger diaphragm a calibrated PiN photodiode is placed, while the unit under test is installed behind the smaller diaphragm.

### B.3.2 Calibration of the Setup

Before the PDE can be measured two more calibrations have to be carried out: (1) determination of the exact ratio of the light intensity behind both diaphragms and (2) the calibration of the PiN diode signal in terms of photoelectrons.

1. It is not sufficient to determine the ratio of the light intensities exiting the two diaphragms just from a calculation because of uncertainties in the dimensions of the mechanical setup. The ratio is directly measured with a LED that is constantly emitting light into the cylinder. At each diaphragm a PiN diode is placed and the photocurrents are measured with a picoampere meter. After that the PiN diodes are exchanged and the currents are measured again. The ratio of the currents (after pedestal subtraction) obtained with the same diode at the two positions is the intensity ratio that had been looked for. This procedure was repeated e.g. with LEDs of different colors and intensities and different PiN diodes. Within 2% all trials yielded the same result of an intensity ratio of 3660.
2. For the absolute calibration of the PiN diode signal in photoelectrons, the PiN diode is irradiated by 59 keV- $\gamma$ 's from an  $\text{Am}^{241}$ -source. Figure B.3 shows a recorded spectrum. From the signal of a fully absorbed  $\gamma$ -ray the PiN Diode signal can be calibrated in photoelectrons. The average number of electrons that a fully absorbed 59 keV- $\gamma$  generates in the depleted layer of the PiN diode is

$$\frac{59000 \text{ eV}}{3.62 \frac{\text{e-h-pairs}}{\text{eV}}} = 16300 \text{ electrons.} \quad (\text{B.4})$$

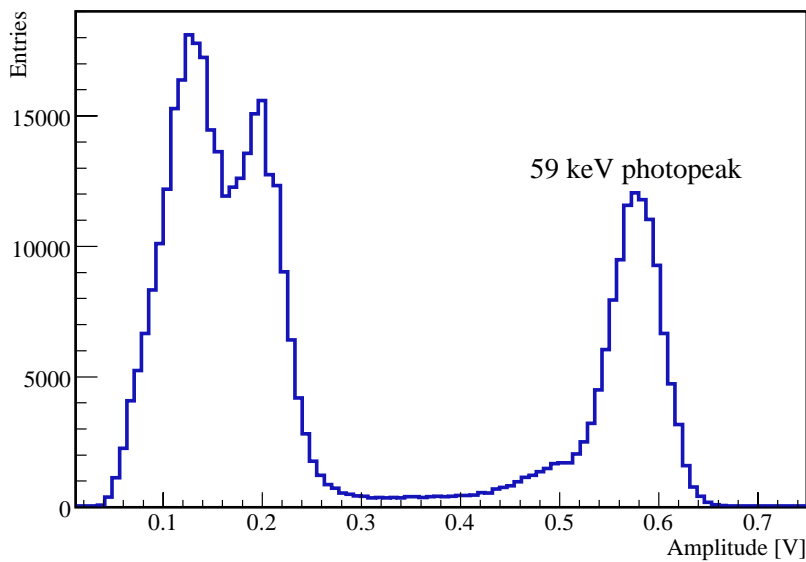


Figure B.3: Pulse height distribution of the PiN diode irradiated with a 59 keV  $\gamma$ -source ( $\text{Am}^{241}$ ). The photo-peak is very well visible.

If the PiN diode is now illuminated with a pulsed light source through the larger port it is possible to determine the average number of photoelectrons and subsequently the average number of photons that are impinging on the diode as the quantum efficiency of the PiN diode is also known. By means of the known intensity ratio of 3660 between the two diaphragms it is then possible to obtain the average number of photons impinging on the SiPM.

### B.3.3 Measurement Procedure of the PDE

The SiPM under investigation is placed behind the diaphragm with the smaller (0,8 mm diameter) hole. With the aid of a microscope it is made sure that the hole is completely covered by the active area of the SiPM. The SiPM signal is amplified by a broadband 500 MHz voltage amplifier MAN-1LN from Mini-Circuits. The signal of the PiN diode<sup>2</sup> (located behind the diaphragm with the larger hole) was amplified with a charge sensitive amplifier (Canberra BT2003) and a spectroscopy amplifier (Canberra 2020, shaping time  $3 \mu\text{s}$ ). The block diagram of the setup is shown in Figure B.4

In the measurement a monochromatic LED in pulsed mode<sup>3</sup> (full width of a light flash is  $< 4 \text{ nsec}$ ) is then flashing into the integrating sphere. Within a time window of 140 nsec after the LED trigger the signal of the SiPM is recorded and the maximum signal amplitude within this time window saved to disk. From the data the mean number of photoelectrons is calculated with Equation B.2. Finally by applying Formula B.3 the PDE is obtained by dividing the mean number of photoelectrons detected by the SiPM and the average number of photons impinging on the SiPM as derived from the PiN diode signal.

## B.4 Results

### B.4.1 PDE of a HPD

The method was verified by measuring the PDE of a calibrated Hybrid Photo Detector (HPD) R9792U-40 from Hamamatsu, which is currently under study for the MAGIC II experiment (Hayashida et al., 2006). The method can be applied without modification as the HPD has single photoelectron resolution. The gain of the studied HPD was less than  $10^5$ . Therefore, the time window to extract the HPD signal was reduced from 140 nsec to 60 nsec to obtain a sufficient high signal to noise ratio and thus an acceptable separation of the pedestal.

The PDE was measured at three different wavelengths and is compared in Table B.1 with the values obtained from a standard quantum efficiency setup in the institute and the values from the data sheet of the HPD. The results obtained with the method that has been described here are systematically  $\sim 15\%$  below the values from Hamamatsu and the values obtained with the QE-setup in the group.

The reason for this difference is not known and subject to further investigation. A likely reason could be a non perfect collection efficiency of photoelectrons in the HPD between the photocathode and the APD as well as backscattering effects. This would give rise to a lower PDE. Also systematic effects in the measurements cannot be excluded.

Table B.1: Measurement of a HPD Typ R9792U-40 by Hamamatsu. **PDE** (this meas.) is the result of my measurement, **QE** (in house) is the result of a “conventional” QE-measurement performed at the institute and **QE** (Hamamatsu) the values from the HPD ticket

$\lambda[nm]$	<b>PDE</b> (this meas.)	<b>QE</b> (in house)	<b>QE</b> (Hamamatsu)
395	$24 \pm 1$	30.1	28.7
590	$27 \pm 1$	32.1	31.5
610	$23 \pm 1$	28.2	27.0

<sup>2</sup>Hamamatsu APD S3590-08

<sup>3</sup>The emission spectra of the LEDs in pulsed mode have been verified with a spectrograph and match within 5 nm the specifications given by the manufacturers.

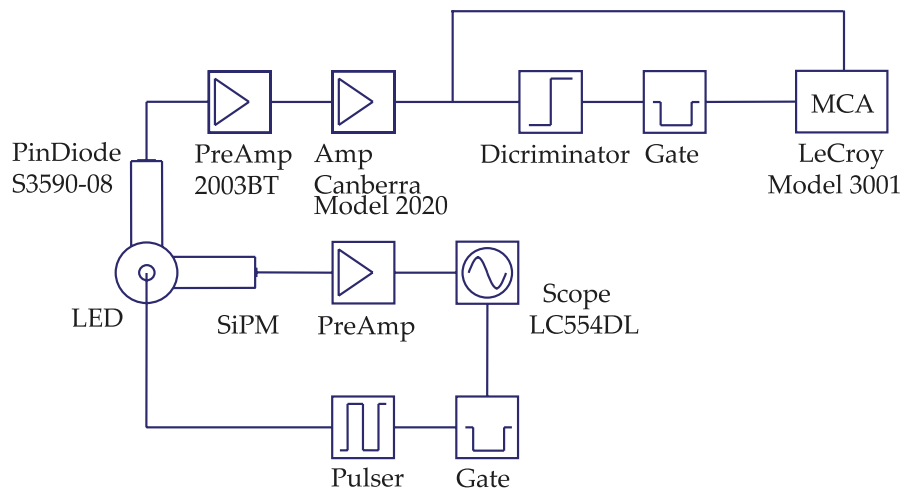


Figure B.4: Block diagram of the setup used in the measurement of the PDE.

### B.4.2 PDE of a SiPM

I have tested the PDE of a prototype SiPM by MEPhI with 1024 cells per  $\text{mm}^2$  and an estimated geometrical efficiency of about 10%. The measurement was done at room temperature at several wavelength and a fixed bias voltage. The result is shown in Figure B.5. As expected from the structure of the tested device ( $n$ -on- $p$  structure), the maximum efficiency is in the red wavelength region and decreases towards blue wavelengths.

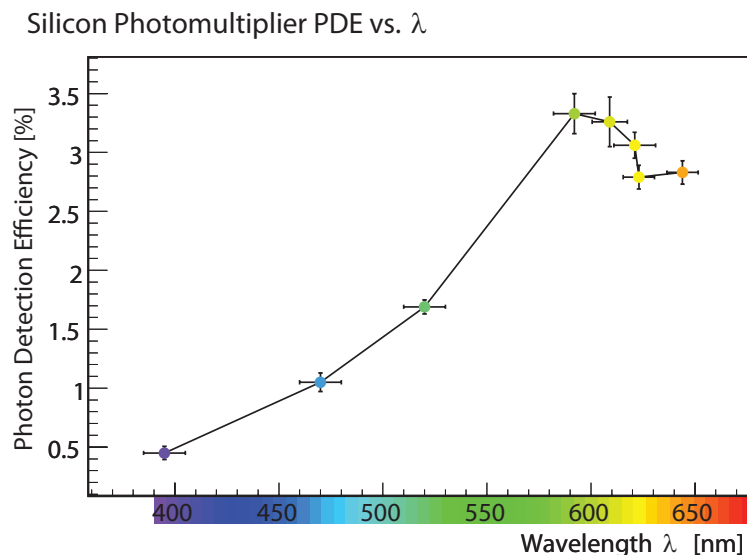


Figure B.5: Photon detection efficiency of a SiPM vs. wavelength. The SiPM tested here has 1024 cells on one square millimeter sensor area with a geometrical efficiency of about 10%.

In a separate measurement the PDE of the same SiPM was measured as a function of the bias voltage (Figure B.6). The PDE saturates at an over-voltage of  $\sim 7\%$  above breakdown voltage. Thus indicating a near 100% probability for a breakdown to take place at these over-voltages.

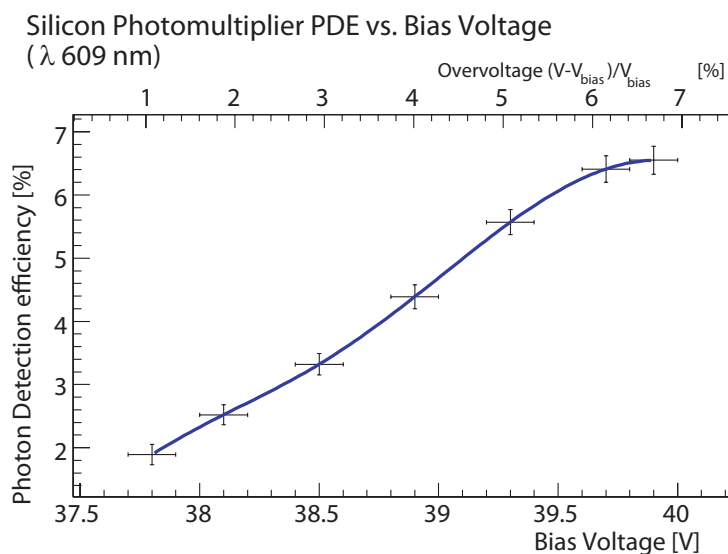


Figure B.6: Photon detection efficiency of a SiPM vs. bias voltage. The measurement shows the strong dependence of the PDE on the bias voltage and indicates a saturation of the PDE at an over-voltage of 7% above breakdown.

## B.5 Summary

I have presented a new method to measure the PDE of SiPMs that is independent of intrinsic SiPM features, which give rise to systematic uncertainties in other methods to measure the PDE. The method can also be applied to other photon detectors that show single photoelectron resolution like e.g. HPDs or classical photomultiplier tubes (PMTs) with a high gain first dynode.

For PMTs this method is especially interesting as it offers the possibility to determine the photoelectron collection efficiency onto the first dynode, which is otherwise difficult to measure.



# Appendix C

## Central Pixel

### C.1 Modification of the Central Pixel Readout

The CP-readout was modified such that the data acquisition (DAQ) of MAGIC digitizes and records the CP-signal every time the MAGIC-readout is triggered by a cosmic ray event. Figure C.1 shows the block diagram of the modified CP-configuration that allows both a dedicated readout and the integration into the MAGIC DAQ.

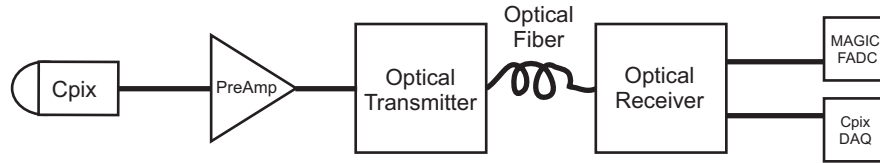


Figure C.1: Blockdiagram of the modified signal chain of the Central Pixel of the MAGIC camera.

The newly designed optical receiver splits the CP-signal. One part of the signal is routed to the dedicated CP-DAQ and another part goes to the DAQ of the MAGIC telescope. The schematics of the developed optical receiver is shown in Figure C.2.

#### C.1.1 Test of the Drift of the MAGIC System Clock

Optical observations of the Crab pulsar were used to test the drift of the MAGIC system clock. The data sample, discussed in Section 6.4, was recorded by one channel of the MAGIC-DAQ. The data were processed as outlined in Section 5.8.1, 5.8.2 and 6.4. For the test presented here the assumed frequency of the pulsar was successively changed in steps of ( $\Delta\nu \sim 3.3 \cdot 10^{-9}$  Hz) with respect to the frequency of the radio ephemeris. For each assumed frequency a  $\chi^2$ -Test and a H-Test was evaluated (see Section 5.8.3 for an explanation of the  $\chi^2$ -Test and a H-Test). To make the H-Test work with the analog information of the CP, the amplitude of the recorded CP-signal  $S_{\text{CP}}$  was included in the coefficients  $\alpha$  and  $\beta$  (cf. Equation 5.17)

$$\alpha(j) = \frac{1}{N} \sum_{i=1}^N S_{\text{CP}} \cdot \cos j\theta, \quad \beta(j) = \frac{1}{N} \sum_{i=1}^N S_{\text{CP}} \cdot \sin j\theta \quad . \quad (\text{C.1})$$

As one can see from Figure C.3 both tests do not have their maximum at zero offset from the frequency of the ephemeris but at  $\Delta\nu \sim 3.3 \cdot 10^{-9}$  Hz. If one assumes that the analysis chain

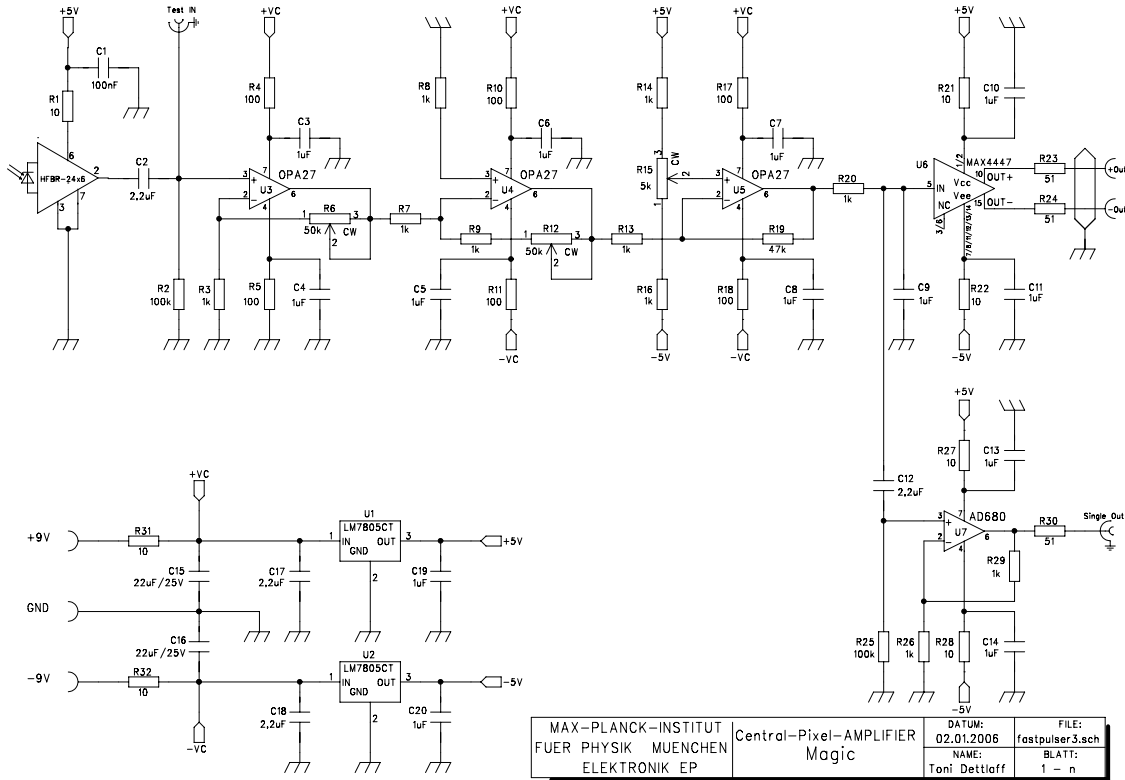


Figure C.2: Schematics of the optical receiver for CP-readout with the DAQ of MAGIC.

is performing accurate, one can estimate the accuracy of the frequency  $\nu$  that is stated in the ephemeris as

$$\frac{\Delta\nu}{\nu} = \frac{3.3 \cdot 10^{-9} \text{ Hz}}{29.77 \text{ Hz}} = 1.1 \cdot 10^{-10} \quad , \quad (\text{C.2})$$

which is in agreement with the quoted accuracy of  $10^{-10}$  (Lyne, 2006). Therefore, one can conclude that the stability of the system clock of MAGIC is better  $10^{-10}$ .

The estimate of the peak position of the main pulse ( $-252 \pm 64 \mu\text{sec}$ ) in Section 6.4.3 and the test of the stability of the clock (better  $10^{-10}$ ) show that the system clock of MAGIC and the set up pulsar-analysis chain are properly working.

### C.1.2 Sensitivity of the Central Pixel

The sensitivity of the CP with its modified readout was tested by evaluating the light curve of the Crab pulsar with an increasing number of events. For each light curve a  $\chi^2$ -Test was calculated. The test results are shown in Figure C.4 vs. the number of events from which the light curve was calculated. The  $\chi^2$  is linearly increasing with increasing number of events, as expected. The fitted slope for a straight line ansatz through the origin is  $5.043 \cdot 10^{-4} \pm 0.004 \cdot 10^{-4} \chi^2/\text{event}$ .

In order to compare the sensitivity of the CP with similar setups of other experiments it is more convenient to talk about samples and not events. The significance of the measured light curve of the Crab pulsar, binned in 18 bins, reaches  $5\sigma$  once 122000 samples are accumulated, It follows a sensitivity of

$$0.014 \frac{\sigma}{\sqrt{\text{samples}}} \quad . \quad (\text{C.3})$$

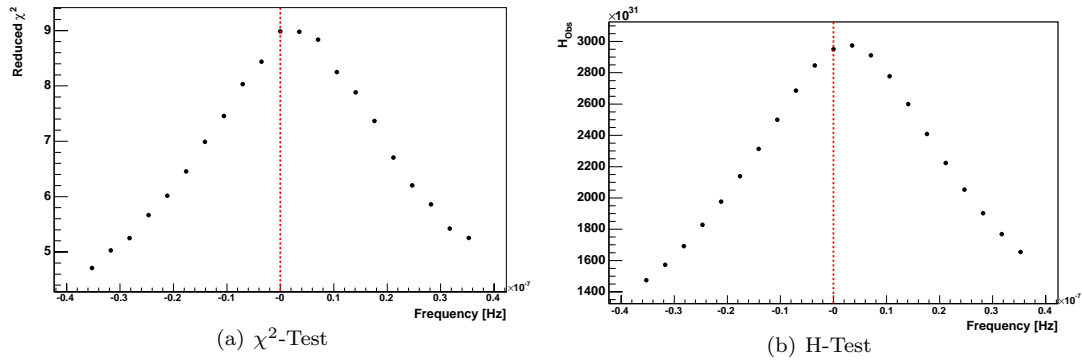
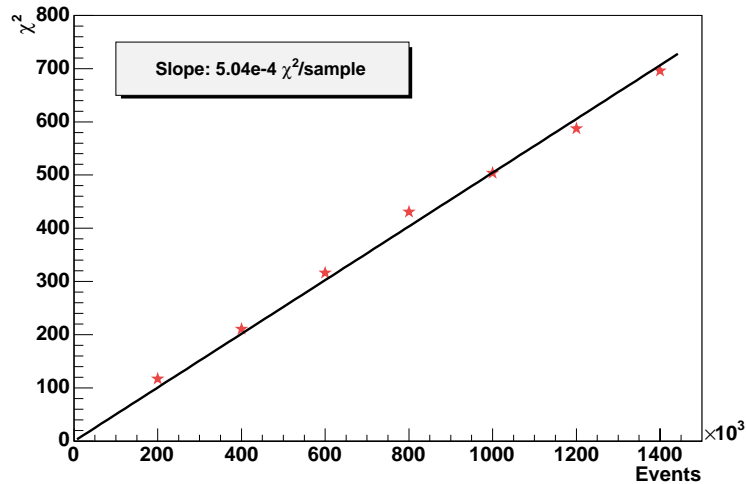


Figure C.3: Scan around the frequency of the radio ephemeris. See text for details.

Figure C.4:  $\chi^2$  vs. the number of events used to calculate the light curve of the Crab pulsar. The number of degrees of freedom is 17.

Hinton et al. (2006) give a sensitivity of their setup of  $4\sigma/\sqrt{\text{sec}}$  at a sampling rate of 40 kHz, which translates to  $0.02\sigma/\sqrt{\text{sample}}$ . This is a 43% higher sensitivity than the one of the MAGIC-CP.

### C.1.3 Future Improvements of the Central Pixel

The sensitivity of the Central Pixel can be improved. The impact of the optical point spread function of the telescope, an aperture in front of the CP, noise in the readout and the use of photon detectors with higher photon detection efficiencies are addressed below. The reasons for the lower sensitivity are: a) the focussing of the telescope to 10 km and not to infinity and b) the lack of an optimized pixel diameter, see below.

**Optical point spread function and the use of an aperture in front of the CP** The optical point spread function (PSF) of MAGIC is such that 66% of the light of a point source at infinity is contained within a circle of 17 mm radius<sup>1</sup>. In the following it is assumed that the shape of the PSF can be described with a 2D-Gaussian (Equation 6.8). The width of the 2D-Gaussian is then  $\sigma_{\text{opt}} = 0.035^\circ$  or normalized to the radius of the circular area of the CP ( $0.05^\circ$ )  $\sigma_{\text{opt}} = 0.7$ .

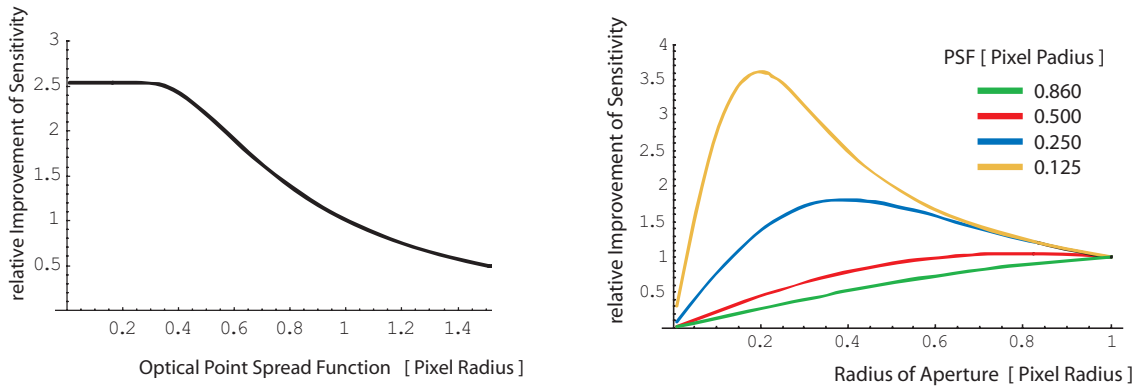
<sup>1</sup>Note that MAGIC is focusing to 10 km. If MAGIC focuses to infinity 66% of the light of a point source at infinity is contained within a circle of radius 13 mm. (Biland, 2006)

The sensitivity of the CP-setup is estimated with the signal ( $S$ ) to noise ( $N$ ) ratio (SNR), which is defined as

$$\text{SNR} = \frac{S}{\sqrt{N}} \propto \frac{\int_0^r \frac{r'}{\sigma_{\text{opt}}^2} \cdot \exp\left(\frac{-r'^2}{2\sigma_{\text{opt}}^2}\right) dr'}{\sqrt{r^2 + \sigma_{\text{el}}^2}}, \quad (\text{C.4})$$

where noise contributions are the NSB that scales with the size of an aperture of radius  $r$  placed in front of the CP ( $\propto r^2$ ) and the noise from the electronics ( $\sigma_{\text{el}}$ ) in units of NSB.

It is shown in Figure C.5(a) how the sensitivity improves with smaller PSF. In the graph the sensitivity is normalized to the sensitivity for  $\sigma_{\text{opt}} = 1$  pixel radius and by assuming no noise in the readout electronics. The sensitivity reaches a plateau once nearly all the pulsar signal is falling into the CP entrance window ( $\sigma_{\text{opt}} \approx 0.4$  pixel radii). Note that currently  $\sigma_{\text{opt}}$  is 0.7 pixel radii, i.e. a significant improvement of the sensitivity can be expected with a smaller optical PSF.



(a) Sensitivity vs. optical PSF without aperture in front of the CP.

(b) Sensitivity vs. radius of an aperture in front of the CP for different optical PSFs.

**Figure C.5:** Dependence of the Sensitivity of the Central Pixel on the optical PSF and the radius of an aperture placed in front of the CP.

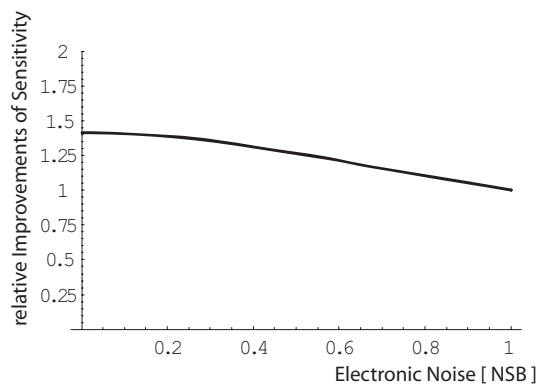
If it is possible to achieve an optical PSF  $\lesssim 0.25$  pixel radii, an additional aperture in front of the CP will improve the sensitivity as the influence of NSB is efficiently suppressed. Figure C.5(b) illustrates the effect. For different PSFs the dependence of the sensitivity on the radius of an aperture is shown. If an aperture is inserted in the existing setup the sensitivity of the CP would degrade, as expected.

**Noise in the readout** Figure C.6(a) illustrates the dependence of the sensitivity of the CP on the noise of the electronics. The electronic noise is given in units of NSB-fluctuations. It is evident that care should be taken to keep the electronic noise level below 25% of the NSB-fluctuations.

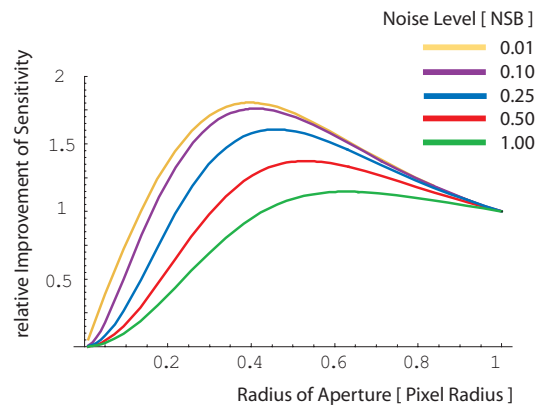
Figure C.6(b) shows for a  $\sigma_{\text{opt}}$  of 0.25 pixel radii, how the sensitivity changes if an aperture is placed in front of the CP and different noise levels apply. As soon as the electronic noise reaches the level of the NSB fluctuations the sensitivity is not more improved by an aperture.

**The photon detector** of the CP is a photomultiplier type 9116A;  $1'' \varnothing$  from the company ET, the same type of photomultiplier as used for the pixels of the inner camera of MAGIC. Replacing the PMT with a detector of the same active area but with single photon counting capability and four times higher photon detection efficiency has two advantages. (1) The sensitivity will improve by a factor of 2. (2) Optical phenomena like giant pulses in pulsars can be sensitively probed down to nanosecond timescales.

A silicon photomultiplier would be a prime candidate for a future CP as devices with 60 % PDE and dark count rates well below the NSB level are now available.



(a) Sensitivity vs. electronic noise.



(b) Sensitivity vs. radius of an aperture in front of the CP for different electronic noise levels and for an assumed optical PSF of 0.25 pixel radii.

Figure C.6: Dependence of the Sensitivity of the Central Pixel on electronic noise.



# Bibliography

- B. S. Acharya, P. N. Bhat, V. N. Gandhi, P. V. R. Murthy, and G. P. Sathyanarayana. Search for TeV gamma ray emission from PSR 1957 + 20. *A&A*, 232:L5–L8, June 1990.
- F. Aharonian, et al. The Crab Nebula and Pulsar between 500 GeV and 80 TeV: Observations with the HEGRA Stereoscopic Air Cerenkov Telescopes. *ApJ*, 614:897–913, October 2004. doi: 10.1086/423931.
- F. Aharonian, et al. Observations of the Crab nebula with HESS. *A&A*, 457:899–915, October 2006a. doi: 10.1051/0004-6361:20065351.
- F. Aharonian, et al. First detection of a VHE gamma-ray spectral maximum from a cosmic source: HESS discovery of the Vela X nebula. *A&A*, 448:L43–L47, March 2006b. doi: 10.1051/0004-6361:200600014.
- F. A. Aharonian, et al. Optimizing the angular resolution of the HEGRA telescope system to study the emission region of VHE gamma rays in the Crab Nebula. *A&A*, 361:1073–1078, September 2000.
- F. A. Aharonian, et al. A possible association of the new VHE  $\gamma$ -ray source HESS J1825 137 with the pulsar wind nebula G 18.0 0.7. *A&A*, 442:L25–L29, November 2005. doi: 10.1051/0004-6361:200500180.
- F. A. Aharonian and A. M. Atoyan. Nonthermal Radiation of the Crab Nebula. In N. Shibasaki, editor, *Neutron Stars and Pulsars: Thirty Years after the Discovery*, pages 439–+, 1998.
- F. A. Aharonian, A. M. Atoyan, and T. Kifune. Inverse Compton gamma radiation of faint synchrotron X-ray nebulae around pulsars. *MNRAS*, 291:162–176, October 1997.
- F. A. Aharonian and S. V. Bogovalov. Exploring physics of rotation powered pulsars with sub-10 GeV imaging atmospheric Cherenkov telescopes. *New Astronomy*, 8:85–103, February 2003. doi: 10.1016/S1384-1076(02)00200-2.
- C. Akerlof, J. Dimarco, H. Levy, C. MacCallum, D. Meyer, P. Radusewicz, R. Tschirhart, and Z. Yama. Detection of High Energy Gamma Rays from the Crab Nebula. In *International Cosmic Ray Conference*, pages 135–+, 1990.
- N. Akil et al. A multimechanism model for photon generation by silicon junctions in avalanche breakdown. *IEEE Trans. Elec. Dev.*, 46:1022–1028, 1999.
- A. V. Akindinov, A. N. Martemianov, P. A. Polozov, V. M. Golovin, and E. A. Grigoriev. New results on MRS APDs. *Nuclear Instruments and Methods in Physics Research A*, 387:231–234, February 1997.
- M. A. Alpar, P. W. Anderson, D. Pines, and J. Shaham. Vortex creep and the internal temperature of neutron stars. II - VELA pulsar. *ApJ*, 278:791–805, March 1984. doi: 10.1086/161849.

- M. A. Alpar, H. F. Chau, K. S. Cheng, and D. Pines. Postglitch relaxation of the VELA pulsar after its first eight large glitches - A reevaluation with the vortex creep model. *ApJ*, 409:345–359, May 1993. doi: 10.1086/172668.
- M. A. Alpar, H. F. Chau, K. S. Cheng, and D. Pines. Postglitch Relaxation of the Crab Pulsar after Its First Four Major Glitches: The Combined Effects of Crust Cracking, Formation of Vortex Depletion Region and Vortex Creep. *ApJ*, 459:706–+, March 1996. doi: 10.1086/176935.
- M. Amenomori, et al., The Tibet As  $\gamma$  Collaboration. Observation of Multi-TeV Gamma Rays from the Crab Nebula using the Tibet Air Shower Array. *ApJ*, 525:L93–L96, November 1999. doi: 10.1086/312342.
- P. W. Anderson and N. Itoh. Pulsar glitches and restlessness as a hard superfluidity phenomenon. *Nature*, 256:25–27, July 1975.
- J. Arons. Some problems of pulsar physics. *Space Science Reviews*, 24:437–510, December 1979.
- J. Arons. Pair creation above pulsar polar caps - Geometrical structure and energetics of slot gaps. *ApJ*, 266:215–241, March 1983. doi: 10.1086/160771.
- A. M. Atoyan and F. A. Aharonian. On the fluxes of inverse Compton gamma-rays expected from the Crab Nebula. *A&AS*, 120:C453+, December 1996a.
- A. M. Atoyan and F. A. Aharonian. On the mechanisms of gamma radiation in the Crab Nebula. *MNRAS*, 278:525–541, January 1996b.
- P. Auger, P. Ehrenfest, R. Maze, J. Daudin, and R. A. Fréon. Extensive Cosmic-Ray Showers. *Reviews of Modern Physics*, 11:288–291, July 1939.
- W. Baade and F. Zwicky. Cosmic Rays from Super-novae. *Proceedings of the National Academy of Science*, 20:259–263, 1934.
- P. Baillon and et al. Observation of the Crab in Multi TeV Gamma Rays by the THEMISTOCLE experiment. In *International Cosmic Ray Conference*, pages 220–+, August 1991.
- W. E. Beadle, J. C. C. Tsai, and R. D. Plummer. *Quick Reference Manual for Silicon Integrated Circuit Technology*. John Wiley & Sons, New York, 1984.
- W. Bednarek. High Energy Processes in Pulsar Wind Nebulae. *ArXiv Astrophysics e-prints*, October 2006.
- W. Bednarek and M. Bartosik. Gamma-rays from the pulsar wind nebulae. *A&A*, 405:689–702, July 2003. doi: 10.1051/0004-6361:20030593.
- W. Bednarek and M. Bartosik. Gamma-rays from the Pulsar Wind Nebulae. In F. A. Aharonian, H. J. Völk, and D. Horns, editors, *AIP Conf. Proc. 745: High Energy Gamma-Ray Astronomy*, pages 329–334, February 2005a.
- W. Bednarek and M. Bartosik. TeV gamma-rays from the Northern sky pulsar wind nebulae. *Journal of Physics G Nuclear Physics*, 31:1465–1474, December 2005b. doi: 10.1088/0954-3899/31/12/008.
- W. Bednarek and R. J. Protheroe. Gamma Rays and Neutrinos from the Crab Nebula Produced by Pulsar Accelerated Nuclei. *Physical Review Letters*, 79:2616–2619, 1997.
- C. R. Benn and S. L. Ellison. Brightness of the night sky over La Palma. *New Astronomy Review*, 42:503–507, November 1998.
- K. Bernlohr. Impact of atmospheric parameters on the atmospheric Cherenkov technique\*. *Astroparticle Physics*, 12:255–268, January 2000.

- M. Bertero. Linear inverse and ill-posed problems. *Electronics and Electron Physics*, 75, 1989.
- A. Biland. Private Communication, 2006.
- D. Bisello, Y. Gotra, V. Jejer, V. Kushpil, N. Malakhov, A. Paccagnella, Z. Sadygov, I. Stavitsky, and E. Tsyganov. Silicon avalanche detectors with negative feedback as detectors for high energy physics. *Nuclear Instruments and Methods in Physics Research A*, 367:212–214, December 1995.
- P. Blasi. On the Origin of Very High Energy Cosmic Rays. *Modern Physics Letters A*, 20:3055–3076, 2005. doi: 10.1142/S0217732305019213.
- R. K. Bock, A. Chilingarian, M. Gaug, F. Hakl, T. Hengstebeck, M. Jiřina, J. Klaschka, E. Kotrč, P. Savický, S. Towers, A. Vaiciulis, and W. Wittek. Methods for multidimensional event classification: a case study using images from a Cherenkov gamma-ray telescope. *Nuclear Instruments and Methods in Physics Research A*, 516:511–528, January 2004. doi: 10.1016/S0168-9002(03)02505-1.
- S. V. Bogovalov and F. A. Aharonian. Very-high-energy gamma radiation associated with the unshocked wind of the Crab pulsar. *MNRAS*, 313:504–514, April 2000.
- S. Bowyer, E. T. Byram, T. A. Chubb, and H. Friedman. Lunar Occultation of X-ray Emission from the Crab Nebula. *Science*, 146:912–917, November 1964a.
- S. Bowyer, E. T. Byram, T. A. Chubb, and H. Friedman. X-Ray Sources in the Galaxy. *Nature*, 201:1307–+, 1964b.
- L. Breiman. Random Forests. *Machine Learning*, 45:5–32, 2001. doi: 10.1023/A:1010933404324.
- T. Bretz. *Observation of the Active Galactic Nucleus 1ES1218+304 with the MAGIC telescope*. PhD thesis, 2006.
- C. Brink, O. C. de Jager, B. C. Raubenheimer, H. I. Nel, A. R. North, D. J. van der Walt, G. van Urk, B. Visser, R. Buccheri, C. M. Carollo, L. Scarsi, V. Schoenfelder, M. Varendorf, and P. von Ballmoos. MeV to TeV gamma-ray observations of PSR 1957 + 20. *ApJ*, 364:L37–L40, December 1990. doi: 10.1086/185869.
- I. Britvich et al. Study of avalanche microchannel photodiodes for use in scintillation detectors. *JINST*, 1:P08002, 2006.
- T. Bulik, B. Rudak, and J. Dyks. Spectral features in gamma-rays expected from millisecond pulsars. *MNRAS*, 317:97–104, September 2000.
- P. Buzhan, B. Dolgoshein, L. Filatov, A. Ilyin, V. Kantzerov, V. Kaplin, A. Karakash, F. Kayumov, S. Klemm, E. Popova, and S. Smirnov. Silicon photomultiplier and its possible applications. *Nuclear Instruments and Methods in Physics Research A*, 504:48–52, May 2003.
- G. Castelleti, G. Dubner, K. Golap, W. M. Goss, P. F. Velazquez, M. Holdaway, and A. P. Rao. New high-resolution radio observations of the SNR CTB 80. *ArXiv Astrophysics e-prints*, October 2003.
- Chandra. Picture of the Crab Nebula in X-Rays, 1999. URL <http://chandra.harvard.edu/photo/0052/>.
- Chandra. Composite Picture of the Crab nebula, 2006. URL <http://www.chandra.harvard.edu/photo/2006/crab/>.
- S. Chandrasekhar. The highly collapsed configurations of a stellar mass. *MNRAS*, 91:456–466, March 1931.
- W.-Y. Chau. Gravitational Radiation from Neutron Stars. *ApJ*, 147:664–+, February 1967.

## BIBLIOGRAPHY

---

- K. Chen and M. Ruderman. Pulsar death lines and death valley. *ApJ*, 402:264–270, January 1993. doi: 10.1086/172129.
- K. S. Cheng, C. Ho, and M. Ruderman. Energetic radiation from rapidly spinning pulsars. I - Outer magnetosphere gaps. II - VELA and Crab. *ApJ*, 300:500–539, January 1986a. doi: 10.1086/163829.
- K. S. Cheng, C. Ho, and M. Ruderman. Energetic Radiation from Rapidly Spinning Pulsars. II. VELA and Crab. *ApJ*, 300:522–+, January 1986b. doi: 10.1086/163830.
- W. E. Cleland and E. G. Stern. Signal processing considerations for liquid ionization calorimeters in a high rate environment. *Nuclear Instruments and Methods in Physics Research A*, 338: 467–497, January 1994. doi: 10.1016/0168-9002(94)91332-3.
- W. J. Cocke, M. J. Disney, and D. J. Taylor. Discovery of Optical Signals from Pulsar NP 0532. *Nature*, 221:525–+, 1969.
- G. W. Collins, II, W. P. Claspy, and J. C. Martin. A Reinterpretation of Historical References to the Supernova of A.D. 1054. *PASP*, 111:871–880, July 1999.
- I. Contopoulos and D. Kazanas. Toward Resolving the Crab  $\sigma$ -Problem: A Linear Accelerator? *ApJ*, 566:336–342, February 2002. doi: 10.1086/324778.
- I. Contopoulos, D. Kazanas, and C. Fendt. The Axisymmetric Pulsar Magnetosphere. *ApJ*, 511: 351–358, January 1999. doi: 10.1086/306652.
- S. Cova, M. Ghioni, A. Lotito, I. Rech, and F. Zappa. Evolution and prospects for single-photon avalanche diodes and quenching circuits. *Journal of Modern Optics*, 51:1267–1288, September 2004.
- S. Cova, A. L. Lacaita, and G. Ripamont. Trapping phenomena in avalanche photodiodes on nanosecond scale. *IEEE Trans. Elec. Dev.*, 12:685–687, 1991.
- J. K. Daugherty and A. K. Harding. Electromagnetic cascades in pulsars. *ApJ*, 252:337–347, January 1982. doi: 10.1086/159561.
- J. K. Daugherty and A. K. Harding. Gamma-Ray Pulsars: Emission from Extended Polar CAP Cascades. *ApJ*, 458:278–+, February 1996. doi: 10.1086/176811.
- O. C. De Jager. On periodicity tests and flux limit calculations for gamma-ray pulsars. *ApJ*, 436: 239–248, November 1994. doi: 10.1086/174896.
- O. C. De Jager and A. K. Harding. The expected high-energy to ultra-high-energy gamma-ray spectrum of the Crab Nebula. *ApJ*, 396:161–172, September 1992. doi: 10.1086/171706.
- O. C. De Jager, A. K. Harding, P. F. Michelson, H. I. Nel, P. L. Nolan, P. Sreekumar, and D. J. Thompson. Gamma-Ray Observations of the Crab Nebula: A Study of the Synchro-Compton Spectrum. *ApJ*, 457:253–+, January 1996. doi: 10.1086/176726.
- O. C. De Jager, B. C. Raubenheimer, and J. W. H. Swanepoel. A powerful test for weak periodic signals with unknown light curve shape in sparse data. *A&A*, 221:180–190, August 1989.
- K. de Kort, P. Damink, and H. Boots. Spectrum emitted by hot electrons in p-i-n cold cathodes. *Phys. Rev. B*, 48:11912–11920, October 1993. doi: 10.1103/PhysRevB.48.11912.
- M. de Naurois, et al. Measurement of the Crab Flux above 60 GeV with the CELESTE Cerenkov Telescope. *ApJ*, 566:343–357, February 2002. doi: 10.1086/337991.
- B. Dolgoshein. Private Communication, 2006a.
- B. Dolgoshein. Talk given at Light06-Large-Area Photon Detectors Workshop, 2006b.

- E. Domingo-Santamaria et al. The DISP analysis method for point-like or extended gamma source searches/studies with the MAGIC Telescope. In *International Cosmic Ray Conference*, pages 363–+, 2005.
- EMIS Datareviews Series, No. 4. *Properties of Silicon*. The Institute of Electrical Engineers (IEE), London, 1988.
- R. A. Fesen, J. M. Saken, and J. M. Shull. Interaction between high-velocity pulsar in CTB80 and an infrared emission shell. *Nature*, 334:229–231, July 1988. doi: 10.1038/334229a0.
- J. M. Fierro. Observations of Spin-Powered Pulsars with the EGRET Gamma Ray Telescope. *Ph.D. Thesis*, 1996.
- J. M. Fierro, P. F. Michelson, P. L. Nolan, and D. J. Thompson. Phase-resolved Studies of the High-Energy Gamma-Ray Emission from the Crab, Geminga, and VELA Pulsars. *ApJ*, 494: 734–+, February 1998. doi: 10.1086/305219.
- V. P. Fomin, A. A. Stepanian, R. C. Lamb, D. A. Lewis, M. Punch, and T. C. Weekes. New methods of atmospheric Cherenkov imaging for gamma-ray astronomy. I. The false source method. *Astroparticle Physics*, 2:137–150, May 1994. doi: 10.1016/0927-6505(94)90036-1.
- A. S. Fruchter, G. Berman, G. Bower, M. Convery, W. M. Goss, T. H. Hankins, J. R. Klein, D. J. Nice, M. F. Ryba, D. R. Stinebring, J. H. Taylor, S. E. Thorsett, and J. M. Weisberg. The eclipsing millisecond pulsar PSR 1957 + 20. *ApJ*, 351:642–650, March 1990. doi: 10.1086/168502.
- A. S. Fruchter, J. E. Gunn, T. R. Lauer, and A. Dressler. Optical detection and characterization of the eclipsing pulsar’s companion. *Nature*, 334:686–689, August 1988a. doi: 10.1038/334686a0.
- A. S. Fruchter, D. R. Stinebring, and J. H. Taylor. A millisecond pulsar in an eclipsing binary. *Nature*, 333:237–239, May 1988b. doi: 10.1038/333237a0.
- H. Gajewski, B. Heinemann, H. Langmach, G. Telschow, and K. Zacharias. *TOSCA – Two dimensional Semiconductor Analysis Package*. Karl-Weierstraß Institut, Berlin, 1992.
- M. Garczarczyk. *First Observations of the GRB Prompt and Early Afterglow Emission Phase at  $\sim 100$  GeV Energy Regime with the 17m  $\varnothing$  MAGIC Imaging Atmospheric Cherenkov Telescope*. PhD thesis, 2007.
- M. Gaug. *Calibration of the MAGIC Telescope and Observation of Gamma Ray Bursts*. PhD thesis, 2006.
- T. Gold. Rotating Neutron Stars as the Origin of the Pulsating Radio Sources. *Nature*, 218:731–+, 1968.
- T. Gold. Rotating Neutron Stars and the Nature of Pulsars. *Nature*, 221:25–+, 1969.
- P. Goldreich and W. H. Julian. Pulsar Electrodynamics. *ApJ*, 157:869–+, August 1969.
- V. Golovin and V. Saveliev. Novel type of avalanche photodetector with Geiger mode operation. *Nuclear Instruments and Methods in Physics Research A*, 518:560–564, February 2004. doi: 10.1016/j.nima.2003.11.085.
- P. Goret, T. Palfrey, A. Tabary, G. Vacanti, and R. Bazer-Bachi. Observations of TeV gamma rays from the Crab nebula. *A&A*, 270:401–406, March 1993.
- R. J. Gould. High-Energy Photons from the Compton-Synchrotron Process in the Crab Nebula. *Physical Review Letters*, 15:577–579, October 1965. doi: 10.1103/PhysRevLett.15.577.
- J. Grahl, I. Kronquist, R. Rusack, A. Singovski, A. Kuznetsov, Y. Musienko, S. Reucroft, J. Swain, K. Deiters, Q. Ingram, D. Renker, and T. Sakhelashvili. Radiation hard avalanche photodiodes for CMS ECAL. *Nuclear Instruments and Methods in Physics Research A*, 504:44–47, May 2003.

- P. C. Gregory and T. J. Loredo. A new method for the detection of a periodic signal of unknown shape and period. *ApJ*, 398:146–168, October 1992. doi: 10.1086/171844.
- K. Greisen. End to the Cosmic-Ray Spectrum? *Physical Review Letters*, 16:748–750, April 1966. doi: 10.1103/PhysRevLett.16.748.
- A. K. Harding. Gamma-ray Pulsars: Models and Predictions. In F. A. Aharonian and H. J. Völk, editors, *American Institute of Physics Conference Series*, pages 115–+, 2001.
- A. K. Harding. Gamma Rays From Rotation-Powered Pulsars. *ArXiv Astrophysics e-prints*, August 2002.
- A. K. Harding. Emission From Rotation-Powered Pulsars: Is It All Relative? *ArXiv Astrophysics e-prints*, March 2005.
- A. K. Harding, M. G. Baring, and P. L. Gonthier. Photon-splitting Cascades in Gamma-Ray Pulsars and the Spectrum of PSR 1509-58. *ApJ*, 476:246–+, February 1997. doi: 10.1086/303605.
- A. K. Harding and T. K. Gaisser. Acceleration by pulsar winds in binary systems. *ApJ*, 358: 561–574, August 1990. doi: 10.1086/169009.
- A. K. Harding and D. Lai. Physics of strongly magnetized neutron stars. *Reports of Progress in Physics*, 69:2631–2708, 2006.
- A. K. Harding and A. G. Muslimov. Pulsar Polar Cap Heating and Surface Thermal X-Ray Emission. II. Inverse Compton Radiation Pair Fronts. *ApJ*, 568:862–877, April 2002. doi: 10.1086/338985.
- M. Hayashida, R. Mirzoyan, and M. Teshima. Development of HPDs with an 18-mm-diameter GaAsP photocathode for the MAGIC-II. *Nuclear Instruments and Methods in Physics Research A*, 567:180–183, November 2006. doi: 10.1016/j.nima.2006.05.213.
- T. Hengstebeck. *In preparation*. PhD thesis, 2006.
- V. Hess. Über Beobachtungen der durchdringenden Strahlung bei sieben Freiballonfahrten. *Physik. Zeitschr.*, 12:1083, 1912.
- J. J. Hester, K. Mori, D. Burrows, J. S. Gallagher, J. R. Graham, M. Halverson, A. Kader, F. C. Michel, and P. Scowen. Hubble Space Telescope and Chandra Monitoring of the Crab Synchrotron Nebula. *ApJ*, 577:L49–L52, September 2002. doi: 10.1086/344132.
- A. Hewish, S. J. Bell, J. D. Pilkington, P. F. Scott, and R. A. Collins. Observation of a Rapidly Pulsating Radio Source. *Nature*, 217:709–+, 1968.
- D. A. Hill and N. A. Porter. Photography of Čerenkov Light from Extensive Air Showers in the Atmosphere. *Nature*, 191:690, 1961.
- A. M. Hillas. The Origin of Ultra-High-Energy Cosmic Rays. *ARA&A*, 22:425–444, 1984. doi: 10.1146/annurev.aa.22.090184.002233.
- A. M. Hillas. Čerenkov light images of EAS produced by primary gamma. In F. C. Jones, editor, *International Cosmic Ray Conference*, pages 445–448, August 1985.
- A. M. Hillas, C. W. Akerlof, S. D. Biller, J. H. Buckley, D. A. Carter-Lewis, M. Catanese, M. F. Cawley, D. J. Fegan, J. P. Finley, J. A. Gaidos, F. Krennrich, R. C. Lamb, M. J. Lang, G. Mohanty, M. Punch, P. T. Reynolds, A. J. Rodgers, H. J. Rose, A. C. Rovero, M. S. Schubnell, G. H. Sembroski, G. Vacanti, T. C. Weekes, M. West, and J. Zweerink. The Spectrum of TeV Gamma Rays from the Crab Nebula. *ApJ*, 503:744–+, August 1998. doi: 10.1086/306005.

- J. G. Hills. The effects of sudden mass loss and a random kick velocity produced in a supernova explosion on the dynamics of a binary star of arbitrary orbital eccentricity - Applications to X-ray binaries and to the binary pulsars. *ApJ*, 267:322–333, April 1983. doi: 10.1086/160871.
- J. A. Hinton, G. Hermann, P. Kroetz, and S. Funk. Precision Measurement of Optical Pulsation using a Cherenkov Telescope. *ArXiv Astrophysics e-prints*, April 2006.
- K. Hirotani. Gamma-ray emission from pulsars: strength of the acceleration field in the outer gap. *MNRAS*, 317:225–233, September 2000.
- K. Hirotani. Gamma-Ray Emissions from Pulsars: Spectra of the TEV Fluxes from Outer Gap Accelerators. *ApJ*, 549:495–508, March 2001. doi: 10.1086/319038.
- K. Hirotani. in press. *ApJ*, 2006a.
- K. Hirotani. paper in preparation. 2006b.
- K. Hirotani. Particle Accelerator in Pulsar Magnetospheres: Super Goldreich-Julian Current with Ion Emission from the Neutron Star Surface. *ArXiv Astrophysics e-prints*, August 2006c.
- D. Horns, F. Aharonian, A. Santangelo, A. I. D. Hoffmann, and C. Masterson. Nucleonic gamma-ray production in Vela X. *A&A*, 451:L51–L54, June 2006. doi: 10.1051/0004-6361:20065116.
- M. Hoshino, J. Arons, Y. A. Gallant, and A. B. Langdon. Relativistic magnetosonic shock waves in synchrotron sources - Shock structure and nonthermal acceleration of positrons. *ApJ*, 390: 454–479, May 1992. doi: 10.1086/171296.
- F. Hoyle, J. V. Narlikar, and J. A. Wheeler. Electromagnetic Waves from Very Dense Stars. *Nature*, 203:914–+, 1964.
- R. A. Hulse and J. H. Taylor. Discovery of a pulsar in a binary system. *ApJ*, 195:L51–L53, January 1975.
- T. E. Ingerson, R. J. Kearney, and R. L. Coulter. Photon counting with photodiodes. *Appl. Opt.*, 22:2013–2018, July 1983.
- J. D. Jackson. *Classical Electrodynamics*. John Wiley & Sons, New York, third edition, 2003.
- J. V. Jelley and N. A. Porter. Čerenkov Radiation from the Night Sky, and its Application to  $\gamma$ -Ray Astronomy. *QJRAS*, 4:275–+, September 1963.
- Jodrell Bank Radio Telescope. Crab Pulsar monthly Ephemeris, 2006. URL <http://www.jb.man.ac.uk/pulsar/crab.html>.
- F. C. Jones. Calculated Spectrum of Inverse-Compton-Scattered Photons. *Physical Review*, 167: 1159–1169, March 1968. doi: 10.1103/PhysRev.167.1159.
- C. F. Kennel and F. V. Coroniti. Confinement of the Crab pulsar’s wind by its supernova remnant. *ApJ*, 283:694–709, August 1984a. doi: 10.1086/162356.
- C. F. Kennel and F. V. Coroniti. Magnetohydrodynamic model of Crab nebula radiation. *ApJ*, 283:710–730, August 1984b. doi: 10.1086/162357.
- W. J. Kindt. *Geiger Mode Avalanche Photodiode Arrays - For spatially resolved single photon counting*. PhD thesis, 1999.
- W. J. Kindt and H. W. van Zeijl. Modelling and fabrication of geiger mode avalanche photodiodes. *IEEE Trans. Nucl. Sci.*, 45:715–719, 1998.
- F. S. Kitaura, H.-T. Janka, and W. Hillebrandt. Explosions of O-Ne-Mg cores, the Crab supernova, and subluminescent type II-P supernovae. *A&A*, 450:345–350, April 2006. doi: 10.1051/0004-6361:20054703.

## BIBLIOGRAPHY

---

- S. R. Kulkarni, T. C. Clifton, D. C. Backer, R. S. Foster, and A. S. Fruchter. A fast pulsar in radio nebula CTB80. *Nature*, 331:50–53, January 1988a. doi: 10.1038/331050a0.
- S. R. Kulkarni, S. Djorgovski, and A. S. Fruchter. Probable optical counterpart of the eclipsing millisecond pulsar system, 1957 + 20. *Nature*, 334:504–506, August 1988b. doi: 10.1038/334504a0.
- A. Lacaita, M. Ghioni, F. Zappa, G. Ripamonti, and S. Cova. Recent advances in the detection of optical photons with silicon photodiodes. *Nuclear Instruments and Methods in Physics Research A*, 326:290–294, March 1993. doi: 10.1016/0168-9002(93)90366-P.
- A. L. Lacaita et al. On the bremsstrahlung origin of hot-carrier-induced photons in silicon devices. *IEEE Trans. Elec. Dev.*, 40:577–582, 1993.
- R. W. Lessard, I. H. Bond, S. M. Bradbury, J. H. Buckley, A. M. Burdett, D. A. Carter-Lewis, M. Catanese, M. F. Cawley, M. D’Vali, D. J. Fegan, J. P. Finley, J. A. Gaidos, G. H. Gillanders, T. Hall, A. M. Hillas, F. Krennrich, M. J. Lang, C. Masterson, P. Moriarty, J. Quinn, H. J. Rose, F. W. Samuelson, G. H. Sembroski, R. Srinivasan, V. V. Vassiliev, and T. C. Weekes. Search for Pulsed TEV Gamma-Ray Emission from the Crab Pulsar. *ApJ*, 531:942–948, March 2000. doi: 10.1086/308495.
- T.-P. Li and Y.-Q. Ma. Analysis methods for results in gamma-ray astronomy. *ApJ*, 272:317–324, September 1983. doi: 10.1086/161295.
- X. H. Li, F. J. Lu, and T. P. Li. X-Ray Spectroscopy of PSR B1951+32 and Its Pulsar Wind Nebula. *ApJ*, 628:931–937, August 2005. doi: 10.1086/430941.
- M. S. Longair. *High Energy Astrophysics, Volume I*. Cambridge University Press, second edition, 1997.
- S. Malcom Longair. *High Energy Astrophysics*. Cambridge University Press, 1992.
- R. Lorimer. Binary and Millisecond Pulsars. *Living Rev. Relativity*, 8, 2005. URL <http://www.livingreviews.org/lrr-2005-7> (cited on 2006-09-26).
- F. Lucarelli et al. Development and first results of the MAGIC central pixel system for optical observations. In *International Cosmic Ray Conference*, pages 367–+, 2005.
- S. C. Lundgren, J. M. Cordes, M. Ulmer, S. M. Matz, S. Lomatch, R. S. Foster, and T. Hankins. Giant Pulses from the Crab Pulsar: A Joint Radio and Gamma-Ray Study. *ApJ*, 453:433–+, November 1995. doi: 10.1086/176404.
- G. Lutz, R. Richter, and L. Strüder. Avalanche Strahlungsdetektor, German patent DE 10 2004 022 948, granted 01.06.2006, 2006.
- A. Lyne. Private Communication, 2006.
- P. Majumdar, B. S. Acharya, P. N. Bhat, D. Bose, V. R. Chitnis, M. A. Rahman, B. B. Singh, and P. R. Vishwanath. Preliminary Results from the Crab Nebula with the PACT Array. In *The Universe Viewed in Gamma-Rays, Tokio, Japan*, 2002.
- R. N. Manchester, G. B. Hobbs, A. Teoh, and M. Hobbs. The Australia Telescope National Facility Pulsar Catalogue. *AJ*, 129:1993–2006, April 2005. doi: 10.1086/428488. URL <http://www.atnf.csiro.au/research/pulsar/psrcat/>.
- G. Marsaglia. Choosing a point from the surface of a sphere. *Annals of Mathematical Statistics*, 43:645–646, 1972.
- F. C. Michel. Theory of pulsar magnetospheres. *Reviews of Modern Physics*, 54:1–66, January 1982.

- J. M. Migliazzo, B. M. Gaensler, D. C. Backer, B. W. Stappers, E. van der Swaluw, and R. G. Strom. Proper-Motion Measurements of Pulsar B1951+32 in the Supernova Remnant CTB 80. *ApJ*, 567:L141–L144, March 2002. doi: 10.1086/340002.
- R. Mirzoyan and E. Lorenz. On the Calibration Accuracy of Light Sensors in Atmospheric Cherenkov, Fluorescence and Neutrino Experiments. In *25th ICRC, Durban, South Africa*, 1997.
- R. Mirzoyan, D. Sobczynska, E. Lorenz, and M. Teshima. Tagging single muons and other long-flying relativistic charged particles by ultra-fast timing in air Cherenkov telescopes. *Astroparticle Physics*, 25:342–348, June 2006. doi: 10.1016/j.astropartphys.2006.03.006.
- D.-S. Moon, J.-J. Lee, S. S. Eikenberry, B.-C. Koo, S. Chatterjee, D. L. Kaplan, J. J. Hester, J. M. Cordes, Y. A. Gallant, and L. Koch-Miramond. PSR B1951+32: A Bow Shock-confined X-Ray Nebula, a Synchrotron Knot, and an Optical Counterpart Candidate. *ApJ*, 610:L33–L36, July 2004. doi: 10.1086/423238.
- W. W. Moses. Current trends in scintillator detectors and materials. *Nuclear Instruments and Methods in Physics Research A*, 487:123–128, July 2002.
- A. G. Muslimov and A. K. Harding. Extended Acceleration in Slot Gaps and Pulsar High-Energy Emission. *ApJ*, 588:430–440, May 2003. doi: 10.1086/368162.
- A. Musquere. Search for VHE pulsed emission from the Crab with the CAT telescope. In *International Cosmic Ray Conference*, pages 460–+, August 1999.
- P. L. Nolan, et al. Observations of the Crab pulsar and nebula by the EGRET telescope on the Compton Gamma-Ray Observatory. *ApJ*, 409:697–704, June 1993. doi: 10.1086/172699.
- E. Oña-Wilhelmi, J. Cortina, O. C. de Jager, and V. Fonseca. Determination of the night sky background around the Crab pulsar using its optical pulsation. *Astroparticle Physics*, 22:95–102, October 2004. doi: 10.1016/j.astropartphys.2004.04.011.
- W. G. Oldham et al. Triggering phenomena in avalanche diodes. *IEEE Trans. Elec. Dev.*, 19: 1056–1060, 1972.
- T. Oosterbroek, J. H. J. de Bruijne, D. Martin, P. Verhoeve, M. A. C. Perryman, C. Erd, and R. Schulz. Absolute timing of the Crab Pulsar at optical wavelengths with STJs. *ArXiv Astrophysics e-prints*, June 2006.
- S. Oser, D. Bhattacharya, L. M. Boone, M. C. Chantell, Z. Conner, C. E. Covault, M. Dragovan, P. Fortin, D. T. Gregorich, D. S. Hanna, R. Mukherjee, R. A. Ong, K. Ragan, R. A. Scalzo, D. R. Schuette, C. G. Théoret, T. O. Tümer, D. A. Williams, and J. A. Zweerink. High-Energy Gamma-Ray Observations of the Crab Nebula and Pulsar with the Solar Tower Atmospheric Cerenkov Effect Experiment. *ApJ*, 547:949–958, February 2001. doi: 10.1086/318415.
- A. N. Otte, J. Barral, B. Dolgoshein, J. Hose, S. Klemin, E. Lorenz, R. Mirzoyan, E. Popova, and M. Teshima. A test of silicon photomultipliers as readout for PET. *Nuclear Instruments and Methods in Physics Research A*, 545:705–715, June 2005. doi: 10.1016/j.nima.2005.02.014.
- A. N. Otte et al. Prospects of using silicon photomultipliers for the astroparticle physics experiments euso and magic. *IEEE Trans. Nucl. Sci.*, 53:636–640, 2006.
- A. N. Otte, J. Hose, R. Mirzoyan, A. Romaszkiwicz, M. Teshima, and A. Thea. A measurement of the photon detection efficiency of silicon photomultipliers. *Nuclear Instruments and Methods in Physics Research A*, 567:360–363, November 2006. doi: 10.1016/j.nima.2006.05.145.
- Nepomuk Otte. The silicon photomultiplier: A new device for high energy physics, astroparticle physics, industrial and medical applications. 2006. In the Proceedings of 9th International Symposium on the Detector Development for Particle, Astroparticle and Synchrotron Radiations Experiments (SNIC 2006), Menlo Park, California, 3-6 Apr 2006.

- F. Pacini. Energy Emission from a Neutron Star. *Nature*, 216:567–+, 1967.
- D. Paneque. *The MAGIC Telescope: development of new technologies and first observations*. PhD thesis, 2005.
- D. Paneque, H. J. Gebauer, E. Lorenz, M. Martinez, K. Mase, R. Mirzoyan, A. Ostankov, and T. Schweizer. A method to enhance the sensitivity of photomultipliers for air Cherenkov telescopes. *Nuclear Instruments and Methods in Physics Research A*, 504:109–115, May 2003.
- B. Pichler et al. A  $4 \times 8$  apd array, consisting of two monolithic silicon wafers, coupled to a 32-channel lso matrix for high-resolution pet. *IEEE Trans. Nucl. Sci.*, 48:1391–1396, 2001.
- B. Pichler et al. Lso block detector readout by apd arrays for high resolution animal pet. *Phys. Med. Biol.*, 49:4305–4319, 2004.
- B. J. Pichler, E. Lorenz, R. Mirzoyan, L. Weiss, and S. I. Ziegler. Production of a diffuse very high reflectivity material for light collection in nuclear detectors. *Nuclear Instruments and Methods in Physics Research A*, 442:333–336, March 2000.
- E. Popova. Private Communication, 2004.
- R. J. Protheroe. Origin and Propagation of the Highest Energy Cosmic Rays. In M. M. Shapiro, R. Silberberg, and J. P. Wefel, editors, *Towards the Millennium in Astrophysics, Problems and Prospects. International School of Cosmic Ray Astrophysics 10th Course*, pages 3–+, 1998.
- P. V. Ramanamurthy, D. L. Bertsch, B. L. Dingus, J. A. Esposito, J. M. Fierro, C. E. Fichtel, S. D. Hunter, G. Kanbach, D. A. Kniffen, Y. C. Lin, A. G. Lyne, J. R. Mattox, H. A. Mayer-Hasselwander, M. Merck, P. F. Michelson, C. von Montigny, R. Mukherjee, P. L. Nolan, and D. J. Thompson. EGRET Detection of Pulsed Gamma Radiation from PSR B1951+32. *ApJ*, 447:L109+, July 1995. doi: 10.1086/309572.
- M. J. Rees and J. E. Gunn. The origin of the magnetic field and relativistic particles in the Crab Nebula. *MNRAS*, 167:1–12, April 1974.
- D. W. Richards and J. M. Comella. The Period of Pulsar NP0532. *Nature*, 222:551–+, 1969.
- W. A. Rolke, A. M. López, and J. Conrad. Limits and confidence intervals in the presence of nuisance parameters. *Nuclear Instruments and Methods in Physics Research A*, 551:493–503, October 2005. doi: 10.1016/j.nima.2005.05.068.
- R. W. Romani. Gamma-Ray Pulsars: Radiation Processes in the Outer Magnetosphere. *ApJ*, 470: 469–+, October 1996. doi: 10.1086/177878.
- M. A. Ruderman and P. G. Sutherland. Theory of pulsars - Polar caps, sparks, and coherent microwave radiation. *ApJ*, 196:51–72, February 1975.
- Saint Gobain, 2004. URL <http://www.saint-gobain.com>.
- E. T. Scharlemann, J. Arons, and W. M. Fawley. Potential drops above pulsar polar caps - Ultrarelativistic particle acceleration along the curved magnetic field. *ApJ*, 222:297–316, May 1978. doi: 10.1086/156144.
- F. Schmidt. Search for Pulsed TeV Gamma-Ray Emission from Pulsars with H.E.S.S. Master’s thesis, Humboldt University, Berlin, 2005.
- E. Sciacca et al. Silicon planar technology for single-photon optical detectors. *IEEE Trans. Elec. Dev.*, 50:918–925, 2003.
- S. Selberherr. *Analysis and Simulation of Semiconductor Devices*. Springer-Verlag, Wien, 1984.

- A. Shearer, B. Stappers, P. O'Connor, A. Golden, R. Strom, M. Redfern, and O. Ryan. Enhanced Optical Emission During Crab Giant Radio Pulses. *Science*, 301:493–495, July 2003. doi: 10.1126/science.1084919.
- A. Spitkovsky. Time-dependent Force-free Pulsar Magnetospheres: Axisymmetric and Oblique Rotators. *ApJ*, 648:L51–L54, September 2006. doi: 10.1086/507518.
- R. Srinivasan, P. J. Boyle, J. H. Buckley, D. A. Carter-Lewis, M. Catanese, M. F. Cawley, E. Colombo, D. J. Fegan, J. P. Finley, J. A. Gaidos, J. Bussons Gordo, A. M. Hillas, F. Krennrich, R. C. Lamb, R. W. Lessard, J. M. McEnery, P. Moriarty, J. Quinn, H. J. Rose, F. W. Samuelson, G. Sembroski, T. C. Weekes, C. Wilson, and J. Zweerink. Very High Energy Observations of PSR B1951+32. *ApJ*, 489:170–+, November 1997. doi: 10.1086/304781.
- D. H. Staelin and E. C. Reifenstein. Pulsating radio sources near the Crab Nebula. *Science*, 162: 1481–1483, 1968.
- B. W. Stappers, B. M. Gaensler, V. M. Kaspi, M. van der Klis, and W. H. G. Lewin. An X-ray nebula associated with the millisecond pulsar B1957+20. *Science*, 299:1372–1374, 2003. doi: 10.1126/science.1079841.
- C. M. Straubmeier. *OPTIMA Entwicklung und erste astronomische Messungen eines optischen Hochgeschwindigkeitsphotometer*. PhD thesis, 2001.
- P. A. Sturrock. A Model of Pulsars. *ApJ*, 164:529–+, March 1971.
- J. H. Swoger and S. J. Kovacic. Enhanced luminescence due to impact ionization in photodiodes. *Journal of Applied Physics*, 74:2565–2571, August 1993.
- T. Tanimori, K. Sakurazawa, S. A. Dazeley, P. G. Edwards, T. Hara, Y. Hayami, S. Kamei, T. Kifune, T. Konishi, Y. Matsubara, T. Matsuoka, Y. Mizumoto, A. Masaike, M. Mori, H. Muraishi, Y. Muraki, T. Naito, S. Oda, S. Ogio, T. Osaki, J. R. Patterson, M. D. Roberts, G. P. Rowell, A. Suzuki, R. Suzuki, T. Sako, T. Tamura, G. J. Thornton, R. Susukita, S. Yanagita, T. Yoshida, and T. Yoshikoshi. Detection of Gamma Rays of up to 50 TeV from the Crab Nebula. *ApJ*, 492: L33+, January 1998. doi: 10.1086/311077.
- J. H. Taylor, R. N. Manchester, D. J. Nice, J. M. Weisberg, Irwin A., and Wex N. Tempo pulsar timing package, 2000. URL <http://www.atnf.csiro.au/research/pulsar/tempo/>.
- D. J. Thompson. Gamma ray pulsars. In K. S. Cheng and G. E. Romero, editors, *ASSL Vol. 304: Cosmic Gamma-Ray Sources*, pages 149–+, October 2004.
- D. J. Thompson, M. Bailes, D. L. Bertsch, J. Cordes, N. D'Amico, J. A. Esposito, J. Finley, R. C. Hartman, W. Hermsen, G. Kanbach, V. M. Kaspi, D. A. Kniffen, L. Kuiper, Y. C. Lin, A. Lyne, R. Manchester, S. M. Matz, H. A. Mayer-Hasselwander, P. F. Michelson, P. L. Nolan, H. Ögelman, M. Pohl, P. V. Ramanamurthy, P. Sreekumar, O. Reimer, J. H. Taylor, and M. Ulmer. Gamma Radiation from PSR B1055-52. *ApJ*, 516:297–306, May 1999. doi: 10.1086/307083.
- A. N. Tikhonov and V. Ja. Arsenin. Methods of Solution of Ill-posed Problem - M. 1979.
- N. Tonello. *Study of the VHE  $\gamma$ -ray emission from the Active Galactic Nucleus 1ES1959+650*. PhD thesis, 2006.
- D. F. Torres and L. A. Anchordoqui. Astrophysical origins of ultrahigh energy cosmic rays. *Reports of Progress in Physics*, 67:1663–1730, 2004.
- N. Turini. Private Communication, 2006.
- V. V. Usov and D. B. Melrose. Pulsars with Strong Magnetic Fields - Polar Gaps Bound Pair Creation and Nonthermal Luminosities. *Australian Journal of Physics*, 48:571–+, 1995.

## BIBLIOGRAPHY

---

- G. Vacanti, M. F. Cawley, E. Colombo, D. J. Fegan, A. M. Hillas, P. W. Kwok, M. J. Lang, R. C. Lamb, D. A. Lewis, D. J. Macomb, K. S. O'Flaherty, P. T. Reynolds, and T. C. Weekes. Gamma-ray observations of the Crab Nebula at TeV energies. *ApJ*, 377:467–479, August 1991. doi: 10.1086/170376.
- A. Venkatesan, M. C. Miller, and A. V. Olinto. Constraints on the Production of Ultra-High-Energy Cosmic Rays by Isolated Neutron Stars. *ApJ*, 484:323–+, July 1997. doi: 10.1086/304304.
- S. Villa, A. L. Lacaita, and A. Pacelli. Photon emission from hot electrons in silicon. *Phys. Rev. B*, 52:10993–10999, October 1995. doi: 10.1103/PhysRevB.52.10993.
- R. M. Wagner. *Temporal and spectral characteristics of the VHE gamma-ray emission of four blazars as observed with the MAGIC telescope and a comparative study of the properties of VHE gamma-ray emitting blazars*. PhD thesis, 2006.
- R. M. Wagner et al. Observations of the Crab nebula with the MAGIC telescope. In *International Cosmic Ray Conference*, pages 163–+, 2005.
- Fridolin Weber. Strange quark matter and compact stars. *Prog. Part. Nucl. Phys.*, 54:193–288, 2005.
- T. C. Weekes, M. F. Cawley, D. J. Fegan, K. G. Gibbs, A. M. Hillas, P. W. Kowk, R. C. Lamb, D. A. Lewis, D. Macomb, N. A. Porter, P. T. Reynolds, and G. Vacanti. Observation of TeV gamma rays from the Crab nebula using the atmospheric Cerenkov imaging technique. *ApJ*, 342:379–395, July 1989. doi: 10.1086/167599.
- L. Woltjer. X-Rays and Type i Supernova Remnants. *ApJ*, 140:1309–1313, October 1964. doi: 10.1086/148028.
- W.-M. Yao, et al. Review of Particle Physics. *Journal of Physics G*, 33:1+, 2006. URL <http://pdg.lbl.gov>.
- G. T. Zatsepin and V. A. Kuz'min. Upper Limit of the Spectrum of Cosmic Rays. *Journal of Experimental and Theoretical Physics Letters*, 4:78–+, August 1966.
- G. Zech. Comparing statistical data to Monte Carlo simulation - parameter fitting and unfolding. Technical Report 95-113, DESY, 1995.





# Acknowledgement

I write this acknowledgement while staying on La Palma for the next fascinating project after my PhD thesis. Being here I very clearly remember the moment when I saw the MAGIC telescope for the first time and how impressed I was by its size. One hour later I helped Roger Firpo and Eva Domingo drilling a hole through the back side of the MAGIC camera for the installation of a fan. In this spirit of aiding one another it continued for the years thereafter.

I joined the MAGIC collaboration in January 2004 when the construction of the telescope had finished and commissioning began. Therefore, I thank all those, who had the great fun building the telescope. In particular I am indebted to Eckart Lorenz, who convinced me within half an hour that MAGIC is the experiment I want to join for the next years — it was the right decision. I am also much obliged for his continuous advice and support.

During my participation in the development of the BaSiPM I appreciated very much the scientific advice and efforts by Rainer Richter. I am also thankful to Jelena Ninkovic for carrying over my responsibilities such that I could concentrate writing my thesis.

I am very glad that Tessa Bayrante was reading this thesis and revising the English.

For the refereeing of my thesis and relaxed atmosphere during my thesis defense I thank Sigfried Bethke and Friedrich von Feilitzsch.

I am in great debt to Masahiro Teshima and Razmick Mirzoyan for many discussions, gentle guidance as well as financial support, which allowed me to attend many inspiring workshops.

The financial support provided by Thomas Schweizer during the last stage of thesis writing is very much appreciated.

The MAGIC group in Munich is a great place to stay. I am grateful for the many discussions and support by seniors, PhD-students and post-docs. Daniel Mazin was always good company during the last years and deserves a special acknowledgement as well as Florian Goebel, Pratik Majumdar and Robert Wagner for close scientific collaboration and a lot of fun. I will not forget Hendrik Bartko, Irina Bavykina, Rudi Bock, Emiliano Carmona, Toni Coarasa, Nicola Galante, Jürgen Gebauer, Markus Garczarczyk, Masaaki Hayashida, Jürgen Hose, Ching Cheng Hsu, Tobias Jogler, Patricia Liebing, Keiichi Mase, Satoko Mizobuchi, David Paneque, Emilija Pantic, Sybille Rodriguez, Anna Romaszkiwicz, Takayuki Saito, Maxim Shayduk, Kenji Shinozaki, Julian Sitarek, Virginia Spanoudaki, Nadia Tonello, Daniela Tridon, Vincenzo Vitale, Ina Wacker, Wolfgang Wittek and all the others for their contributions.

The success of an experimental work very much depends on the infrastructure available. The MPI für Physik is extraordinary in this respect. Many of my projects became reality only because of the possibilities in the institute and the continuous efforts by technicians like Lothar Weiss, who provided excellent mechanic work or, Wendelin Pimpl and Toni Dettlaff, who provided me with electronics.

When moving to Munich I could take advantage of being a member of a large family. As one example I gratefully acknowledge my cousin Konstanze who provided space for sleeping before I moved to the house of Uli Lynen. Uli also had the idea that I should apply in Munich.

I am very happy about the continuous interest of Herbert Orth in the work I am doing.

I finish as I have started this thesis; with Pia, my love who has been accompanying me since ten years, supporting me wherever possible and sharing life with me. She is my fortune.

... to be continued